Advanced Magnetostrictive Device for Non-Destructive Testing of Critical Assets
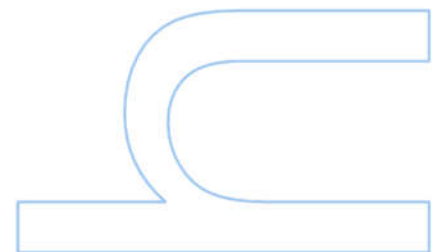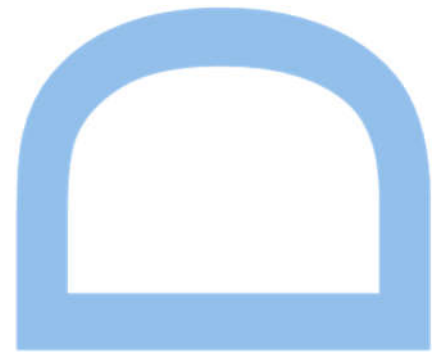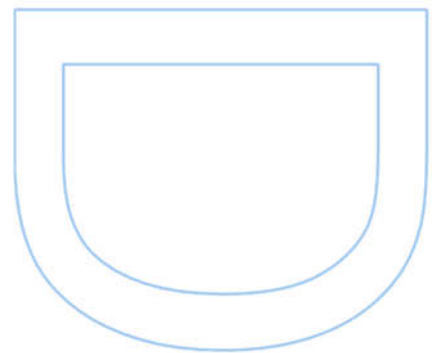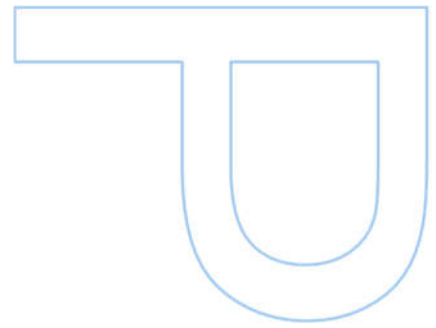
Joana Silva
MAP-fis Doctoral Program in Physics
Department of Physics and Astronomy
2023

Supervisor
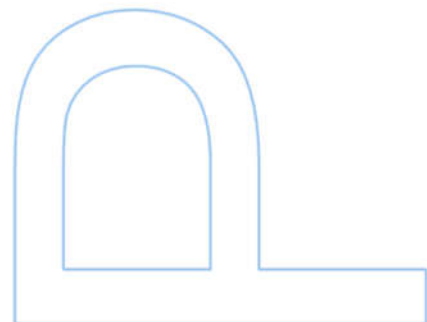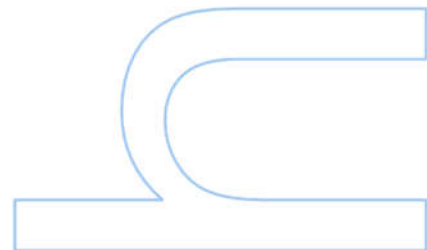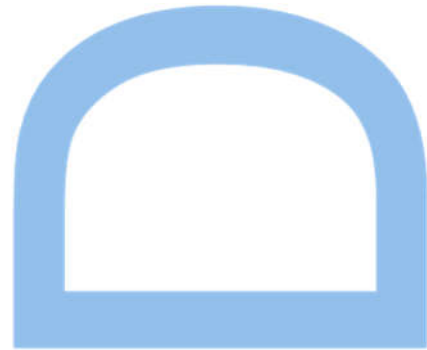Prof. Dr. André Miguel Trindade Pereira, Assistant Professor, FCUP
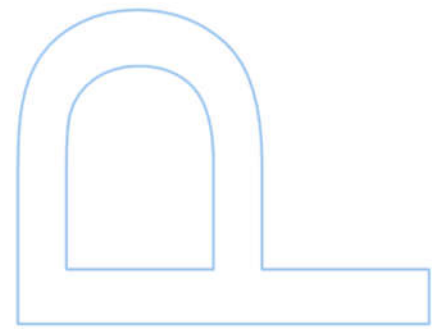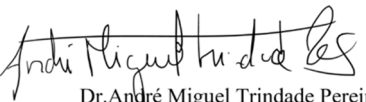
All the corrections determined by the jury, and only those, were made.

The Supervisor,

Dr. André Miguel Trindade Pereira

Porto, 1/08/2023
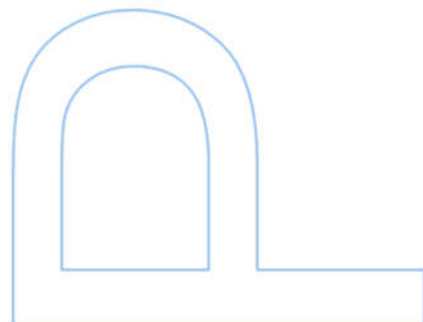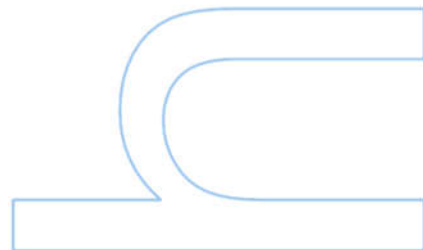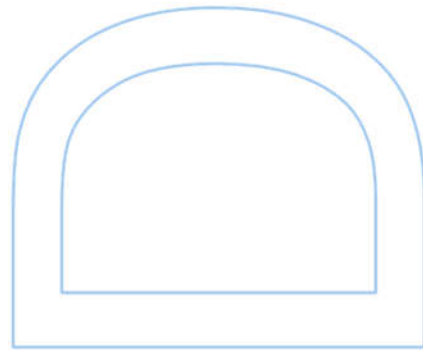
Dedicated to my family

Sworn Statement

I, Joana Alves Silva, enrolled in the Doctor's Degree MAP-fis at the Faculty of Sciences of the University of Porto hereby declare, in accordance with the provisions of paragraph a) of Article 14 of the Code of Ethical Conduct of the University of Porto, that the content of this thesis reflects perspectives, research work and my own interpretations at the time of its submission.

By submitting this thesis, I also declare that it contains the results of my own research work and contributions that have not been previously submitted to this or any other institution.

I further declare that all references to other authors fully comply with the rules of attribution and are referenced in the text by citation and identified in the bibliographic references section. This thesis does not include any content whose reproduction is protected by copyright laws.

I am aware that the practice of plagiarism and self-plagiarism constitute a form of academic offense.

6/01/2023

Acknowledgements

Over the course of my PhD thesis, I had the privilege of working with people and institutions that have cooperated with me, and without whom this thesis would not have been possible. I would like to thank:

Professor André Pereira, the supervisor of this work, for the challenge. Even though the past few years were tough, I could not be more grateful for the motivation and support that he was able to provide all the way. I sincerely thank you for the trust, the advice and for never giving up on me.

Helder Araujo, my co-supervisor at EQS Global, for giving me the opportunity to make science with a truthful impact. I am grateful for the challenge and for giving me a goal to this seemingly endless journey.

Doctor João Pedro Araújo, the head of IFIMUP-IN, who provided me an incredible opportunity to join the team during my time as a PhD student, granting me access to the laboratories and research facilities.

I am very grateful to all the teaching and research staff from the **MAP-fis program.** I am very grateful for my scholarship provided by FCT, SFRH/BD/143943/2019, that supported my tuition fees and paid my bills. Also, a big thank you to all the projects that supported my research, namely MAGSENSE, financed by Portugal 2020, POCI-01-0247-FEDER-033783, POCI-01-0247-FEDER-033783 and NORTE-01-0145-FEDER-022096 from NECL.

Doctor Maryam Sadeghi, who provided immeasurable support in the development of this project, particularly in the preparation of MAE samples.

Doctor Carlos Gouveia, Bruno Moreira and **Gabriel Dinis,** from EQS Global, for their constant collaboration, for keeping us on the track of the goal, and for kindly answering to my stupid questions.

Doctor Oscar and **Doctor Caroline**, from CMEMS, for their precious help in the mechanical characterization of samples and on the constant flows of new ideas.

Doctor Artur Pinto, from LEPABE (FEUP), for providing the means to perform mechanical characterization of the soft samples, for taking the time to figure out my struggles and providing unmatching advice. Thank you for the fruitful collaboration.

My closest friends, **Joana Sqiuts**, **Joana Almeida**, **Glória Gonçalves**, **João Pacheco**, **Pedro Cunha**, **Tiago Pinto**, **Tânia Carvalho**, **Margarida Martins** (and probably others that I will regret to forget, but my brain is exhausted). Life is so much better with you.

My closest and most important friend, **Gilberto Loureiro**. Thank you for the unconditional support, for drying my tears and for always providing the light at the end of the tunnel. Thank you for always keeping me on track to what is important.

Last, but certainly not the least, I would like to thank **my family**, my parents, and my siblings, who have always given me the right example in life. A particular thank you to my grandmother who is so proud of me!

Resumo

Em 2019, houve um total de 632 incidentes em oleodutos e gasodutos na Europa e nos EUA [1]–[4]. Incidentes nestas estruturas podem ser evitados, através da inspeção regular destes ativos e corrigindo quaisquer defeitos precocemente. Para isso utilizam-se técnicas de testes não-destrutivos (NDT), tais como testes ultrassónicos (UT). Este método tem sido usado para inspecionar dutos e usa geralmente transdutores piezoelétricos (PZ) ou acústico-eletromagnéticos (EMAT) para gerar e detetar ondas acústicas nos ativos. Devido às limitações destes sensores, como a alta manutenção e inadequação em muitas estruturas isolantes e não magnéticas, transdutores magnetostritivos estão a surgir como uma alternativa.

Sensores magnetostritivos (MsS) baseiam-se em materiais que se deformam com a variação da sua magnetização. Podem assim converter um campo magnético alternado numa onda acústica que se propaga num material adjacente. Estes materiais apresentam um elevado potencial por fornecerem um melhor desempenho e facilidade de instalação e operação. Assim, este trabalho, em estreita colaboração com a empresa EQS Global, consiste na elaboração de duas soluções MsS inovadoras em 2 configurações distintas: onda guiada (GW) e onda longitudinal (BW). O nosso foco nesta tese foi o desenvolvimento de transdutores com elevada magnetostrição, e 3 estratégias principais foram seguidas:

- 3D – A partir de uma fita comercial de FeCo-2V, otimizamos um tratamento térmico que resulta numa melhoria da magnetostrição e do desempenho do MsS.
- Compósitos magnetoreológicos (MAEs) – Obtivemos magnetostrição gigante misturando partículas ferromagnéticas numa matriz polimérica hiperelástica.
- 2D – Fabricamos um dispositivo magnetostritivo inovador utilizando filmes finos para aplicação em UT na configuração BW.

Na abordagem 3D, relatamos o efeito da temperatura do tratamento térmico (T_a) e da dinâmica de arrefecimento na evolução da microestrutura e estequiometria. Concluímos que o principal mecanismo a influenciar a evolução mecânica e magnética é o crescimento do grão. Também abordamos a evolução cristalográfica e mostramos que a oxidação resultante provoca mudanças estequiométricas na liga. Correlacionamos o desaparecimento da tensão interna com a diminuição da magnetostrição, visto que estão ligadas pelo acoplamento magnetoelástico. O aumento da magnetostrição de saturação (74ppm) com T_a>650ºC foi associado à formação de uma fase fcc de Fe-Co.

Quanto aos MAEs, estes foram preparados com partículas de FeCo-2V com 2 geometrias diferentes: esférica e helicoidal, ambas utilizando distribuições de partículas isotrópicas e anisotrópicas na gama de concentrações entre 0.3vol% e 25.6vol%. Os MAEs de partículas helicoidais exibem menos resistência e ductilidade devido às arestas afiadas das partículas, que resulta na acumulação de tensão nesses pontos. Nos MAEs com partículas esféricas, H=6500 Oe é suficiente para quase saturar a magnetostrição, enquanto os MAEs de partículas helicoidais exibem uma tendência linear com o campo magnético, indicando que ainda estão longe da saturação. A magnetostrição gigante foi obtida em todas as composições de MAEs, inclusivamente na menor VF=0.6vol%, tendo sido o maior valor obtido com o MAE de partículas esféricas de 9.2vol% (6 649ppm).

Na abordagem 2D, produzimos um dispositivo inovador que consiste num sensor totalmente integrado com bobinas de emissão e deteção e um filme fino magnetostritivo, que foi produzido por deposição por *magnetron sputtering*. A influência do substrato e de espessura foi investigada. A formação de duas fases bcc de FeCo com o aumento da espessura é relatada. A segunda fase é formada quando a espessura (t) >100nm e exibe uma forte textura (110) perpendicular ao plano. Demonstramos que a coexistência das duas fase resulta na alteração das propriedades magnéticas e no aumento da resistividade elétrica.

Finalmente, os materiais desenvolvidos foram testados como transdutores nas duas configurações de UT. As fitas 3D foram implementadas com sucesso no set-up GW UT, com um aumento de desempenho (V_{pk}>0.1V) que supera em muito a fita original de FeCo-2V (V_{pk}=0.032V), aumentando o sinal em 357 vezes. Os MAEs com partículas esféricas, apesar da magnetostrição DC gigante, foram incapazes de gerar ondas acústicas com modo de torção nítido, devido à incapacidade de reter remanência magnética e à forte atenuação de vibração da matriz. Os MAEs com partículas helicoidais fornecem um sinal mais claro, mas alcançando apenas uma fração do obtido pela fita FeCo-2V (V_{pk}=0.032V). O uso de nanotubos de carbono para melhorar a transmissibilidade da vibração mecânica resultou num aumento de sinal de cerca de 25%. Os filmes finos no dispositivo BW UT também tiveram sucesso em melhorar a operação em comparação com um EMAT, mas apenas em filmes com espessura de 400nm e 800nm, levando a uma melhoria de 50%. Um método alternativo foi usado para produzir revestimentos magnetostritivos de alta concentração para BW UT. O revestimento consiste em partículas esféricas de FeCo-2V embebidas numa solução de

álcool polivinílico (PVA) e aplicado diretamente na superfície do tubo. O sinal melhorou mais de 65x em relação ao do EMAT.

Os resultados obtidos neste trabalho representam um avanço na utilização de técnicas de NDT baseadas em sistemas magnetostritivos. Pelo seu carácter inovador, estas soluções permitirão à EQS e a Portugal aumentar a sua competitividade internacional no campo de NDT.

Palavras-chave: Magnetostrição, Ferromagnetismo, Ligas Ferro-Cobalto, Elastómeros magneto-ativos, Deformação magneto-induzida, Testes ultrassónicos, Sensores, Filmes finos

Abstract

There has been a total of 632 pipeline incidents in 2019 in Europe and the USA combined [1]–[4]. Pipeline incidents can be avoided by inspecting these assets and correcting any defects in advance. These defects can be identified using non-destructive testing (NDT) techniques, such as ultrasonic testing (UT). This method has been in use to test pipelines and mainly uses piezoelectric (PZ) or electromagnetic acoustic transducers (EMAT) to generate and detect acoustic waves in the pipe. Due to limitations of these sensors, such as high maintenance and inadequacy in many insulating and non-magnetic pipes, magnetostrictive transducers are emerging as an alternative.

Magnetostrictive sensors (MsS) are based on materials that deform with changing magnetization. Thus, they can convert an alternating magnetic field into an acoustic wave on an adjacent material. They have high potential as UT sensors given their ability to provide improved performance and ease of installation and operation. Thus, in close collaboration with EQS Global, we devised the development of two innovative MsS solutions in 2 different configurations: guided wave (GW) and bulk wave (BW). Our focus in this thesis was on the fabrication of transducers with large magnetostriction, and 3 main strategies were followed:

- 3D – From a commercial strip of FeCo-2V, we established a thermal treatment that can largely improve of the magnetostriction and MsS performance.
- Magnetoactive composites (MAEs) – We developed giant magnetostriction using FeCo-2V ferromagnetic particles embedded in polydimethylsiloxane (PDMS).
- 2D – Innovative magnetostrictive all-in-one device using thin films to be applied in UT in the BW configuration.

On the 3D approach, we report the effect of the annealing temperature (T_a) and the cooling dynamics on the evolution of the microstructure and stoichiometry. We concluded that the main mechanism behind mechanical and magnetic transformation is grain growth. We also report on the crystallographic evolution and showed that the oxidation caused by the annealing results in stoichiometric changes in the alloy. We correlated the vanishing of the internal stress with the decrease of the magnetostriction, as they are linked via the magnetoelastic coupling. The increase in saturation magnetostriction (74ppm) with $T_a \geq 650^\circ C$ was linked to the formation of an additional fcc Fe-Co phase.

The prepared composites were based on FeCo-2V particles with 2 different geometries: spherical and helicoidal, both with isotropic and anisotropic particle distributions in the concentration range between 0.3vol% and 25.6vol%. Helicoidal particle-MAEs exhibit

less strength and ductility because of the particles' sharp edges that promote stress concentration. In the MAEs with spherical particles, H=6500 Oe is sufficient to nearly saturate magnetostriction, while the helicoidal particle-MAEs exhibit a linear trend with the magnetic field, indicating they are still far from saturation. Giant magnetostriction was obtained in every MAE composition, even in the lowest concentration of VF=0.6vol%, being the largest value obtained with the 9.2vol% spherical particle MAE (6 649ppm).

In the 2D approach, we produced an innovative device consisting of a fully integrated sensor with emission and detection coils, and a magnetostrictive thin film prepared using magnetron sputtering. The influence of the substrate and the thickness of the film was investigated. The formation of two FeCo bcc phases with incremental thickness is reported. The second phase is formed when the thickness (t) is >100nm and it exhibits a strong (110) off-plane texture. We show that the coexistence of the two phases can result in changes in the magnetic properties of the film and lead to increased electrical resistivity.

Finally, towards the main application, the materials were tested as transducers in the UT set-ups. The strips were successfully implemented in the GW UT set-up, with an increase in performance (V_{pk}>0.1V) that largely surpasses that of the original strip of FeCo-2V (V_{pk}=0.032V), increasing the signal by 357-fold. The MAEs with spherical particles, despite the giant magnetostriction, were unable to generate acoustic waves with a clear guided wave mode, due to the inability to retain magnetic remanence and the strong vibration attenuation of the matrix. MAEs with helicoidal particles yield a clearer signal but only achieving a fraction of that obtained by the FeCo-2V strip (V_{pk}=0.032V). The use of carbon nanotubes to improve the transmissibility of the mechanical vibration yielded an increase in the signal of about 25%. The thin films in the BW UT device were also successful in improving the operation compared to an EMAT, but only in films with thickness of 400nm and 800nm, leading to an improvement in 50%. An alternative method was used to produce high concentration magnetostrictive coatings for BW UT. The coating consisted of spherical FeCo-2V particles embedded in a polyvinyl-alcohol (PVA) solution and applied directly on the surface of the pipe. The signal was improved by more than 65x with respect to the EMAT operation.

Due to its innovative character, these solutions will allow EQS and Portugal to increase their international competitiveness in the NDT field. The obtained results represent a step forward in the use of NDT techniques based on magnetostrictive systems.

Keywords: Magnetostriction, Ferromagnetism, Iron-Cobalt alloys, Magnetoactive elastomers, Magneto-induced deformation, Ultrasonic testing, Sensors, Thin films

Table of Contents

List of Tables

List of Figures

List of Abbreviations (by alphabetical order)

AE	Acoustic Emission
BCC	Body Centered Cubic
BSE	Backscattered Electrons
BW	Bulk Wave
CEMUP	Centro de Materiais da Universidade do Porto
CMEMS	Center for Microelectromechanical Systems
CNT	Carbon Nanotubes
CPU	Control and Processing Unit
DGAOT	Departamento de Geociências, Ambiente e Ordenamento do Território
ECT	Eddy Current Testing
EDS	Energy Dispersive X-ray Spectroscopy
EGIG	European Gas pipeline Incident Group
EMAT	Electromagnetic Acoustic Transducer
FCC	Face Centered Cubic
FCUP	Faculty of Sciences of the University of Porto
FM	Ferromagnetic
GF	Gauge Factor
GW	Guided Wave
IFIMUP	Institute of Physics for Advanced Materials, Nanotechnology and Photonics
INMA	Instituto de Nanociencia y Materiales de Aragón
LEPAB	Laboratory for Process Engineering, Environment, Biotechnology and Energy
MPI	Magnetic Particles Inspection
MAE	Magnetoactive Elastomer
MR	Magnetorheological Effect
MsS	Magnetostrictive Sensor
NDT	Non-Destructive Testing
PDMS	Polydimethylsiloxane
PHMSA	Pipeline and Hazardous Materials Safety Administration
PM	Paramagnetic
PT	Penetrant Testing
PVA	Polyvinyl-Alcohol

PZT	Lead-Zirconate-Titanate
Q	Quenched
RI	Radiographic Inspection
SB	Seeman-Bohlin (geometry)
SC	Slow Cooled
SE	Secondary Electrons
SEM	Scanning Electron Microscopy
SQUID	Superconducting Quantum Interference Device
SWRI	Southwest Research Institute
UP	University of Porto
UT	Ultrasonic Testing
UT	Ultrasonic Inspection
VF	Volume Fraction
VSM	Vibrating Sample Magnetometer
VT	Visual Testing
XRD	X-Ray Diffraction
XRR	X-Ray Reflectometry

List of Symbols (by order of appearance)

a	Lattice parameter
d	Average grain size
$(dM/dH)_{H=0}$	Magnetization sensitivity to magnetic field / magnetic susceptibility at H=0
E	Young's modulus
f	Frequency
FeCo-2V	2%V-FeCo
H	Magnetic field intensity
H_c	Coercive field
I	Electrical current
I_{sp}	Sputtering current
M	Magnetization
M_r	Remanent magnetization
M_s	Saturation magnetization
p_w	Work Pressure (sputtering chamber)
P_w	Sputtering power
R	Electrical resistance
R_d	Sputtering deposition rate
t	Thickness
t_a	Annealing temperature
T_c	Curie temperature
$T_{order-disorder}$	Order-disorder transition temperature
V	Voltage
V_{pk}	Peak voltage
ε	Mechanical strain
ε_{frac}	Strain at fracture point
ρ	Electrical resistivity
ρ^*	Volumetric mass density
λ	Magnetostriction
λ_{iso}	Magnetostriction in isotropic MAEs
λ_s	Saturation magnetostriction
$\lambda_{||}$	Magnetostriction in anisotropic As in the particle alignment direction
μ_0	Vacuum magnetic permeability

θ	X-ray diffraction angle with sample surface
$\boldsymbol{\sigma}$	Mechanical stress
$\boldsymbol{\sigma_y}$	Yield stress

Outline

Regular inspection of petrochemical electrical power generation facilities and infrastructure is critical to ensure safety and avoid health and environmental disasters. The periodic evaluation of the integrity of these infrastructures requires non-destructive testing (NDT) as well as equipment that can withstand demanding conditions (e.g. high temperatures, corrosive environment, etc). Ultrasonic testing (UT) is a non-hazardous and versatile method used in pipeline inspection. It consists of the propagation of acoustic waves in the medium under test. Any defects or discontinuities (such as oxidation or mechanical deformation) can be detected since they cause reflections of the acoustic wave, such that the distance at which they are located can be estimated. UT can cover up to 100m in length in one single reading point, which makes it a very attractive NDT method.

Generally, UT sensors are based on piezoelectric (PZ) transducers or electromagnetic acoustic transducers (EMAT). These types of sensors have some limitations including high maintenance and limited number of materials they can test on. An alternative solution is the Magnetostrictive Sensor (MsS), which is based on a magnetostrictive transducer. It consists of the coupling of a magnetostrictive transducer to an EMAT configuration. MsS can operate at high temperatures, and are not limited on the type of material they can test on. The large cost of large magnetostriction materials is the primary reason MsS have yet to establish themselves in the UT market.

The demand for inexpensive magnetostrictive transducers highlights the potential of the Fe-Co alloy. This material is typically used for its high magnetic saturation and large permeability and finds its main application as a soft ferromagnet in the aerospace and automotive industries. Generally, such applications require excellent soft ferromagnetic properties, such that the manufacturing of the Fe-Co alloy aims at the minimization of the magnetostriction, to avoid energy loss. Consequently, limited work has been done regarding the enhancement of magnetostriction in the Fe-Co system.

We concentrated our efforts on the investigation of this alloy and demonstrated that giant magnetostrictive materials could be fabricated and tailor-made. In this endeavour, we've collaborated with EQS Global, an industrial partner focused to developing a competitive MsS, due to its commitment to bringing innovation to their products.

Main Objective

The creation of high-performance magnetostrictive materials based on Fe-Co alloys to use as transducers in UT devices is the main objective of this thesis. For this purpose, we devised three distinct material development strategies: bulk strips, microparticles, and nanometer-sized thin films.

This strategy has produced scientific breakthroughs as well as attained practical industrial applications.

Scientific achievements

The research that was conducted within this work has resulted in relevant scientific and technical contributions, summarized below.

Development of materials with giant magnetostriction: the production of magnetorheological composites of low concentration using off-the-shelf precursors and in-house prepared materials has yielded a substantial improvement of the magnetostriction of such materials with respect to the state of the art.

Tailoring of the magnetostriction in a FeCo-2V strip: the magnetostriction of these alloys is profoundly related to their magnetic and mechanical properties. The relationship of the crystal structure and morphology with the physical properties of Fe-Co alloys thus enables the tailoring of the magnetostrictive performance. This work has provided the understanding of the evolution of the magnetoelasticity with other properties of the ternary Fe-Co system, which was absent from the literature.

Establishment of magnetostrictive transducers as a viable alternative to PZ and EMAT in the ultrasonic testing industry. These two achievements were key milestones in the collaboration with EQS Global since they resulted in two commercial solutions.

- ***Guided wave UT:*** we were able to implement a simple procedure to transform a commercial strip of FeCo-2V into a high-performance magnetostrictive transducer, with a signal that surpasses that of the current competitor.
- ***Bulk wave UT:*** a high-concentration composite coating made of ferromagnetic FeCo-2V particles embedded in a soft PVA matrix was able to

generate and detect bulk acoustic waves with an amplitude 65x greater than the EMAT alternative.

Structure of the Dissertation

This document is organised in 7 chapters that include the motivation and overview of the state of the art, the experimental techniques that were used, the results and discussion, and the main conclusions and technological achievements, finishing with future perspectives.

Chapter 1 introduces the motivation behind this work, namely the need to develop high performance, easy to use and affordable NDT equipment for pipes. A review of the state-of-the-art of such methods is provided, along with the introduction to ultrasonic testing, the different configurations and the transducers that are currently in use. The magnetostrictive sensor is presented as a viable alternative with considerable advantages with respect to PZ and EMAT. A brief theoretical context is provided of the magnetostriction in ferromagnetic materials.

Chapter 2 is focused on the description of the experimental methods that were used in this work and is clustered into two main sections: the sample preparation techniques (where a description of the prepared samples is provided) and the physical characterization techniques.

Chapter 3 entails the description of the work and of the evolution of the physical properties of a strip of FeCo-2V with different thermal treatments, involving annealing temperatures from 450ºC to 850ºC and different cooling rates. A correlation between different characteristics of the alloy and the magnetostriction is established.

Chapter 4 is dedicated to the development of soft composites with giant magnetostriction. The magnetoactive elastomers (MAEs) with concentration ranging from 0.6vol% to 25.6vol% were characterized, and a thorough discussion of the properties is presented. A comparison between MAEs prepared with particles of different shape, size and particle distribution is provided.

Chapter 5 addresses the structural, magnetic, and electrical characterization of FeCo thin films prepared by magnetron sputtering. The influence of the thickness of the film (50nm to 850nm) on the physical properties is investigated. It also describes the fabrication of an innovative magnetostrictive device using thin film transducers.

Chapter 6 is dedicated to the application of the developed magnetostrictive materials of Chapters 3, 4 and 5 as transducers in both guided wave and bulk wave Magnetostrictive Sensor set-ups. The results of the tests are discussed and compared with the measured properties of each material. Alternative materials that were developed with the acquired knowledge are investigated and tested as well.

Chapter 7 closes the circle by highlighting the main conclusions. Our perspective on the future work is also described.

List of contributions

The work performed in this thesis in collaboration with EQS yielded several outstanding achievements in the form of industrial solutions, but also as scientific milestones.

Patents

"Couplant-free, all-in-one, flexible magnetostrictive sensor for non-destructive ultrasonic inspection and monitoring", Under preparation, Inventors: Joana Silva, André Pereira, Oscar Carvalho, Carlos Gouveia, Gabriel Dinis, Bruno Moreira

Articles in international scientific journals

Silva, J. A., C. Gouveia, G. Dinis, A. M. Pinto, A. M. Pereira., "Giant magnetostriction in low-concentration magnetorheological elastomers." *Composites Part B: Engineering* 243 (2022): 110125.

Moura, C., **Silva, J. A.**, Gouveia, C., Dinis, G., Pereira, A. M., Carvalho, O., **"Effect of alloying elements (V, Cu and Ti) on the magnetic and magnetostrictive properties and microstructure of FeCo alloy"**, in preparation (2023)

Silva, J. A., Moreira, B., Gouveia, C., Dinis, G., Lucas, I., Morellón, L., Carvalho, O., Pereira, A. M., **"Tailoring the physical properties and magnetostriction of Hiperco 50 via thermal treatment"**[1], in preparation (2023)

---

[1] Subject to change

Silva, J. A., Strichovanec, P., Moreira, B., Gouveia, C., Dinis, G., Lucas, I., Morellón, O., Pereira, A. M., **"Thin films FeCo: effect of thickness on the structural properties"**[2], in preparation (2023)

International and national conferences with oral presentations

Silva, J.A., Moreira, B., Gouveia, Pinto, A. M., C., Dinis, H. Pereira, A. M., "Giant magnetostriction in magnetorheological elastomers." 4th International Conference on Material Science and Nanotechnology (ICMSN 2022), online, 24-25 March, 2022

Silva, J.A., Moreira, B., Gouveia, C., Dinis, H. Pereira, A. M., "Morphological, magnetic and magnetoelastic properties of annealed FeCo-2V alloy." 4th International Workshop on Materials and Design (MatDes 2022), Udine, Italy, 18-20 March, 2022

Silva, J.A., Gouveia, C., Pereira, A. M., "Large magnetic field-induced strain in low concentration magnetorheological elastomers." 4th Doctoral Congress in Engineering (DCE2021), Porto, Portugal, 28-29 June, 2021

Silva, J.A., Gouveia, C., Dinis, G., Araújo, H. Pereira, A. M., "Non-Destructive Testing Using Advanced Magnetorheological Elastomers." 3rd Doctoral Congress in Engineering (DCE19), Porto, Portugal, 27-28 June, 2019

Silva, J.A., Gouveia, C., Dinis, G., Araújo, H. Pereira, A. M., "Innovative Magnetostrictive Inks Towards Monitoring Applications", (E-MRS 2019), Nice, France, 27-31 May, 2019

Proceedings

Silveira, B.M., Belo, J.H., Pinto, R., **Silva, J.A.**, Ferreira, T.D., Pires, A.L., Chu, V., Conde, J.P., Frazão, O. and Pereira, A.M., "Magnetostriction in Amorphous Co66Fe34 Microcantilevers Fabricated with Hydrogenated Amorphous Silicon." *EPJ Web of Conferences*, vol. 233, p. 05003. EDP Sciences, 2020.

---

[2] Subject to change

International and national conferences with poster presentations

Silva, J. A., Gouveia, C., Dinis, Pereira, A. M., "Effect of Particle Shape in Giant Magneto-Induced Deformation in Magnetoactive Elastomers." 23º Encontro Nacional de Física (Física 2022), Porto, Portugal, 7-10 September, 2022

Silva, J. A., Gouveia, C., Dinis, G., Araújo, H., Pereira, A. M., "Composite Magnetostrictive Transducer for Monitoring Applications." 4as Jornadas em Engenharia Física, Física, Física Médica e Astronomia 2019 (JEFFA2019), Porto, Portugal, 16 May, 2019.

Awards

Best poster presentation award, "Effect of Particle Shape in Giant Magneto-Induced Deformation in Magnetoactive Elastomers." 23º Encontro Nacional de Física (Física 2022), Porto, Portugal, 7-10 September, 2022

Best presentation award, "Morphological, magnetic and magnetoelastic properties of annealed FeCo-2V alloy." 4th International Workshop on Materials and Design (MatDes 2022), Udine, Italy, 18-20 March, 2022

Chapter 1   Introduction

1.1   The current state of pipelines in Europe and the US

There is an underestimated length of oil and gas pipelines of 1.6M km worldwide [5]. These structures enable the direct transportation of hazardous liquids, gases and water from their sources to gathering centers and to the end consumer. Pipelines are arguably one of the safest ways to transport hazardous fluids (gas and oil-related liquids) over long distances [6]. Long-distance pipelines have been seeing a rise in popularity since the 1950s, but little to no records were kept on the length, capacity, and the properties of these structures for a long time [7]. As demand increased, new pipelines were built, while keeping the ones from the mid-20th century in use, despite their outdated construction methods and ageing material. As the mileage of pipelines rose, so did the incidents related to their use [8]. Pipeline incidents have a catastrophic potential, since they can lead to fires, explosions, and massive spillages, resulting in possible supply interruption, casualties, infrastructural damage, wildlife impact and contamination of drinking water supplies [6].

This led to the establishment formal groups responsible for the gathering of data related to pipelines and their incidents, but also for the introduction of regulations and certification. Notably, the Pipeline and Hazardous Materials Safety Administration (PHMSA) keeps a detailed public record of USA pipeline related incidents, and European Gas pipeline Incident Group (EGIG) (gas pipelines) and Concawe (oil pipelines) in Europe. They have, however, significantly different reporting criteria, therefore their data should be compared conservatively. In 2019, PHMSA reports to have been a total of 614 pipeline incidents in the USA [3], [4]. In Europe in 2019, only 17 have been reported [1], [2]. The substantial difference is related to the massive difference in total pipeline length, estimated to be 180,000km [1], [2] in Europe (Figure 1.1) and about 4,500,000km in the USA [9]! But also, the fact that pipelines in the USA have long lacked regulatory standards and the respective enforcement as opposed to pipelines in Europe.
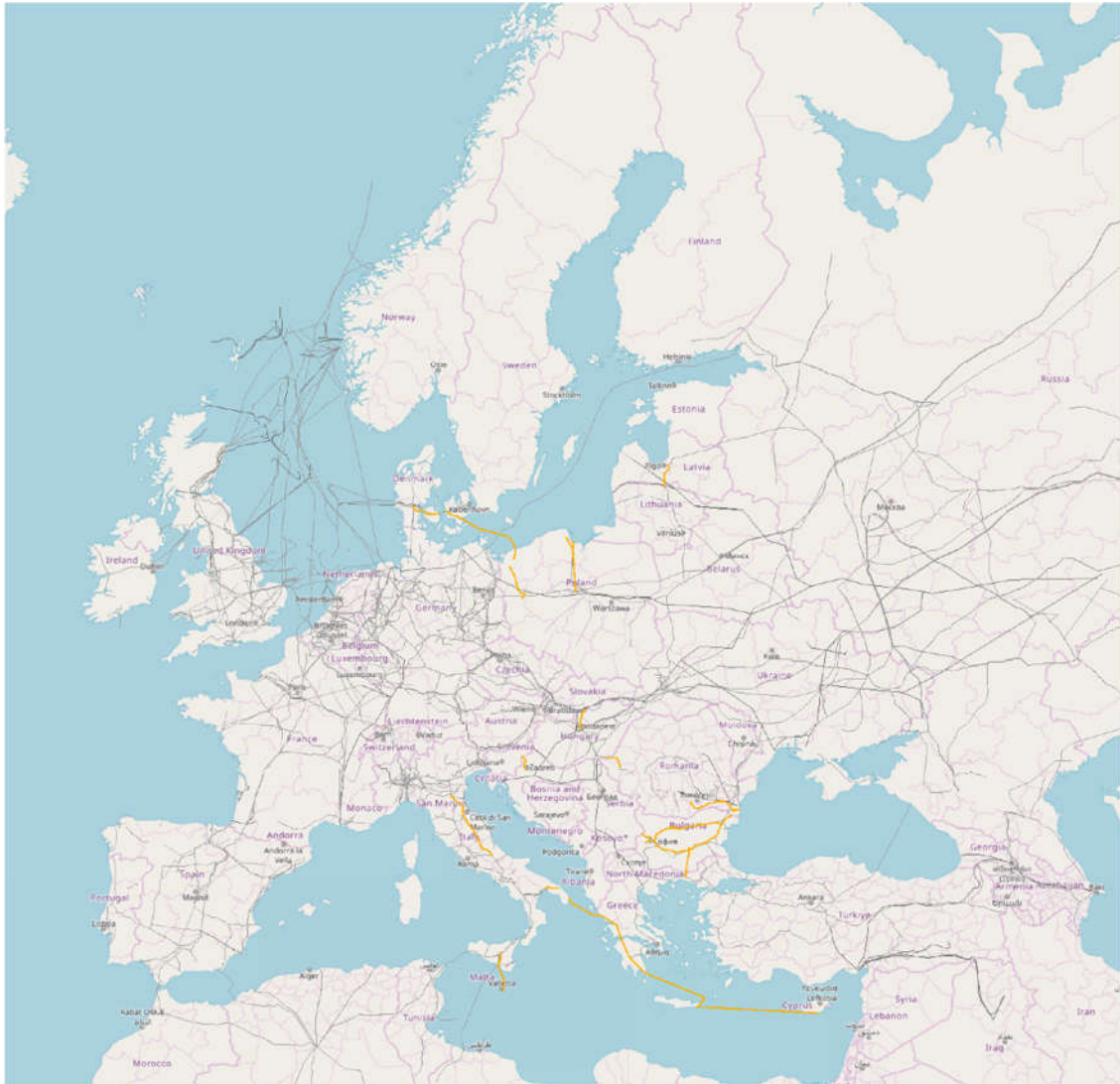
Figure 1.1 – Distribution of oil and gas pipelines (existing and proposed) in Europe and connecting with Europe, obtained from the Climate, Infrastructure and Environment Executive Agency / Energy of the European Commission [10]. The yellow lines represent gas pipelines, and the grey lines represent oil and oil products pipelines.

Pipeline failure is caused mainly by corrosion, construction defects, mechanical damage, manufacturing defects and natural disasters. Figure 1.2 shows some defects that can occur in a pipeline [11]. In the USA, PHMSA reports that 38% and 15% of the incidents were related to equipment/material failure and to corrosion, respectively. In Europe, EGIG reports that 26% and 15.8% are due to corrosion and material failure, being external interference the main reason for incidents to occur (27.2%). This highlights the difference in infrastructure safety regulation between the USA and Europe. The US Department of Transportation [12] compiled the causes of significant onshore incidents in both hazardous liquids and gas transmission pipelines from 2006-2010. The data in plotted in Figure 1.3.

Figure 1.2 – Examples of defects that can be found in pipelines (adapted from [11]).

Belvederesi and Dann [13] have compiled PHMSA data between 2010 and 2015 and established a relationship between the pipeline properties (location, year of installation, diameter and maximum allowable operating pressure) and the consequence of pipeline accidents, such as ignition, explosion, fatalities, property damage and spilled volume. They concluded that the largest ignitions rates occurred for recently installed large diameter and high operating pressure liquid pipelines. Larger injury rates are caused by small diameter distribution pipelines located in areas with high population density, while higher property damaged occurs in incidents in older transmission pipelines in sparsely populated areas. The number of incidents has steadily climbed down, due to increased quality inspection methods, but improvements are still necessary. Namely in the transition to automated methods, as well as the integration of full-time monitoring solutions. This can be achieved by implementing large-range inspection methods as well as by driving inspection costs down.

Hazardous Liquids

Gas Transmission

- Material and/or weld failures
- Incorrect operation
- Excavation damage
- Corrosion
- Natural force damage
- Other outside force damage
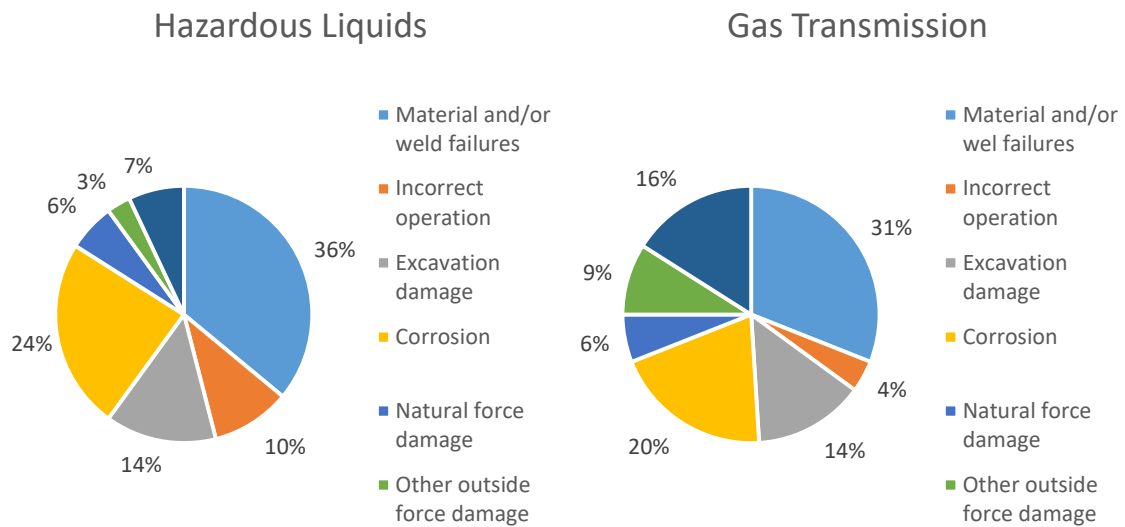
Figure 1.3 – Causes of pipeline significant incidents in the US in the period of 2006-2010 [12].

There are a number of ways to prematurely assess the integrity of a pipe. Usually, inspectors and technicians look for defects in pipes that can eventually lead to a disruption of the structure. A defect is an imperfection in a product that can restrict its service life by impeding its performance, eventually causing it to fail. These anomalies can arise during the manufacturing stages or during the operation of the product. Such anomalies must be detected, and if possible, rectified in advance [14].

1.2   Non-Destructive testing of pipelines

The goal of testing is to inspect the quality of the infrastructure, to analyze its structure and detect defects prematurely. The range of techniques usually employed are called Non-Destructive Testing (NDT) methods and they are used to inspect assets without causing them any damage [14]. NDT is important when the asset under testing is either an expensive equipment, is under permanent operation, or is difficult to replace.

The methods of NDT that are adequate to pipelines can be aggregated in the following clusters: visual inspection, penetrant testing, magnetic particle inspection, radiographic testing, ultrasonic testing, eddy current testing and acoustic emissions. A brief explanation of each method as well as the major advantages and disadvantages is given in Table 1.1.

Table 1.1 – Summary of the main characteristics of some NDT techniques [14], [15]

Method	Operation mode	Advantages	Limitations
Visual Testing (VT)	Surface examination by visual aids. Can be performed directly, or remotely in sites that do not have proper accessibility.	Can be used in all stages of the product lifetime	Only surface anomalies are visible; very dependent on the inspector's experience
Penetrant Testing (PT)	A penetrant liquid is applied on the surface of the test specimen and fills any discontinuities that may be present. The surface anomalies become visible after the application of a developer.	Detection of surface anomalies of mass-manufactured products	Only surface anomalies are visible; complex process with a lot of variables affecting the result
Magnetic Particles Inspection (MPI)	Under the application of a magnetic field, a ferromagnetic material becomes magnetized in the field direction. Field lines bend around discontinuities if these are present. The magnetic particles are placed on the surface and will distribute along the field lines. If there is a leakage of the magnetic field, they will tend to accumulate in that area.	Detection of anomalies in the vicinity of the surface in ferromagnetic materials	Only sensitive to anomalies near the surface; only works in ferromagnetic materials with simple shapes; requires the surface of the material to be free of any coating
Radiographic Inspection (RI)	Radiation is emitted on the material (X-rays or gamma rays). In regions with anomalies, the attenuation of the radiation is different comparing to areas without discontinuities. This allows the detection of spotlights, where the anomalies are located.	Detection of surface and subsurface anomalies	Time consuming; expensive; safety hazards; waste disposal issues; dependent on the direction of the anomalies
Ultrasonic Testing (UT)	An acoustic pulse is propagated in the material. Any anomalies that exist will cause a disturbance in the wave, either changing its speed or causing a reflection of the sound. The detection of these changes in the wave property enables the identification of discontinuities.	Detection of surface and subsurface anomalies	Very small anomalies can go undetected; very dependent on the operator's experience; possible misinterpretation of signals can occur
Eddy Current Testing (ECT)	The eddy currents are induced by a DC and AC magnetic fields. Operates with the principles of Lorentz force and magnetostriction.	Detection of surface and subsurface anomalies in electrically conducting materials with or without coatings (e.g. paint)	Only works in electrically conducting materials and ferromagnetic materials
Acoustic Emission (AE)	Consists of the detection of elastic waves emitted by the deformation of the material. It is a passive technique, that only depends on the material and no external source.	Detection of surface and subsurface anomalies	Attenuation of the stress waves by the material; other sounds may cause misinterpretation

Bickestaff and co-authors [16] have compiled a review on sensor technology for natural gas pipelines using in-line inspection techniques. They present a critical analysis of the different methods, highlighting the major advantages and disadvantages of each. The NDT industry is moving towards more digitized solutions since it is generally understood that automated techniques present the least errors in sizing for internal defects and are less time-consuming and thus more cost efficient [17], [18]. Finally, it is expected that a wider inspection of pipes leads to further technological developments and eventually reduce the cost of NDT [19].

Comparing to other methods, ultrasound testing offers many advantages. The advantages will be addressed in the following section, as well as current limitations that need to be overcome.

1.3   Ultrasound testing of pipelines

UT has become a widespread technique for the inspection of assets given its high versatility and sensitivity. This defect detection method has been in use since 1942 [20] and gained popularity as a non-intrusive procedure, which eliminates the need of inserting inspection probes inside the pipeline that would require operation shutdowns. UT provides high penetrating power, sensitivity and accuracy comparing to other NDT methods. It is a non-hazardous technique to people, equipment, and materials. Operation-wise, it is a portable and highly automated system, and results can be immediately obtained. Depending on the configuration of the test, it enables the estimation of the size, orientation, shape, and nature of the defects. The technique has its shortcomings, like every other NDT method. Typically, experienced technicians are required to operate UT testing, and to correctly interpret data. Moreover, as it is a contact technique, rough or irregular shapes are often difficult to inspect, and proper preparation of the surface of the test specimen should be ensured. For these reasons, the use of various NDT methods is generally advised since they provide complementing data and allow for a better assessment of the state of the pipe.

The principle of operation of UT is that a directional wave will scatter when it encounters a discontinuity or an abrupt geometry change. The acoustic wave interacts with these discontinuities (Figure 1.4), generating differential time of arrival of the scattered waves, as well as changes in the wave amplitude and phase. Such changes provide information on the location, size, and orientation of the defect.
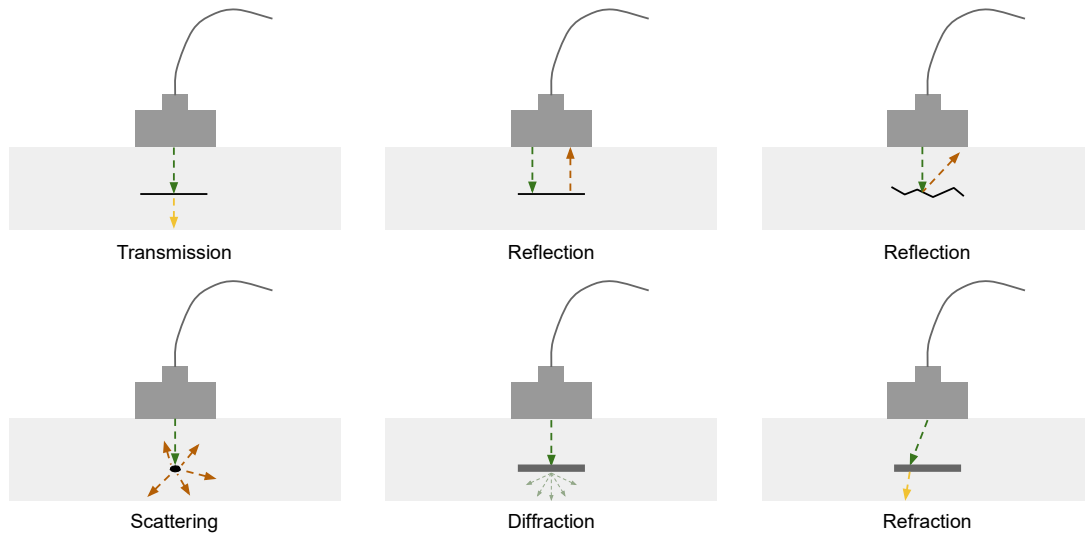
Figure 1.4 – Different interactions that the acoustic wave can have with a discontinuity of a test specimen.

There are two main configurations of UT: reflection (pulse-echo) and attenuation (pitch-catch). These configurations are illustrated in Figure 1.5. In the first arrangement, the emitter and receiver coils are the same, so that the signal that is read gives information on the distance of the anomaly. In the latter arrangement, two transducers are used independently for transmission and reception. In this case, the changes in signal amplitude provide information on the existence of defects.
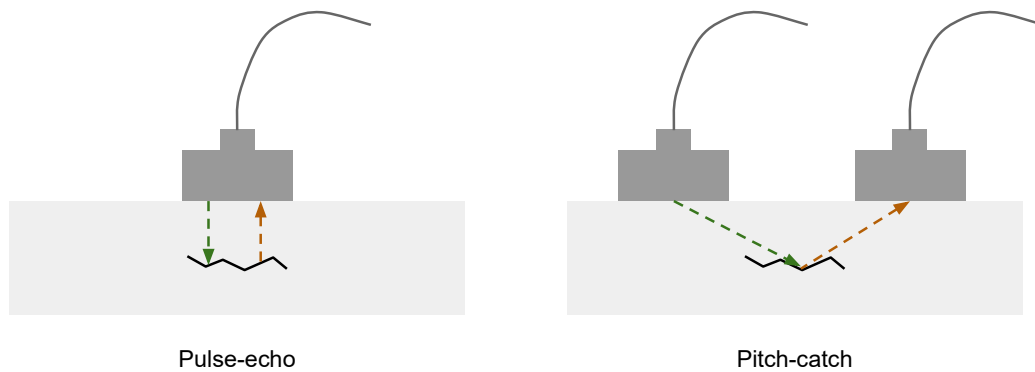
Figure 1.5 – The different configurations of UT: pulse-echo and pitch-catch.

1.3.1   Piezoelectric transducer

The commercial devices of UT usually employ piezoelectric (PZ) materials as transducers (Figure 1.6). These materials convert electrical voltage into deformation. An AC voltage can cause a cyclic compression-dilation deformation of the material, such that it vibrates at the frequency of the voltage oscillation. The vibration of the PZ in turn

generates an acoustic wave in the adjacent material. Lead-zirconate-titanate (PZT) is a widely used PZ material since it is easy to manufacture and has some of the largest piezoelectric coefficients at room temperature [21]. One of the main disadvantages of PZ materials in UT is the loss of electrical polarity, for which it requires frequent maintenance, as well as mechanical brittleness, aging and poor bonding [22]. Another great disadvantage is the fact the mostly used PZ materials contains Lead (Pb), which is highly hazardous for the environment and for humans. Some examples of commercial products using PZ transducers can be found in Table 1.2.

1.3.2   Electromagnetic acoustic transducers (EMAT)

Electromagnetic acoustic transducers (EMAT) induce the wave directly on the material under testing, so their operation is not so dependent on the quality of the interface compared to PZ (Figure 1.6). An EMAT consists on the superposition of a permanent magnetic field and a perpendicular oscillating magnetic field, typically generated by a permanent magnet and a coil, respectively. The principle of operation of these devices depends on the physical properties of the pipe. In the case of ferromagnetic pipes, the superposition of the magnetic fields results in the generation of an acoustic wave via the magnetostriction effect, in the case of a non-FM conductive material, an electromagnetic wave in generated by the Lorentz force. These waves propagate in the adjacent material and are affected by the interaction with discontinuities such as edges or defects. Due to its operation method, the use of EMAT is limited to either ferromagnetic or electrically conductive materials. Some examples of commercial products using EMAT can be found in Table 1.2.
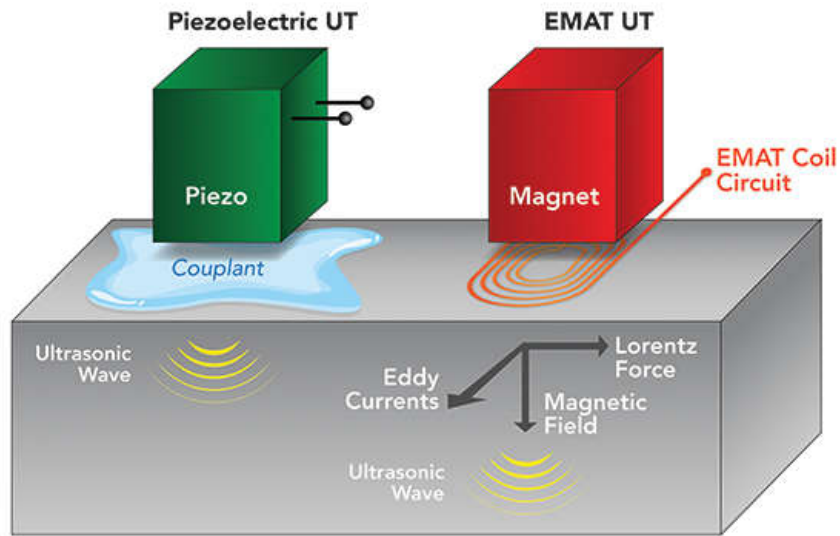
Figure 1.6 – Illustration of the operation of the piezoelectric transducer and the EMAT. Obtained from [23].

Table 1.2 – UT products for inspection of pipelines and their transducer

Supplier	Monitoring Solution	Transducer technology	Thickness measurement
Sensor Networks	Smart PIMS	Piezoelectricity	No
Permasense	ET210	EMAT	Yes
Mistras	Caliperay	EMAT	Yes
Clampon	CEM	EMAT	No
A3 Monitoring	Spoton U	Piezoelectricity	Yes

1.3.3 Magnetostrictive Sensors (MsS)

Magnetostrictive sensors (MsS) are a new class of UT sensors that have become increasingly popular [24]. They use a magnetostrictive transducer to generate an ultrasound wave which can be transmitted to an adjacent material. The sensor consists of the coupling of a magnetostrictive transducer to an EMAT, such that the sound wave is generated by the transducer. Magnetostrictive transducers are materials that can convert magnetization into mechanical deformation, and vice-versa. The magnetostrictive effect is detailed in Section 1.5 below. The combination of a bias field with an alternating magnetic field has the effect of generating an oscillating deformation

on the magnetostrictive transducer. This vibration then propagates as an acoustic wave to the adjacent material.

This enables the application of this sensor in a pipe of any material. Additionally, MsS require less power to drive measurements compared to PZ materials because the constant field can be generated by permanent magnets. Magnetostrictive transducers have the advantage that they can be made flexible, such that they can conform to curved surfaces. The availability of relatively inexpensive magnetostrictive materials is considered an opportunity to develop improved UT testing systems.
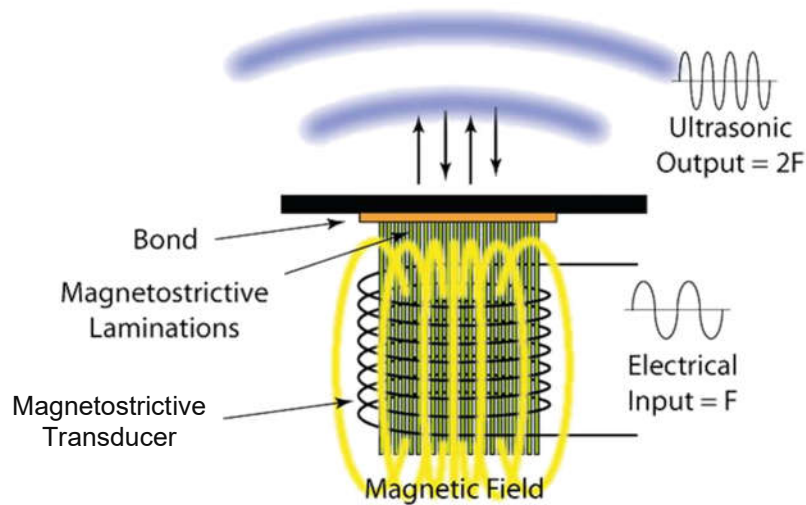
Figure 1.7 – Operation of an MsS (adapted from [25]).

The field of NDT is becoming more relevant, as concerns for health and safety are becoming more mainstream. The search for more sensitive and versatile solutions is driving the investigation for new and improved materials that can perform efficiently.

1.4   Principle of operation of a Magnetostrictive Sensor

NDT ultrasonic waves are mainly separated into two categories: bulk waves (BW) and guided waves (GW). The BW consist of longitudinal and shear modes. These types of waves are generally difficult to coherently propagate for long distances, and are mainly used for inspection near the detector, as they are simple to use and interpret. On the other hand, GW are typically employed in pipeline detection as they allow for long coverage lengths and offer fast scanning methods. GW can inspect up to 100 meters from the transducer position [14]. Figure 1.8 illustrates the direction propagation of the acoustic waves in guided wave UT and bulk wave UT.
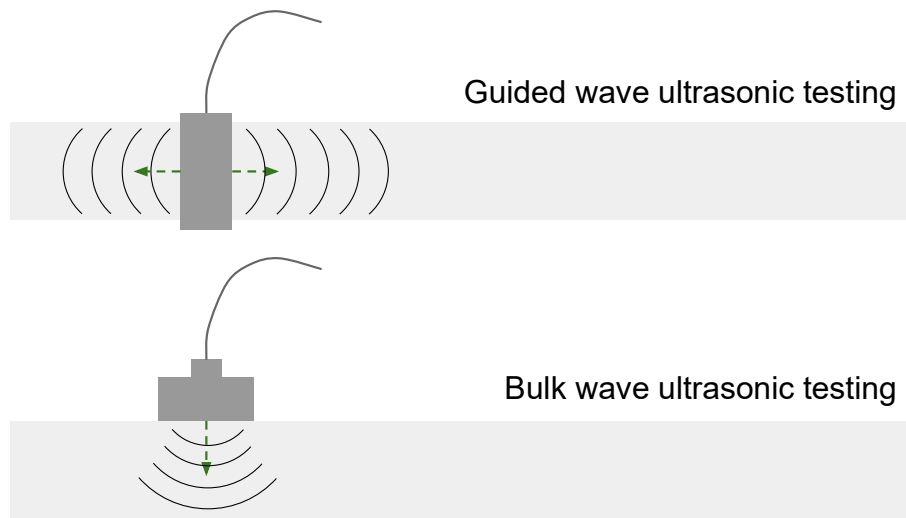
Figure 1.8 – Difference between BW and GW.

1.4.1   Guided wave testing using torsional guided waves

GW consists of the propagation of a torsional wave along the length of the pipe (Figure 1.9). Long distance testing is used to assess large areas of the pipe in one single reading point. The typical anomalies that can be detected include cracks, weld defects, etc. Used frequencies in this regime sit in the range of 20kHz to 200kHz. The use of low ultrasound frequencies reduces signal attenuation and avoids the generation of additional wave propagation modes that bring complexity to the signal interpretation. Figure 1.10 depicts the configuration of the MsS for GW testing. The transducer is the strip that encircles the pipe. The permanent field is oriented in the circumferential direction, and in the present case is generated by the transducer's remanent magnetization.
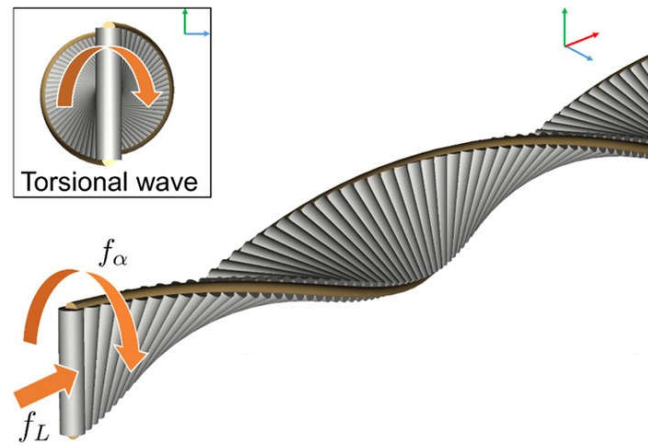
Figure 1.9 – Illustration of a torsional wave, adapted with permission from [26].

A dynamic magnetic field is induced by a solenoid coil surrounding the transducer. The interference of the perpendicular fields generates a shearing deformation in the transducer, by the Wiedemann effect. The transmission of the shearing deformation to the pipe results in the induction of a torsional wave [24]. The UT wave is emitted and propagates to both directions of the pipe. As previously mentioned and illustrated (Figure 1.5), the detection of the signal can be made using a second transducer, positioned at a distance from the emitter (pitch-catch), or the same emitter transducer can be used to detect scattered waves (pulse-echo).
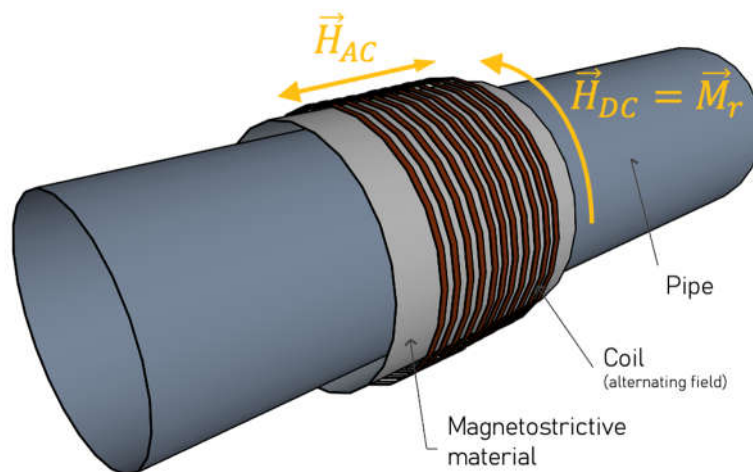
Figure 1.10 – Configuration of a magnetostrictive sensor which uses the remanent magnetization for the generation of a permanent magnetic field.

1.4.2 Conventional ultrasonic testing using bulk waves

Magnetostrictive sensors can also be designed to generate and measure bulk waves. In this configuration, the acoustic waves propagate through the thickness of the pipe and are mainly used to detect wall thinning and corrosion. This configuration uses high frequency UT, of the order of MHz. This enables the detection of small features with great accuracy.
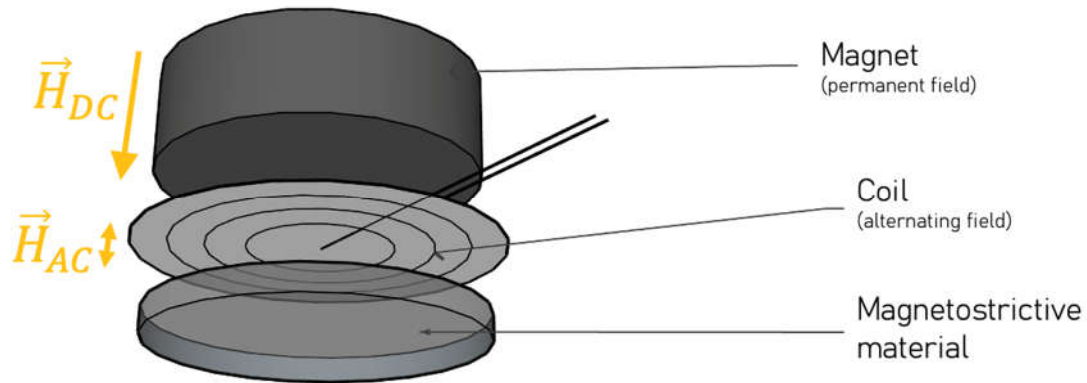
Figure 1.11 is an illustration of a MsS in a pulse-echo configuration. These sensors can also be produced in a pitch-catch configuration. The device consists of one permanent magnet and one meander coil (oscillating magnetic field).
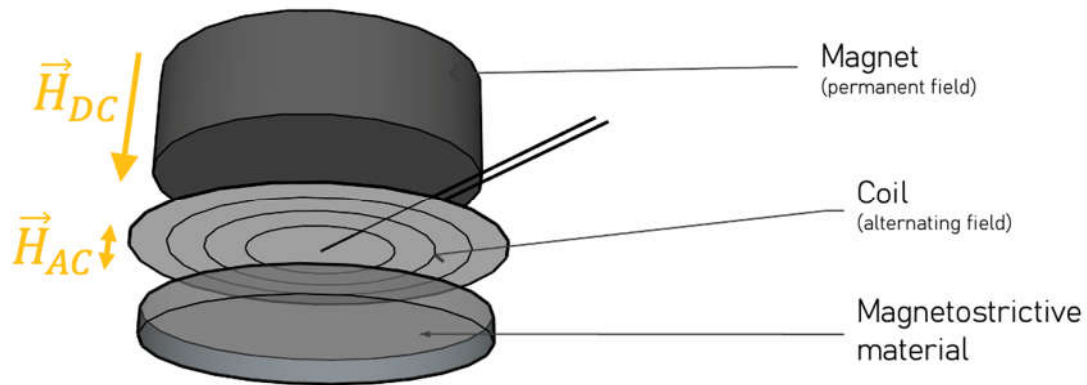
Figure 1.11 – A pulse-echo configuration MsS for bulk ultrasonic wave generation.

1.5 Magnetostriction: fundaments and concept

In order to understand the physical effects behind the magnetostrictive transducer, a section on the fundaments of magnetostriction is provided. Magnetostriction refers to the interaction between magnetization and mechanical stress. This effect was first described by James Prescott Joule in 1842, who detected a change in length of a piece of iron in

response of a magnetic field [28]. This effect occurs in FM materials due to their magnetic anisotropy and to better understand it, a revision of the concept of ferromagnetism and magnetic domains is provided.

1.5.1   Ferromagnetism and domain wall motion

In 1929, Pierre Weiss proposed that, in the demagnetized state, a macroscopic ferromagnet is composed of multiple regions called magnetic domains. The magnetic moments of each domain are aligned in a single direction, meaning that every domain has a spontaneous magnetization [29]. This short-range order is governed by the exchange interaction between the magnetic moments, and it is generally represented by its Hamiltonian:

$$\hat{H} = -2J\boldsymbol{S_1}\boldsymbol{S_2}$$

(1)

The alignment direction of the spins is not random. It generally sits in specific crystallographic directions, which are governed by the symmetry of the material, and this is known as *magnetic anisotropy*. The preferential direction of magnetization is generally called easy axis of magnetization. The direction of the domains, however, is set to minimize the overall magnetostatic energy of the material, such that, statistically, all available directions may be equally distributed in the material (Figure 1.12). This can result in an overall zero net magnetization in the absence of an external magnetic field.

Randomly aligned domains   Domains aligned with field
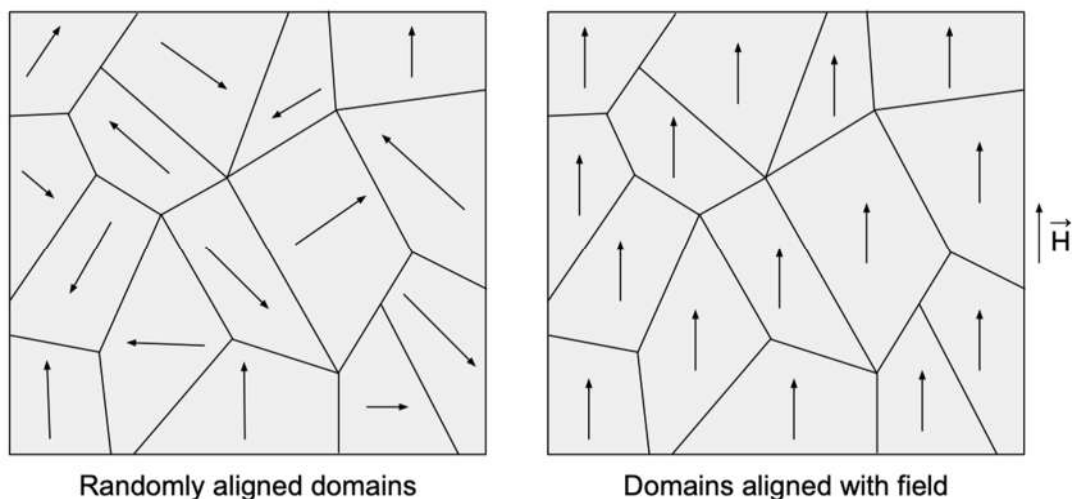
Figure 1.12 – Illustration of the distribution of the magnetic domains when they are randomly aligned (resulting in net magnetization zero) and when they are aligned with the external magnetic field.

Under a magnetic field, a ferromagnet will change its magnetization following a behavior like the one shown in Figure 1.13. For small applied magnetic fields, the domains with a magnetization direction closer to the direction of the field will grow at the expense of other domains. This process is called domain wall motion and it consists of the shift of the domain boundaries, enlarging the domains with an energetically favorable orientation. In this stage, no domain rotation occurs, so the magnetic moments retain their alignment in the easy axis direction of the crystal, Zone A in Figure 1.13. Imperfections, impurities, and dislocations in the material can interfere with the domain wall motion, resulting in a non-uniform motion. To overcome these barriers more energy is required by the boundaries, thus larger applied magnetic fields. As the field is increased, the rotation of the domains starts to occur. Domain rotation can have two modes:

- 90º turning or 180º reversal of the spins (Zone B in Figure 1.13 a and b);
- Gradual turning of the spins towards the field direction (Zone C in Figure 1.13 a and b).

In the first mode, the domains will align towards the crystalline direction closer to the direction of the magnetic field. This rotation is most impactful in the magnetization of the material and corresponds to the steepest variation of the magnetization with the magnetic field. From this results that the entire material has the same orientation since all the magnetic moments are aligned in the same crystalline direction (Zone B). As for the second mode of rotation, it consists of the gradual turning of the magnetic moments from the crystal axis to the magnetic field direction. This rotation mode consists of shifting the magnetization from a lower energy axis, so it takes more energy hence larger magnetic field. This rotation process also occurs for smaller fields, but most FM materials have large crystalline anisotropy so that the fields required to rotate domains is significantly larger than that for domain wall motion (Zone C).
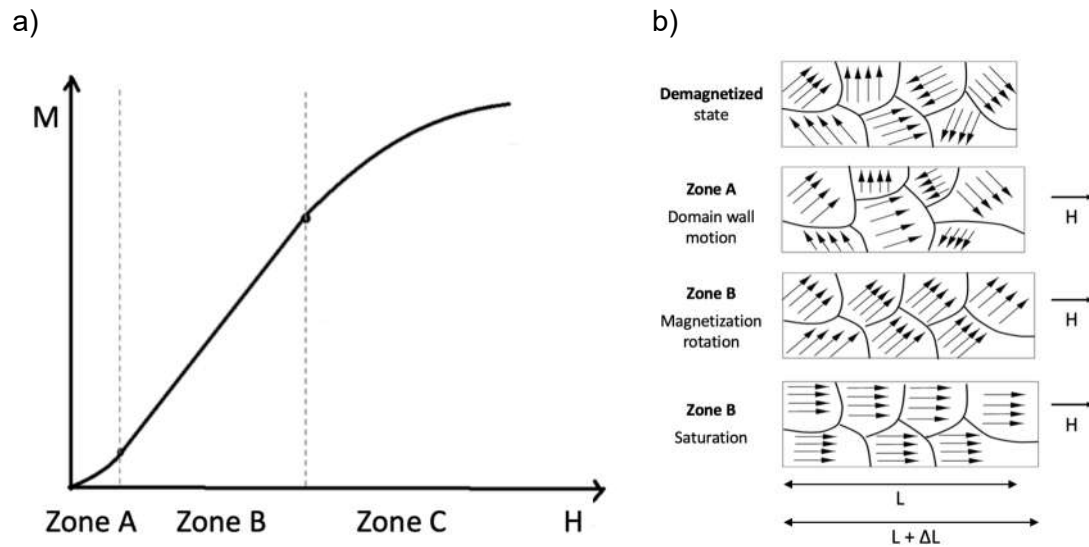
Figure 1.13 – a) Typical magnetization behavior of an initially unmagnetized ferromagnetic sample, b) domain alignment with the field, adapted from [30].

1.5.2   Origin of the magnetic anisotropy

Magnetic anisotropy entails any magnetic related effect that is dependent on the material's direction. Magnetocrystalline anisotropy is a particular case, and it emerges from the fact that the magnetization of a ferromagnetic material prefers to lie along specific crystallographic directions to minimize its internal energy.

The magnetocrystalline anisotropy originates from the spin-orbit coupling and the partial quenching of the orbital momentum. This interaction links the electron orbits to the crystal lattice, such that their spin exhibits preferential orientation along specific crystallographic directions.

The magnetoelastic anisotropy or magnetostriction is a form of anisotropy, which also originates from the spin-orbit coupling. It correlates the state of magnetization of the material with its strain. Kittel [31] established that magnetostriction would not occur in case the anisotropy of the material was independent of the state of strain of the material.

1.5.3   Types of magnetostriction

The magnetostriction covers any change in dimension or volume during the magnetization process of a material. Each magnetostriction effect has a reciprocal effect, and these are summarized in Table 1.3.

Table 1.3 – Summary of magnetoelastic effects [32]

Direct Effect	Inverse Effect
Joule effect Change in the dimensions of the material	**Villari effect** Change in the magnetization of the material due to applied stress
Wiedemann effect Torque induced by helical anisotropy	**Matteucy effect** Helical anisotropy induced by torque
Magnetovolume Volume change induced by magnetic field	**Nagoka-Honda effect** Change in magnetic state due to change in volume

The basic form of magnetostriction is the Joule effect, denoted by λ. In this regime, the volume stays constant, and it consists of a magneto-induced deformation produced along the magnetic field direction, which can either be positive (elongation, $\lambda>0$) or negative (compression, $\lambda<0$). The strain in each domain is a function of the domain magnetization with respect to the applied magnetic field.

Figure 1.14 shows the magnetization and the magnetostrictive behavior of a typical sample of a generic magnetostrictive material. As one can see from the graph, the saturation magnetostriction λ_{sat} takes the same values both for the positive and negative saturation magnetizations. Thus, under an alternating magnetic field, the magnetostriction oscillates at twice the field frequency. Also, the magnetostriction for the longitudinal and transversal directions takes opposite signs, which is consistent with the fact that the volume of the material stays constant under an applied magnetic field.
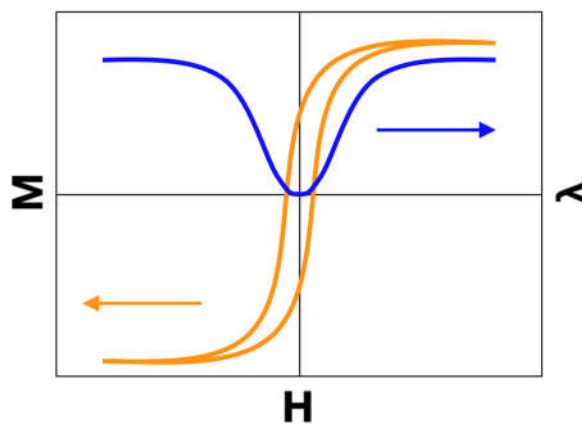
Figure 1.14 – Magnetization and magnetostriction of a generic magnetostrictive material.

Considering a polycrystalline material with no relevant anisotropy. The magnetostriction λ is given by:

$$\lambda = \frac{dl}{l} = f(\theta),$$

(2)

where dl is the strain, l is the initial demagnetized dimension and θ is the angle between the magnetic domain vector and the applied field. For 180º rotations, the magnetostriction is invariant, so the equation $f(\theta) = A\cos^2\theta$ is regarded as the simplest description of the effect, where A is a constant of the material. The magnetostriction is measured from a hypothetical demagnetized state, which is defined by a uniform distribution of domain magnetization vectors in all directions. In this state, the magnetization is zero, so the magnetostriction is also considered zero. The value of $\cos^2\theta$ for such a distribution is $1/3$, so it becomes $\lambda = A(\cos^2\theta - \frac{1}{3})$. Moreover, the saturation of magnetostriction is obtained when $\theta = 0$. Hence, for a single domain, it becomes:

$$\lambda = \frac{3}{2}\lambda_s\left(\cos^2\theta - \frac{1}{3}\right),$$

(3)

where λ_s is a constant that represents the total strain when the material is magnetized to saturation from the demagnetized state. This result suggests that the magnetostriction can be represented by a single constant, which seems to be hardly supported by experiments. Lee [34] has stated that this equation can be used in two cases:

1. Polycrystalline material at saturation;
2. Individual magnetic domains.

Usually, ferromagnets exhibit some level of magnetocrystalline anisotropy, such that magnetostriction is intrinsically coupled to their crystal structure. In the case of cubic lattices, a conceptual derivation of the magnetostriction with the crystalline structure of the material is presented in the next section.

1.5.4   Magnetostriction in cubic crystals

Becker and Döring [35] have suggested a general expression of the linear magnetostriction at saturation for cubic crystals, both body- and face-centered structures like Ni and Fe.

$$\lambda = h_1 \left(\alpha_1^2 \beta_1^2 + \alpha_2^2 \beta_2^2 + \alpha_3^2 \beta_3^2 - \frac{1}{3} \right)$$

$$+ 2h_2 (\alpha_1 \alpha_2 \beta_1 \beta_2 + \alpha_2 \alpha_3 \beta_2 \beta_3 + \alpha_3 \alpha_1 \beta_3 \beta_1)$$

$$+ h_4 \left(\alpha_1^4 \beta_1^2 + \alpha_2^4 \beta_2^2 + \alpha_3^4 \beta_3^2 + \frac{2}{3} A - \frac{1}{3} \right)$$

$$+ 2h_5 (\alpha_1 \alpha_2 \alpha_3^2 \beta_1 \beta_2 + \alpha_2 \alpha_3 \alpha_1^2 \beta_2 \beta_3 + \alpha_3 \alpha_1 \alpha_2^2 \beta_3 \beta_1)$$

$$+ h_3 \left(A - \frac{1}{3} \right), \text{ when } K_1 < 0$$

$$+ h_3 A, \text{ when } K_1 > 0$$

(4)

In this equation, the direction cosines of the magnetization vector and direction of observation relative to the crystal axes are represented by α_i and β_i and $(i = 1,2,3)$ (denoted by the angles φ_n and ψ_n in Figure 1.15), $h_1, \dots, h_5$ are the magnetostrictive coefficients, K_1 is a magnetocrystalline anisotropy constant that can take positive or negative values, and $A = \alpha_1^2 \alpha_2^2 + \alpha_2^2 \alpha_3^2 + \alpha_3^2 \alpha_1^2$ is a simplification term.
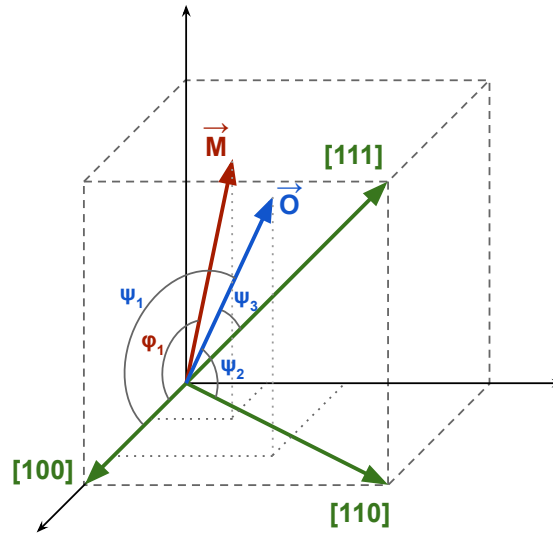
Figure 1.15 – Representation of the magnetization vector (M), the direction of observation (O) and of the crystal axes.

In many materials, h_3, h_4 and h_5 are often much smaller than h_1 and h_2, so they can be generally neglected. Moreover, the magnetostriction can be expressed in terms of λ_{100} and λ_{111} which represent the cases when the directions of magnetization and observation are aligned in the [100] and [111] directions, respectively.

$$\lambda = \frac{3}{2} \lambda_{100} \left(\alpha_1^2 \beta_1^2 + \alpha_2^2 \beta_2^2 + \alpha_3^2 \beta_3^2 - \frac{1}{3} \right)$$

$$+ 3\lambda_{111} (\alpha_1 \alpha_2 \beta_1 \beta_2 + \alpha_2 \alpha_3 \beta_2 \beta_3 + \alpha_3 \alpha_1 \beta_3 \beta_1)$$

(5)

Note that if we assume the materials to have isotropic magnetostriction then $\lambda_{100} = \lambda_{111} = \lambda_S$, the last equation becomes:

$$\lambda = \frac{3}{2}\lambda_s \left(\cos^2\theta - \frac{1}{3} \right),$$

(6)

which is similar to the simple isotropic polycrystalline case, as seen in Eq. (3).

Other two cases can be highlighted. The first one is related with the longitudinal magnetostriction (magnetostriction along the field direction), where $\alpha_i = \beta_i$, hence:

$$\lambda = \lambda_{100} - 3(\lambda_{100} - \lambda_{111})(\alpha_1^2\alpha_2^2 + \alpha_2^2\alpha_3^2 + \alpha_3^2\alpha_1^2).$$

(7)

The second case deals with the longitudinal magnetostriction in polycrystalline materials, where an average of λ_s is obtained. Taking that $\overline{\alpha_1^2\alpha_2^2 + \alpha_2^2\alpha_3^2 + \alpha_3^2\alpha_1^2} = 1/5$, we get that:

$$\overline{\lambda_s} = \frac{2}{5}\lambda_{100} + \frac{3}{5}\lambda_{111}$$

(8)

The last expression is typically used to correlate the magnetostriction measurements of polycrystalline samples to single crystalline samples in cubic crystals. An example of some magnetostrictive constants is given in Table 1.4.

Table 1.4 – Magnetostriction constants of Fe and Ni, obtained from [34]

	λ_{100} (x10^6)	λ_{111} (x10^6)
Fe	20.7	-21.2
Ni	-45.9	-24.3

1.5.5   Overview of magnetostrictive materials

In Figure 1.16, the magnetostriction range of different materials is shown in a logarithmic scale. Terfenol-D, Galfenol and Fe-Co based alloys are the materials which exhibit the largest magneto-induced strains. PZT, a common piezoelectric material, is in the chart for reference. Materials with magnetostriction values of the order of 10^{-3} or larger at room temperature are known as giant magnetostriction materials [36].
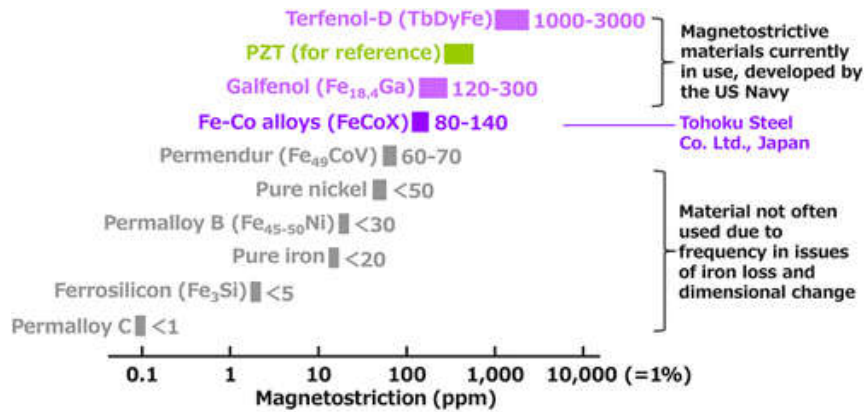
Figure 1.16 – Magnetostrictive materials and typical magnetostrictive coefficients at room temperature [37].

1.5.5.1   Tb-Dy-Fe

Terbium and Dysprosium have large magnetostrictive coefficients at low temperatures, of the order of 10 000ppm [38], [39]. However, due to their low Curie temperature, their magnetostriction becomes insignificant at room temperature. By alloying these elements with *3d* transition elements, namely iron, which has a significantly higher Curie temperature T_c, magnetostrictive coefficients of 2630ppm for $TbFe_2$ and 650ppm for $DyFe_2$ were achieved at room temperature. However, they require large magnetic fields to drive them to saturation because of their large magnetocrystalline anisotropy. This property can be tuned by controlling the content of Tb and Dy, from which $Tb_{0.3}Dy_{0.7}Fe_2$ was formulated [40], named Terfenol-D. This proportion exhibits giant magnetostriction at room temperature (~2000ppm), while having lower magnetocrystalline anisotropy.

Terfenol-D finds application in numerous fields, such as sonar systems and high-power ultra-large ultrasonic devices [41]. However, Terfenol-D has serious shortcomings that limit its wider application, one of them being the high eddy current loss in frequencies above a few kHz. Several methods have been explored to reduce this effect, such as combining with a piezoelectric material [42] and increasing the domain walls [43], to drive the eddy current loss down at high frequency. Other severe limitations are its high price, extreme brittleness and the need of high magnetizing field to generate large strains.

1.5.5.2   Fe-Ga

Alternatively, Fe-Ga alloys combine low hysteresis with moderate magnetostriction at low magnetic fields and have, since their development, become an exciting new class of magnetostrictive materials. The magnetostriction coefficient of Fe-Ga-based alloys as a function of Ga content is shown in Figure 1.17, where we can see two distinct peaks. The first peak corresponds to Galfenol, with a stoichiometry of $Fe_{81.6}Ga_{18.4}$. Its properties and processing methods have been synthesized in the work by Atulasimha and Flatau

[44]. Even though the magnetostriction is not as notable in Galfenol as it is in Terfenol-D, this material offers a good tensile strength (~500GPa) and machinability, as well as an improved material processing technology [45]. Among its most distinctive characteristics, Galfenol exhibits a moderate magnetostriction of about 350ppm and has a high Curie temperature (675ºC), enabling its use in high temperature environments. Moreover, the precursor raw materials are relatively inexpensive, and the resulting alloy is corrosion resistant [46] and substantially more ductile than Terfenol-D (for Ga content up to 20 at.%) [45].
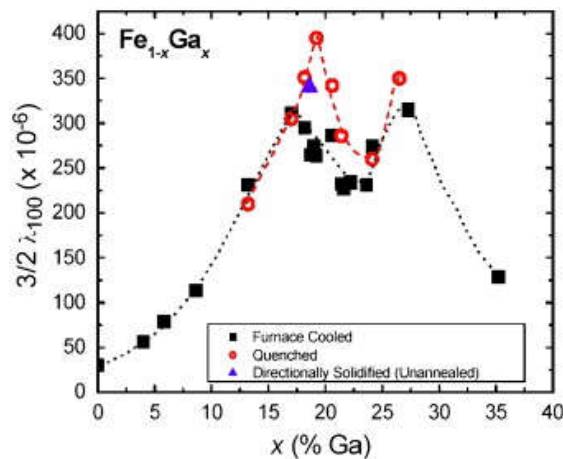
Figure 1.17 – Magnetostriction performance of Fe-Ga-based alloys as a function of Ga content [47].

1.5.5.3 Fe-Co

Among the Fe-, Ni- and Co-based binary alloys, Fe-Co alloy is the one exhibiting largest saturation magnetic flux density and softest magnetic properties [48], [49]. It exhibits a bcc structure at room temperature and presents moderate saturation magnetostriction (Figure 1.18). Fe-Co alloys offer a good alternative to magnetostrictive Terfenol-D and Galfenol due to their abundance and low cost. Fe-Co alloys are known for their large permeability, particularly near the equiatomic distribution [50]. Furthermore, Fe-Co has a high Curie temperature, which can be up to 912°C in the equiatomic composition and exhibits large mechanical strength. After the development of $Fe_{50}Co_{50}$ in 1929 [51], this alloy did not find many applications, due to its severe brittleness, which brings significant complexity to its manufacturing. The addition of 2at% V to stoichiometric Fe-Co was able to significantly improve its ductility. This new alloy, named Permendur, became very popular among applications requiring very soft ferromagnetic properties. It is also possible to obtain a particular type of Permendur alloy that has a higher control over its composition and is magnetically annealed, called Supermendur. It exhibits lower coercivity and larger permeability, but these properties are dependent on the thermal

treatment that is applied. It is commercialized by the name of Hiperco 50 by Carpenter Technologies. In particular, due to its high saturation flux density, 2%V-FeCo (also FeCo-2V) is used in the aircraft and aerospace engineering fields, where weight concerns are imperative.

a)   b)
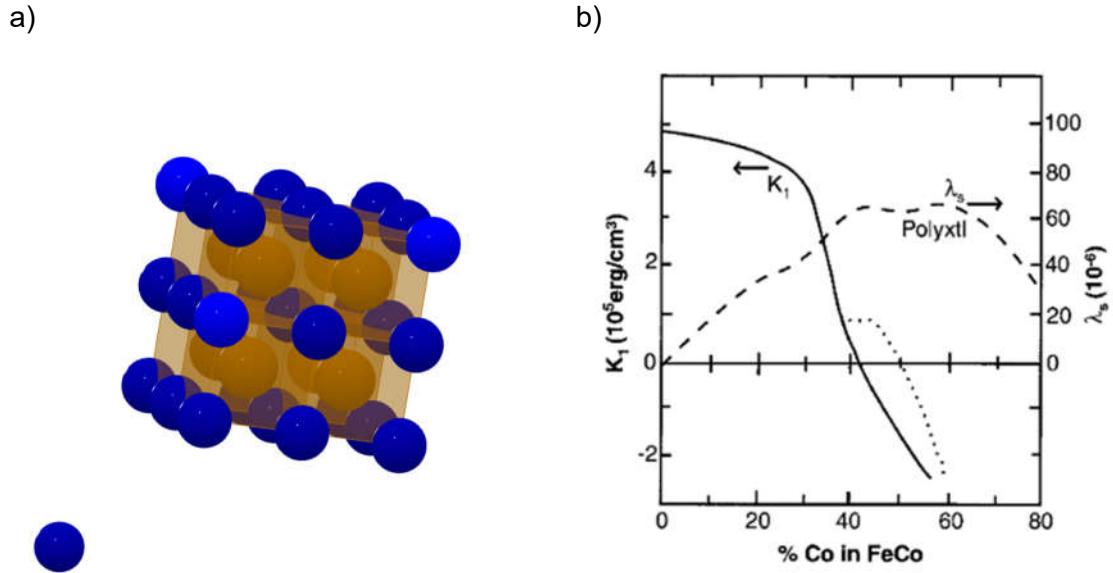
Figure 1.18 – a) Illustration of the crystal structure of ordered bcc equiatomic FeCo [52] and b) variation of the magnetic anisotropy constant (K1) and saturation magnetostriction with Co concentration [53].

A critical factor that determines the properties of FeCo-2V is its processing and thermal history, so there have been studies investigating their impact in the properties of the material [50], [54]. Nowadays, FeCo-2V is used for its soft ferromagnetic properties, and proper investigations have been undertaken to improve both its magnetic and mechanical performance. Its magnetostriction has been a source of concern and efforts have been made to reduce it, driven by the industrial needs. A limited number of works have focused on finding processes to improve its magnetostriction instead, especially in bulk commercial FeCo-2V. The Southwest Research Institute (SwRI) was able to improve the magnetostrictive performance of a strip of FeCo-2V [55], [56]. The processing method to achieve good performance in FeCo-2V has not been disclosed, but the strip is being applied in UT devices, such that SWRI is currently the main competitor in the field of UT MsS.

The following table summarizes the main physical properties of Terfenol-D, Galfenol and Fe-Co alloys.

Table 1.5 – Summary of the main physical properties of the most widely investigated magnetostrictive materials [37]

		Terfenol-D	Galfenol	Fe–Co alloys
Magnetostrictive	Magnetostriction (ppm)	800–1200	120–240	80–140
Magnetic	Coercivity (A/m)	300	3000	< 200
	Saturation flux density (T)	1.0	1.5	2.0 <
	Relative permeability	< 10	< 100	100
Mechanical	Tensile strength (MPa)	30	400	600 <
	Elongation (%)	< 1	1 <	< 30
	Young's modulus (GPa)	< 100	< 100	200
Thermal	Curie temperature (°C)	~ 380	~ 680	~ 900

We believe that the potential of the Fe-Co system has not been sufficiently explored for magnetostrictive applications. Moreover, the link between the structural and morphological properties with the magnetoelastic properties of this alloy are lacking in the literature, and that has been a major obstacle to its development as an ultrasonic transducer.

1.6 Objectives of the work

There has been evolution regarding the development of MsS in the literature, both in ultrasonic guided wave [57], [58] and bulk wave [59], [60]. However, currently, only one commercially available GW MsS has been developed, by SwRI [55], [61]. This equipment has been associated with some limitations such as the lack of mode conversion configuration, which makes it more difficult to interpret test results [62] and generally gives less satisfactory results when compared with piezoelectric transducers. Given the limitations that are currently in place, we have, in collaboration with EQS Global, accepted the challenge to develop new and improved MsS systems for GW and BW UT inspection.

Some of the early requirements that served as guidelines to drive the investigation were provided by EQS Global, and they include a device that:

- is easy to use,
- is flexible,
- is sturdy enough for application in harsh environments,
- is easy to couple with the rest of the elements of the set-up,
- does not require a couplant between the transducer and the pipe,
- requires a simple and inexpensive fabrication process.

With this in mind, the present work involved the investigation and improvement of magnetostriction transducers to obtain very precise properties. Materials with considerable magnetostriction are usually composed of transition metal elements, such as Fe, Ni and Co, and/or rare-earth elements, such as Tb and Dy. Notably, Terfenol and Galfenol exhibit large magnetostriction. These materials are however expensive and hard to process into flexible sheets. Their application is thus severely limited by their availability and cost, and widespread industrial use is unlikely. Fe-Co emerges as an alternative since it is generally available, is relatively inexpensive and is made in flexible form. As this alloy is mostly used in applications that make use of its soft magnetic properties, its use as a magnetostrictive transducer has been significantly ignored. Research on the magnetostrictive performance is severely lacking, as well as on how to improve it, which became one of the focus points of this thesis.

The work that was undertaken and is herein described focused on the development of innovative transducers based on Fe-Co with improved magnetostrictive performance. A scale down dimension approach was performed. The first involving the use of bulk magnetostrictive materials 3D (Chapter 3), the second consisted of the development of magneto-sensitive composites (Chapter 4) and the third involved the preparation of thin films 2D (Chapter 5). The distinction between them is significant, so each is its own independent research line. The research lines are divided into 4 main work categories, presented in Figure 1.19.

3D (Chapter 3)
- Effect of the thermal treatment on the physical properties of the alloy
- Correlation of the physical properties with the magnetostriction of the alloy

Composites (Chapter 4)
- Development of elastomer composites based on Fe-Co alloy particles
- Influence of the particle size and shape on the physical properties of the composites

2D (Chapter 5)
- Influence of the substrate and thickness on the physical properties of the films
- Inovative magnetostriction device using thin films for ultrasonic testing

Technology transfer (Chapter 6)
- Industrial tests with the produced transducers, using GW and BW
- Alternative materials: preparation and testing

Figure 1.19 – Representation of the 3 lines of investigation and the technology transfer to the partner company.

This effort was a collaboration between the Institute of Physics for Advanced Materials, Nanotechnology and Photonics (IFIMUP), EQS Global and Center for Microelectromechanical Systems of the University of Minho (CMEMS). This relationship was fundamental to build the concept for the magnetostrictive device. EQS Global is a company with many years of experience in the field of infrastructure quality assessment, particularly in the field of oil and gas pipelines. They aimed at developing a new sensor with improved capabilities comparing to other market alternatives and reached out to two research institutes in the Universities of Porto and Minho: IFIMUP and CMEMS. The collaboration highlights the importance of having science-industry partnerships that enable the transfer of knowledge from one sector to the other.

Chapter 2   Sample Preparation &
Experimental Methods

2.1   Sample preparation techniques

In this section we describe the methods used in the preparation of the different samples used in this thesis.

2.1.1   Magnetron Sputtering

Sputter deposition is a physical vapor deposition method for growing thin films. This technique involves bombarding a target with an ionized gas, which causes particles to be ejected from it, via momentum transfer. To accelerate the ionized gas towards the target, a voltage is applied between the target and the sample holder creating an ionic current. As the acquired kinetic energy of the ionized gas particles is greater than the binding energy of the target, atoms are removed from it. The ejected atoms are diffused and deposit on the surfaces of the chamber resulting in a thin film coating of the substrate. Sputtering can be performed using an inert gas, usually Ar, or a combination of inert and reactive gases, like O_2. Sputtering yields a uniform deposition, with very low impurity, and high reproducibility.
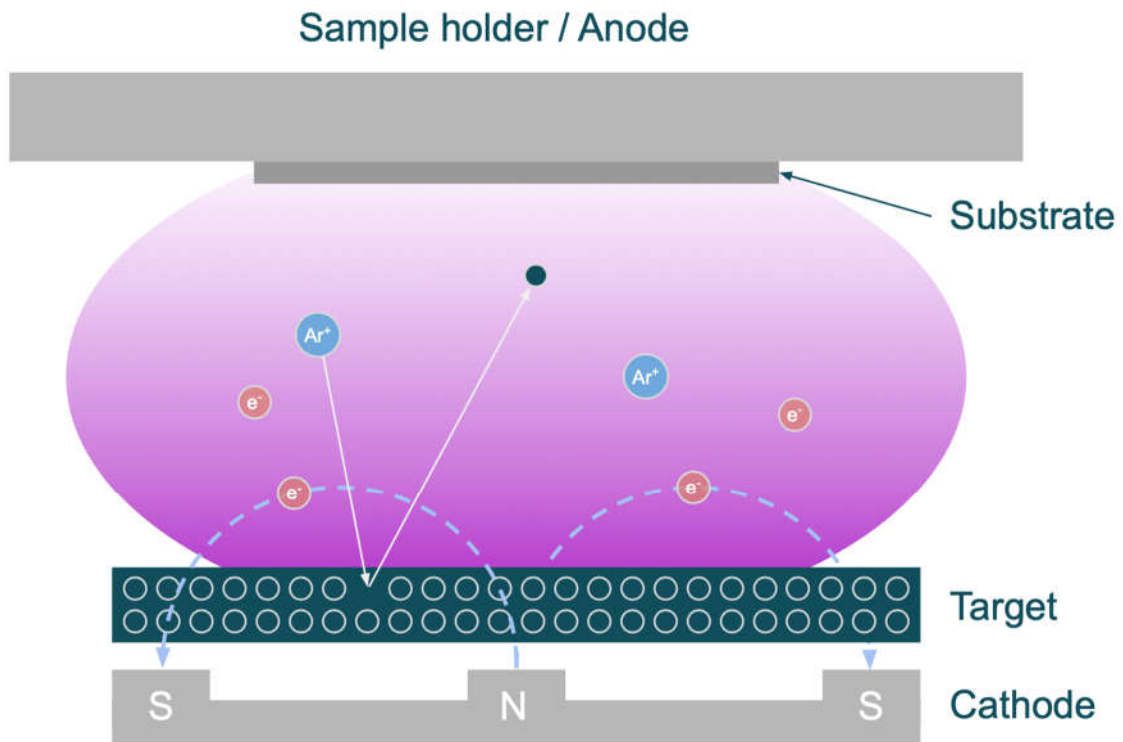
Figure 2.1 – Illustration of a magnetron sputtering deposition.

Magnetron sputtering was introduced in the 1970s to overcome some limitations of a simple sputtering configuration, particularly low deposition rates. This method uses magnets to produce a magnetic field parallel to the target [63], so as to maintain the discharge close to it. As a result, the electrons can circulate close to the target surface. This increases the probability of ionization as well as the density of the plasma, resulting in higher sputtering rate.

The list of materials that can be used in sputtering is vast and include metals, alloys (DC sputtering) and insulators (RF sputtering), which explains why this technique is so popular. A combination of targets could also be used to perform co-sputtering. The power of the discharge in each target can be adjusted to obtain specific stoichiometries.

The sputtering equipment that was used in the course of this work is located at Instituto de Nanociencia y Materiales de Aragón (INMA), Zaragoza (Spain). The prepared samples are summarized in Figure 2.2.
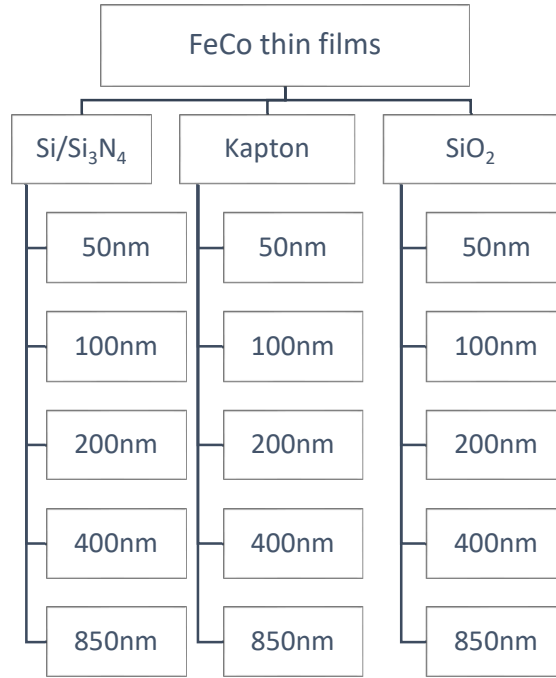
Figure 2.2 – List of the produced thin film samples.

The depositions were performed on rigid and flexible substrates, namely SiO_2, Si/Si_3N_4 and Kapton (polyimide). The use of different substrates is relevant in the investigation of their influence on the physical properties of the film. The use of a flexible 50μm Kapton foil stems from the fact that a flexible transducer is desirable since it enables conformability to the surface where it will be applied. Additionally, Kapton can withstand high temperatures, such that it can be used in industrial applications where operating temperatures reach up to of 400°C.

2.1.1.1 Magnetron sputtering at INMA

The sputtering system is an ATC Orion, supplied by AJA International Inc. The chamber is equipped with 5 target heads and the vacuum system consists of two vacuum pumps.

The samples prepared at INMA used a $Fe_{50}Co_{50}$ target (99.9% purity) supplied by FHR, with 5cm of diameter and 2mm in thickness. The base pressure was 10^{-6}Pa. The used sputtering power P_w was 125W and the work pressure was 0.4Pa.

FeCo films of varying thickness were deposited on Si/Si_3N_4, Kapton and SiO_2 substrates using a working pressure of 3mTorr and a power of 125W, considering the determined deposition rate of 6nm/min. The sputtered films have the following thickness: 50nm, 100nm, 200nm, 400nm and 850nm.

2.1.2 Helicoidal Fe-Co particles by milling

Electric milling cutters are versatile tools that are usually used to carve, mill, grind and cut. A high precision rotary grinding tool was used to obtain files of Hiperco 50. Helicoidal shaped files were removed from the strip as it was grinded. This process was conducted inside a closed environment to keep the files from being contaminated by the environment. The helicoidal FeCo-2V particles were then collected with the help of a magnet and stored for later use.

Figure 2.3 – Milling process. The files are shot in every direction, so a transparent cover is used to keep them contained.

2.1.3 Elastomer-based composites preparation

This process consists of combining a liquid polymer with ferromagnetic particles. The cured mixture yields a solid composite. Two distinct sets of composites were prepared in this work: one based on Polydimethylsiloxane (PDMS) and the other on Polyvinyl alcohol (PVA). Each set has a specific preparation process, which is described in the following sections. Figure 2.4 depicts the samples that were produced with this method.
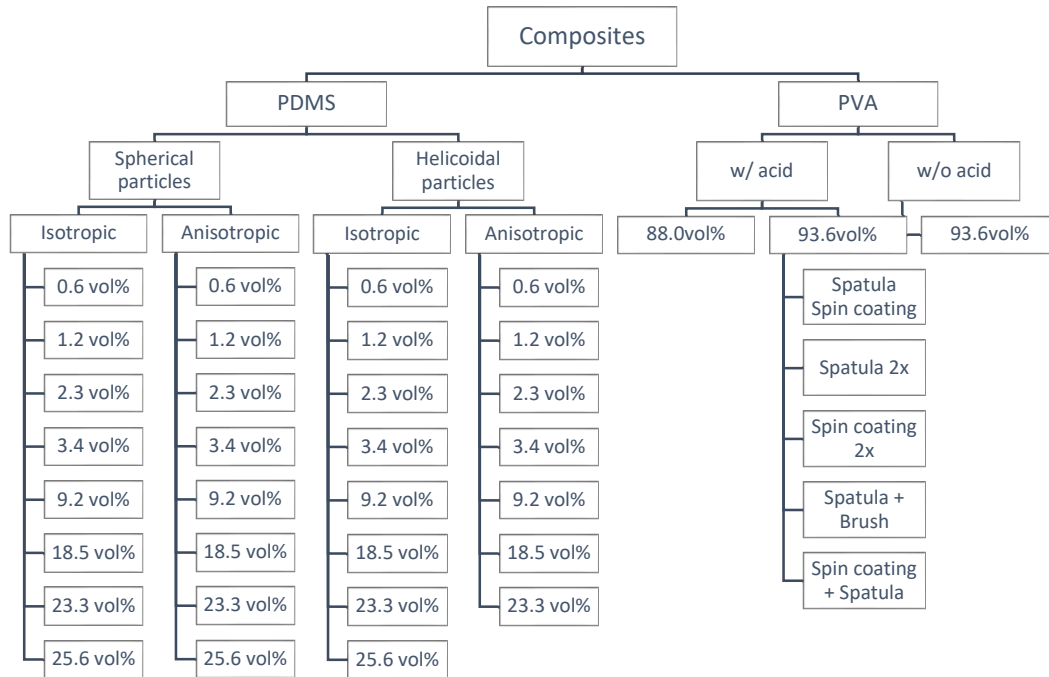
Figure 2.4 – Depiction of the produced elastomer composite samples.

2.1.3.1 Preparation of PDMS-based composites

Sylgard 184 is a room temperature curing elastomer. It is a commercial silicone rubber containing two liquid components, a base and a hardener. PDMS is a very popular elastomer to prepare magneto-sensitive composites since it provides a liquid medium to mix the ferromagnetic particles before curing and becoming solid. Approximately, a 10:1 mass ratio is used to combine the two parts, respectively. Prior to curing, the elastomer is degassed by placing the mixture in a vacuum environment for at least 30min. The curing occurs at room temperature and may take up to 48h hours. It can be accelerated by heating the mixture to 80°C for 20min.

To produce the composites, ferromagnetic samples are added to the liquid parts as illustrated in Figure 2.5. Isotropic samples are obtained using the steps that are depicted, while the anisotropic samples undergo an additional step before curing which consists of placing them under a uniform magnetic field, to align the ferromagnetic particles. Soft-polymer-based composites with ferromagnetic particles are commonly called Magnetoactive elastomers (MAEs).

Two different sets of particles were used to produce PDMS-based composites. Both powders are composed of FeCo-2V, one of them consists of nanometric spherical particles and the other of micrometric helicoidal particles. The different powders are used

to produce MAEs with composition ranging between 0.6vol% and 25.3vol%, with isotropic and anisotropic particle distribution. After preparation, the MAEs are removed from the mold and cut into samples of 6cmx1.5cm, for characterization. The measurement of the anisotropic MAEs was performed both parallel (||) and perpendicular (|-) to the direction of the particle alignment.

2. Mixing

3. Molding

1. Definition of composition

4. Curing

5. Magnetorheological elastomer
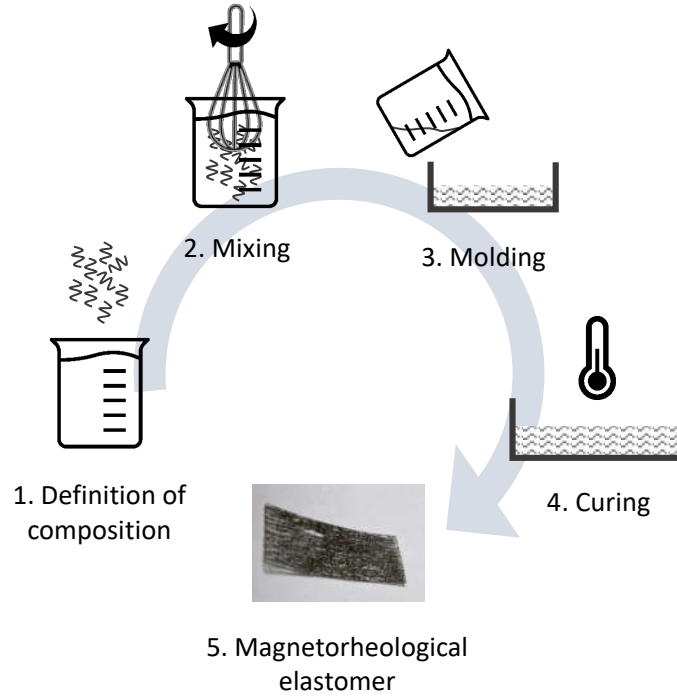
Figure 2.5 – Diagram of the fabrication process.

The volume fraction (VF) of the MAEs was determined using equation (9).

$$VF = \frac{V_{powder}}{V_{powder} + V_{elastomer}}$$ (9)

The weight of the components was calculated from their volume using the density values given by the suppliers of ρ^*_{PDMS} = 1.1 g/cm^3 and of $\rho^*_{Hiperco\ 50}$ = 8.12 g/cm^3.

Preparation of the PDMS-based composite with spherical particles

Particles of FeCo-2V were supplied by Sandvik Osprey Ltd. The powder is composed of spherical particles with an average diameter of 22±9μm. This information was verified by electronic microscopy (2.2.3), as seen in Figure 2.6. The composition of the powder was determined by Energy Dispersive X-ray Spectroscopy (2.2.3.1) and the elemental analysis confirms the data provided by the supplier.
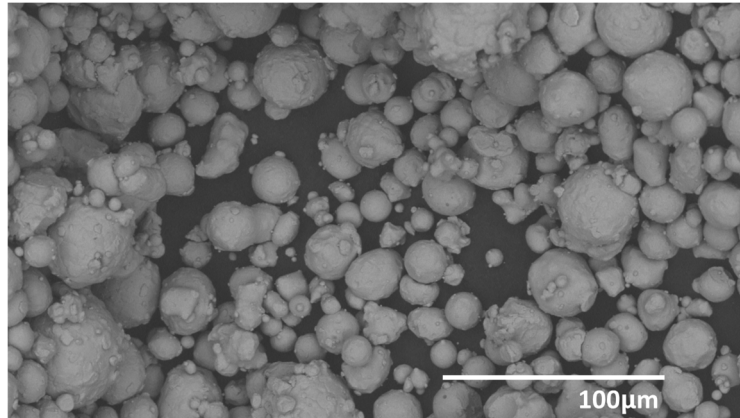
Figure 2.6 – SEM picture of the FeCo-2V powder obtained with backscattered electrons, with a magnification of 1400x.

The prepared samples are depicted in Figure 2.7. It can be observed that the darkness of the composite increases with VF. This is natural as the FeCo-2V particles are opaque to visible light while PDMS is transparent. Moreover, in Figure 2.7 b), the anisotropic MAEs are depicted. The particles are organized in chains because of the magnetic alignment prior to the curing step. The aligned structures are visible in the lower concentration MAEs. We see that the alignment has followed the magnetic field lines, such that they are not parallel throughout the whole sample. For this reason, only specimens obtained from the central homogeneous part of the sample were used in the characterization.

a) Isotropic MAEs
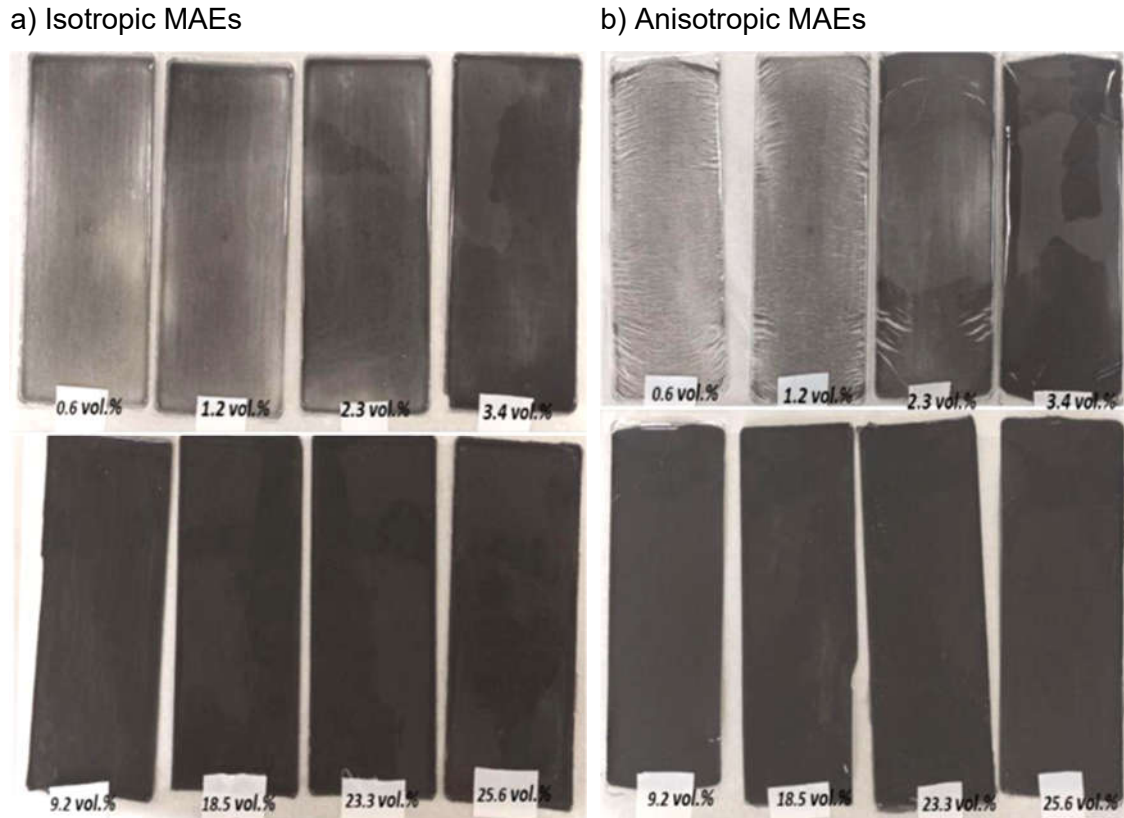
b) Anisotropic MAEs

Figure 2.7 – Pictures of the spherical particle MAEs: a) isotropic and b) anisotropic.

Preparation of the PDMS-based composite with helicoidal particles

The strip of Hiperco 50 was cleaned with isopropanol and the helicoidal fillings were obtained by using an electric milling cutter, as described in Section 2.1.2. The average length of the helicoidal particles is 250µm. The particles were used without further processing.

a)

b)
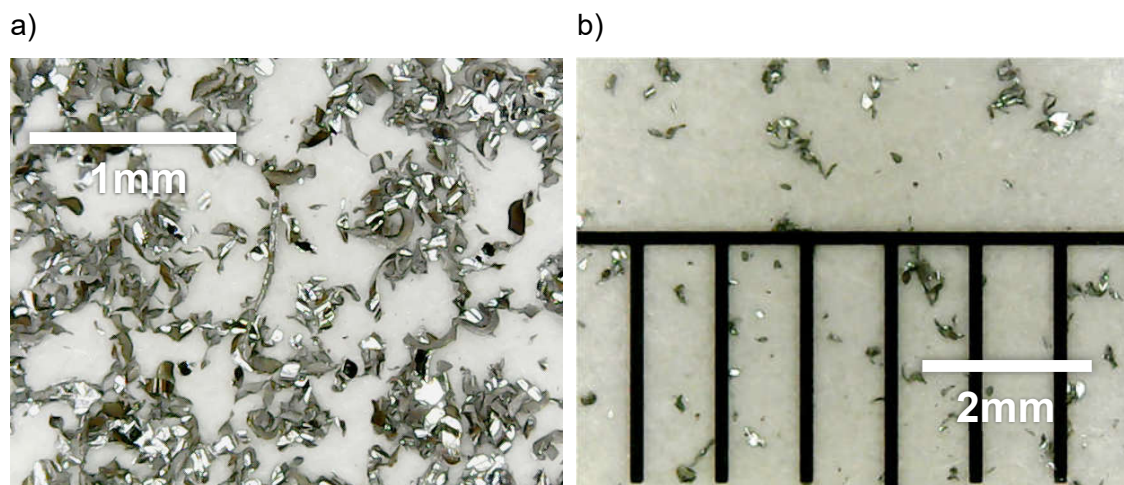
Figure 2.8 – Optical images of the helicoidal particles of FeCo-2V.

The volume fraction of the composites was varied between 0.6vol% and 25.6vol%. Figure 2.9 depicts a sample of each MAE. The samples on the top row have an isotropic particle distribution, while the one on the bottom row are anisotropic.
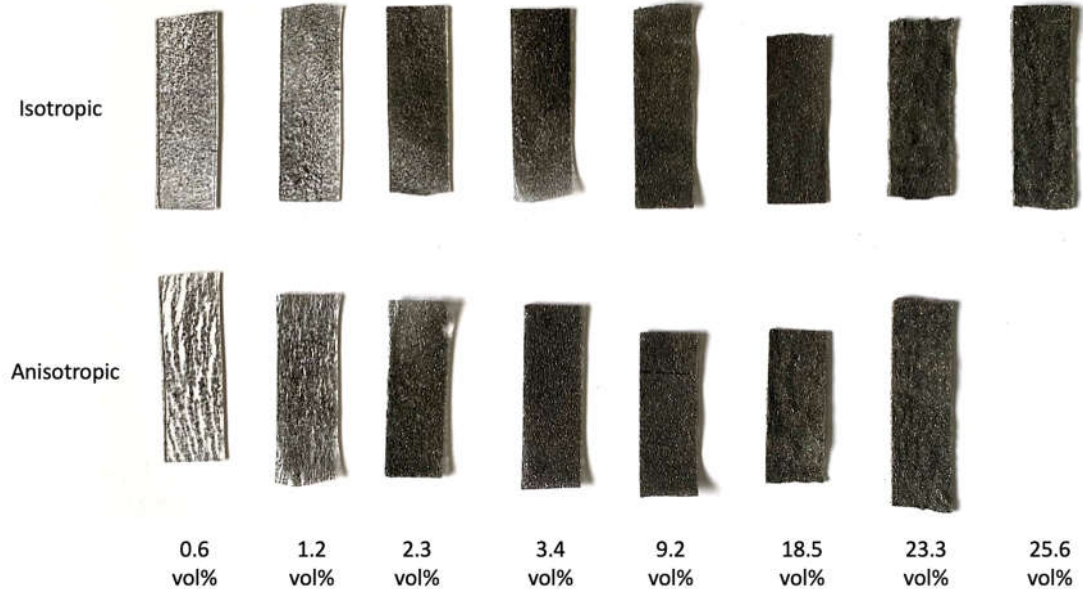
Figure 2.9 – Image of the samples of MAEs prepared with helicoidal particles: a) isotropic and b) anisotropic.

2.1.3.2   High-particle-concentration PVA coating

High concentration elastomers were prepared with a PVA base. The PVA solution is prepared on a concentration of 5wt% of PVA to water. Pellets of PVA are added to water and heated to 80°C for at least 4h, while constantly stirring. A transparent thick liquid solution is obtained, which can be stored at room temperature for up to a month. The solution can be cured at room temperature or up to 80ºC until the water is removed.

The same solution can also be prepared with phosphoric acid. The addition of the acid provides elasticity to the cured polymer, as well as ionic conductivity. The acid is added along with the PVA into the water before heating in the same weight quantity as PVA.

The spherical particles of FeCo-2V supplied by Sandvik Osprey Ltd were also used in the PVA-based composites. The particles were subject to a thermal treatment before being added to the PVA solution. The annealing consisted of inserting the particles inside a quartz tube with a constant flux of Ar, which in turn is placed inside a furnace. The temperature was increased to 640°C at a rate of 5°C/min, the powder was then kept at 640°C for 1h, followed by natural furnace cooling.

The resulting powder was used to prepare PVA-based composites with and without phosphoric acid, with concentrations of 88vol% and 93.6vol%. The particles are added to the PVA solution, such that a paste is formed, and which can be spread on a substrate. The mixture was used to coat steel prisms of base dimensions 2cmx2cm. The method of coating was either by applying the mixture with a spatula or with a brush. It was then cured at room temperature for 30min.

2.1.4 Tailoring of the properties of commercial FeCo-2V strips using Heat treatment and Cooling

Thermal treatments are a straightforward way to alter the physical properties of an FeCo-2V commercial strip. The annealing temperature T_a, annealing time and cooling rate influence how the properties are changed.

FeCo-2V is usually provided in the form of cold rolled sheets by the commercial name of Hiperco 50. Cold rolled Hiperco 50 sees its thickness reduced by more than 90% by the application of mechanical stress. This yields a material with grains elongated along the rolling direction, with concentrated dislocations and internal stresses. Hiperco 50 has considerable strength due to the strain hardening but is magnetically poor. A post-cold deformation annealing is always necessary to develop a stress-free microstructure and good magnetic properties, at the expense of the mechanical strength of the material. The desired properties (mechanical or magnetic) determine the annealing time and temperature, and a slow cooling to room temperature is usually necessary to obtain an ordered structure for optimum magnetic properties. Notably, even after re-crystallization, which occurs during annealing, the magnetic properties reflect the presence of crystallographic texture [64].

FeCo-2V alloy strips were annealed at different temperatures and two distinct cooling rates. The annealing temperatures T_a were varied between 450°C and 850°C in 100°C-steps. The cooling processes consisted of quenching (Q) and slow cooling (SC) inside the furnace. The prepared samples are summarized in Figure 2.10. Moreover, the annealing curves of T_a=850°C with quenching and slow cooling are plotted as a function of time (Figure 2.11).
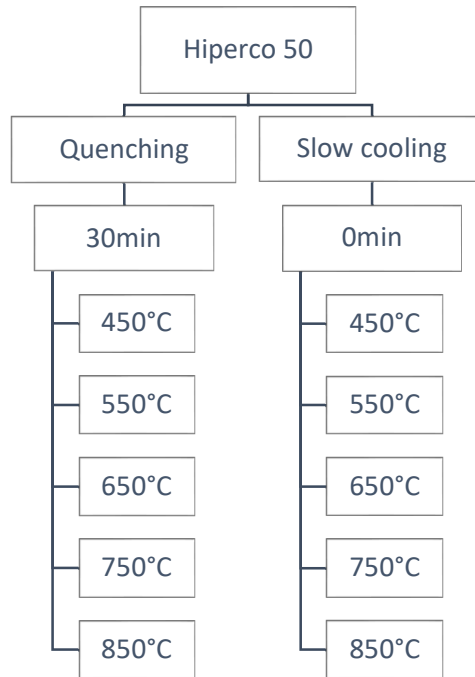
Figure 2.10 – Thermal treatments employed on samples of Hiperco 50.

The notation of the samples is as follows:

- Quenched samples are identified by the [annealing temperature] + [Q]uenching + [30]min. Example:

    450Q30 → Sample annealed at 450°C for 30min and quenched

- Slow cooled samples are identified by the [annealing temperature] + [S]low [C]ooled. Example:

    450SC → Sample annealed at 450°C for 0min and slow cooled

The annealed samples consisted of 0.5m of 0.05m-wide strip of Hiperco 50. The strip was rolled onto itself and was fixed by a ring made of the same material to avoid contamination. The sample roll can then fit inside the furnace for the annealing.
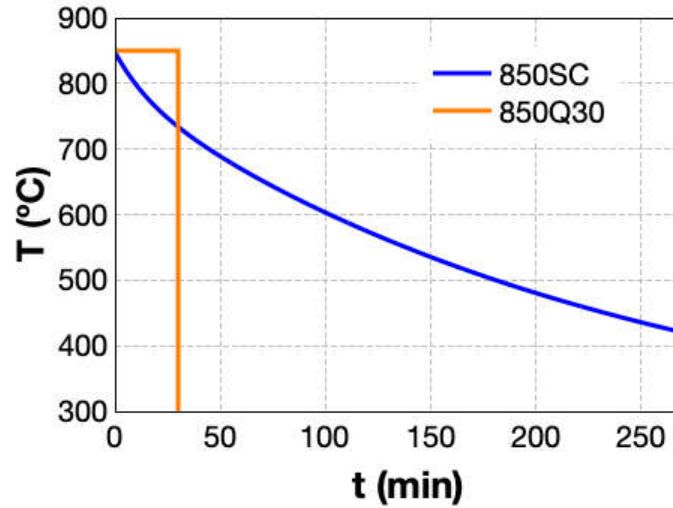
Figure 2.11 – Temperature versus time of the thermal treatments performed at 850ºC, with quenching (Q) and slow cooling (SC).

2.1.4.1 Quenching

Quenching is a cooling process that involves a sudden drop from the annealing temperature by immersing the material in a cooling fluid. Usually, a high thermal conductivity medium is necessary to ensure the effective temperature drop right after removing the material from the furnace, such as water ice brine solution or oil. Quenching is employed when specific high temperature crystallographic or morphological properties want to be maintained at room temperature. A fast temperature transition may enable some of the high temperature characteristics to "freeze" without changing to more stable forms at lower temperature.

In this work, samples were quenched in an ice and water bath. After annealing for 30min, they are removed from the furnace and immediately inserted into the bath, where they undergo a fast cooling. We estimate that the temperature is dropped from the annealing temperature to ~0°C in less than 1s.

2.1.4.2 Slow cooling

For the slow cooling treatments, the furnace is heated at the annealing temperature and the samples are introduced and kept at that temperature for <1min. After this step, the furnace is let to cool down naturally. Bellow 316°C, the employed cooling rate does not affect the physical properties of the alloy [65], so the samples are removed from the furnace once bellow said temperature. The natural cooling rate of the furnace from 650°C and 850°C was measured and is depicted in Figure 2.12.
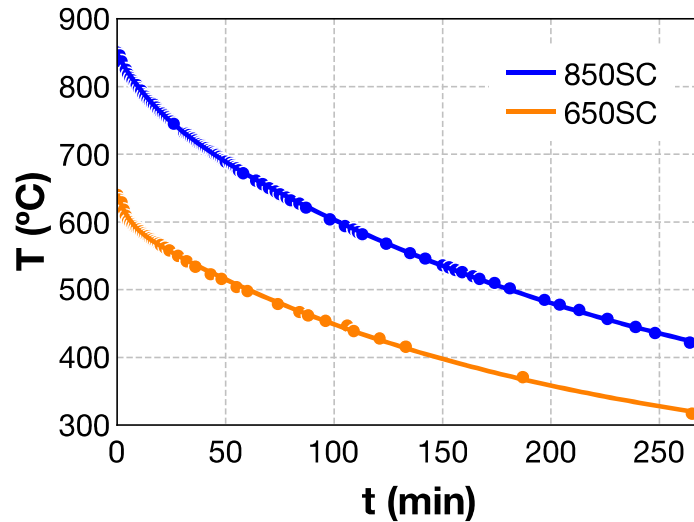
Figure 2.12 - Furnace natural cooling rate from 650ºC and 850ºC.

After the annealing, the samples were characterized without further processing. Smaller samples can be cut from the annealed strip using heavy duty scissors.

2.2   Characterization Techniques

The characterization of the prepared samples is performed using physical characterization equipment and methods, which will be described in this section.

2.2.1   Polishing of hard samples

Surface polishing is a necessary step to enable the proper characterization of the morphology and composition of the samples. To prepare them accordingly, the surface of the samples was grinded using silicon carbide abrasive papers (Grit 120/P120, Grit 280/P320, Grit 369/P600, Grit 600/P1200), to remove the surface oxide layer and to provide a coarse polish. The polishing process was aided by a Buehler Vector Power Head. Diamond suspensions with particle size 9μm, 3μm and 1μm (Buehler) were subsequently used to polish the surface of the samples on a soft pad. The final step consisted of hand polishing the samples with a solution of alumina particles of 0.6 μm of diameter in an ultra-soft pad. The surface was cleaned with isopropanol in an ultrasound bath for 15 minutes. Figure 2.13 exhibits images taken by optical microscopy, after a partial polishing (a) and after the entire polishing process (b). The dark spots in b) are precipitates that occur after annealing the strip.

a)   b)
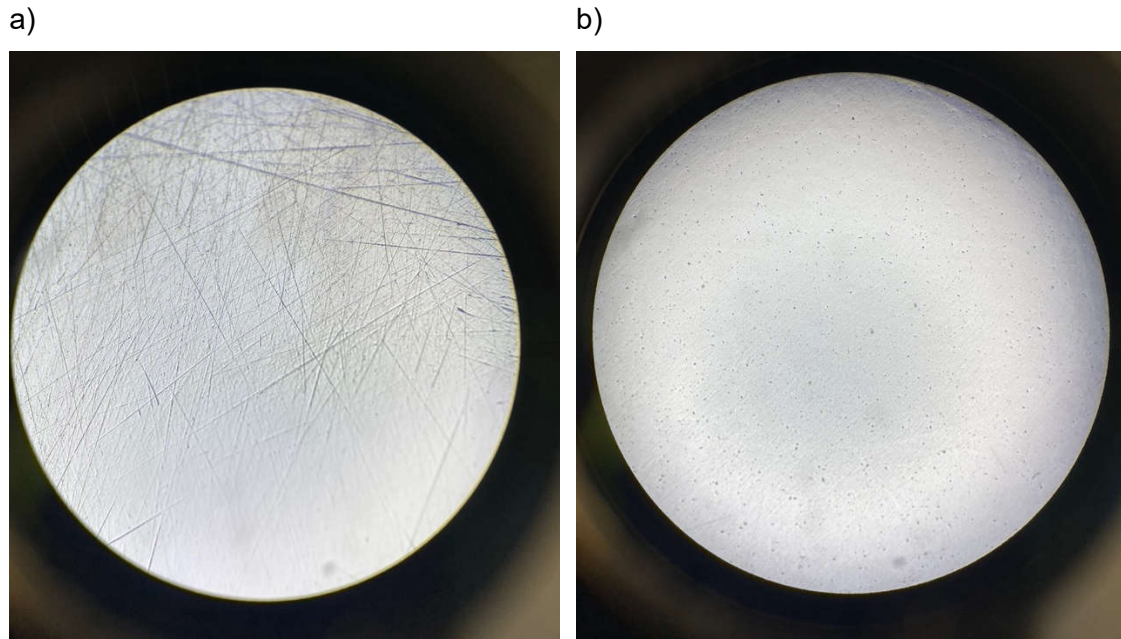
Figure 2.13 – Microscope images of the surface of polished samples annealed at 850ºC: a) after using abrasive papers, and b) in the end of the polishing process.

2.2.2   Optical microscopy

Optical microscopes use light and a set of lenses to generate enlarged images of objects [66]. Typically, the object under observation is placed on a stage and lit either with light coming from below (applicable in transparent samples), from the top or from the sides. Microscopes are usually equipped with several objective lenses that provide different levels of magnification, which are mounted on a turret, such that the user can select which one to use. Due to the wavelength of visible light, the magnification of optical microscopes is limited to 1000x. Larger magnifications are possible, but they do not improve the resolution power of the microscope. A typical microscope in a laboratory has a resolution limit at $\sim 0.5 \mu$m.

A digital microscope uses a digital camera to allow the visualization of the magnified images on a computer. In this work, a low-power UBS digital microscope was used to observe the microstructure of samples. Images of the observed object can be taken up to 200x of magnification and can be digitally stored. The microscope has an intensity-controllable LED light that illuminates the samples from above.

Despite the versatility of the optical microscope, nanometer-sized features cannot be resolved. Electron microscopy is an alternative more powerful imaging method, which can provide a maximum resolutions down to >0.1nm [66].

2.2.3   Scanning Electron Microscopy

SEM operates essentially with a beam of electrons and detectors. Electrons can be used resolve smaller features than visible light can due to the possibility to reduce their wavelength [67]. The generated beam of electrons is focused by electromagnetic lenses and apertures. This beam is scanned on the sample. The interaction of the electrons with the surface of the material is dependent on the characteristics of topography and composition of the sample (Figure 2.13). Two common detectors are located inside the chamber: a secondary electron (SE) and a back-scattered electron (BSE) detector.

SE are low energy electrons that interact inelastically with the sample's atoms, and that can only penetrate the surface at a few nm. The scattering of these electrons is very much dependent on the shape of the surface, such that they give information on its topography. Because these electrons are scattered very near the surface, they allow for very good resolution.

BSE are high energy electrons that elastically scatter with the atoms on the surface. Because these electrons have higher energy, they penetrate deeper into the surface, so the topography resolution of BSE is not as good as in the case of secondary electrons. They interact electrostatically with the nucleus of the atoms, which cause them to deviate from their trajectory. The probability of interaction with an atom on the surface of the sample is directly related to their atomic number Z, such that the higher the atomic number the more likely it is for scattering to occur. These interactions are visible as a map of scattering intensity, where the lightest areas correspond to heavier atoms.

In this work, samples were analyzed using a FEI Quanta 400 FEG ESEM, located at Centro de Materiais da Universidade do Porto (CEMUP), a FEI Inspect F50 from the Advanced Micrscopy Laboratory (LMA) at INMA and FlexSEM 1000 by Hitachi at the Departamento de Geociências, Ambiente e Ordenamento do Território (DGAOT) at FCUP.
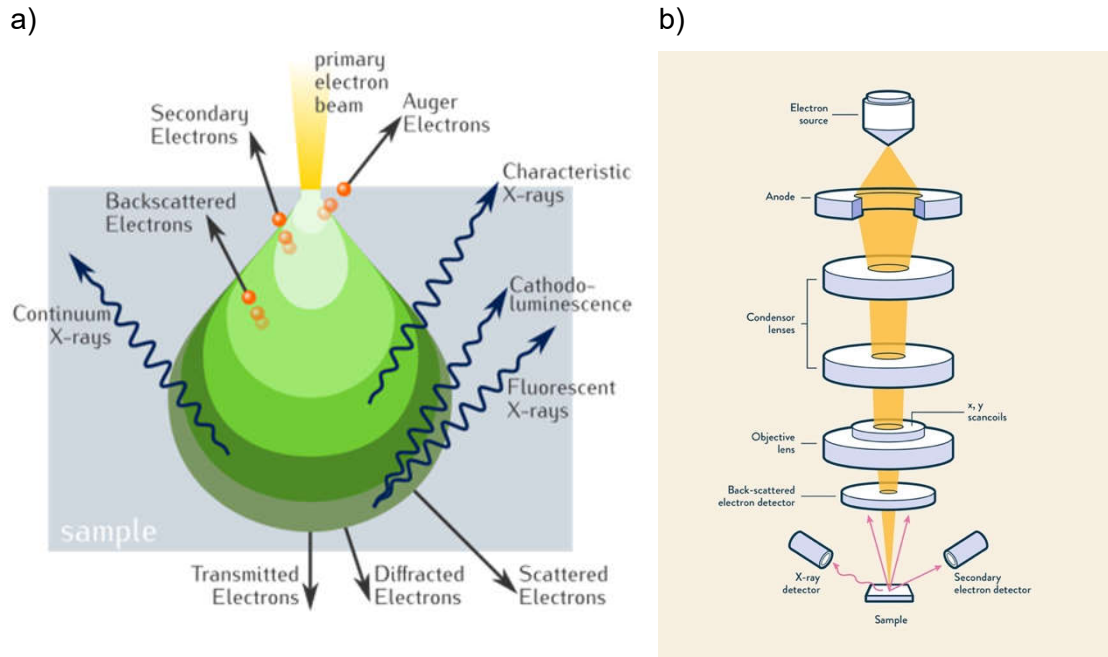
Figure 2.14 – a) Penetration of SE and BSE [68] and b) structure of a SEM [69].

2.2.3.1   Energy Dispersive X-ray Spectroscopy

Energy Dispersive X-ray Spectroscopy (EDS or EDX) is a technique usually coupled to a SEM system. It consists of a detector of X-ray radiation. X-ray photons are generated from the interaction between the electrons and the atoms on the surface of the sample. Very energetic electrons can knock out an inner orbital electron of the surface atoms. As the vacancy is occupied, energy is released in the form of X-ray photons. The wavelength of said photons is related to the energy transition of an electron between an outer and an inner shell in the atom. The energy related to the transition is characteristic of each element. A detector of X-ray radiation is able to identify elements and provide information on their abundance. The used EDS system is an EDAX Genesis X4M unit which is coupled to the SEM at CEMUP and a Quantax by Bruker at DGAOT.

2.2.4   X-Ray Diffraction

X-ray diffraction is a characterization technique that is used to obtain information on the crystallography of a sample [70]. It is based on Bragg's law, which correlates the radiation wavelength, interplanar spacing, scattering angle and the lattice parameter. It occurs whenever the wavelength of the incident radiation is of the order of the inter-atomic distances of the lattice of the sample. The radiation is diffracted by the atoms in the sample, and a diffraction pattern is generated for different angles of incidence. A Bragg peak appears in the diffraction pattern when constructive interference occurs. Each of

these peaks corresponds to a crystallographic plane that is identified by the Miller indices *(hkl)*. The Bragg's law is represented in Eq. (10) and the effect is illustrated in Figure 2.15.

$$n\lambda = 2d_{hkl}\sin\theta,$$ (10)

where n is a positive integer, λ is the wavelength of the incident wave, d_{hkl} is the interplanar spacing, θ is the angle of incidence of the radiation. From the interatomic spacing, it is possible to determine the lattice parameter of a crystal:

$$d_{hkl} = \frac{a}{\sqrt{h^2 + k^2 + l^2}} \ .$$ (11)
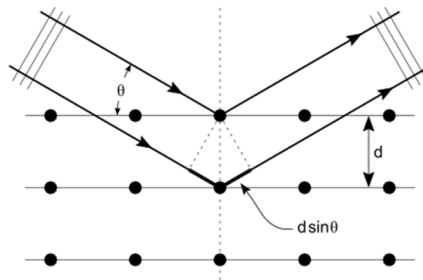
Figure 2.15 – Illustration of a reflection of X-ray radiation by a lattice.

The measurement of X-ray diffraction was performed using a SmartLab Rigaku diffractometer, which operates in a θ-θ geometry, using Cu K_α radiation the wavelength 0.1540593nm at room temperature.

The shape of the reflection peaks and the angle of incidence at which they occur are influenced by the sample and the equipment. As such, a diffraction pattern can also be a source of information regarding lattice microstrain, particle shape, lattice ordering, and equipment line broadening. Moreover, the intensity of the reflection peaks can also be revealing of the microstructure and provide information on the preferential orientation of the crystallites.

2.2.5   Profilometry

In the growth of thin films, the determination of the thickness resulting from deposition is essential for the correct determination of the sample's parameters. One way of achieving this goal is using a profiler, which consists of a thin tip which slides through the sample

and detects variations in its topography. The tip is cantilever-shaped, so a laser is reflected on its top surface, changing its direction according to the topography of the sample. This reflection is detected by a photosensitive diode and the software creates a 2D mapping of the topography of the area under study. It is then possible to evaluate the homogeneity of the sample and its thickness in different points.

Several conditions must be fulfilled in order to guarantee the quality of the measurement, such as the steadiness of the samples according to the tip, and consequently avoid external influences of the measurement. The measurement system must be closed to avoid environment variations (such as temperature and pressure) and it should not be moved or touched in order to not induce vibrations during the measurement.

The sharpness of the tip is also of great importance since it defines the resolution of the measurement. In Figure 4.3 it is shown how the structure of the tip can influence the output result. A Dektak XT from Bruker has been used for the measurement of samples' thickness.
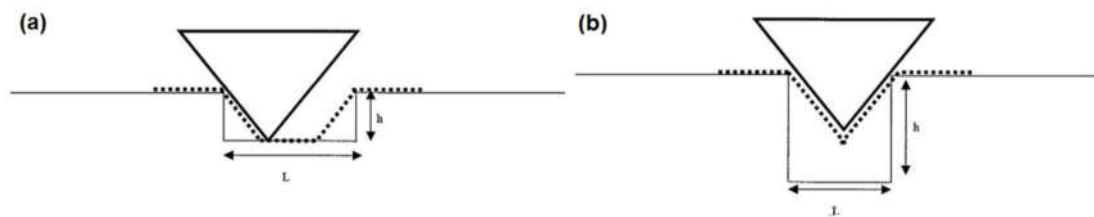
Figure 2.16 – Depiction of the influence of the size of the tip on the determination of the topography of the sample.

2.2.6 Vibrating Sample Magnetometer

This technique uses the Faraday's law of magnetic induction to determine the magnetic moment of a sample [69]. The configuration consists of a two-coil electromagnet, pick-up coils, a Hall sensor, and a sample holder. An axial constant magnetic field is generated by the electromagnet, which induces a magnetization on the sample. The sample holder vibrates perpendicularly to the magnetic field at constant frequency and amplitude, which causes a change in the magnetic flux, that in turn is proportional to the magnetic moment of the sample. This variation generates an AC voltage in the pick-up coils. The detected AC voltage is supplied to a lock-in amplifier to determine the magnetic moment of the sample.

Besides the strong dependence on the magnetic moment of the sample, the signal is also dependent on the sample position, as well as frequency and amplitude of vibration. The sample must be carefully positioned in the "saddle point", which is determined from positioning calibration. The instrument is usually calibrated with a reference Ni sample to properly determine the measured magnetic moment. Additionally, pick-up coils can be designed to sense magnetic flux variations in two orthogonal directions. Temperature control can also be introduced, both cryogenic and high temperature.
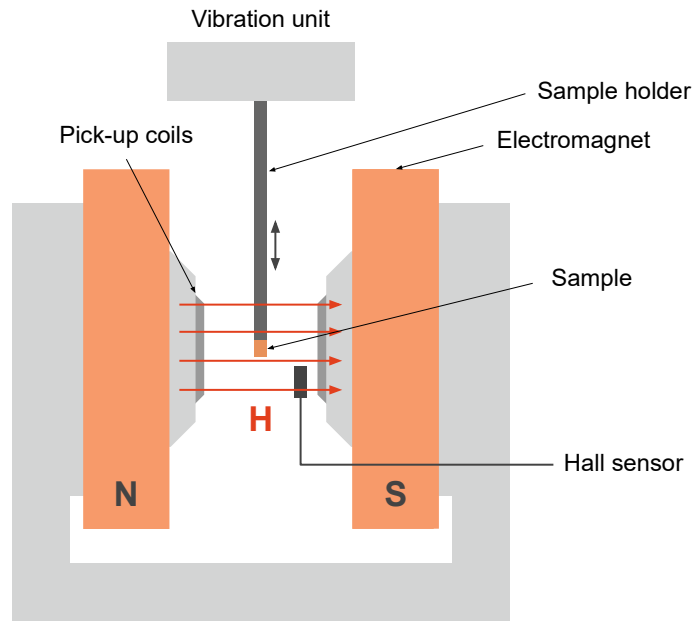
Figure 2.17 – Illustration of a VSM.

The VSM used in this work was supplied by MicroSense, LLC, with commercial name EV7, located at INMA. The magnetic field H can be generated by a set of Helmholtz coils between -1T and 1T. The sample holder can be switched to enable in-plane and out-of-plane measurements. Additionally, the equipment has a 3-axis positioning system, that enables optimum sample placement. Rotation is also possible about the vertical axis. Isothermal magnetization M measurements as a function of magnetic field were performed, by swiping the field from -1T up to 1T, and back down to -1T. From the curves, it was possible to obtain information on the magnetic saturation M_s, remanence M_r, and coercive field H_c of the samples.

2.2.7 Superconducting Quantum Interference Device VSM

A Superconducting Quantum Interference Device, or SQUID-VSM, is a magnetometer that operates at cryogenic temperatures using superconducting loops that are extremely sensitive to small magnetic fields, enabling the measurement of fields as low as 10^{-7}emu [72].

In this work, a MPMS-3 SQUID VSM by Quantum Design was used. The SQUID is equipped with a 70kOe superconducting coil in a cryogenic bath and a magnet control system. The measurement temperature can be varied between 2K and 380K, enabling the detection of phase transition temperatures if they exist within this range. This can be done by performing temperature-dependent magnetization measurements such as FC-ZFC (Field Cooled-Zero Field Cooled).

Measurements of the magnetic moment as a function of the applied magnetic field H were carried out at constant temperature of 300K. The field is swept between 50kOe and -50kOe and back to 50kOe, and the magnetic moment is acquired at each point. In the case of bulk samples, the magnetization M is determined from the fraction of the magnetic moment by the weight. In thin films, the volume is calculated from the thickness (determined from XRR or profiler measurements) and the surface area of the sample, and the magnetization is obtained from the fraction of the measured moment by the volume of each sample. From the M-H curves it is possible to obtain data of the remanent magnetization, coercive field and magnetic saturation.

2.2.8 Electrical transport measurements

The electrical resistivity was determined by performing measurements of the resistance of the samples. A 4-point probe method was employed, since it can eliminate parasitic resistance from the contact probes and take only the contribution from the resistance of the sample. The method consists of four collinear probes, spaced out by a distance s_n, where n=1, 2 and 3 (Figure 2.18). The outer probes apply a current that flows through the sample. The two inner contacts read the voltage drop across a distance s_2 in the sample and the resistance can be determined with the Ohm's law $V = RI$.
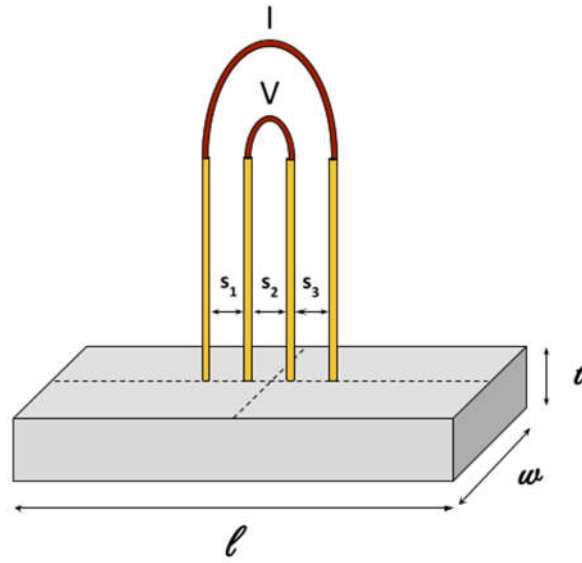
Figure 2.18 – Illustration of a resistance measurement using the 4-point probe method.

Considering an infinite sample, the expression of the resistivity is given by [73]:

$$\rho = \frac{2\pi}{\left(\dfrac{1}{s_1} - \dfrac{1}{s_2 + s_3} + \dfrac{1}{s_1 + s_2} + \dfrac{1}{s_3}\right)} \frac{V}{I},$$
(12)

where s_1, s_2 and s_3 are the distance between probes as illustrated in Figure 2.18. The collinear probe set-up herein used has probes distanced such that $2s_1 = 2s_3 = s_2$. Equation (12) becomes

$$\rho = \frac{6\pi}{5} s \frac{V}{I}.$$
(13)

In the case of finite sample geometries, a correction factor F must be included in (13):

$$\rho = \frac{6\pi}{5} sF \frac{V}{I}.$$
(14)

In samples thinner than the probes' spacing, F is a product of independent correction factors.

$$F = F_1 F_2 F_3 ,$$
(15)

where F_1 is the correction factor for the sample's thickness, F_2 for lateral sample dimensions and F_3 for the placement of the probes relative to the sample's edges. In thin samples on insulting substrates F_1 becomes

$$F_1 = \frac{t/s}{2\ln(2)}.$$

(16)

The factor F_2 is dependent on the geometry of the samples and the placement of the probes. It is determined from the width, length, and thickness of the sample and the spacing between probes. The values of F_2 were obtained from [74] for each sample.

Regarding factor F_3, since the distance between the probes and the edges of the sample is at least 4 times larger than the probe spacing, it reduces to 1.

The current was applied using a DC Voltage and Current Calibrator by Time Electronics and the voltage was read with an Agilent 34405A multimeter.

2.2.9   Tensile tests

Uniaxial tensile tests consist of applying tensile force to a specimen while measuring its deformation [75]. These tests are destructive and are used to obtain information on the mechanical properties of the material, including tensile strength, elastic modulus and ductility [76]. Generally, two claws are used to grip two ends of a sample with well-defined geometry, and one of them pulls away from the other at constant speed. A load gauge is used at one claw to determine the applied force at each moment. The result is a force-deformation graph. It is then converted into a stress-strain graph, using the geometric information from the sample, namely length, width, and thickness, such that the stress is given by $\sigma = F/A$ and the strain is given by $\varepsilon = \Delta d/d_0$.

The mechanical property profile can be identified from the stress-strain curve of a material (Figure 2.19 b). If the relation between stress and strain is linear (A-B section), it is considered an elastic regime, as defined by Hook's law. In this regime the material recovers its original shape when the load is removed, meaning that the deformation is reversible. In the case of a non-linear correlation, it is called plastic deformation (B-D section). In this regime, the material is permanently deformed and cannot recover to its original shape, even after the removal of the stress. The minimum stress at which permanent plastic deformation occurs corresponds to the yield stress σ_y. The application of permanent stress in the material leads to strain hardening, such that if the load is removed and subsequently the material is subject to elastic deformation, the yield stress would be larger than in the case where no strain hardening had occurred. Additionally, there is a regime known as hyperelasticity, which is common in soft matter, and is also characterized by a non-linear dependence [77]. The ductility of the material is defined by

its tensile profile as is directly related to the total elongation that it can endure. The largest the elongation, the more ductile is the material.

From the stress-strain curves, as illustrated in Figure 2.19 b), the elastic modulus *E*, the yield strength σ_y and the ductility (elongation at fracture in %) can be determined. *E* is obtained from the slope of the initial linear region, using the relation $E = \sigma/\varepsilon$, where σ is the stress in MPa, and ε is the strain (adimensional). σ_y is the minimum stress at which the sample suffers plastic deformation (denoted as point B), and the ductility is often represented by the elongation at break in % (point D), represented as ε_{frac}.

a)   b)
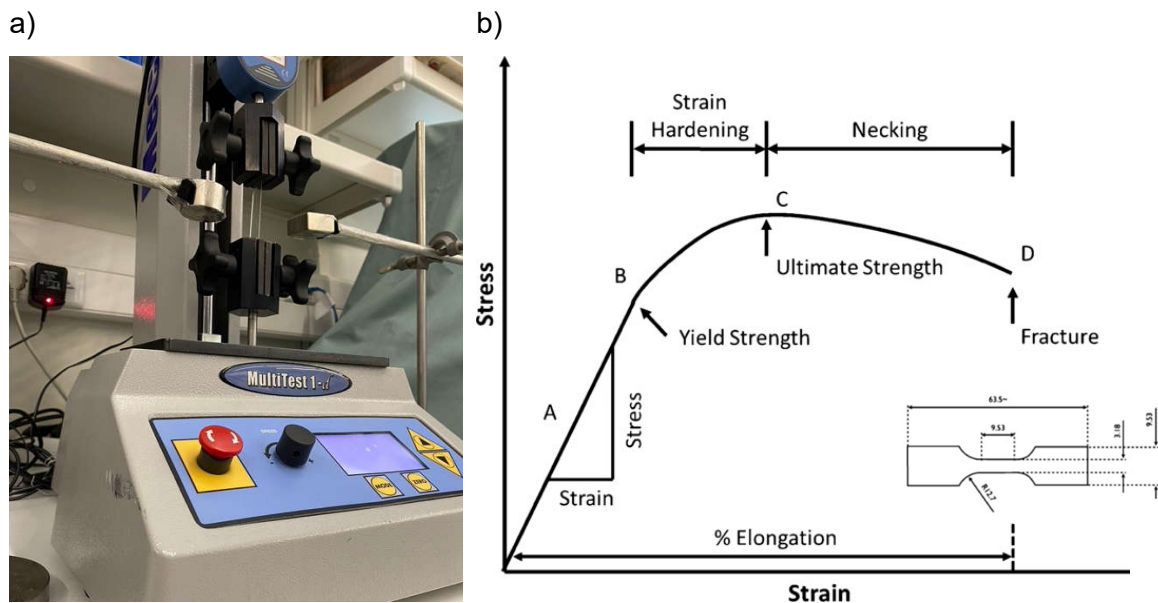
Figure 2.19 – a) Experimental set-up used to test soft sample at LEPAB and b) example of a stress-strain curve with elastic and plastic deformation (obtained from [78]).

Tensile tests were conducted in metal strips at the CMEMS facilities, in Guimarães, using a universal servo hydraulic testing equipment (Instron 8874, USA). The samples were cut into an "dog bone" shape, having dimensions of 0.5cm in width and 1.8cm in inner length, after which they were annealed. The tests were then performed at room temperature, in air and at H=0. The stress was applied in the rolling direction.

Soft samples were tested in the Laboratory for Process Engineering, Environment, Biotechnology and Energy (LEPAB) using a Mecmesin Multitest 1-D equipment and a 200N load gauge. Specimens were 5cmx1.5cm in size and had an average thickness of 650μm. The tests were performed in isotropic and in anisotropic samples, where the stress was applied in the direction of the alignment. For each composition and distribution, the tests were carried out under H=0 and H=200Oe, with the field being applied in the direction of the applied stress. The elastic modulus was obtained from the

tangent elastic modulus at near-zero strain. A strain range of 0 up to 0.25 was employed in its determination.

2.2.10   Magnetostriction measurement

During the dissertation period, given the relevance of the magnetostriction measurement, an in-house-built system was devised to measure λ versus H under room conditions.

2.2.10.1 Strain gauge method

A strain gauge consists of a deformation-sensitive conductive pattern on an insulating patch. The patch is bonded to the test specimen with an adhesive.

The way it operates is such that, if the test specimen is deformed, so is the strain gauge, which in turn causes the electrical resistance to change is proportion to the strain it experiences [79]. Given their ability to measure deformation, strain gauges can be used to measure deformation caused by H on magnetostrictive materials. The magnetostriction $\lambda = \frac{\Delta l}{l_0}$ is related to the strain gauge's resistance by:

$$\lambda = \frac{GF}{\Delta R / R_0},$$ (17)

where *GF* is the gauge factor, R_0 is the original value of resistance and ΔR is the resistance variation [41].

The strain gauges were bonded to the samples according to the indications of the manufacturer. The surface of the samples is polished with rough abrasive paper to clear the surface from oxides and other contaminants. The samples are then cleaned with isopropanol and a fibreless cloth to remove any debris from the polishing. A smaller sample is cut out from the polished strip and orientation marks are drawn to place the strain gauge oriented on the desired angle. The strain gauges are then placed on the specimen and their position is fixed using tape. One end of the tape is lifted until the strain gauge is not touching the surface and a drop of catalyzer and M-Bond 200 adhesive are applied. The strain gauge is then pressed down against the surface of the sample and pressure is applied for at least one minute. According to the manufacturer's instructions, one minute is enough time to ensure proper curing of the adhesive.
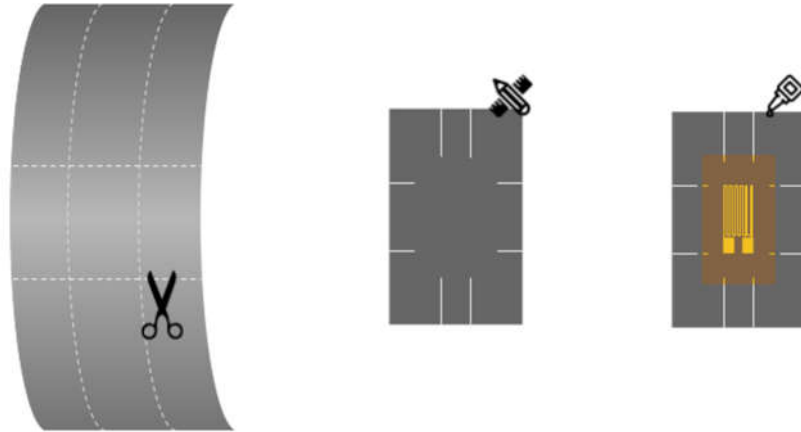
Figure 2.20 – The samples are cut from the polished strip, after which orientation marks are applied and the strain gauge is bonded.

Magnetostrictive materials experience strain changes in the magnitude of 10^{-6} under the influence of magnetic fields. Thus, the change in resistance is small, of the order of $10^{-4}\Omega$ ($\Delta V=0.1\mu V$ in a 10mV reading using I=1mA), such that conventional resistance measurement methods are inadequate. The use of a Wheatstone bridge provides more accuracy and a more stable measurement of the resistance [80]. The change in the resistance is measured by the amount of imbalance of the bridge.

The bridge circuit as depicted in or:

$$\lambda = \frac{4}{GF} \frac{V_{out}}{V_{in}}.$$

(22)

One shortcoming of the quarter bridge configuration is that any change in resistance is considered as a strain related change. Notoriously, the resistance can also be changed by temperature or by magnetoresistance. As a consequence, the quarter bridge circuit is sensitive to both magnetostriction and temperature changes. This challenge can be overcome by using a dummy strain gauge in place of R_2. It results that both R_2 and R_4 will change similarly to temperature changes and keep the bridge balanced temperature-wise.

The dummy gauge must be identical to the test gauge and be placed under the same conditions (temperature and magnetic field). Additionally, the test gauge must be bonded to a non magnetostrictive material. It results that any thermal and magnetic related effects of the strain gauge are cancelled out, and only magnetostriction induced stress on the test gauge can cause an imbalance on the bridge. This configuration also reduces wire resistance impact, since the wires connecting the strain gauges are similar in length. This adaptation of the quarter bridge is called quarter bridge with temperature

compensation. The quarter bridge with temperature compensation circuit is introduced in the measurement setup as displayed in Figure 2.21 b).

a) b)

Figure 2.21 a) is a simple quarter bridge. If the bridge is balanced, we know that $V_{out} = 0$ and that:

$$\frac{R_1}{R_3} = \frac{R_2}{R_4}, \tag{18}$$

However, if the bridge is out of balance ($R_4 \rightarrow R_4 + \Delta R$), the output voltage becomes:

$$V_{out} = V_{in} \left[\frac{R_1}{R_1 + R_3} + \frac{R_2}{R_2 + R_4 + \Delta R} \right], \tag{19}$$

Assuming the case that $R_1 = R_2 = R_3 = R_4 = R$ and that $\Delta R << R$, it results that:

$$V_{out} = V_{in} \frac{\Delta R}{4R + 2\Delta R} \approx V_{in} \frac{\Delta R}{4R}, \tag{20}$$

Using (17) in (20):

$$V_{out} = V_{in} \times GF \times \lambda, \tag{21}$$

or:

$$\lambda = \frac{4}{GF} \frac{V_{out}}{V_{in}}. \tag{22}$$

One shortcoming of the quarter bridge configuration is that any change in resistance is considered as a strain related change. Notoriously, the resistance can also be changed by temperature or by magnetoresistance. As a consequence, the quarter bridge circuit is sensitive to both magnetostriction and temperature changes. This challenge can be overcome by using a dummy strain gauge in place of R_2. It results that both R_2 and R_4 will change similarly to temperature changes and keep the bridge balanced temperature-wise.

The dummy gauge must be identical to the test gauge and be placed under the same conditions (temperature and magnetic field). Additionally, the test gauge must be bonded to a non magnetostrictive material. It results that any thermal and magnetic related effects of the strain gauge are cancelled out, and only magnetostriction induced stress on the test gauge can cause an imbalance on the bridge. This configuration also reduces wire resistance impact, since the wires connecting the strain gauges are similar in length.

This adaptation of the quarter bridge is called quarter bridge with temperature compensation. The quarter bridge with temperature compensation circuit is introduced in the measurement setup as displayed in Figure 2.21 b).

a)   b)

Figure 2.21 – Illustration of a) a quarter bridge and b) a quarter bridge with temperature compensation (obtained from [81]).

The sample holder is made of copper and has the shape depicted in Figure 2.22. The samples are placed on the holder and fixed with two copper strips, which allow the longitudinal deformation of the sample.
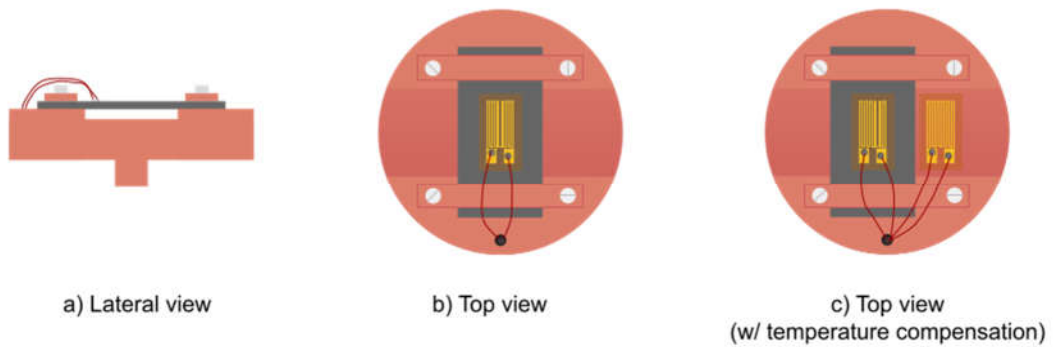
Figure 2.22 – Illustration of the sample-holder: a) lateral view, b) top view using a quarter bridge and c) top view using a quarter bridge with temperature compensation.

The sample holder is placed in a fitting holder where it is fixed during the measurements. The placement is ensured to be in the geometric center of the yoke of the coils, to maximize the homogeneity of the magnetic field in the sample. The strain gauges in the sample holder are connected to the bridge using shielded cables. The bridge is supplied with 0.1V with a DC Current and Voltage Calibrator 9818 by Time Electronics. A potentiometer is used as one of the resistances that allows the bridge to be balanced at

H=0. The output of the bridge is measured using an Agilent 34420A nanovoltmeter. A Hall sensor is positioned in the space between the sample holder and one of the coils. The sensor is connected to a power supply by Hopesun and to a Keithley 181 Nanovoltmeter. The magnetic field is manually altered by changing the current supplied. The electromagnet is controlled by the respective power supply from Oxford Instruments. The data is gathered using a LabView program, which also converts the measured signal from the Hall sensor into magnetic field intensity, and into magnetostriction, in the case of the bridge. An illustration of the described set-up is shown in Figure 2.23 and a picture of the set-up in Figure 2.24.
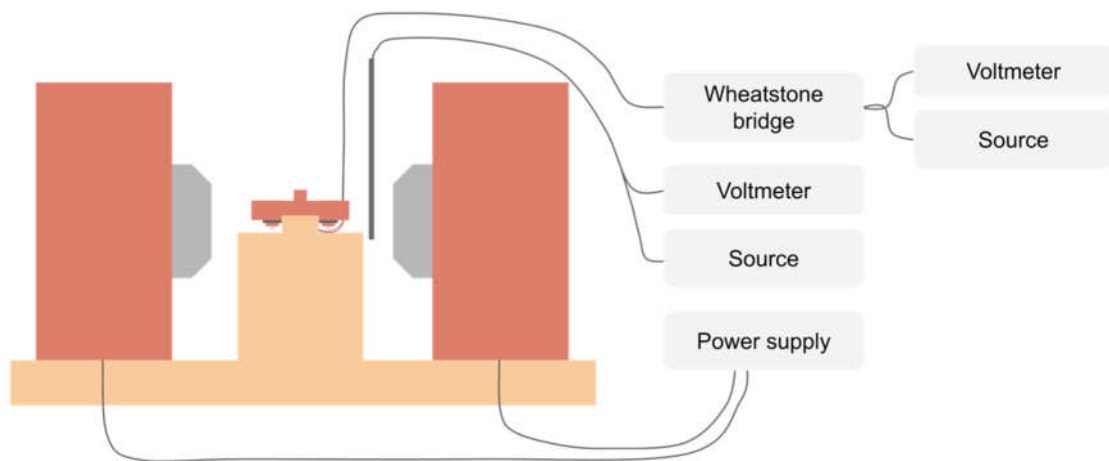
Figure 2.23 – Illustration of the magnetostriction measurement set-up.

a)

b)
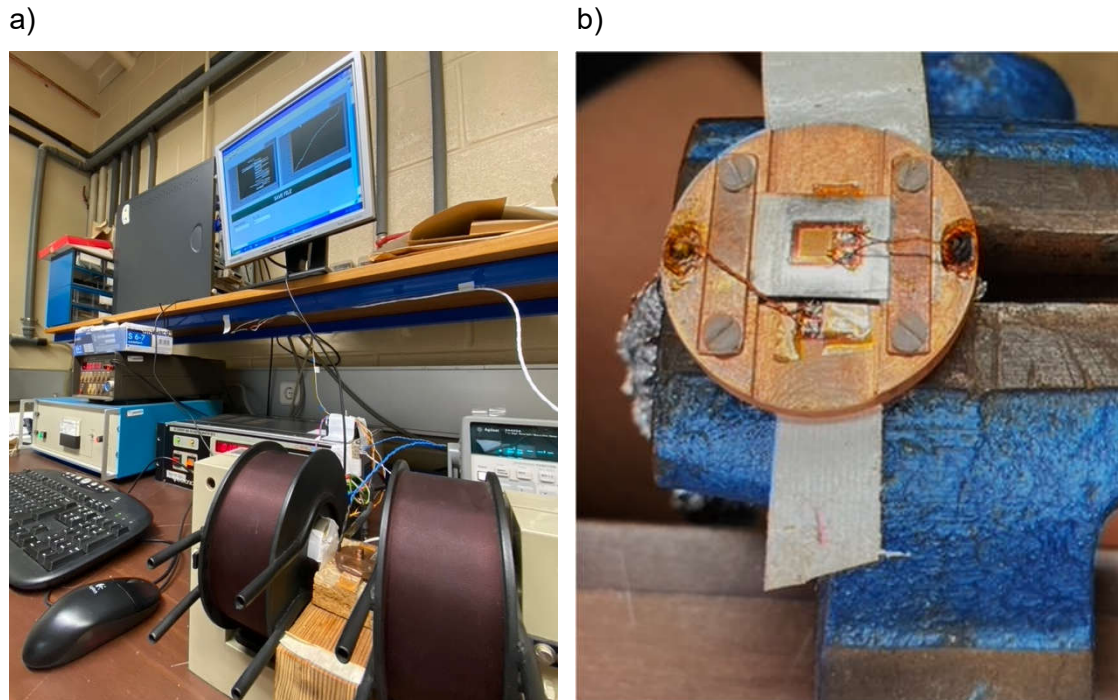
Figure 2.24 – a) Picture of the set-up where we can see the coils, where the sample holder is centered, the nanovoltmeter, the voltage source, the magnet power supply, the nanovoltmeter of the Hall sensor and the computer that acquires the data, b) picture of the sample holder with a mounted sample and a dummy gauge.

2.2.10.1 *Optical method*

Soft materials can generate giant deformations. In these cases, strain gauges are unsuitable due to their elastic limit. Alternatively, we used a method consisting of optical imaging. A digital microscope was used to take images of the samples under magneto-deformation. The set-up consists of a sample holder lined-up with a millimeter grid paper. Each sample is placed on the holder with its edges parallel to the grid and fixed using silicone glue in one of the ends (as depicted in Figure 2.25 a). The sample holder is then positioned inside an electromagnet and fixed using the position-adjustable yokes. The electromagnet is controlled by the respective power supply from Danfysik, model System 8000. The magnetic field is measured using a gaussmeter Lakeshore 421. The microscope is placed over the sample's free edge using a lever and is digitally controlled.
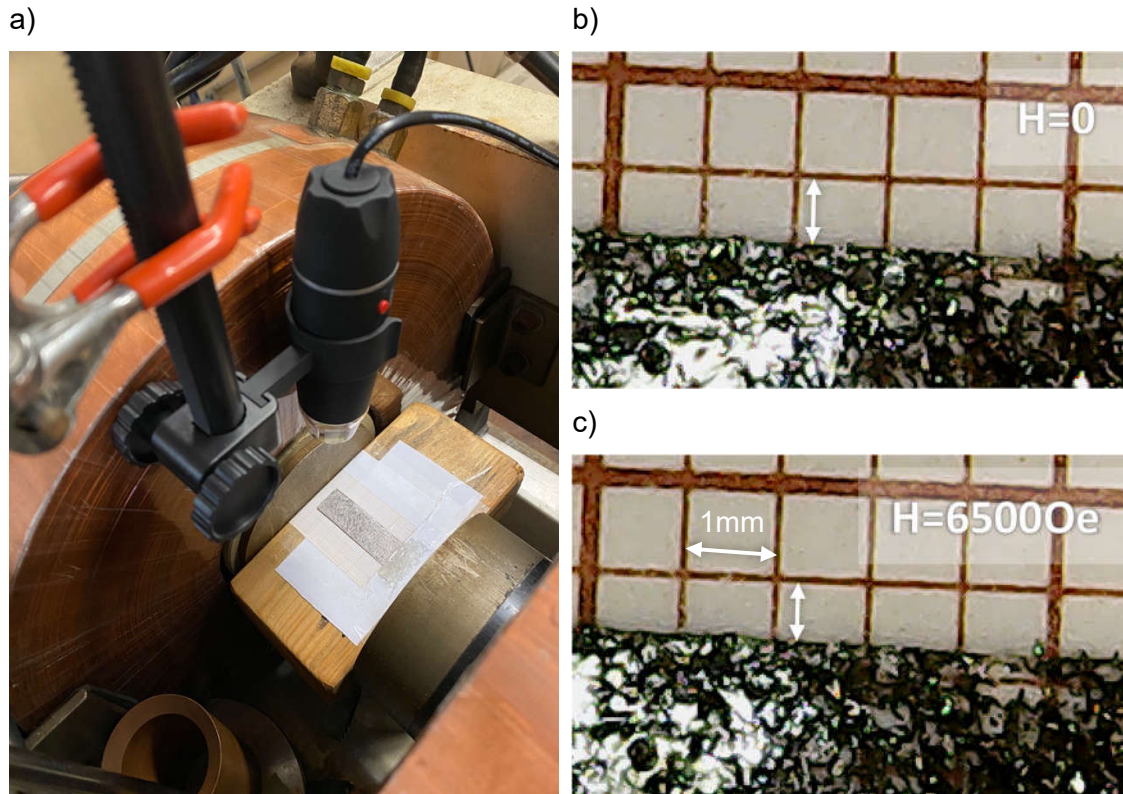
Figure 2.25 – a) Depiction of the set-up to measure magnetostriction in soft samples, b) microscope image of an isotropic sample of 2.3vol% under H=0, and c) microscope image of an isotropic sample of 2.3vol% under H=6500Oe.

Images of the sample were taken at different H values, until reaching H=6500Oe. Each sample is measured individually. The images are then processed using ImageJ software [82]. The used scale is provided by the grid paper, and the deformation is measured by determining the distance change of the edge of the sample to a grid mark. In Figure 2.25 b) and c), an isotropic sample with VF=2.3vol% is shown under H=0 and H=6500Oe, respectively. Several points along the sample were taken to improve accuracy.

The specimen shape influences the degree of magneto-induced deformation, due to the inhomogeneous distribution of field lines in the sample and its edges [81]. This influence can potentially change the amplitude of deformation of the material. Moreover, the aspect ratio also leads to varying results, as reported by Diguet and co-authors [82]. In fact, they have shown that the magnetostriction reduces as the length of the sample is increased. Other geometric factors like the corners of the sample [83], [84] and the spacing between the sample and the magnetic field source [83], [85] can also induce a non-uniform magnetic field in the sample.

A material's magnetostriction can be significantly affected by shape effects, so that the intrinsic properties of the material cannot be determined without considering its geometric properties. It can, however, provide information about the magnitude of the

magneto-induced deformation, as well as enable direct comparison between samples measured using the same method.

2.2.11 Testing of the transducer in the guided wave ultrasonic testing equipment

Testing of the samples was carried out in an industrial ultrasound guided wave set-up developed by EQS. In this testing method, we used a pulse-echo configuration, meaning that the strip was responsible for generating the ultrasound and sensing the reflected waves.

The samples were cut into 30cm-long and 5cm-wide patches and were then fixed around a steel pipe with duct tape (Figure 2.26 a) with 3.5m of length. The samples are placed at 0.8m from one of the ends. No couplant was applied between the samples and the pipe. The strips were magnetized with a permanent magnet, which was subsequently removed, such that they were tested using their remanent magnetization. A coil was placed around the strip and the pipe, as illustrated in Figure 2.26 b). The alternating signal is generated by the control and processing unit (CPU) (Figure 2.26 c), and is sent through the coil, generating an AC magnetic field. The testing frequencies f_T are 32kHz, 64kHz and 128kHz, with amplitudes of 100mV, 50mV and ~20mV, respectively.

a) b) c)
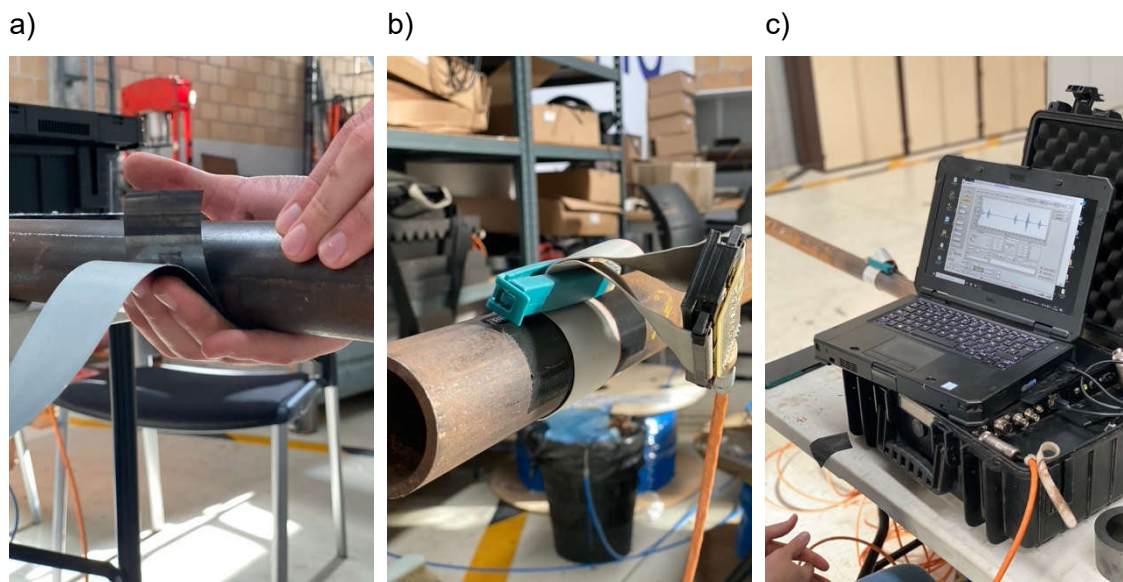
Figure 2.26 – Conducting a test using guided waves: a) fixing the strip to the pipe using duck-tape, b) placing the coil around the strip and c) acquiring the signal.

The detected signal is read and averaged over 50 measurements, which helps to discern the signal from a noisy background. This reading is the output of the measurement.

However, to better analyze the data, the signal is further processed. To the obtained data is applied a band filter of Δf=12kHz around 32kHz, and of Δf=20kHz around 64kHz and 128kHz. The envelope is determined using a Hilbert transform. Figure 2.27 shows the signal as obtained and after processing with a bandpass and a Hilbert transform.
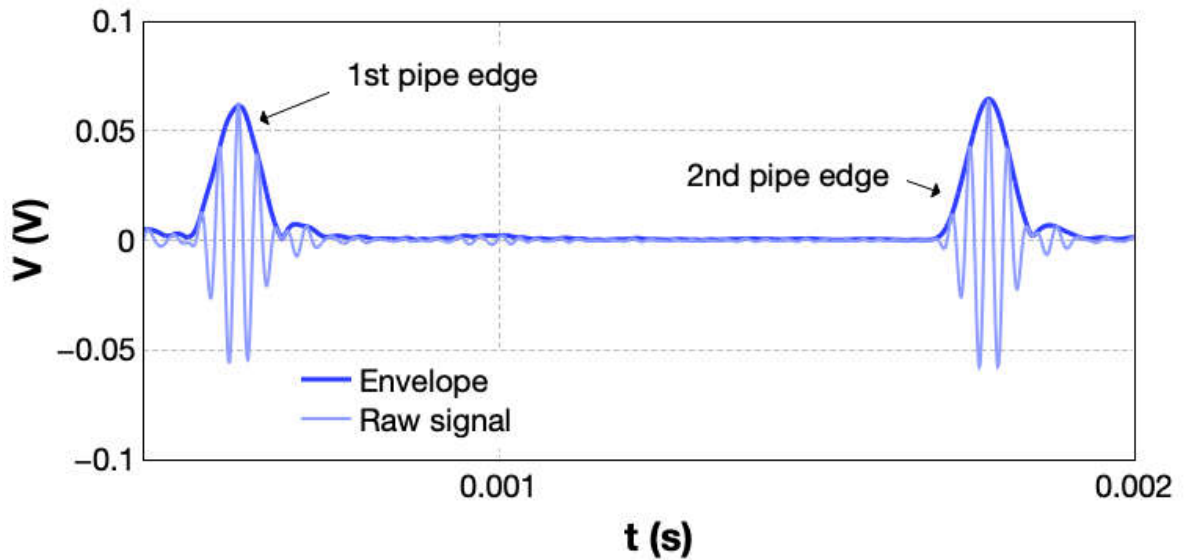
Figure 2.27 – The signal before and after processing.

2.2.12 Testing of the transducer in the bulk wave ultrasonic testing equipment

The set-up that was used to generate and detect bulk horizontal waves was developed by EQS with the purpose of measuring the thickness of pipes. The system operates in a pulse-echo configuration, such that there is an emitter and a receiver coil. The unit is composed of a signal generating circuit, a signal reading circuit, a processing unit, a communication unit and a power supply unit. The control and processing unit (CPU) was designed by EQS and its function is to generate the emission signal, read the received signal, process it and communicate it.

The samples used in this test must have no less than 2cm in diameter. They are fixed to the test object with a Neodymium magnet with a cylindrical shape and a diameter of 2cm, as depicted in Figure 2.28. The permanent magnet generates a magnetic field of around 100Oe at the surface of the cylinder. Between the sample and the magnet are inserted two induction coils, one for emission and the other for reception. The coil is excited by the CPU, which emits a signal with maximum voltage of V_{pk}=240V (580V peak-to-peak)

and a current of 20A. The short impulse has 5 cycles and only lasts 1μs, with a frequency of 5MHz.

The ultrasonic probe is fixed to the test object, which consists of either a steel calibration multi-step block, as depicted in Figure 2.28 a), or of a small steel square prism with an area of 2cmx2cm and varying thickness.

a)

b)
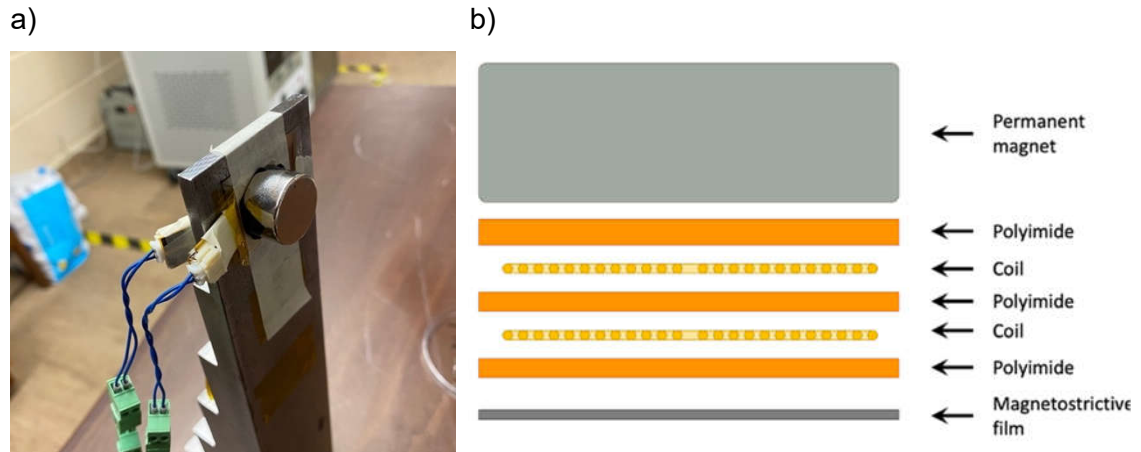
Figure 2.28 – Pitch catch measurement using an ultrasound shear longitudinal wave set-up: a) example of a thickness measurement, b) illustration of the different components.

The signal is averaged over 500 measurements to reduce the background noise. The signal is then filtered using a bandpass of 2MHz centered at the emitting frequency, which can be selected within the range of 3MHz to 5MHz. A Hilbert transform is applied to obtain the envelop of the detected impulses. Figure 2.29 depicts the signal before and after processing.
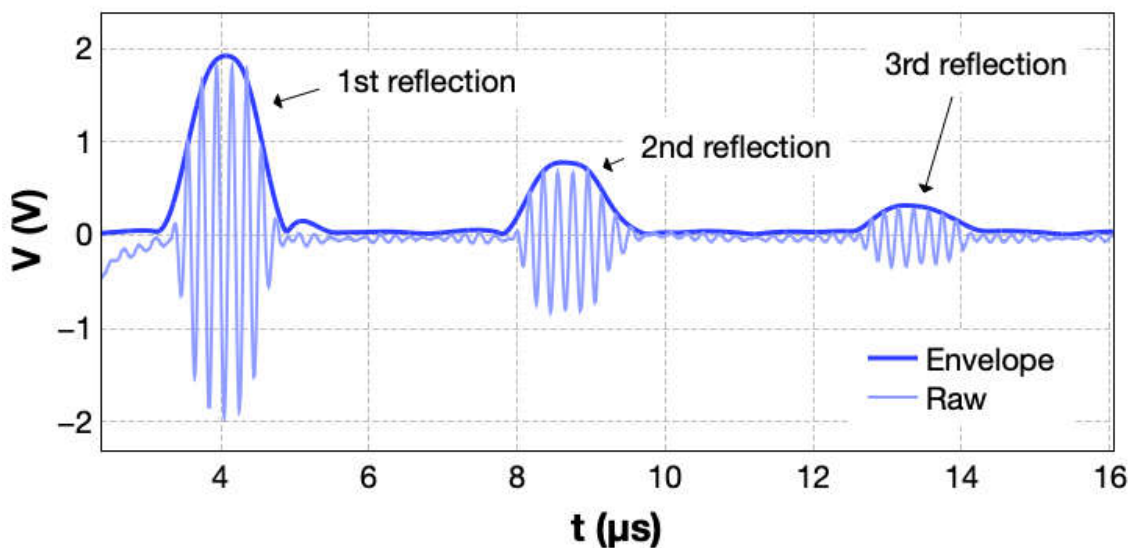
Figure 2.29 – Signal before and after processing.

Chapter 3   Tailoring the magnetostrictive properties of FeCo-2V strips

In Chapter 3, we will mainly focus on the study of the structural, morphological, magnetic and mechanical properties of the bulk FeCo-2V alloy. The material that will be studied is a commercial grade called Hiperco 50, and it enables fast scale-up of this solution. Samples of Hiperco 50 will be subject to thermal treatments to determine the influence of temperature and cooling rate on the material. Additionally, the magnetostriction will be investigated and correlated with the determined physical properties of the alloy. The annealed strips will then be subject to testing as transducers in the GW UT set-up and the results will be presented in Chapter 6. The conclusions from this study will enable the tailoring of the magnetostriction of Hiperco 50 using thermal treatments as well as enable its use as a magnetostrictive transducer in the field of NDT.

The scientific achievements that will be reported in this chapter are being used in the preparation of a scientific publication.

3.1   Fe-Co-V: Introduction and State of the Art

The widely accepted phase diagram of the binary alloy, $Fe_{100-x}Co_x$ with x=%Co, as proposed by Sourmail, is depicted in Figure 3.1 a) [86]. The alloy stabilizes on a face centered cubic (fcc) structure bellow the melting transition temperature, represented by a γ phase in all the composition range.

a)

b)
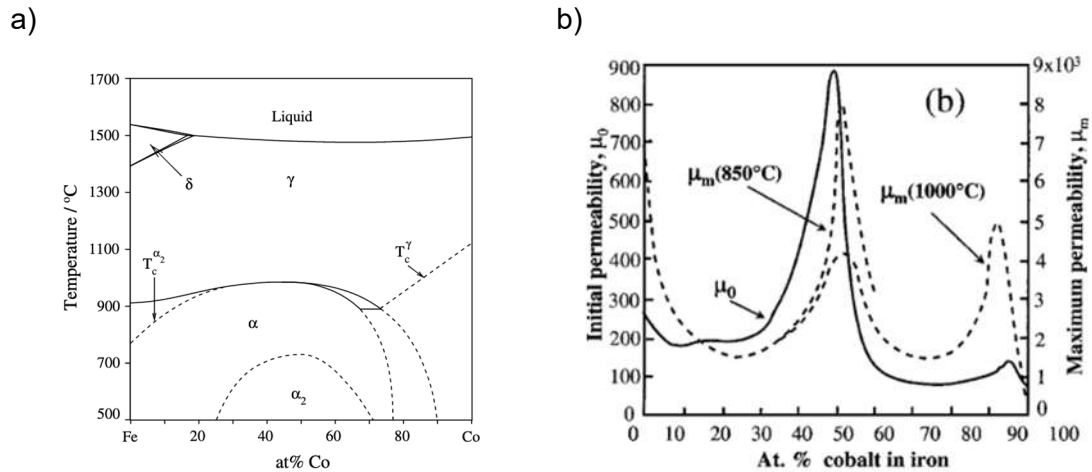
Figure 3.1 – a) Phase diagram of Fe-Co alloy [86] and b) initial and maximum permeability as a function of the concentration of Co [87].

In the equiatomic composition ($\sim$50% Co), the T_c=912°C marks the paramagnetic (PM) – ferromagnetic (FM) transition temperature, which also corresponds to a structural transition to a body centered cubic (bcc) lattice, represented by α [53]. This phase shows short-range disorder. The state of disorder consists of the random occupation of lattice sites by Fe and Co atoms. At T=730°C, $Fe_{50}Co_{50}$ undergoes an order-disorder transition to a bcc (α_2) ordered crystal structure, which cannot be suppressed by quenching, regardless of how severe [52], [88]. The degree of order influences the physical properties of stoichiometric Fe-Co particularly the strength and ductility of the alloy. The inability to suppress ordering has inhibited the widespread use of Fe-Co since, among other things, it develops extreme brittleness.

Notably, the addition of 2% of V in stoichiometric Fe-Co is known to slow down the kinetics of the order-disorder transition, such that order can ultimately be suppressed by quenching the material from a high temperature (see Figure 3.2 b) [89]. By rapid cooling, the alloy undergoes a martensitic transformation from the fcc austenitic γ phase to a metastable bcc disordered phase (α'). This α' phase is not represented in the phase diagram as it is unstable.

a)   b)
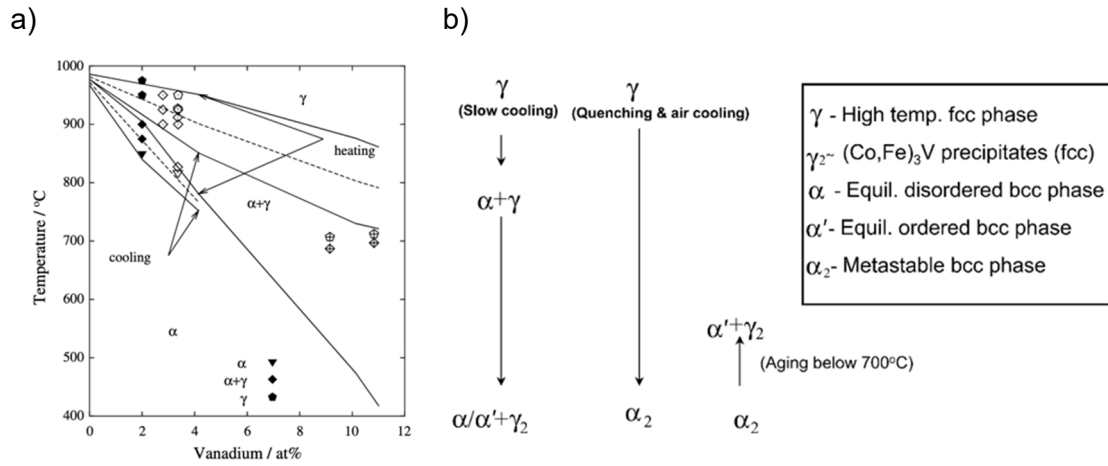
Figure 3.2 – Crystal structure and lattice distribution diagram of FeCo-2V alloys[86] and change in the transition temperatures due to the introduction of V in the alloy[86].

In the ordered α_2 phase, the atoms of Fe and Co have an ordered distribution, as represented in Figure 3.3 a). The α_2 structure of FeCo is a CsCl-type structure, consisting of two interpenetrating simple cubic sub-lattices, where Fe atoms occupy the body center site of the Co lattice, and vice-versa, as illustrated in Figure 3.3 a). In the disordered α' and α phases, the atoms occupy random sites in the lattice, as depicted in b). Some discussion remains regarding the distribution of V in the FeCo lattice. Conflicting reports suggest that V atoms occupy the Fe sub-lattice [90] while others suggest that V atoms occupy the Co sub-lattice [91]. The overall accepted configuration is that the V atoms occupy interstitial sites and further precipitate in the form of (Co, Fe)$_3$V [53].
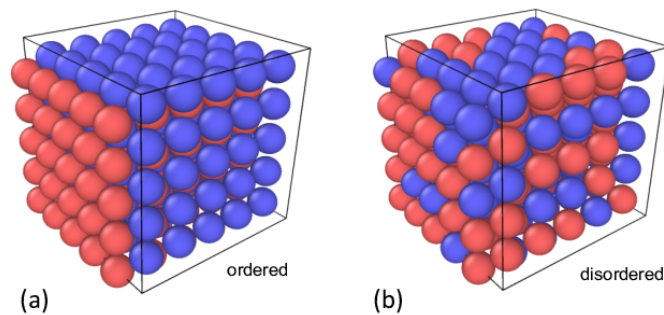
Figure 3.3 – Schematic representation of (a) ordered and (b) disordered structures of bcc structure alloys [92].

Notably, the transition from the fcc γ phase to the disordered bcc α phase is extended over a range of temperatures, such that the two phases can coexist in the ternary alloy [86]. A decrease in T_c is also observed, as well as thermal hysteresis. These changes to the phase transition temperature have been plotted by Sourmail, as seen in Figure 3.2 a).

The temperature from which FeCo-2V is cooled influences its degree of order (Figure 3.2 b). Slow cooling from a high temperature γ phase yields an ordered bcc structure. Quenching, on the other hand, yields a disordered bcc phase. If the material is annealed at a temperature bellow the order-disorder transition, it develops order, independently of the cooling rate. Quenching from the $\alpha+\gamma$ region results in a mixed structure of ordered and disordered $\alpha_2+\alpha'$ phases, since the γ phase will undergo a martensitic transformation to the metastable bcc α' phase, and the disordered α phase evolves the ordered α_2 ordered bcc structure. These transitions imply that, for the degree of order is dependent on the previous state of the alloy.

Commercial sheets of FeCo-2V can be obtained from different manufacturers, being Carpenter Technology Corporation the one to develop and trademark Supermendur as Hiperco 50. The manufacturing process includes cold rolling the alloy to obtain sheets with a thickness of <1 mm. The rolling leads to plastic deformation of the material resulting in a highly stressed structure, with a large density of dislocations [93]. Due to the unidirectional rolling, the grains of the polycrystalline alloy are elongated in the direction of deformation. The amount of plastic deformation caused by cold work has been shown to influence the precipitation kinetics of V-rich nucleus. More deformation density results in a increasingly uniform distribution of precipitates [94]. The Hiperco 50 strip is highly textured, resulting in anisotropic magnetic and mechanical properties.

FeCo-2V has been extensively studied for its remarkable magnetic properties combined with mechanical strength. A number of studies focus on improving the saturation, permeability and magnetic core loss of Hiperco 50 [95]–[99]. It is well known, however, that the magnetic performance of the alloy is enhanced at the expense of the mechanical strength because of the strong magnetoelastic coupling [52], [100]. As a result, efforts are being made to establish procedures that achieve superior mechanical and magnetic properties at the same time.

It is well known that the industrial applications have been the main drive for the investigation of this alloy. Hiperco 50 is used where high saturation flux density is necessary and weight is a concern. Its use is generally directed to commercial and defense aircraft generator applications and to the aerospace industry. Such applications are focus on reducing power loss and magnetoelastic effects, which in this case are also a source of energy dissipation. As a result, research into the enhancement of the magnetostriction of this alloy is severely lacking. Studies on the magnetostriction of Hiperco 50 have been performed as a function of the temperature [101], [102]. But still,

there is a significant void of information correlating the magnetic and mechanical properties with the magnetoelastic profile of bulk FeCo-2V.

In light of this, the present work aims at establishing a relationship between the magnetic, mechanical and magnetoelastic properties of annealed Hiperco 50 strips. This will be done by performing thermal treatments at varying temperatures between 450ºC and 850ºC and by slow cooling or quenching them to room temperature. The physical properties of each sample will be determined. By understanding the effect of the temperature and cooling dynamics on the morphology and atomic structure, we will be able to tailor the physical properties and the magnetostriction of the alloy.

3.2   Influence of the Thermal Treatments on FeCo-2V

This section describes our research on the effects of different heat treatments on the properties of the alloy.

As explained above, the phase diagram of the Fe-Co alloy is complex and dependent on the annealing temperature, cooling dynamics and the amount of previous cold work. For this reason, heat treatments using different annealing temperatures and cooling rates were employed, as detailed in 2.1.4.

Prior to any treatment, the surface of the alloy was observed using electron microscopy to understand our starting point (Figure 3.4). It was cleaned with isopropanol to remove any residues from the surface, such as oil (used to delay oxidation) and dust.

From Figure 3.4, we see that the samples exhibit a surface with aligned crevasses. These result from the cold rolling of the alloy during its manufacturing. Some dark spots are visible on the surface that can be related to oxidation or oil stains.
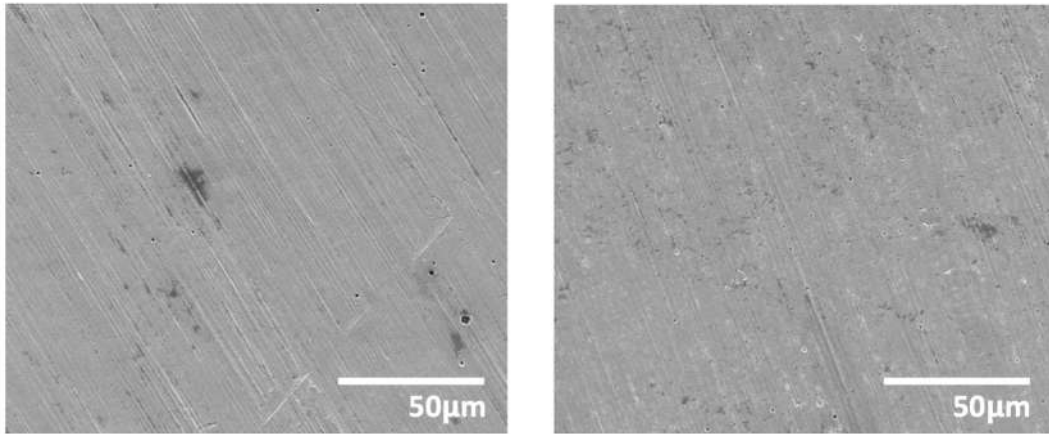
Figure 3.4 – SEM images of the surface of Hiperco 50 without any treatment under a magnification of 1500x and obtained using secondary electrons.

A complementary analysis was performed using EDS analysis unveiling a similar composition to the one provided by the supplier, as shown in Table 3.1.

Table 3.1 – Atomic composition of a sample of polished Hiperco 50, determined from EDS and compared to the nominal composition provided by the supplier

Sample	Element	Atomic composition (%) (EDS)	Nominal composition (%) (supplier)
Hiperco 50	Fe	50.19	49.25
	Co	47.94	48.75
	V	1.88	2.00

Further physical properties were measured and will be presented in the following sections that, for simplicity, will be directly compared with those of the annealed samples.

3.2.1   Influence of quenching on the physical properties of FeCo-2V strip

The annealing treatments were performed at temperatures in the range 450°C to 850°C, and it was carried out in atmospheric air. Because of the presence of oxygen during the treatment, superficial oxidation of the samples occurred.

3.2.1.1 Morphological & elemental properties

The evolution of grain size and shape was investigated by morphological characterization with electronic microscopy. This is done by observing the polished

surface of the material using the BSE detector of SEM (Figure 3.5). The surface of the samples was prepared as described in 2.2.1.

Notice that the analysis of SEM surface images allows to determine the grain size and grain boundary evolution with increasing annealing temperature. This is possible because if the surface is polished down to below μm-roughness (using the polishing process described in 2.2.1), the scattering of high intensity electrons with the crystalline direction of the grain becomes visible. These differences are observable as different tones in the grey scale. As one can see from Figure 3.5, the grains annealed at $T_a \geq 550°C$ acquired well defined grain boundaries as compared to Hiperco 50 in its original state. In the sample annealed at 450°C, no significant morphological alteration is reported, suggesting that the temperature and annealing time were insufficient to result in relevant morphological evolution. Annealing at 550°C leads to grain coalescence, with clearer boundaries between them. The grains tend to increase in size with the rise of annealing temperature. The image obtained from the sample annealed at 850°C exhibits scratch lines oriented in one direction. This is a result of poor polishing.
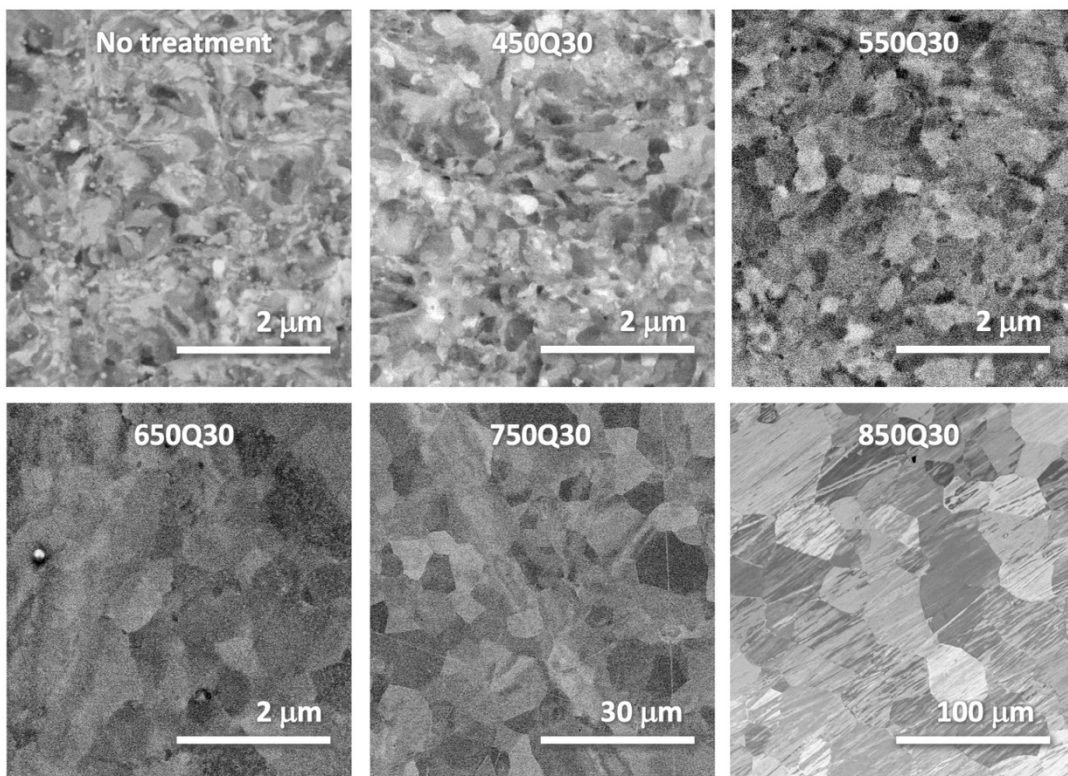
Figure 3.5 - SEM images of the polished surface of annealed samples of Hiperco 50 at different temperatures, followed by ice and water bath quenching. Attention should be taken to the different scales of each sample.

The average grain size D was determined for each annealing temperature using the average grain intercept technique, and it is plotted as a function of the latter in Figure 3.6 a). Annealing between 450°C and 650°C results in the average grain diameter to increase from 280nm to 580nm, which is within the same order of magnitude. Annealing at 750°C and 850°C raises the diameter to ~8.5μm and ~48μm, respectively. We can see that the grain size follows an exponential function of the type $D = Ae^{bT_a}$, where A=0.01432 and b=0.01768.

The EDS analysis of the samples is depicted in Figure 3.6 b). Despite the oxidation of the samples during the annealing, no oxygen was detected, suggesting that the oxidation occurred only at the surface and did not contaminate the core of the samples. Due to the large affinity of Fe with oxygen, the annealing can result in the segregation of Fe to the surface of the sample, where it oxidizes into some form of Fe-O. The oxidation of Fe, and its subsequent removal in the polishing step, lead to a stoichiometry change into a higher atomic composition of Co in the alloy. It should be noted that the stoichiometry could be dependent on the distance of the measured layer to the original surface (before the polish). As the segregation occurred at the surface, it is expected that the largest stoichiometry changes occur near the surface and reduce towards the core of the alloy. However, during the polishing, there is no control over the thickness of the removed layer, so that it is unlikely that the samples are being analyzed at the same distance from their oxide layer. Moreover, the EDS detector is only able to draw information from no more than a few micrometers below the surface of the sample [103], so the data may not be representative of the stoichiometry of the annealed alloy. Thus, it is recommended that these results are compared conservatively.

a)

b)
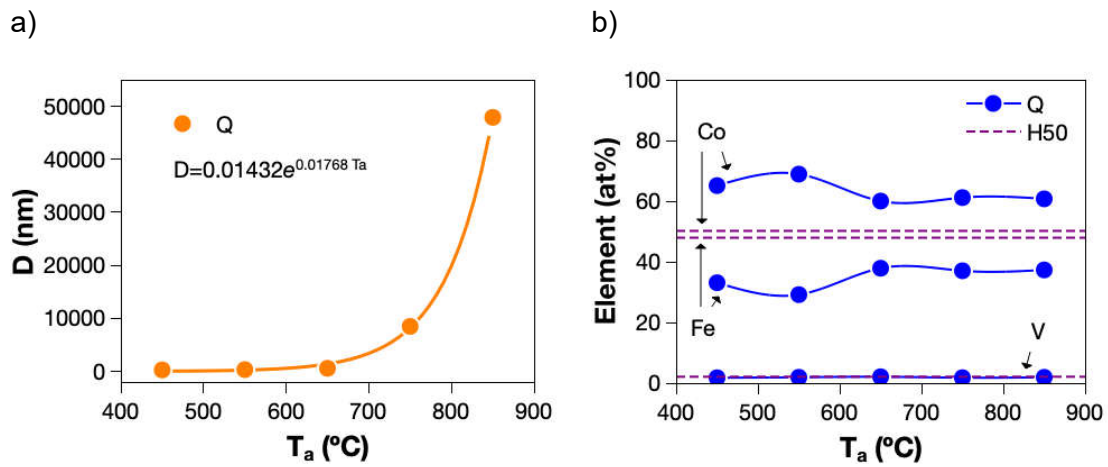
Figure 3.6 – a) Grain size as a function of the annealing temperature (the line is a fit of the data) and b) composition of the quenched Hiperco 50 samples.

3.2.1.2   Mechanical properties

The change in mechanical ductility between each sample is easily noticeable by manually handling them. To quantify this variation, mechanical tensile tests were carried out. The stress-strain curves measured in the rolling direction of the strip are plotted in Figure 3.7.
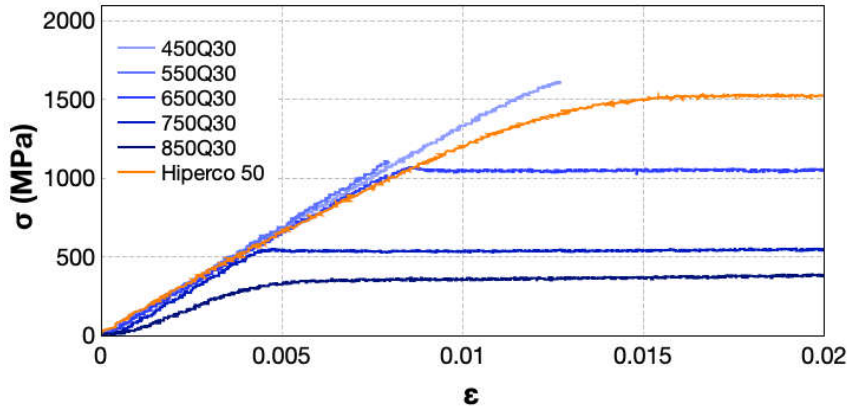
Figure 3.7 – Stress-strain curves of the annealed and quenched samples in the direction of rolling at RT.

All the samples exhibit a linear behavior at small tensile stresses. The samples annealed at 450°C and 550°C fracture within the linear regime, while the samples annealed at 650°C and higher temperature exhibit a second regime characterized by a flat slope. In this regime the samples are strained with negligible change in the applied stress. This behavior is characteristic of a perfect plastic deformation.

The sample of Hiperco 50 with no thermal treatment was also subject to tensile testing. Its stress-strain curve is depicted in orange color in Figure 3.7. It is characterized by the same linear elastic regime as the annealed samples. However, instead of transitioning immediately to a perfect plastic deformation, it exhibits an intermediate regime. For strains >0.01, the slope of the curve decreases until it reaches a flat slope at $\varepsilon \approx 0.017$. This intermediate behavior is in fact a cooperation between elastic and plastic deformation. This transition is also visible in the stress-strain curve of the sample annealed at 850°C.

The Young's modulus of each sample was obtained from the initial linear deformation, and it is plotted in Figure 3.8 a). The sample of Hiperco 50 has an elastic modulus of 120GPa, as indicated in the graph by a dashed purple line. The yield stress in plotted in Figure 3.8 b). Since the samples annealed at 450°C and 550°C do not show plastic behavior, the yield stress was taken to be the stress at the fracture point.

a)   b)
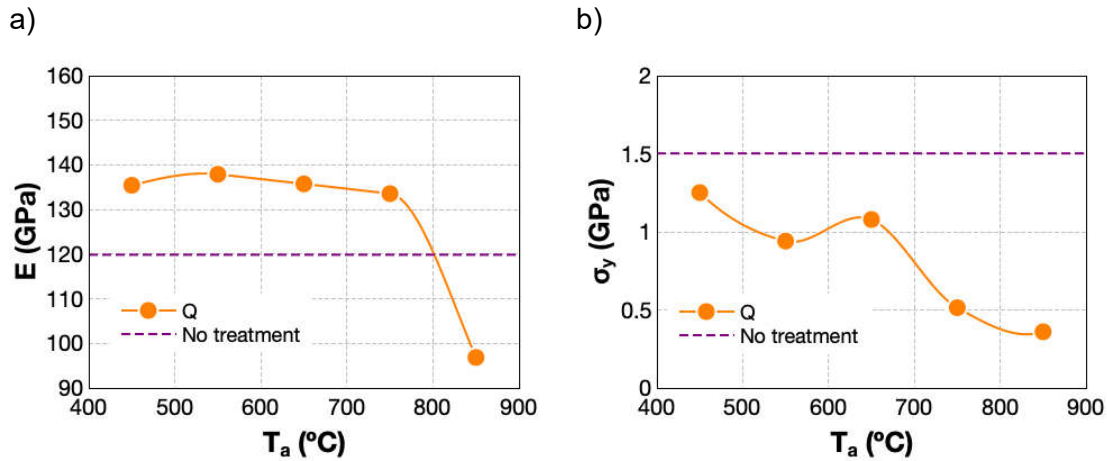
Figure 3.8 – Mechanical properties plotted as a function of T_a: a) E and b) σ_y.

Regarding the annealed samples, *E* shows a relatively constant value with T_a, averaging 135GPa, higher than the elastic modulus of the original sample. It drops significantly in the sample annealed at 850°C, to bellow 97GPa.

As for the yield stress shown in Figure 3.8 b), the original sample of Hiperco 50 takes a value of 1.5GPa, higher than that of any annealed sample. This is due to the strain hardening caused by the intensive cold work. σ_y exhibits a negative trend with increasing annealing temperature. The sample annealed at 450°C takes σ_y=1.3GPa and at T_a=850°C takes σ_y=0.4GPa.

3.2.1.3 Structural properties

Figure 3.9 a) shows the normalized diffraction patterns of the samples as annealed. In the samples annealed at temperatures of 650°C and bellow, peaks are visible at $2\theta\approx45°$, 65° and 82°, corresponding to the crystal planes (110), (200) and (211) of equiatomic FeCo, respectively [104]. Since V only exists in trace amounts (V$\leq$2at%), its presence in the alloy does not result in crystallographic changes, hence why the annealed sample spectra are similar to the spectrum of the stoichiometric FeCo. The samples annealed at $T_a\geq$650°C exhibit sharp oxide-related reflection peaks, along with a reduction in intensity of the peaks related with FeCo. The asterisk * identifies the peaks corresponding to reflection planes of iron oxide. The annealing at 450°C also resulted in surface oxidation of the alloy, but no related peaks are visible, suggesting it is a very thin layer.

XRD was performed on the samples one more time after the oxide surface layer was removed by polishing with silicon carbide abrasive paper and diamond suspensions. Figure 3.9 b) shows the XRD spectra of the polished samples and it reveals data that

was previously hindered by the oxide layer. It is observable from the spectra in Figure 3.9 b) that the relative intensity of the bcc peaks (110) and (200) changes with the annealing temperature of the samples. This indicates that the texture changes from (200) to (110) in the off-plane direction, suggesting that recrystallization occurs. A positive shift of the bcc Fe-Co peaks occurs as the annealing temperature increases. Moreover, new peaks emerge at 2θ=43.88° and 2θ=50.9°. These peaks are reported as the fcc γ phase of Fe-Co and match the reflection of the crystal planes (111) and (200). This phase is only formed at room temperature in the presence of a higher concentration of Co, which is in line with the results obtained with EDS. Additionally, a peak corresponding to the reflection of the crystal plane (311) of $CoFe_2O_4$ is also detected at 2θ=35.2°.

a)   b)
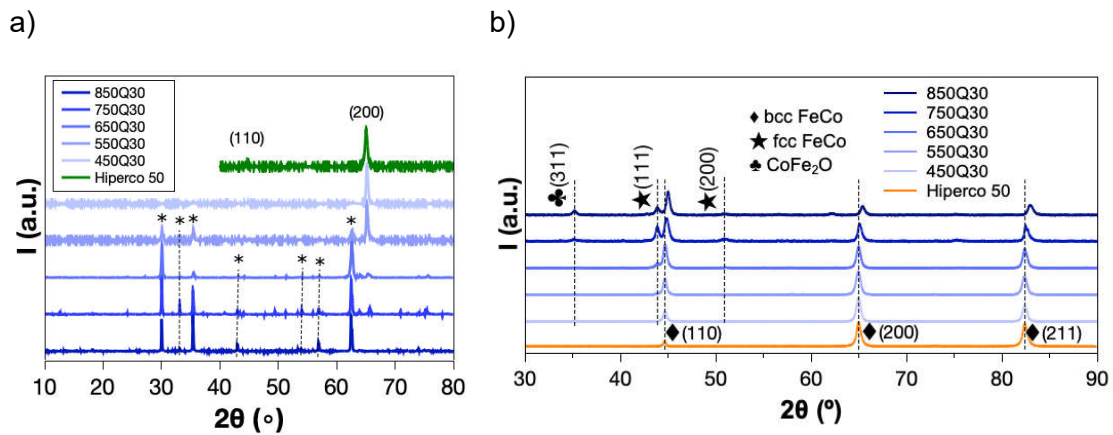
Figure 3.9 - XRD spectra of the samples annealed between 450°C and 850°C followed by an ice bath quenching: a) before and b) after removal of the oxide surface layer.

The determined lattice parameter a of the polished samples is plotted in Figure 3.10 and it was obtained from the Bragg's law. Up to the annealing temperature of 650°C, the lattice parameters are relatively constant, taking an average value of a=2.866Å. A small increase is observed after annealing at 450°C and 550°C, which is related to the ordering of the alloy. As the annealing temperature is increased to 750°C and then to 850°C, the lattice constant decreases significantly to a=2.860Å and a=2.848Å, respectively. This change is related to the appearance of the fcc phase (V-rich precipitates, close to the Co_3V composition) or due to stoichiometric changes in the alloy towards Fe-Co compositions with larger concentration of Co [105]. This stoichiometric change was also observed in the compositional data from EDS.
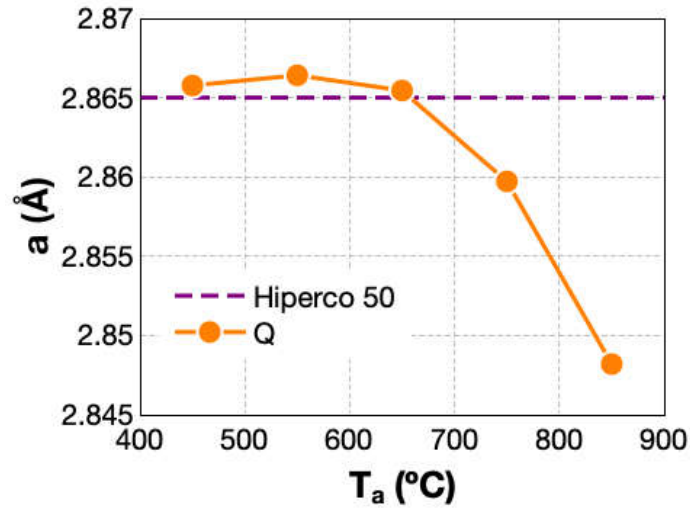
Figure 3.10 – Lattice parameters determined from XRD spectra and plotted as a function of the annealing temperature.

3.2.1.4 Magnetic properties

The magnetization M was measured as a function of the magnetic field H in a VSM system at room temperature, and it is plotted in Figure 3.11. The samples were prepared by cutting into squares of 1mmx1mm and were subsequently measured along the two in-plane directions. The longitudinal direction corresponds to the strip's rolling direction, while the transversal direction is perpendicular to it. The isothermal M-H curves exhibit a hysteresis cycle with small coercivity (H_c < 50Oe), typical of a soft ferromagnet. In the longitudinal direction, the curves corresponding to the annealed samples have a steeper slope (susceptibility), compared to the Hiperco 50 sample with no treatment. Apart from that, the magnetic curve is not significantly changed for different T_a. In the transversal direction, there is no significant alteration of the M-H cycles from the original sample to the annealed samples. M_s is essentially unchanged by the annealing, taking values between 225emu/g and 210emu/g for increasingly higher annealing temperatures. The small drop in M_s could be related to the stoichiometric changes that were previously observed with EDS and XRD [106]. The sample of Hiperco 50 without any thermal treatment has an M_s=215 emu/g.

a)

b)
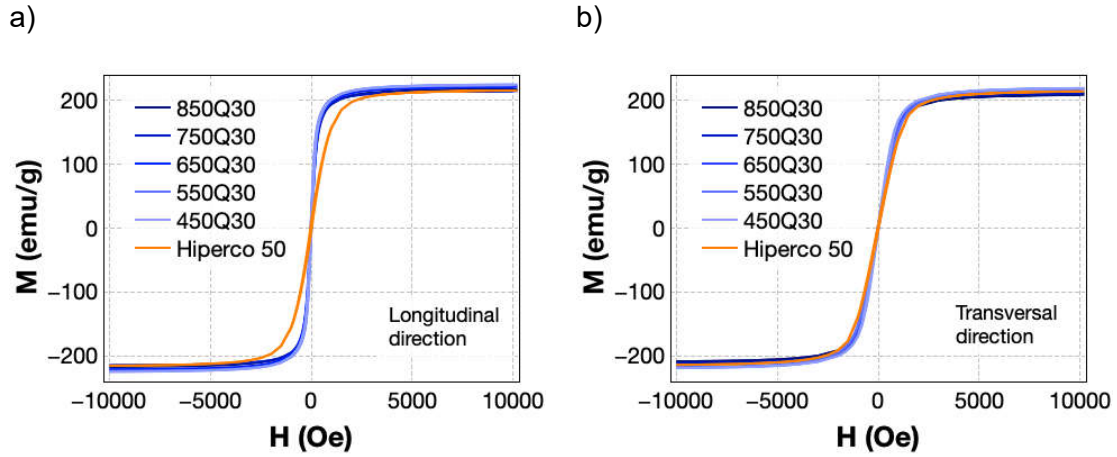
Figure 3.11 - Isothermal M-H curves of annealed and quenched samples: a) longitudinal direction and b) transversal direction.

An analysis of the magnetic properties of annealed and quenched polished samples as a function of T_a is shown in Figure 3.12, in both longitudinal and transversal directions, as a function of annealing temperature, namely M_r and H_c. In the transversal direction, the remanence exhibits a small decrease with the annealing temperature, from 6.3emu/g to 1emu/g for increasingly higher T_a. In the longitudinal direction, M_r is greatly enhanced by annealing the material at 450°C and 550°C. It rises from 8.7emu/g (no treatment) to 21emu/g and 14emu/g, respectively. With increasing T_a, in the longitudinal direction, the remanence decreases down to 1.5emu/g (T_a=850°C). The anisotropy, consequently, is also reduced.

Likewise, the coercivity exhibits a decrease with increasing annealing temperature. The H_c values are similar in both in-plane directions and vary between 30Oe for T_a=450°C and 3Oe for T_a=850°C. The largest value is obtained for the sample of Hiperco 50 with no treatment, H_c=35Oe (longitudinal) and H_c=32Oe (transversal). The drop in H_c suggests that boundaries are decreased as the annealing temperature is increased, which could include dislocations, internal stress, and grain boundaries.

a)

b)
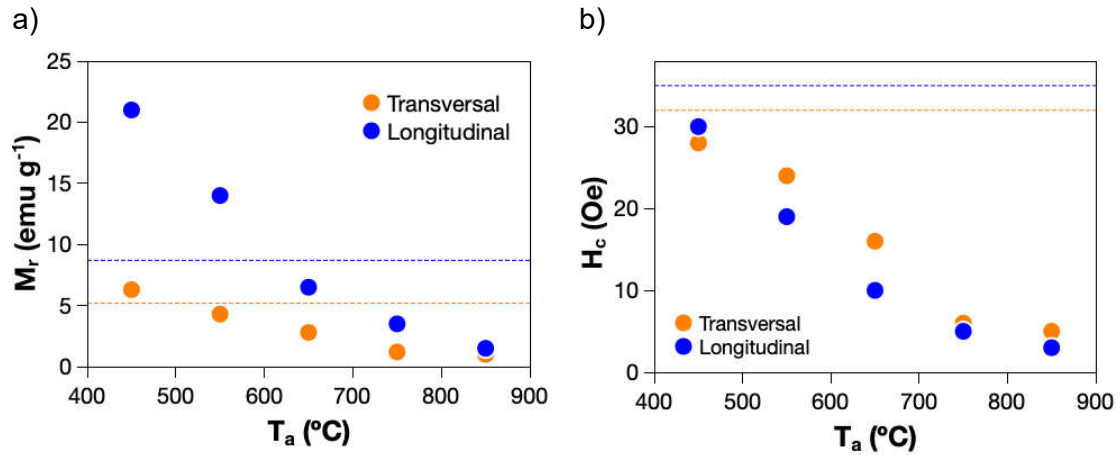
Figure 3.12 - Magnetic properties of annealed and quenched samples of Hiperco 50: a) remanent magnetization and b) coercive field.

3.2.1.5 Magnetoelastic properties

The magnetostriction λ of the samples was measured in the direction longitudinal and transversal to the rolling. The curves of λ as a function of the magnetic field H are plotted in Figure 3.13. The characteristic V shape of λ-H can be seen in each measurement. In the longitudinal direction (Figure 3.13 a), the curve of the original sample with no treatment follows a butterfly curve (in red), which is distinctive of hysteretic behavior. The same sample measured in the transversal direction does not exhibit hysteresis but does not saturate either. After annealing, the hysteresis is suppressed in all samples. The longitudinal direction yields larger values of λ, which suggests that the anisotropy of the material also influences its magnetoelastic properties.

a)

b)
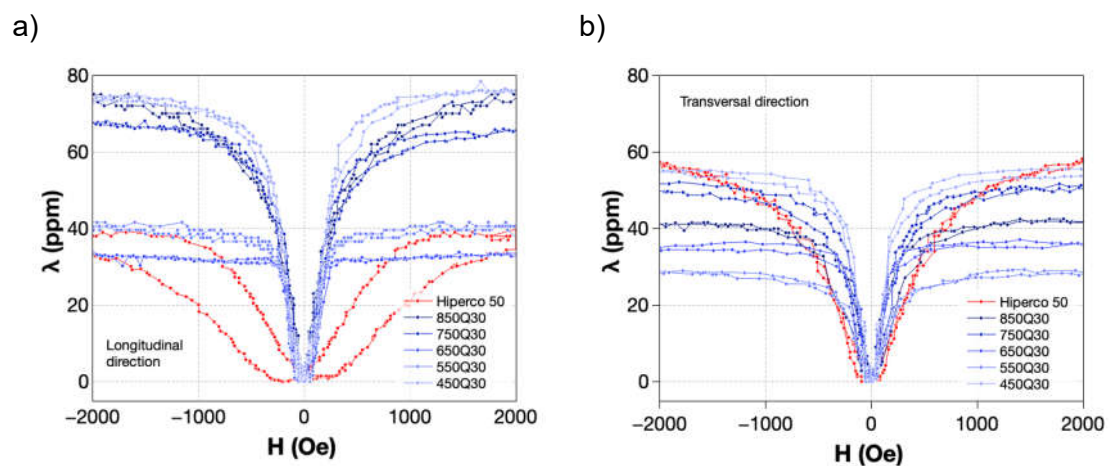
Figure 3.13 – Magnetostriction measurement as a function of H of the quenched samples in the a) logitudinal and b) transversal directions.

The values of λ for different H were determined and plotted as a function of the annealing temperature in Figure 3.14. The measurements in the longitudinal direction are depicted in a). They show that in the different magnetic field intensities, the samples that exhibit lower λ are the samples annealed at 550°C and 650°C. The same occurs in the measurements in the transversal direction, as seen in b).

a)   b)
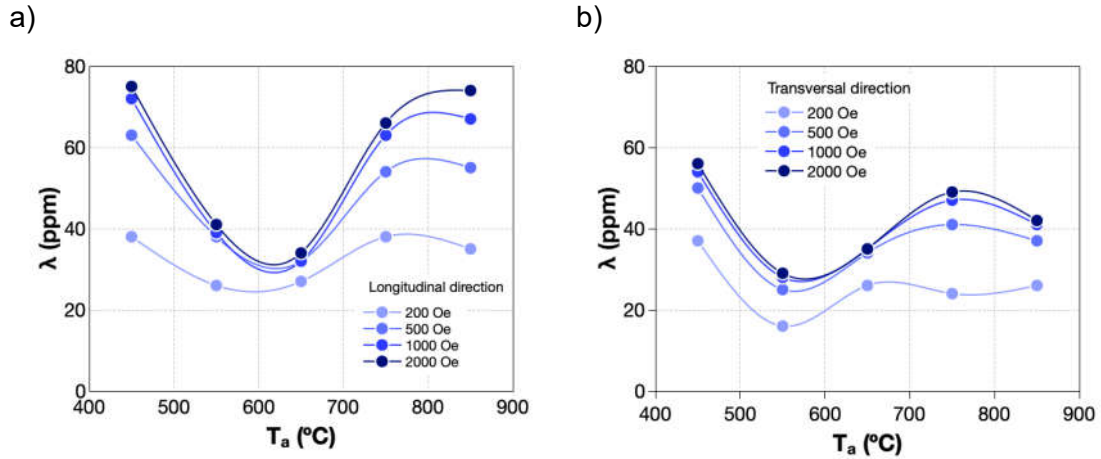
Figure 3.14 – Magnetostriction values measured in different H as a function of T_a, in the a) logitudinal and b) transversal directions.

3.2.2   Influence of slow cooling on the physical properties of FeCo-2V strip

3.2.2.1   Morphological & elemental properties

The samples were heated at temperatures ranging between 450°C and 850°C followed by slow cooling. After the annealing, the samples were polished, and their surface was observed using electron microscopy. Figure 3.15 shows the morphology of the polished surface of the samples. The sample without treatment exhibits a disorganized structure with no clear boundaries between grains. This is a consequence of its manufacturing process, that results in a highly plastically deformed material. The strained morphology is partially maintained after annealing at 450°C, but some grain coalescence is visible. Annealing at T_a=550°C or above yields a homogeneous grain distribution with clear boundaries.

A rise in grain size is observed with increasing T_a (Figure 3.16 a). The samples annealed between 450°C and 650°C exhibit an average grain size within the same order of magnitude. The average diameter rises from 170nm (450°C) to 497nm (650°C). The samples annealed at higher temperatures show a severe increase in particle size, taking average diameters of 3.4μm for 750°C and 19.6μm for 850°C.
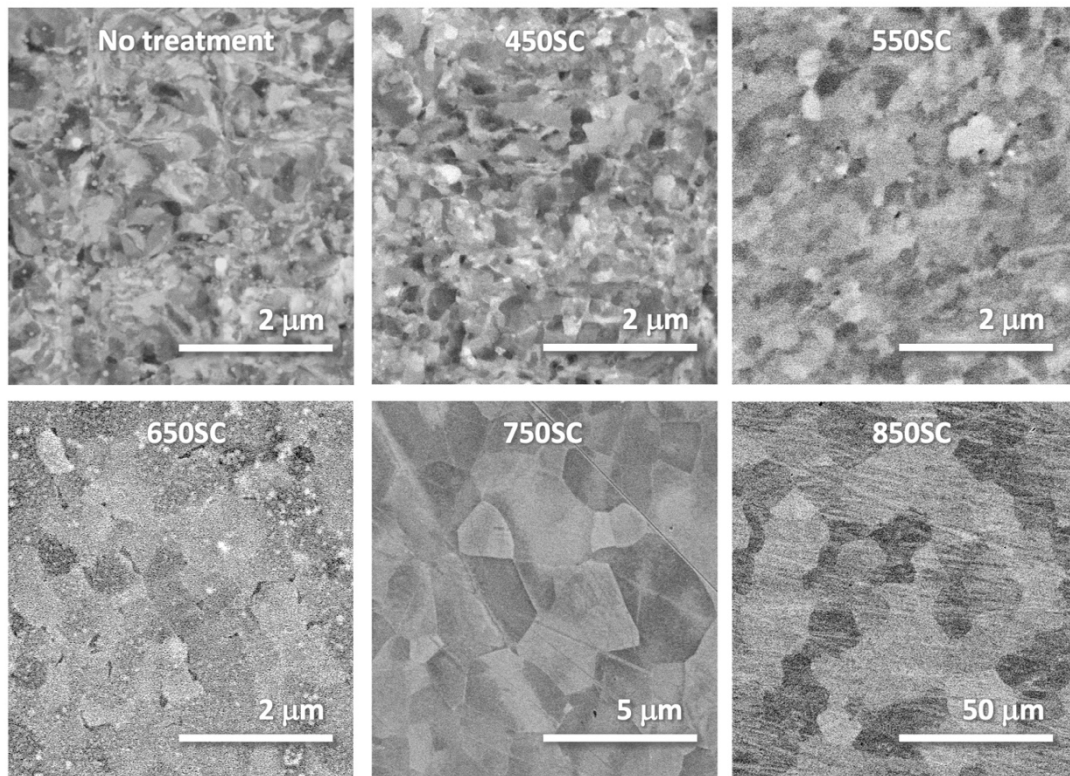
Figure 3.15 - SEM images obtained with BSE of the polished surface of annealed and slow cooled samples of Hiperco 50.

The results are plotted in Figure 3.16 as a function of the annealing temperature. D rises with T_a in an exponential trend. The curve is also plotted and it follows an equation of the type $D = D_0 + Ae^{bT_a}$, where D_0=149, A=0.00468 and b=0.01794.

Elemental analysis was performed to investigate the presence of oxygen or if a different elemental distribution was formed. Similar to the Q samples, a change in stoichiometry is noted in the SC samples (Figure 3.16 b). Annealing at $T_a \leq 550°C$ yielded $Fe_{41}Co_{57}$-2V, but the stoichiometry diverges for increasing temperatures.

a)

b)
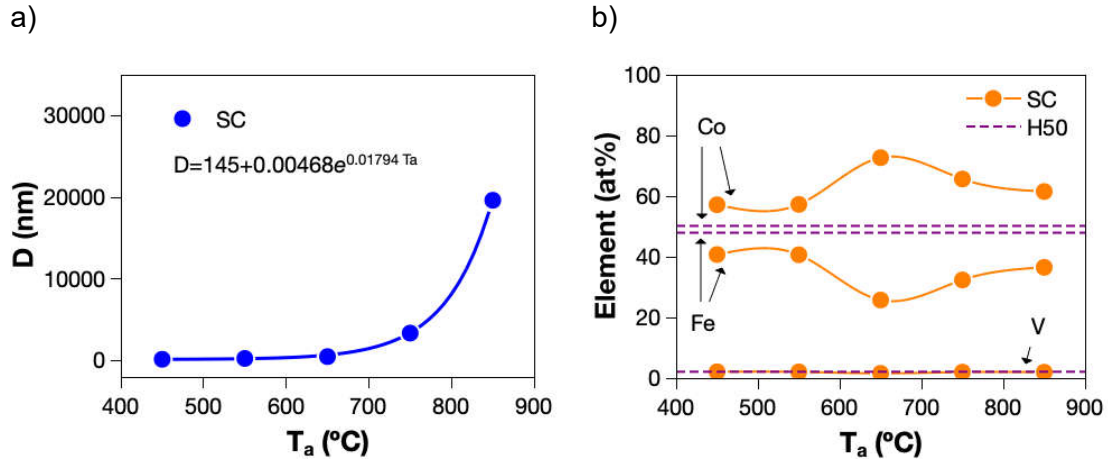
Figure 3.16 – Average grain size of samples that were annealed and slow cooled as a function of T_a. The curve is an exponential function fit to the data.

Figure 3.17 shows another image obtained from the surface of a sample of Hiperco 50 annealed at 850°C and slowly cooled. On the surface of the sample annealed at 850°C, there appears to be a discontinuity in the grain boundaries. The analyzed points are represented by the numbers 1, 2 and 3. The last two are positioned at the grain boundaries and the last point is placed at the center. The elemental analysis of the center of the grain (1) shows the expected atomic distribution of elements of the alloy. Both Co and Fe have equivalent atomic concentration, with an atomic presence of V of approximately 2 at%. On the other hand, the points 2 and 3 placed at the grain boundaries show a much higher concentration of V, respectively, 8.85 at% and 12.42 at%. This significant difference in atomic distribution indicates that the thermal treatment has caused interstitial segregation of V. Additionally, at the point 517, there is an increase in the concentration of Co, with Co taking ~29at% and Fe ~24at%, suggesting that V couples more easily with Co.
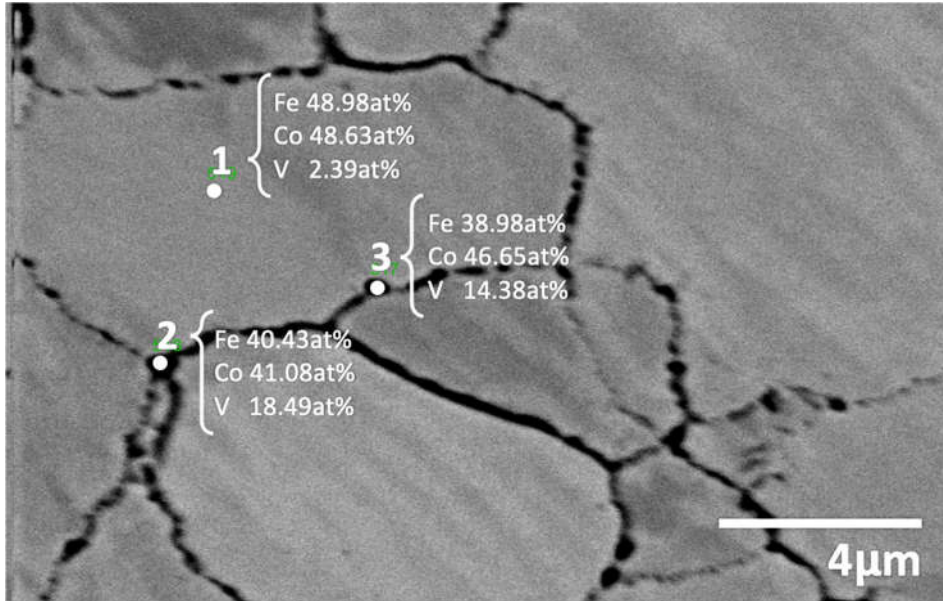
Figure 3.17 - Elemental analysis of three different points on the surface of a sample of Hiperco 50 slow cooled from 850°C.

3.2.2.2   Mechanical properties

Uniaxial tensile tests were performed at room temperature. The Hiperco 50 sample with no treatment exhibits a linear regime until ε=0.01. The slope of the curve then decreases until it reaches a plateau at ε=0.017. This indicates that between for ε<0.01 the sample suffers plastic deformation. The sample annealed at 450°C shows a similar behavior without, however, reaching the perfect plastic regime. Regarding the samples annealed at 550°C and 650°C, the curves only depict a linear elastic deformation and fracture within that regime. For higher temperature annealing, the samples acquire a perfect plastic regime.
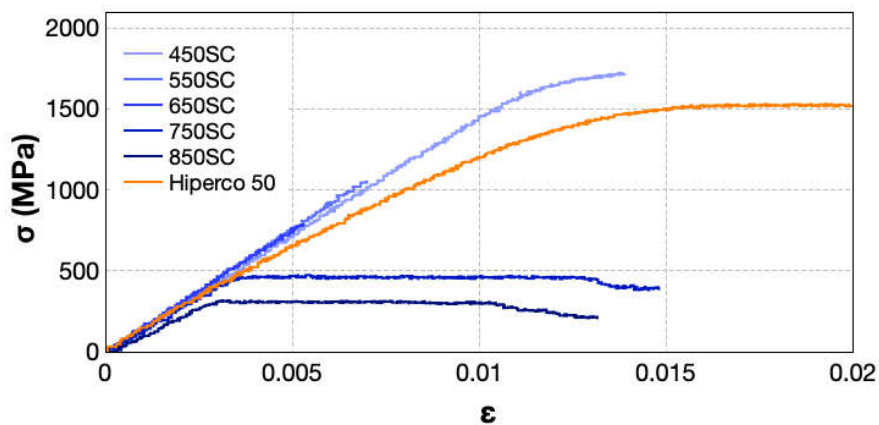
Figure 3.18 – Stress-strain curves of samples annealed at different temperatures and slow cooled.

The elastic modulus E was determined for each sample from the slope of the stress-strain curve in the elastic regime. E is plotted as a function of T_a in Figure 3.19 a). The elastic modulus of the annealed samples is larger than that of the original sample without treatment (120GPa). Annealing at temperatures $450°C \leq T_a \leq 650°C$ results in an elastic modulus that averages 150GPa. For increasingly higher temperatures, E drops and takes a value of 120GPa in samples annealed at 850°C.

The yield stress σ_y was obtained from the data of Figure 3.18, and is plotted as a function of T_a in Figure 3.19. The yield stress of Hiperco 50 without thermal treatment is 1.5GPa, which coincides with the yield stress obtained for samples annealed at 450°C. σ_y follows a negative trend with increasing temperature. At 850°C, the yield stress drops to ~20% of the initial value to 0.3GPa.

a)

b)
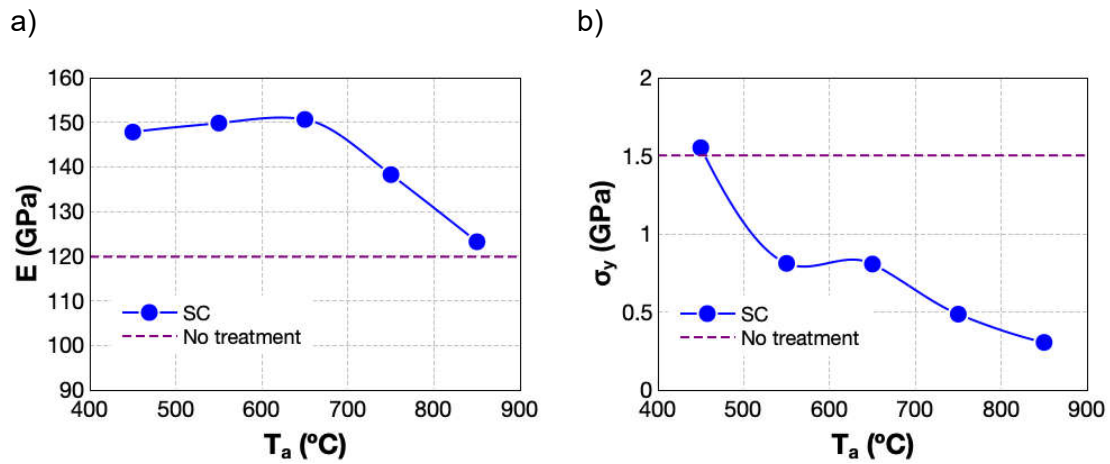
Figure 3.19 – Mechanical properties of annealed and slow cooled samples: a) elastic modulus E and b) yield stress σ_y.

3.2.2.3 Structural properties

Figure 3.20 shows the diffractograms of the samples before and after polishing. In Figure 3.20 a) oxide related peaks appear on the spectra of samples with annealing temperatures $\geq 650°C$. The absence of peaks corresponding to the Fe-Co diffraction planes in diffractograms of samples annealed at 750°C and 850°C indicates that the oxide layer is sufficiently thick to obscure the bulk of Fe-Co. In Figure 3.20 b) however, the peaks corresponding to the crystal planes with Miller indices (110), (200) and (211) are clearly visible in the spectra of all the polished annealed samples. A small shift of the peak corresponding to the crystal plane with Miller indices (110) occurs in the samples annealed at 750°C and 850°C. The remaining peaks see a very small change in their shape, suggesting that a smaller peak is formed at a slightly higher 2θ.

The determined lattice parameters are plotted in Figure 3.21 as a function of the annealing temperature. The lattice parameter is essentially unchanged by the annealing temperature up to 650°C. However, performing a thermal treatment at 750°C and 850°C resulted in a reduction of the lattice parameter. This is expected since the stoichiometry change was confirmed by the EDS analysis towards higher concentration Co in the alloy.

a)

b)
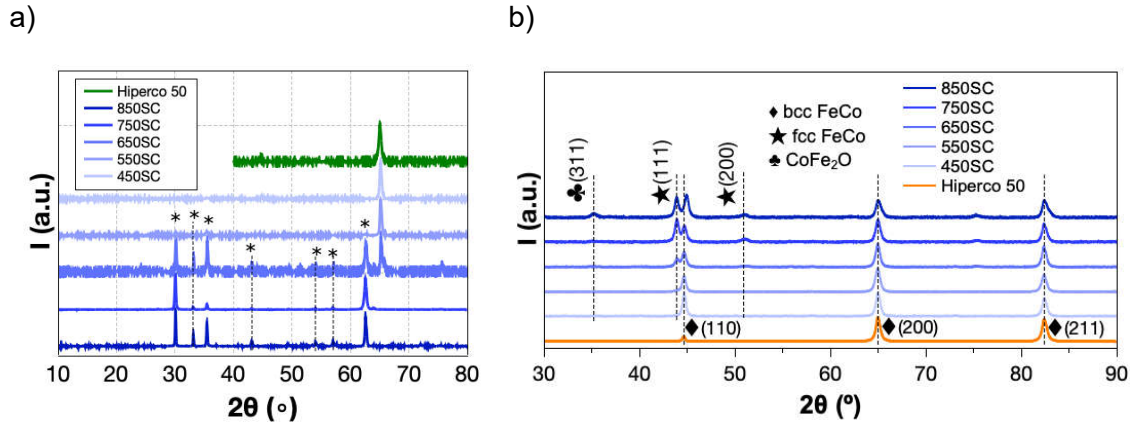
Figure 3.20 - XRD spectra of the slow cooled samples of Hiperco 50, a) as annealed and b) after removal of the surface oxide layer.
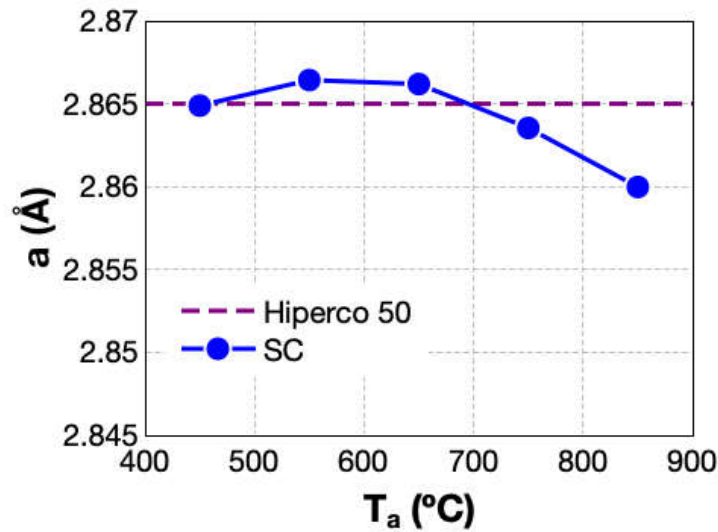
Figure 3.21 - Lattice parameter as a function of the annealing temperature.

3.2.2.4   Magnetic properties

The isothermal M-H curves of the annealed and slow cooled samples were obtained from VSM measurements in the longitudinal and transversal directions (Figure 3.22). The measurement of the original samples of Hiperco 50 was also included in the graph. In comparison to the annealed samples, it exhibits a smaller magnetostriction slope at H=0,

as well as a slightly smaller magnetic saturation (in the longitudinal direction). The curves exhibit a small hysteresis, indicating that the samples are soft ferromagnets.
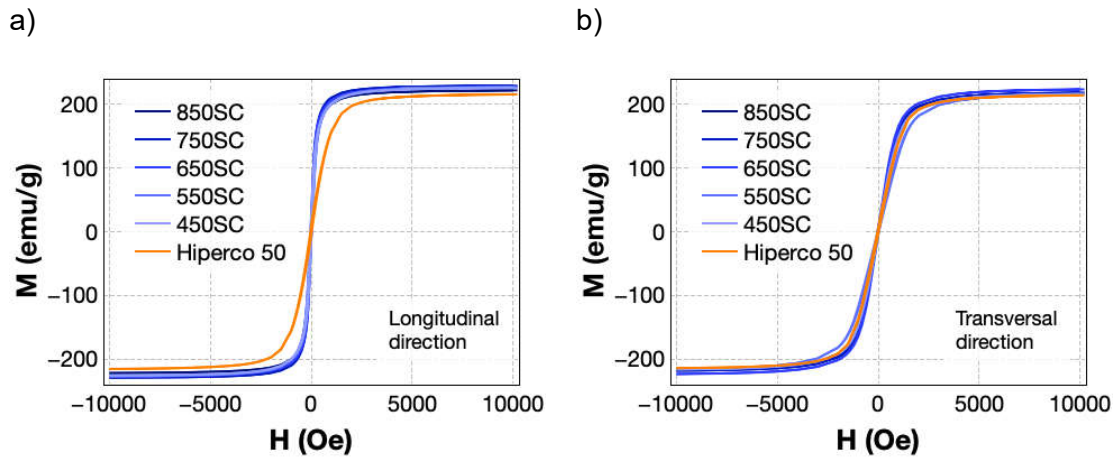
Figure 3.22 - Isothermal M-H curves of the Hiperco 50 samples annealed at different temperatures and slowly cooled: a) full-range measurement and b) detail of the same curve.

The remanence M_r and coercivity H_c are depicted in Figure 3.23 a) and b), respectively. The values of the Hiperco 50 sample with no treatment are represented in the graphs by dashed lines, in the colors representing the direction of measurement.
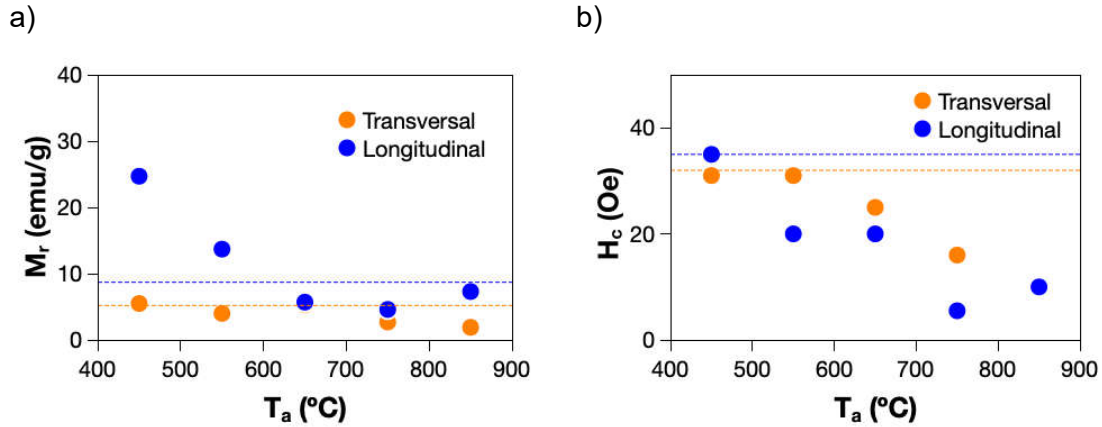
Figure 3.23 – Magnetic properties of the Hiperco 50 samples annealed at different temperatures and slow cooled: a) remanent magnetization and b) coercivity as a function of the annealing temperature.

Significant differences in M_r are observed in perpendicular in-plane directions. Overall, the remanence follows a negative trend with increasing T_a in the longitudinal direction. In this case, the remanence is increased from the initial value after annealing at temperatures of 450°C and 550°C. M_r drops from 24emu/g after the annealing performed at 450°C, down to 5emu/g when annealed at 750°C. The variation in M_r in the transversal direction, however, is almost negligible. As for the coercivity, it exhibits a negative trend

with increasing annealing temperature, in both directions of measurement. H_c reduces from 35Oe when T_a=450°C to 10Oe when annealed at 850°C.

3.2.2.5   Magnetoelastic properties

The magnetostriction as a function of the magnetic field was measured for each sample, in the longitudinal and transversal direction, and it is plotted in Figure 3.24. Hiperco 50 with no treatment in the longitudinal direction exhibits a butterfly curve with significant hysteresis comparing to the annealed samples. In the transversal direction, the same sample exhibits no hysteresis, although it takes larger strain values without saturation. Annealing the material at any T_a between 450ºC and 850ºC yields λ-H curves without hysteresis. The sample annealed at 450°C stands out in the longitudinal direction, for yielding the largest field induced strain, compared to the other samples, reaching λ_s=68ppm.
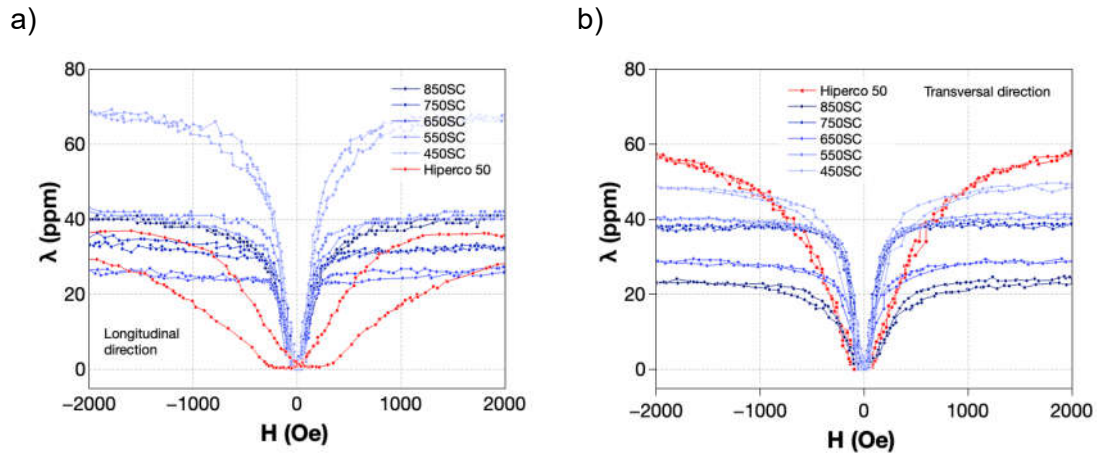
Figure 3.24 – Magnetostriction as a function of the magnetic field in slow cooled samples up to 2000Oe at room temperature: a) longitudinal direction and b) transversal direction.

The magnetostriction as a function of the annealing temperature is plotted in Figure 3.25 in the longitudinal (a) and transversal (b) directions. At 2000Oe (which results in saturation magnetostriction), in the longitudinal direction, λ_s exhibits the largest values in the samples annealed at 450°C, reaching 68ppm. At T_a=650°C, it drops to 26ppm, which is the lowest. Further increasing the annealing temperature results in larger λ, 42ppm (T_a=850°C). In the transversal direction, the behavior of λ_s with T_a is similar, except for the largest temperature, where the magnetostriction takes the lowest value (λ_s=23ppm).

a)

b)
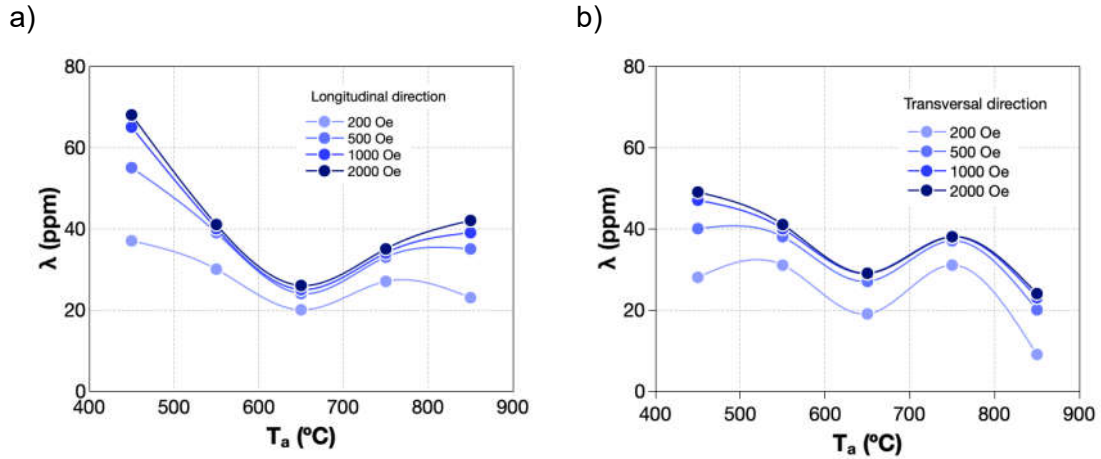
Figure 3.25 – Magnetostriction values in slow cooled samples as a function of the annealing temperature measured in a) longitudinal and b) transversal directions.

3.2.3   Quenching vs Slow Cooling: discussion

In the two previous sections, it has been shown that the annealing and the cooling dynamics have an impact on the physical and mechanical properties of the 2%V-FeCo alloy. Notably, the lattice structure is altered, which is clear from the XRD spectra of the annealed samples (Figure 3.9 and Figure 3.20). The samples annealed at 650°C or bellow, show a small increase in the lattice parameter. This corresponds to the ordering of the lattice at $T_a < T_{order-disorder}$ (Figure 3.26 b) [107]. A shift of the bcc-related reflection peaks towards larger 2θ occurs with the rise of T_a, corresponding to a reduction of the lattice parameter (Figure 3.26 a). The change in the lattice parameter is a consequence of a compositional change, towards a Co-rich stoichiometry. This effect is more evident in the Q samples, where the oxidation occurred more extensively. As proposed above, Fe reacts with O in the atmosphere to form a layer of oxide at the surface, causing a stoichiometric imbalance below the newly formed oxide layer. We propose that this separation leads to the shift of the Fe-Co bcc phase to a higher Co concentration bcc phase, which explains the variation in the lattice parameter [107] .

a)

b)
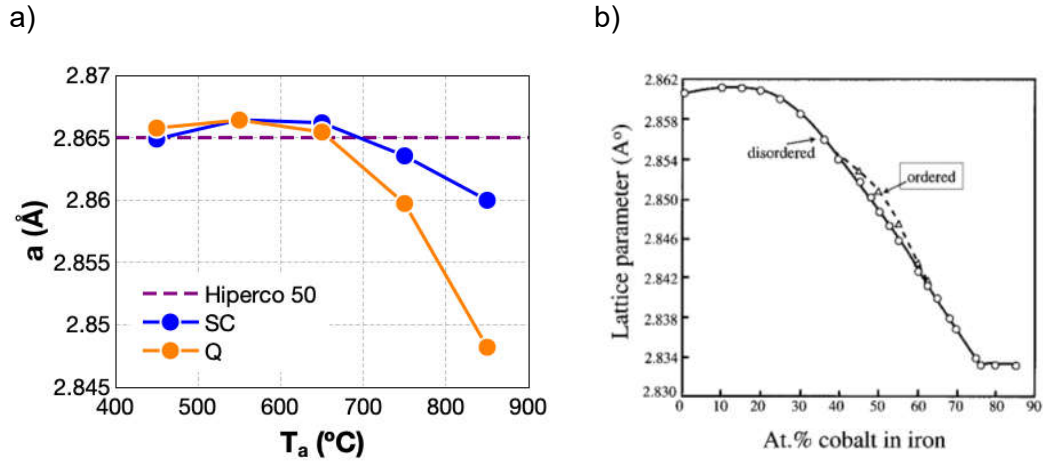
Figure 3.26 – a) Determined lattice parameter as a function of the annealing temperature and b) lattice parameter as a function of the Co at.%, as retrieved from[107].

We highlight the appearance of reflection peaks related to the Fe-Co fcc structure in samples annealed at $\geq650°C$. In the literature, Fidler and Davies reported that V-rich precipitates with fcc structure can be found in stoichiometric FeCo alloys after a thermal treatment of 48h at 680°C [108]. Figure 3.27 shows the appearance of the fcc structure in $Fe_{32}Co_{68}$ alloy, after annealing at 840°C (1113K) for 1h [109]. Suggestions as to why the γ phase appears in FeCo-2V include a proposal from Ashby and co-authors that states that the fcc phase is not a prolongation of the high temperature γ but instead a Fe-substituted variant of the Co_3V precipitate with an ordered fcc structure, represented by γ_2 (Figure 3.2 b) [110]. In fact, recent reports indicate that the room temperature fcc phase is a result of the formation of tetragonal nanoinclusions in the bcc matrix and confirm that they are independent of the high temperature γ phase [111]–[113]. These precipitates have been reported to be formed at temperatures as low as $T_a=600°C$ [112].
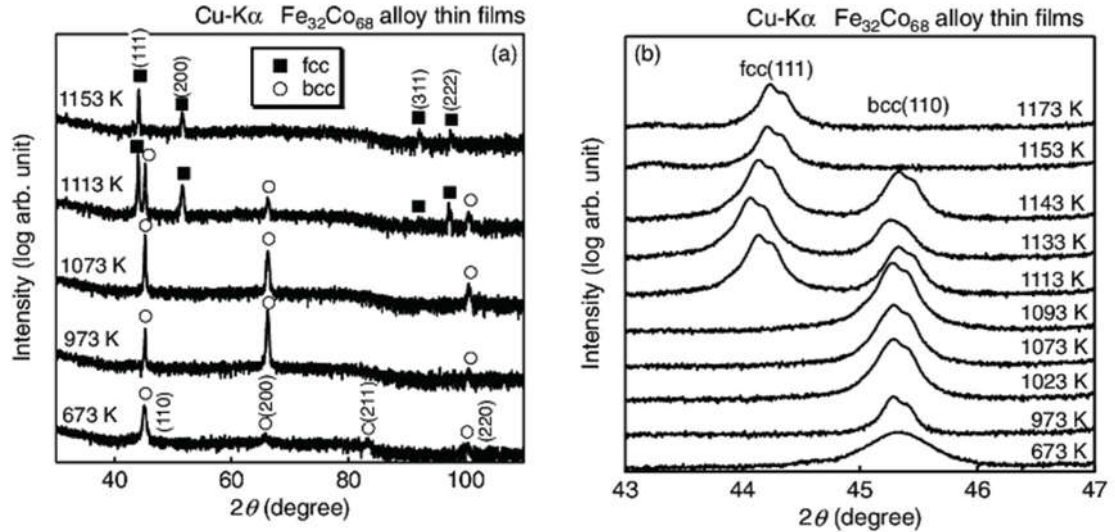
Figure 3.27 – Example of evolution from single bcc to bcc+fcc with temperature in thin films of $Fe_{32}Co_{68}$ [109].

The appearance of an fcc phase, evidenced by the XRD spectra in Q and SC samples indicates that structural changes occur in the alloy, which stem from two sources:

1- The appearance of V-rich precipitates, a process which is intensified by the extensive plastic deformation caused by the previous cold work [94]. This would explain the appearance of reflection peaks corresponding to an fcc structure.

2- The formation of a bcc phase with higher concentration of Co. This occurs due to the segregation of Fe to form an oxide. The imbalance of Fe and Co leads to stoichiometric changes in the alloy, resulting in the transition to higher Co concentration bcc phase. This transition explains the considerable drop in the lattice parameter values.

The annealing temperature that Hiperco 50 is subject to results in different morphological changes. The samples annealed at 450°C exhibit a very disorganized morphology. The lack of clear grain boundaries suggests that coalescence occurs very slowly at this temperature. This consists of the growth of grains at the expense of others. As the temperature of annealing is increased to 650°C, both quenched and slow cooled samples exhibit increasingly defined grains. Full recrystallization is clear in the samples annealed at 750°C and 850°C, with significant grain growth.

Notably, there is a significant difference in grain growth depending on the annealing and cooling process. The main difference between the thermal treatments is that the quenched samples are subject to constant T_a for 30 minutes, while the slow cooled samples are simply cooled from T_a. In Figure 2.11 we depicted the temperature variation with time using the example of thermal treatments undertaken at 850°C. Above the order-

disorder transition temperature, the atomic diffusion in the lattice is extensively promoted along with nucleation [114]. This leads to disorder, but also promotes the growth of new grains, that replace the original ones. The grain size is exponentially enhanced with increasing T_a, as Figure 3.28 shows. The fact that the quenched samples were subject to half an hour at a fixed temperature justifies the difference in average grain sizes between the Q and SC samples with the same T_a. Besides grain growth, the effect of the temperature is also in the reduction of internal stresses and disorder in the lattice. All samples are expected to acquire some degree of long-range order since all of them are annealed bellow the γ phase region [94]. However, ordering occurs more extensively below $T_{order-disorder}$, hence Q sample annealed at $T_a \geq 750^oC$ develop less order than the rest of the Q and SC samples.
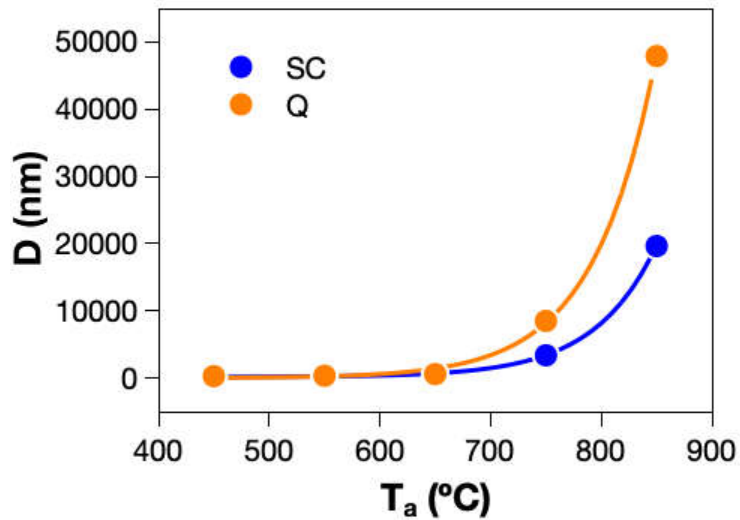
Figure 3.28 – Average grain size as a function of the annealing temperature.

The degree of order and the grain size of the alloy have influence on the mechanical properties of the annealed samples. In the previous sections, we have seen the change in elastic modulus, yield strength and ductility with the annealing temperature. We have also seen that the alloy develops plasticity when annealed at temperatures of 750^oC or above. Samples annealed below 650°C have only shown elastic deformation, with roughly unchanged elastic moduli.

We see a decrease in the ductility at lower T_a compared to the Hiperco 50 sample (Figure 3.29 a). This drop is caused by an increase in the order of the lattice. As T_a is increased, so does the ductility. The quenched samples exhibit larger elongation at fracture point, as compared to slow cooled samples, indicating that annealing for 30min and quenching leads to improved ductility. Stoloff and Davies went as far as correlating the quenching

temperature with the degree of order of the alloy, and concluded that the ductility was expressively improved above the order-disorder transition temperature, around 730°C (Figure 3.29 b) [96]. They justify this with the availability of slip planes, that reduce in ordered FeCo-2V, which could explain why higher temperature annealing ($T_a \geq 650$°C) and quenching lead to increased ductility. Essentially, our results confirm that the ductility has a direct correlation with the degree of order in the alloy.

a)   b)
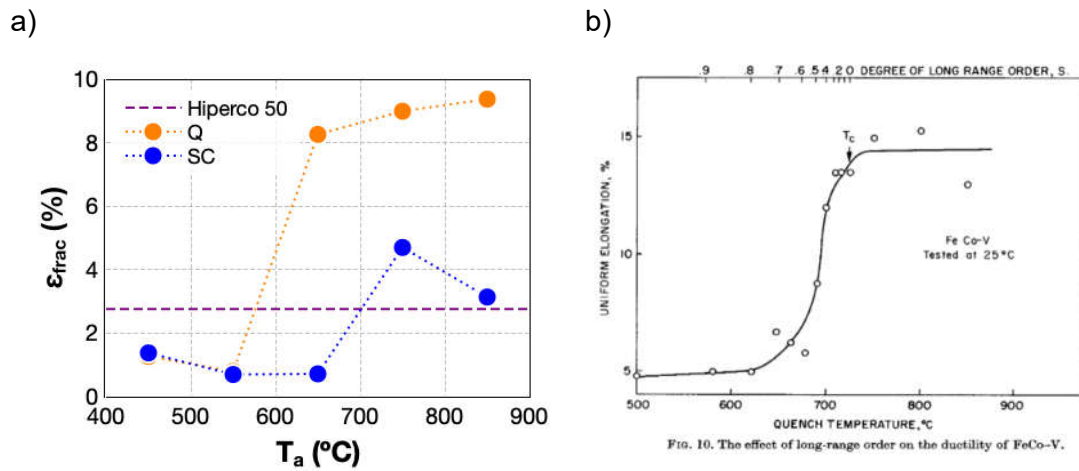
Figure 3.29 – Effect of the annealing temperature on the ductility of Hiperco 50: a) experimental results, b) as measured by Stoloff and Davies [96].

As the SC samples are allowed to develop order, the ductility is not greatly enhanced with T_a as in the Q samples. The small improvement is related to the ability to deform plastically, which is developed after annealing at $T_a \geq 750$ºC and is essentially linked to the grain size.

The annealing also contributes to reducing the internal stresses of the lattice caused by dislocations during the cold rolling process. It is well known that dislocations contribute to the strengthening of the alloy [96]. They also influence the magnetization process as a consequence of the magnetoelastic coupling between the stress field and magnetostriction [38]. In fact, Chen suggests that the coercivity and initial susceptibility of the alloy can be theoretically determined by knowing how the stresses are applied on the main walls by the dislocations [50]. As thermal energy is provided, the dislocations tend to be removed, leading to the reduction of strength of the alloy (Figure 3.8 b and Figure 3.19 b). Thornburg [115] and Stoloff [116] have also reported that the yield strength decreases with increasing annealing temperature.

The Young's modulus is plotted as a function of the temperature and the grain size in Figure 3.30 a) and b), respectively. *E* exhibits a negative linear trend with the average grain size, with slopes of -0.839MPa/nm for the Q and -1.319MPa/nm SC samples,

respectively. This result suggests that the alloy loses elasticity with increasing grain size. This holds true since the ability to deform plastically is improved instead [50].

a)

b)
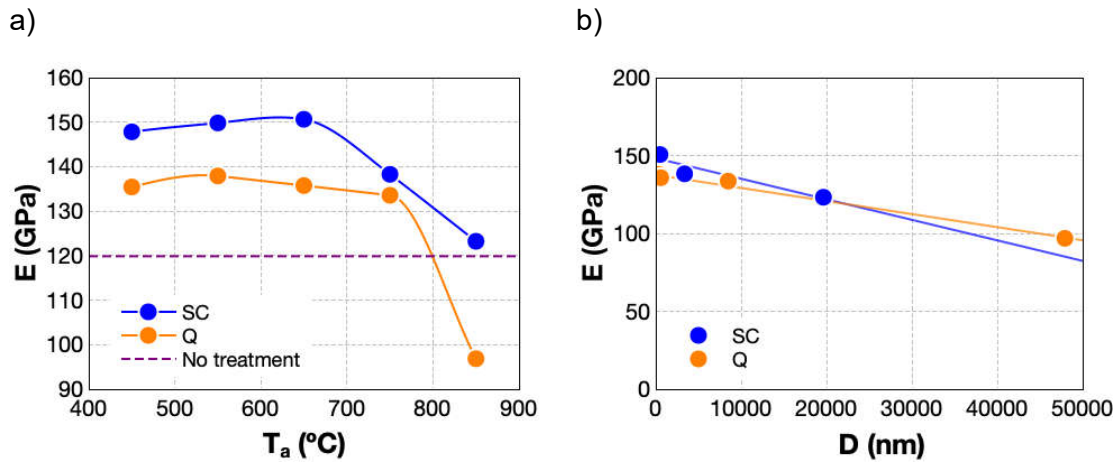
Figure 3.30 – Young's modulus as a function of a) the annealing temperature and b) the average grain size.

The relationship between the coercivity and the annealing temperature in Fe-Co alloys had already been observed in the work of both Thornburg [115] and Hailer [98]. Notably, Sourmail has used data reported by Davies and Stoloff [114] to show that variations in the coercivity and yield strength could be explained by changes in the grain size [86]. Sourmail further proposed that these properties can be fully understood in terms of grain size in completely recrystallized samples.

The correlation between the yield stress σ_y and the grain size D is known. It is called the Hall-Petch relationship, which states that the strengthening effect in polycrystalline materials can be related to the grain size [98]. In this relationship, the yield stress is proportional to $D^{-1/2}$, where D is the grain size.

$$\sigma_y = \sigma_0 + \frac{k_y}{\sqrt{D}} \qquad (23)$$

In the expression above, σ_y is the yield strength, σ_0 is the material's initial stress for dislocation movement and k_y is the strengthening coefficient, which is related to the required stress to unlock dislocations at the grain boundaries. In theory, grain boundaries act as pinning sites to prevent the propagation of dislocation between grains [86]. Increasing the grain size allows further dislocations to pile-up at the grain boundaries where the atomic mismatch between different grains creates repulsive stress to oppose propagation motion. The accumulation of dislocations and respective repulsive forces lead to the reduction of the energetic barrier for diffusion across the boundary. Further dislocation pile-up causes dislocation diffusion between grains, enabling further

deformation of the material. Smaller grain size reduces the amount of possible dislocation pile-up, increasing the amount of stress needed to move a dislocation through the boundary, which in turn relates to an increase in yield strength. Essentially, smaller grains produce greater strength. In turn, large grain size leads to plastic deformation.

The yield stress of the Q and SC samples was plotted versus $D^{-1/2}$ in Figure 3.31. The obtained linear fits of the yield stress with $D^{-1/2}$ are the following: for the Q samples, the fit yielded $\sigma_y = 0.321 + 12.317 D^{-1/2}$, and for the SC samples, the fit resulted in $\sigma_y = 0.343 + 14.178 D^{-1/2}$. The approximately linear dependence indicates that the strength of the material is governed by the grain size of the material [117].
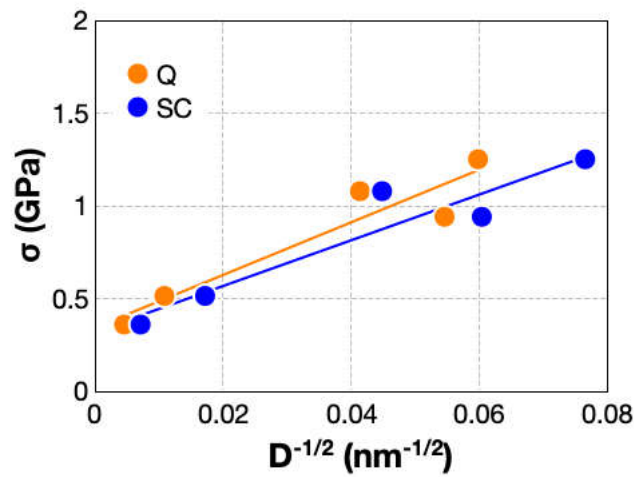
Figure 3.31 – Yield stress as a function of D$^{-1/2}$, in quenched and slow cooled samples (Hall-Petch relationship).

Moreover, a relationship between the grain size and the magnetic properties can also be established, in particular with the coercive field. Figure 3.32 plots the obtained values of the coercivity of the annealed samples as a function of D^{-1}.
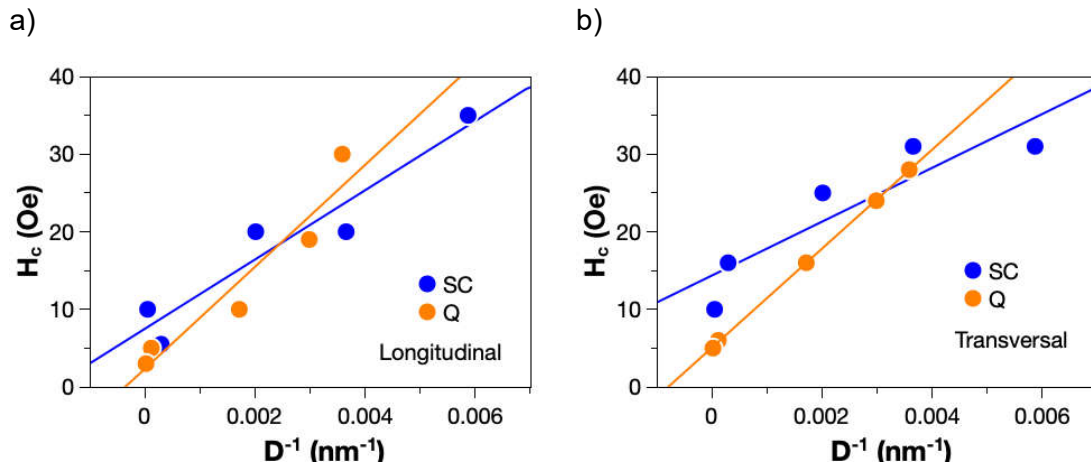
Figure 3.32 – Coercive field as a function of D^{-1} in the a) longitudinal and b) transversal directions.

The linear trends can be determined from the obtained data. We see that the slope is larger in Q samples (6573Oe.nm in the longitudinal direction and 6383Oe.nm in the transversal direction), compared to the SC samples (4465Oe.nm in the longitudinal direction and 3470Oe.nm in the transversal direction). The slope difference is a consequence crystal imperfections, such as grain boundaries, impurities, dislocations and precipitates, which act as barriers to the movement of domain walls [50]. Such examples contribute to the change of the coercive field of the alloy and disrupt the slope of the curves, as depicted in Figure 3.32. The density of grain boundaries, which reduces with increasing grain size, is the main responsible for the coercivity, as is confirmed by the linear relationship.

In the measurements of the isothermal M-H cycles, it became clear that the direction of measurements yields slightly different curves, suggesting that the samples have anisotropy. Both the magnetic saturation and coercive field are invariant to the measurement direction, however the influence of the anisotropy is visible in the remanent magnetization and in the susceptibility.

As shown in Figure 3.33, M_r exhibits a different dependence with the annealing temperature in the two directions of measurement. In the transversal direction, M_r sees a small negative trend in the Q and SC samples. It takes values that are very close to that of the sample of Hiperco 50. However, in the longitudinal direction, the significant increase of M_r in samples annealed at 450°C and 550°C could be initially related to the induced order and removal of dislocations. The fact that some interatomic diffusion is permitted at such temperatures enables the development of order, which leads to increased remanence. The effect of ordering is gradually surpassed by the recrystallization and grain growth, which results in the overall improvement of soft ferromagnetic properties, including the drop in M_r.

a)

b)
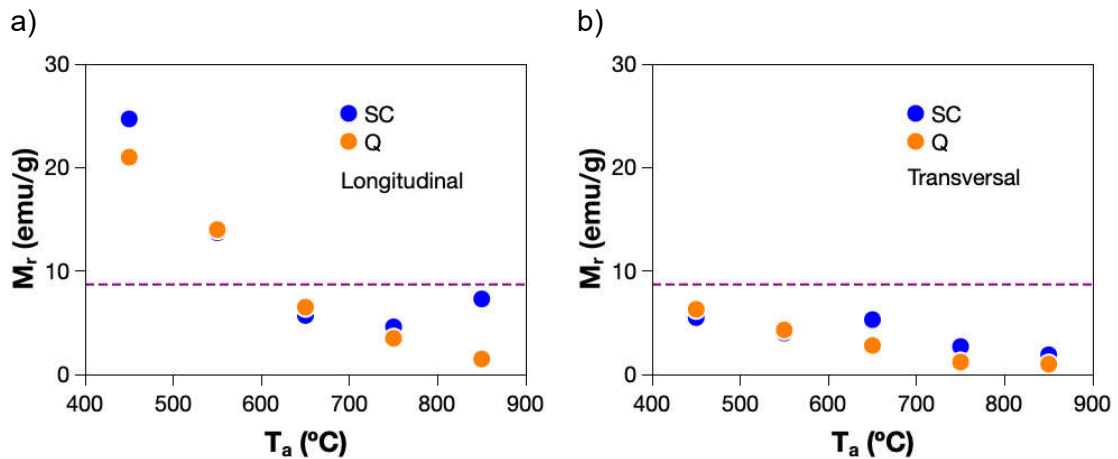
Figure 3.33 – Remanence as a function of the annealing temperature in the a) longitudinal and b) transversal directions.

Figure 3.34 depicts the saturation magnetostriction λ_s of the annealed samples in the longitudinal (a) and transversal (b) directions. As observed previously with the magnetic properties, the magnetostriction in the transversal direction exhibits less variability with the annealing temperature in contrast with the longitudinal direction. This stems from the fact that Hiperco 50 is a severely textured material with a preferred morphologic and crystallographic orientation in the rolling direction (longitudinal), such that the main physical changes after annealing are observed in that same direction.

a)

b)
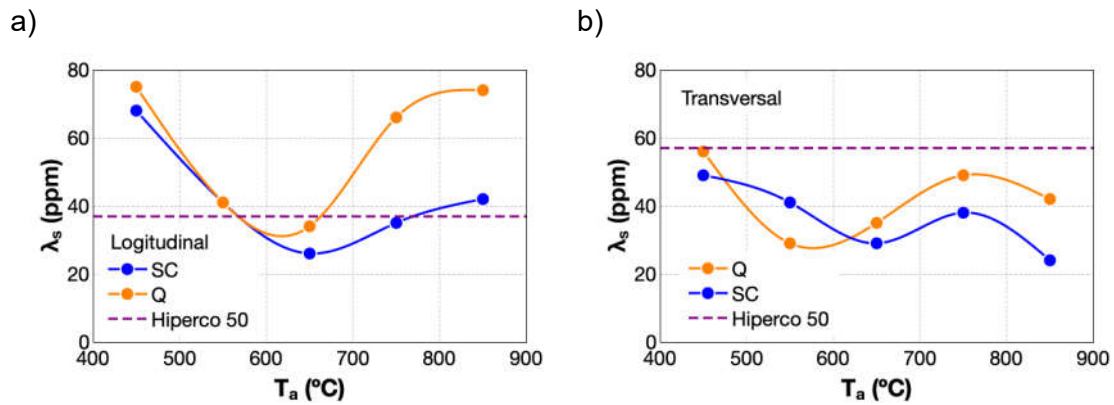
Figure 3.34 – Saturation magnetostriction as a function of the annealing temperature in a) the longitudinal and b) the transversal directions.

In the longitudinal direction, λ_s exhibits a drop in samples annealed at 650°C followed by quenching and slow cooling. This is explained by the suppression of internal stresses via thermal treatments. The higher the temperature and annealing time, the more efficient is the removal of stress. As the state of internal stress is directly related to the magnetization of the material via the magnetoelastic anisotropy, it is expected that the reduction of stress in the lattice would lead to a drop in λ. Above 650°C, the formation of a fcc phase occurs, as evidenced by the XRD data. On the other hand, the coexisting bcc and fcc phases have been linked to increased magnetostriction [109], [113]. The fcc phase has been described by Han [112] as nanoinclusions that extend along specific crystallographic directions, and lead to an increase in the macroscopic magnetostriction.

The homogenization of the alloy at intermediate annealing temperatures seems to decrease λ. On the other hand, when anisotropy and small grains are not entirely removed (450°C and 550°C) and when an additional fcc phase is present (750°C and 850°C), the magnetostriction increases. Seems that both the dislocations and precipitates enhance the internal stress of the material. The contribution of the smaller

grain size is on the increased anisotropy and internal strength of the material. Both of which are linked to the magnetostriction of the material via the magnetoelastic and magnetocrystalline anisotropies.

3.3 Conclusion

Heat treatments were effective in altering the physical properties of Hiperco. A change in the stoichiometry of the material after annealing was verified and it was concluded that this is due to the segregation of Fe to form a layer of oxide on the surface. The composition evolves from $Fe_{50}Co_{50}$-2V to approximately $Fe_{40}Co_{60}$-2V in Q and SC samples.

The evolution of stoichiometry can be observed in the XRD spectra, and particularly in determination of the lattice parameter. It is verified that it decreases from 2.866Å to 2.848Å in Q samples, corresponding to a change of 0.018Å. The SC samples reveal a more conservative variation of 0.005Å. Additionally, the XRD spectra exhibits the presence of an FeCo fcc phase after annealing above 650°C in both Q and SC samples. Precipitation usually takes place in interstitial sites or locations with a high concentration of dislocations in the form of V-rich fcc precipitates. Because the stoichiometry moves away from the stoichiometric concentration, the precipitation of the alloy in the fcc phase at room temperature is enhanced.

The evolution of the mechanical properties with the thermal treatments was also analyzed and it was verified that the hardness of the alloy decreases with increasing T_a. Above T_a=550°C and T_a=650°C for Q and SC samples respectively, the samples demonstrate plastic deformation and develop greater ductility. It was found that the evolution of plasticity and ductility are related to the grain growth that occurs through the Hall-Petch relationship. The Q samples have greater ductility because the state of disorder of the alloy was maintained since the annealing was carried out above the order-disorder transition temperature.

The grain size also has influence on the coercivity. Since grains grow with increasing rate with T_a, the density of grain boundaries decreases, facilitating the magnetization process and lowering H_c. In Q samples, the coercivity decreased from 30Oe (T_a=450°C) to 3Oe (T_a=850°C), and 35Oe (T_a=450°C) to 10Oe (T_a=850°C) in SC samples. The existence of anisotropy is visible in the remanence, being significantly higher in the rolling direction and reducing with the increase of T_a, which is expected due to the recrystallization and reduction of the material texture.

Magnetostriction measurements yielded characteristic curves with saturation in all samples. λ_s reveals its lowest value at intermediate annealing temperatures, both in the longitudinal and transverse directions. This phenomenon is explained by the fact that with $T_a<500°C$, the internal stress of the sample is not completely removed, which contributes to enhancing magnetostriction via the magnetoelastic coupling. On the other hand, as the strain dissipates at $T_a=650°C$, λ decreases. Annealing at $T_a\geq750°C$ results in λ to increase again. We associate this increase to the coexistence of the fcc γ and the bcc α phase, since it has already been proposed that fcc phase precipitates as nanoinclusions in the bcc lattice, which interact with the magnetic field to amplify the magnetostrictive effect. Moreover, quenching the alloy from $T>T_{order-disorder}$ leads to increased internal stress.

Knowing the correlations here established, it is possible to tailor de magnetoelastic behavior of the FeCo-2V strip by designing annealing treatments that would yield the necessary structural and morphological properties.

Chapter 4   Giant magnetostriction in magnetoactive elastomers

The work presented in this chapter addresses an alternative to the state-of-the-art of magnetostrictive transducers. It consists of magneto-active elastomers, which are composites prepared with ferromagnetic particles and a hyperelastic elastomer. We report on the fabrication of the soft ferromagnetic composites, with different composition and distribution and their characterization.

Part of the results herein presented have been peer-reviewed and were published in the Composites Part B: Engineering journal [118].[3] The fabrication, characterization, data analysis and writing of the paper was a core part of the work in this Chapter.

4.1   Introduction and State of the art

The magnetoactive elastomer (MAE) (also called magnetorheological elastomers - MRE) belongs to the group of smart composites whose mechanical properties change in response to a magnetic field [119]. Among these properties are the elastic modulus, the tensile strength, the strain [120] and the electrical conductivity [121]. MAEs can exhibit many shape-morphing phenomena, including elongation, contraction, deflection, twisting, and coiling [122]. By using non-uniform magnetic fields, more complex behaviors can be induced, such as crawling and jumping. Having a field-induced response, MAEs can be used for a wide range of applications, such as vibration absorbers and isolators [123]; controllable valves, such as linear and radial actuators[124]; sensing devices, using the variation in resistance and impedance of the MAEs by the magnetic field and mechanical force[125], or using the positive piezoconductivity in liquid-filled MAEs [126]; actuators, such as self-sensing and multifunctional shape manipulation actuators [127]; tactile displays [128] and switches

---

[3] J. A. Silva, C. Gouveia, G. Dinis, A. M. Pinto, A. M. Pereira, *Composites Part B* **2022**, *243*, 110125.

[129]. It is possible to find extensive information on the various applications of MAEs in [130] and [131].

MAEs are emerging as an alternative to magnetostrictive materials. They offer several benefits over monolithic magnetostrictive materials, namely the increased flexibility and elasticity, higher stress and strain failure, reduced costs, and reduced eddy currents. The latter allows to overcome problems in operating at frequencies above 1kHz [132].

A MAE in general is composed of ferromagnetic microparticles, an elastomer matrix, and additives. High saturation magnetization, high magnetic permeability, and low remanent magnetization are among the desirable magnetic properties of the microparticles [133]. Iron are the most popular material in the development of MAEs. It has been demonstrated that the particle size and volume fraction of MAEs affect the magnetorheological effect (MR) effect [134] (explained below), the tensile response of MAEs [135], as well as the magnetic field and frequency-dependent shear modulus [136]. There have also been investigations of other soft ferromagnetic particles such as Co [137] and $CoFe_2O_4$ [138], as well as on the use of hard ferromagnetic particles, such as Nd-Fe-B [139].

In terms of elastomers, silicone rubbers are the most commonly used [140], followed by natural rubbers [141], nitrile rubbers [142], thermosets/thermoplastics [143] and polyurethanes [144]. The particular properties of silicone rubbers have made them extremely popular, including their availability as a liquid resin with a low viscosity, as well as their chemical inertness, non-flammability, high deformability, and fast curing [119]. A further benefit of the elastomer is its mechanical softness, which allows for shape-morphing [122]. A study published in 2015 [145] examined the effects of different plasticizers on the storage modulus of MAEs. Other additives, such as silicone oil [146] and rosin glycerin ester [147], are also used to enhance wettability and dispersion of magnetic particles. As a result of using carbon-based materials, such as carbon black [148] and carbon nanotubes [149], it has been reported that these materials can improve MR effects, increase tensile strength, and improve dynamic mechanical behavior [150].

An important characteristic of MAEs is the MR effect, which occurs when the elastic modulus of a material changes under the influence of a magnetic field [151]. To investigate the MR effect of a given material, different tests can be conducted, including uniaxial tensile, compressive, and shear tests, as well as biaxial tests [140]. According to Kumar and co-authors [152], the volume, size, and distribution of Fe particles have a significant influence on the mechanical properties of MAEs. Moreover, the dynamic mechanical properties have also been investigated [153].

Magnetostriction is a less explored feature of MAEs, which refers to the magneto-dependent mechanical deformation of the material [140], [154], [155]. This consists of the change in shape of the material when subject to a non-zero magnetic field. This deformation usually comes in the form of elongation in the direction of the magnetic field, which we will denote by λ. A particle's shape can greatly contribute to magnetostriction [156]. Compared to spherical particles, flake-shaped particles have shown to significantly improve deformation amplitudes [157]. The homogenization model used by Ponte Castañeda and Galipeau [158], [159] uses elliptical particles in a mechanically soft matrix and they have reached the same conclusion. Due to the anisotropy of the particles' shape, the particles rotate within the matrix as a result. A similar conclusion was experimentally reached by Na and co-authors, who concluded that a MAE consisting of 10wt% Fe-Co-based powder in a phenol-type binder exhibits greater λ with granular particles (100ppm) than with spherical particles ($\approx$85ppm) [160]. Rodriguez and co-authors explored the relationship between particle size and magnetostriction in MAEs consisting of Terfenol-D particles in a PU matrix [144]. In their study, they concluded that the λ_s increases with particle size, with the highest strain of 1390ppm obtained for 50wt% of Terfenol-D particles with sizes ranging from 212μm to 300μm [144]. A similar conclusion was reached by Jin and co-authors [161], who concluded that while small particle sizes result in better homogeneity and increased particle interaction, larger particles have a smaller surface-volume ratio, which reduces the demagnetizing field and increases the magnetic torque, resulting in higher strain responses.

A further advantage of MAEs is that the particle distribution can be controlled during the preparation of the material, resulting in isotropic or anisotropic composites. A homogeneous magnetic field is used to orient the magnetic particles in the polymer matrix in order to induce anisotropy. As the matrix is cured under a magnetic field, the particles are locked into chain-like structures. As opposed to isotropic MAEs, which have field-dependent properties that are equivalent in all directions, an anisotropic counterpart will have field-dependent properties that differ based on the direction in which the field is applied to the particle alignment. This is true for both mechanical properties [162] and magnetostriction [163]. Anisotropy has been found to improve the strain of MAEs in several reports. By inducing anisotropy in the system, Lim and co-authors [164] obtained an increase from ~490ppm to ~540ppm. Similarly, Rodriguez *et al.* [163]. found an increase in λ_s of 182ppm to 526ppm for anisotropic Terfenol-D-based MAEs compared to non-oriented composites. In contrast, Guan and co-authors reported that the anisotropy can significantly reduce magnetostriction if the magnetic field is applied

parallel to the alignment of the sample [165]. They further report that magnetic fields applied perpendicularly to particle alignment increase magnetostriction, while isotropic samples achieve strain values in between.

According to research, materials, particle size, shape, distribution, and specimen shape can significantly alter the properties of MAEs [165]–[171]. Furthermore, the wide range of applications of such materials encourages further research in this field [140]. Most reports on MAEs focus on the MR effect. Due to the low popularity of strain studies, the investigation of MAEs below the concentration of 30vol% has been limited. The literature reports volume fraction values ranging from 20vol% [172] to 50vol% [154], whereas weight fraction values range from 10wt% [173] to 60wt% [136].

Hence, the present study focused on the investigation of magneto-induced deformation in MAEs with particle concentrations below 30vol%, with a particular focus on VF<5vol%. We were able to achieve giant magnetostriction with low concentration MAEs, whilst revealing that the concentration range that yield the largest λ in MAEs is below the VFs reported in the state-of-the-art. We further compare MAEs prepared with different particle shape and size, revealing that the magnetostriction peaks around the same VF.

4.2   Characterization

The samples herein used were prepared under the conditions mentioned in 2.1.3.1, where the matrix is PDMS and the samples are FeCo-2V spherical microparticles (4.2.1) and helicoidal microparticles (4.2.2).

4.2.1   PDMS / Spherical particles MAEs

4.2.1.1   Morphological and structural properties

Figure 4.1 shows pictures taken with an optical microscope of the MAEs with spherical particles. The top row consists of anisotropic samples, and the bottom row of isotropic samples. The VF is indicated at the top. As the VF increases, the samples exhibit a darker color, consistent with the higher concentration of particles. The alignment of the particles is clear in the anisotropic samples, until VF=1.2vol%, after which it becomes indiscernible.
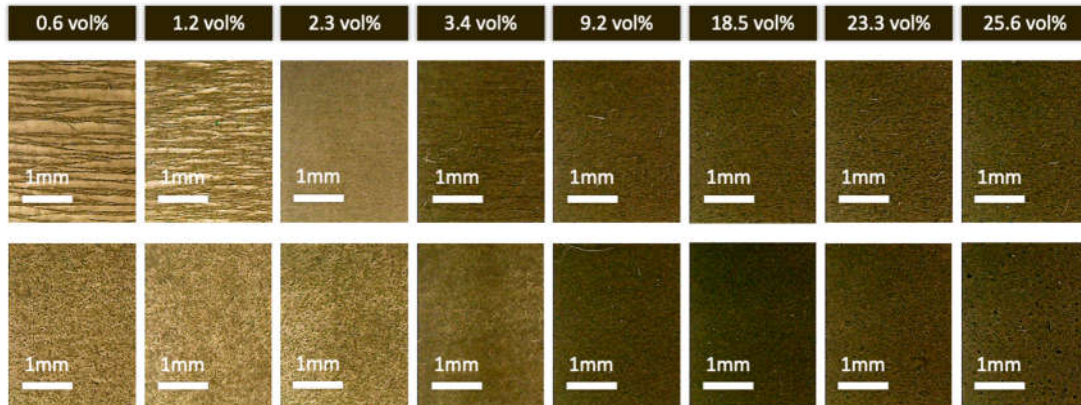
Figure 4.1 – Microscope images of the MAE samples with spherical particles.

X-ray diffraction was performed on the composite samples, as well as on samples of PDMS and isolated FeCo-2V powder. The spectra are plotted in Figure 4.2. In the diffractogram of the PDMS, there is a broad peak around $2\theta = 12.2°$ and another around $2\theta = 22.0°$, which are characteristic of amorphous PDMS [174], [175]. PDMS is also shown to be present in the diffractograms of the MAEs, represented by the peak near $2\theta = 12.2°$. The observed peaks at $2\theta = 45.1°$ and $2\theta = 65.7°$ in the diffractograms of the MAEs correspond to the crystal planes (110) and (200) of stoichiometric bcc FeCo, respectively. These peaks are also visible in the spectrum of the isolated powder. Notably, the reflection peak of PDMS is less intense as the particle content increases (Figure 4.2 b).
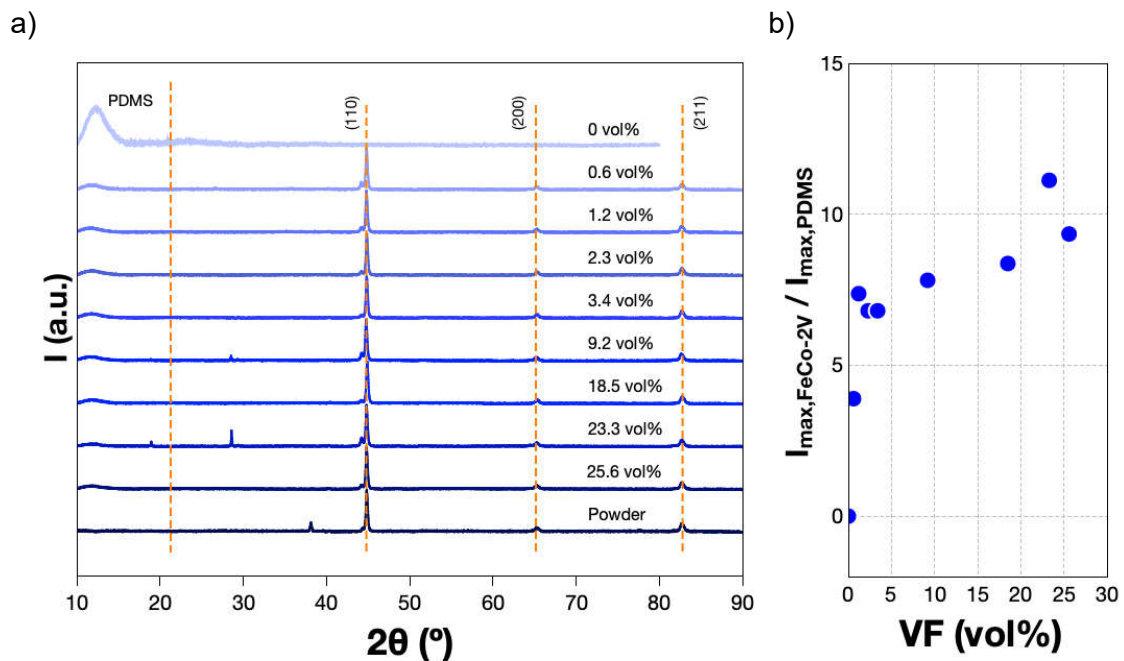
Figure 4.2 – XRD spectra of the MAE samples of PDMS with the spherical powder.

The diffractograms exhibit two distinct crystallographic phases, one of them belonging to the PDMS elastomer, and the other to the FeCo powder. This indicates that the fabrication process of the MAE did not cause any chemical reaction between the two components.

4.2.1.2 Magnetic properties

Isothermal M-H curves of composite samples with different VF and particle distributions were measured. In Figure 4.3 a), the field-dependent magnetization of the samples with composition 25.6vol% and different particle distribution are plotted as an example. The magnetic saturation M_s and remanence M_r of the samples of different VF and particle distribution are plotted in Figure 4.4 a) and b), respectively. Increasing volume fraction results in an increase in M_s, which exhibits an agreement with the bulk value (M_s=239.5emu/g). The same is true for M_r, but its slope depends on the particle distribution as well as on the direction of measurement with regard to particle alignment. Comparing the anisotropic and isotropic MAEs, the anisotropic samples show the highest values of remanence in the particle alignment direction. Isotropic samples exhibit a positive trend, but with a decreasing slope, as the VF increases. The M_r of the anisotropic samples takes similar values to the isotropic MAEs, with exception of the two highest concentrations.

a)   b)
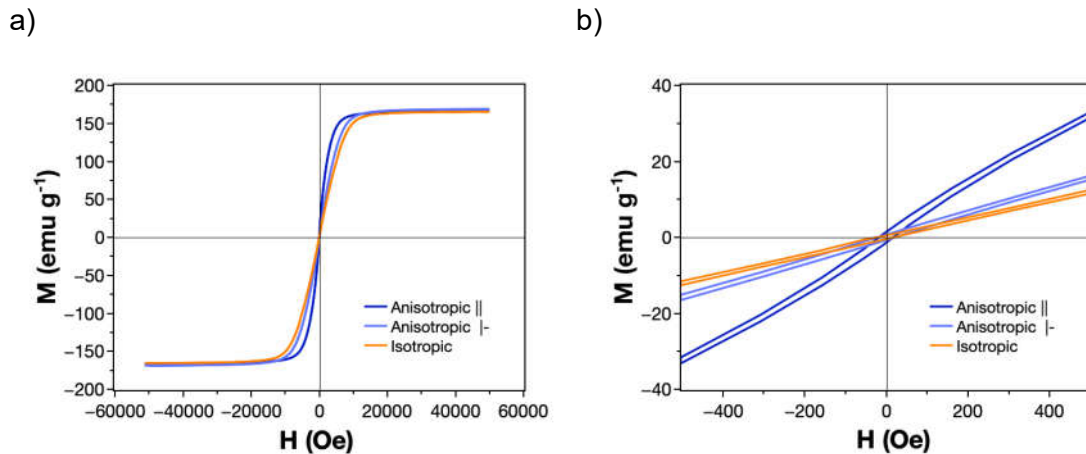
Figure 4.3 – a) Isothermal M-H curves of samples with composition 25.6vol%, b) detail of the same curves in the range -500Oe to 500Oe.

a)

b)
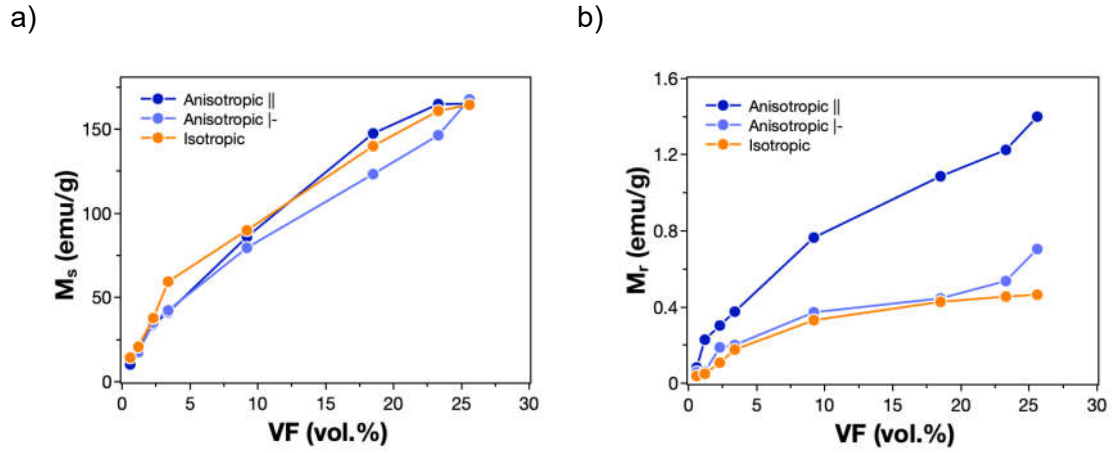
Figure 4.4 – Magnetic saturation (a) and remanence (b) of samples of different composition and particle distribution.

The magnetic sensitivity at H=0 $(dM/dH)_{H=0}$ is plotted in Figure 4.5 a) as a function of the VF. It shows a positive trend with concentration. Such a trend would be expected as the magnetization is directly dependent on the concentration of FM material. The behavior of $(dM/dH)_{H=0}$ with VF is very similar to that of M_r. The anisotropic MAEs show significantly more sensitivity in the direction of the particle alignment than perpendicular to it. The isotropic samples show a positive trend with decreasing slope, similar to the anisotropic MAEs |-. At the highest concentration of 23.3vol% and 25.6vol%, the anisotropic MAEs exhibit an increase in $(dM/dH)_{H=0}$, much like in the case of the remanence. This further agrees with the suggestion that the MAEs reach a critical magnetic concentration threshold.

a)

b)
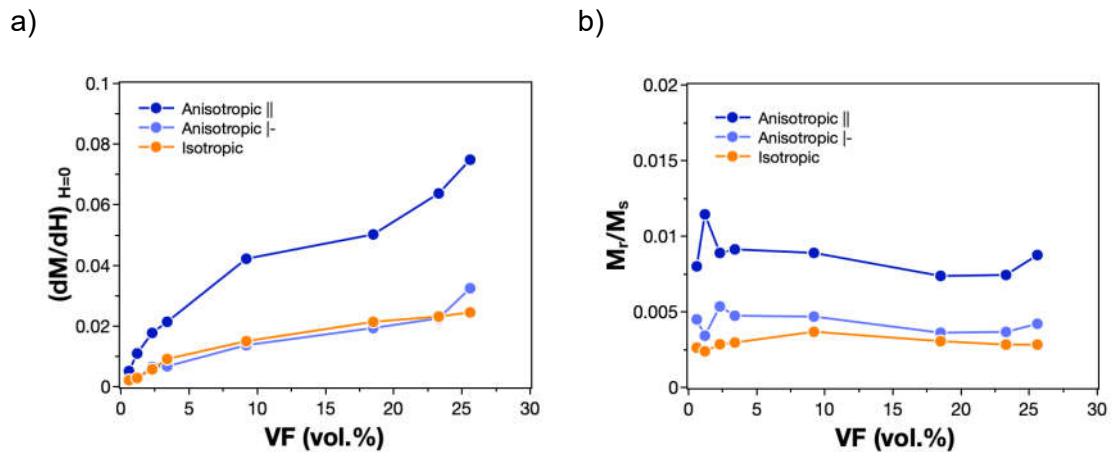
Figure 4.5 – Magnetic sensitivity at H=0 (a) and ratio M_r/M_s (b) of samples of different composition and particle distribution.

The ratio M_r/M_s is plotted as a function of VF in Figure 4.5 b). We observe that it does not significantly change with the concentration. This result suggests that the remanence

is related to the magnetic saturation, such that the particle concentration does not alter the ratio. However, M_r/M_s is different depending on the particle distribution and orientation. The largest M_r/M_s is obtained in anisotropic samples in the particle alignment direction, and the lowest occurs in isotropic MAEs. This is a clear consequence of the induced anisotropy. By curing the MAE with a preferential magnetic orientation, the particles are more susceptible to maintain a larger magnetization due to the minimization of the shape anisotropy energy of the particles when the magnetic field is removed. The anisotropic samples measured perpendicular to the alignment and the isotropic samples exhibit similar values of M_r/M_s.

4.2.1.3 Mechanical properties

Isotropic and anisotropic MAEs were subject to uniaxial tensile tests. The obtained stress-strain curves exhibit the characteristic hyperelastic behavior of PDMS. For reference, the elastic modulus E of the native PDMS matrix was also measured and is 1.22MPa. The determined elastic modulus of the samples is plotted in Figure 4.6.
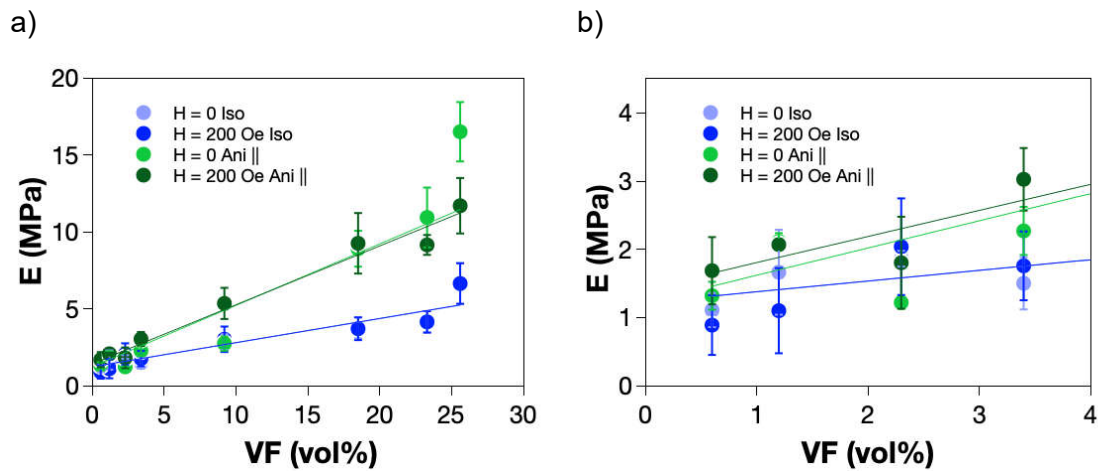
Figure 4.6 – Elastic modulus as a function of the concentration of isotropic and anisotropic MAEs under H=0 and H=200Oe, where a) shows the whole range of VF and b) shows up to VF=3.4vol%.

Figure 4.6 shows that E rises with increasing VF in both isotropic and anisotropic samples. The anisotropic samples have more stiffness than the isotropic samples, both at H=0 and H=200Oe. The positive slope of E with VF is not suppressed nor changed by the application of a magnetic field of H=200Oe. The isotropic samples yield a slope of 0.16MPa/vol% (in both H conditions) and the anisotropic samples yield 0.40MPa/vol% and 0.38MPa/vol% under H=0 and H=200Oe, respectively. This result suggests that the magnetic field intensity applied was not sufficient to cause alterations in the elasticity of the MAEs. Additionally, it leads to the conclusion that the anisotropic samples are stiffer

than the isotropic ones. This can be explained by the particle chain-like structures in the anisotropic MAEs. In areas of greater density, the hyperelastic PDMS occupies less space between the particles, resulting in a significant macroscopic stiffening of the composite.

The strength and the ductility of the samples were determined from the stress-strain curves and are summarized in Figure 4.7. The yield stress sees an increase at low VF until 3.4vol% and stabilizes at ~2MPa. For increasing VF, σ_y drops slightly. The addition of particles to the PDMS matrix does not increase the strength even though the particles have larger yield strength than the matrix. This suggests that the interface between the particle and the rubber contributes negatively to the strength. The ductility follows a negative trend with increasing concentration, leading to the conclusion that the inclusion of particles leads to the failure of the material at lower deformations. This further confirms that the interface between the particle and the matrix negatively impacts the mechanical properties of the MAE.

a)   b)
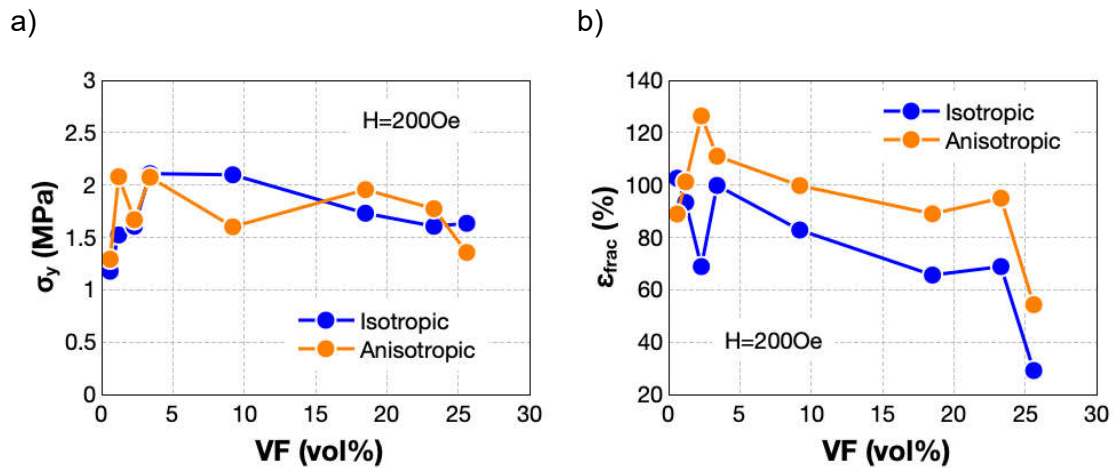
Figure 4.7 – a) Yield stress and b) ductility of isotropic and anisotropic MAEs at H=200Oe.

4.2.1.4 Magnetostriction

The magnetostriction λ of the composites was measured as a function of the magnetic field. Samples with different particle distribution and different concentrations were measured. The obtained λ values of the isotropic and anisotropic samples are plotted in Figure 4.8. The deformation increases for increasing H with a typical magnetostriction curve approaching saturation. By comparing the isotropic samples (a) with the anisotropic samples (b) of the same VF, it becomes clear that λ is larger in isotropic

samples. When the field is removed, the shape deformation is reversible, and further cycles confirmed its reversibility and reproducibility.

a)   b)
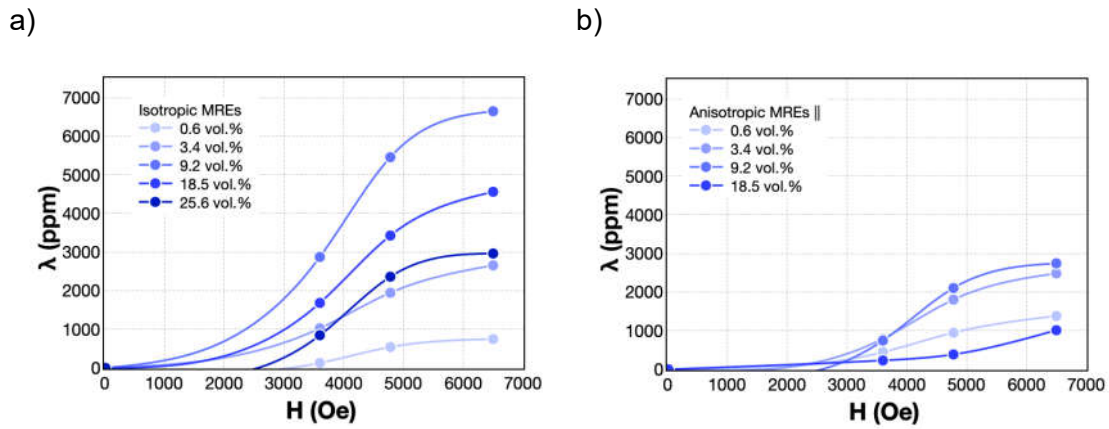
Figure 4.8 – λ as a function of the magnetic field of isotropic (a) and anisotropic samples (b), with VF ranging from 0.6vol% to 25.6vol%, at RT.

The magnetostriction exhibits a positive trend with increasing magnetic field in MAEs of any VF. Figure 4.9 shows λ as a function of VF, for different values of magnetic field. We see that in both isotropic (a) and anisotropic (b) MAEs, λ has a positive trend with increasing particle concentration, until VF=9.2vol%. For increasing concentration, the magneto-induced strain drops. The largest magnetostriction was obtained with isotropic MAEs with VF=9.2vol%, at H=6500Oe, with a value of λ=6649ppm. The drop in λ with VF could be predicted from the stiffening of the composite. In fact, the giant magnetostriction obtained in these materials is only achievable due to the hyperelasticity of the PDMS matrix. As the VF increases, the stiffness increases, causing the material to require more energy to be magnetically deformed. This explains the drop in λ for VF>9.2vol%.

a)   b)
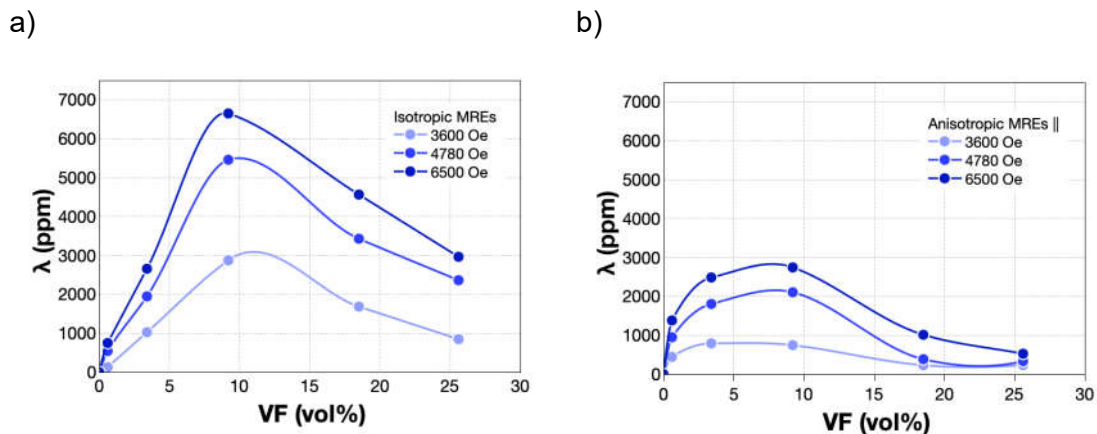
Figure 4.9 – λ as a function of VF of isotropic (a) and anisotropic samples (b).

The ratio $\lambda_{iso}/\lambda_{ani}$ was determined and plotted as a function of the magnetic field in Figure 4.10 a) and as a function of the concentration in b). A few conclusions can be drawn from the graphs. In a) we see that the ratio increases with H until 4780Oe and then drops. Moreover, the low concentrations of 0.6vol% and 3.4vol% show a very small change in the ratio values across the investigated magnetic field range. In b), it becomes clear that increasing concentration results in a rise in the ratio $\lambda_{iso}/\lambda_{ani}$, except for VF=25.6vol% where it drops. This decrease suggests that at VF=25.6vol% the isotropic and anisotropic samples become more similar to each other. This can happen since as VF increases, the distance between neighboring particles is reduced, and an isotropic homogeneous distribution will become more similar to the aligned MAE.

a)

b)
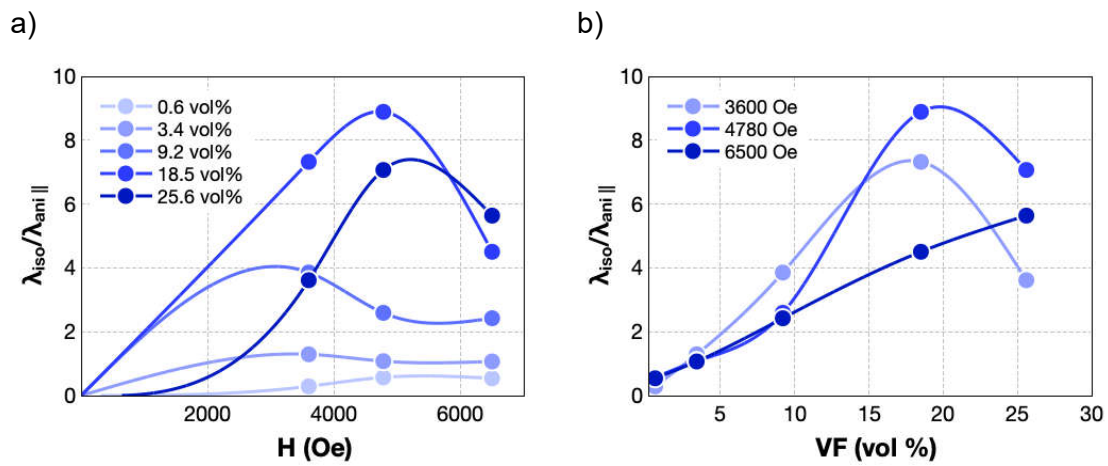
Figure 4.10 – Ratio between λ of isotropic and anisotropic MAEs.

4.2.2 PDMS / Helicoidal particles MAEs

4.2.2.1 Morphological and structural properties

The samples were visualized with the help of a digital optical microscope. Figure 4.11 depicts the pictures that were taken of each sample. As the VF is increased, the particle occupation in the PDMS matrix is also increased. Additionally, the orientation of the particles is clear in the low concentration anisotropic samples, where chain-like structures are formed, and becomes increasingly harder to distinguish due to the superposition of the particles.
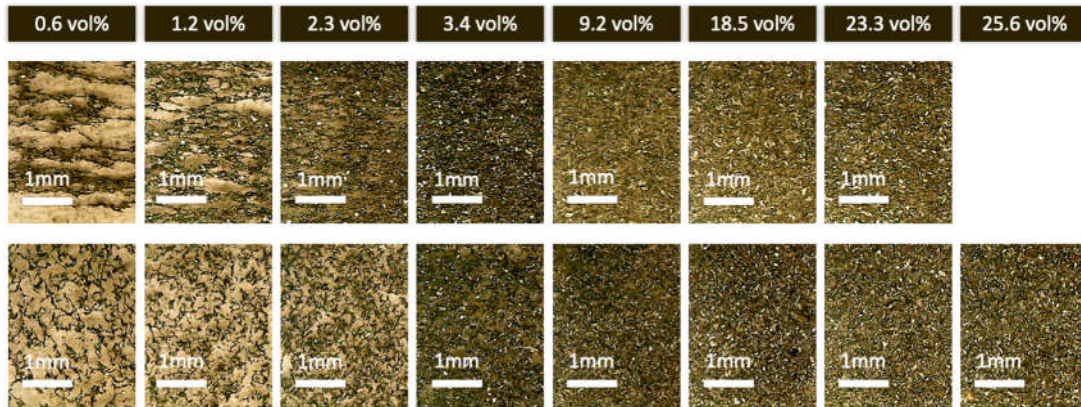
Figure 4.11 – Microscope images of the MAE samples with helicoidal particles.

The spectra of the X-ray diffraction of the FeCo-2V powder, silicone rubber, and each isotropic composition of the MAE are depicted in Figure 4.12. A broad peak around $2\theta = 12.2°$ and another around $2\theta = 22.0°$ are identified. The MAEs' spectra show sharp peaks at $2\theta = 45.1°$ and $2\theta = 65.7°$, which correspond to the crystal planes (110) and (200) of stoichiometric FeCo, respectively [104], along with the broad PDMS peak at $2\theta = 12.2°$. The isolated powder only depicts the characteristic reflections of the crystal planes of bcc FeCo, which place it in the cubic Pm$\bar{3}$m group [176]. The diffraction peaks visible at $2\theta = 44.1°$ and $2\theta = 51.3°$ are related to the diffraction pattern of the sample holder that was used for the samples with VF=1.2, 2.3 and 3.4vol.%. As with the previously reported composite, the XRD analysis has revealed distinct phases of Fe-Co alloy particles (sharp peaks) and amorphous PDMS (broad peaks) that exist independently in the composites. It is therefore confirmed that no crystallographic changes or further chemical reactions have been induced by the fabrication process.
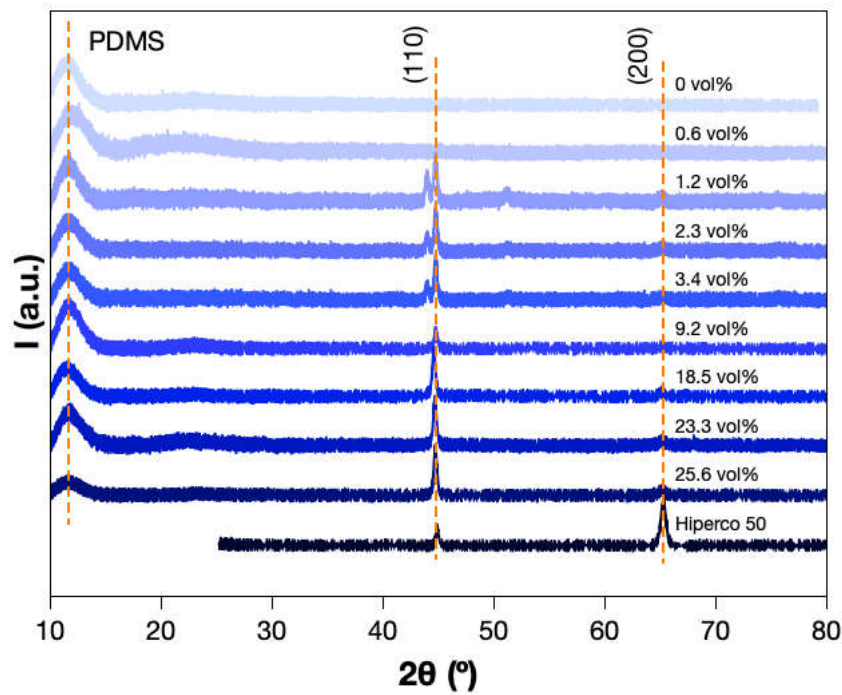
Figure 4.12 – XRD spectra of isotropic samples of volume fraction values between 0.6vol% and 25.6vol%.

4.2.2.2 Magnetic properties

The isothermal M-H curves of isotropic and anisotropic MAEs were obtained using SQUID magnetometer at T=26.85ºC. The field-dependent magnetization of the MAEs and Hiperco 50 powder is characterized by magnetic hysteresis, with small coercive field of $H_c \approx 35 Oe$, which indicates their soft ferromagnetic nature. The samples with composition 3.4vol% and different particle distribution are plotted in Figure 4.13 as an example. The figure shows that M-H curves are affected by the distribution and orientation of particles in the MAE with respect to the magnetic field. This difference can be attributed to the magnetic anisotropy, which results from the shape and alignment of the magnetic particles in the elastomer matrix.

a)

b)
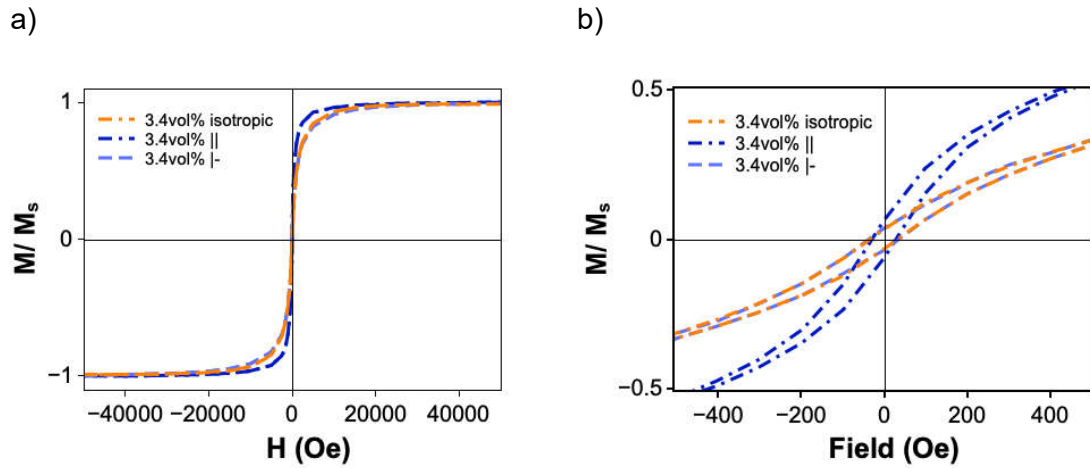
Figure 4.13 – a) Isothermal M/M_s-H curves of MAEs with VF=3.4vol% and with different particle distribution, b) the same graph zoomed in between -500Oe and 500Oe.

The composition-dependent magnetic saturation M_s was determined from the M-H curves of the MAEs (Figure 4.14), taking values between 12 to 167emu/g, for VF ranging from 0.6vol% to 25.6vol%, respectively. As expected, increasing VF results in progressively larger magnetic saturation. There is agreement between the measured M_s and the bulk counterpart's expected value (M_s=239.5emu/g) as indicated in Figure 4.14 a). The magnetic contribution is therefore primarily attributed to the magnetic filling, with no influence from the PDMS.

The coercive field remains unchanged as the concentration of powder in the polymer matrix varies, and there is negligible variation in the perpendicular directions of the anisotropic MAE (ΔH_C<35 Oe). In other words, H_c depends primarily upon the particles' coercive field, regardless of their concentration, thus presenting a soft ferromagnetic nature. The remanence M_r plotted in Figure 4.13 b) rises linearly with increasing particle concentration both in isotropic and anisotropic MAEs until VF=3.4vol%. MAEs with VF>3.4vol% exhibit a constant remanence of ~1.5emu/g in anisotropic samples (|| and |-) and ~2emu/g in isotropic samples. Anisotropic || samples see a sharp decline in M_r between 3.4vol% and 18.5vol%.

a)

b)
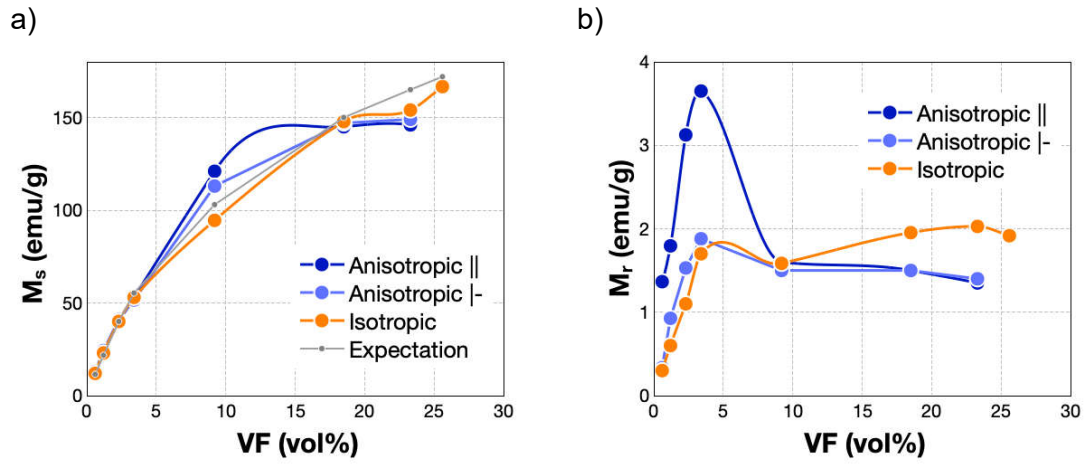
Figure 4.14 – a) Saturation and b) remanent magnetization as a function of VF.

Figure 4.15 a) depicts the volume fraction-dependent $(dM/dH)_{H=0}$, that was determined for both isotropic and anisotropic (|| and |-) MAEs. The $(dM/dH)_{H=0}$ of isotropic MAEs and anisotropic |- MAEs take similar values and follow an identical increase with VF until VF=18.5vol%. As for the anisotropic || MAE, $(dM/dH)_{H=0}$ is larger, suggesting that the anisotropic MAE has more sensitivity to small magnetic fields in the direction of the particle alignment.

M_r/M_s follows a negative trend with VF. At VF=18.5vol% and higher, M_r/M_s takes similar constant values of 0.011 in isotropic samples and 0.009 in anisotropic samples. Bellow VF=18.5vol%, the MAEs exhibit larger values of M_r/M_s that decrease as VF rises. Isotropic and anisotropic |- MAEs follow a similar behavior with VF. The largest M_r/M_s is obtained by the anisotropic || MAE, peaking at 0.114 with the lowest concentration, indicating that VF=0.6vol% is the concentration with the largest anisotropy.

a)

b)
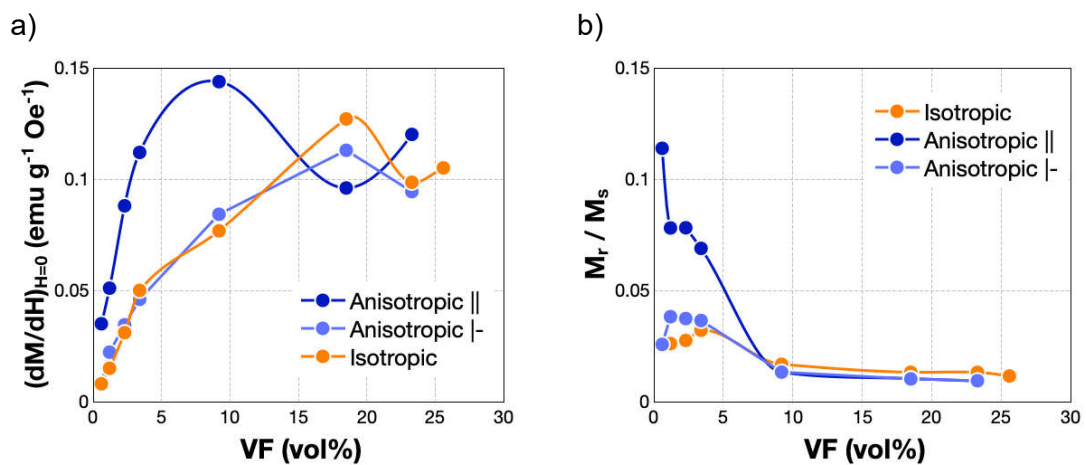
Figure 4.15 – a) Susceptibility and b) M_r/M_s as a function of VF.

4.2.2.3   Mechanical properties

Uniaxial tensile tests were performed on the isotropic and anisotropic MAEs with VF ranging from 0.6vol% to 25.6vol% and at RT, to which they exhibited characteristic hyperelastic stress-strain curves [177]. E was obtained at H=0 for each composition and particle distribution and is plotted as a function of VF in Figure 4.16 a). In b), the elastic moduli at H=200Oe were plotted versus VF. Each composition and condition were tested with a statistically relevant number of samples, between 5 and 10. The Young's modulus of the native matrix was also determined and takes a value of 1.22MPa.

a)   b)
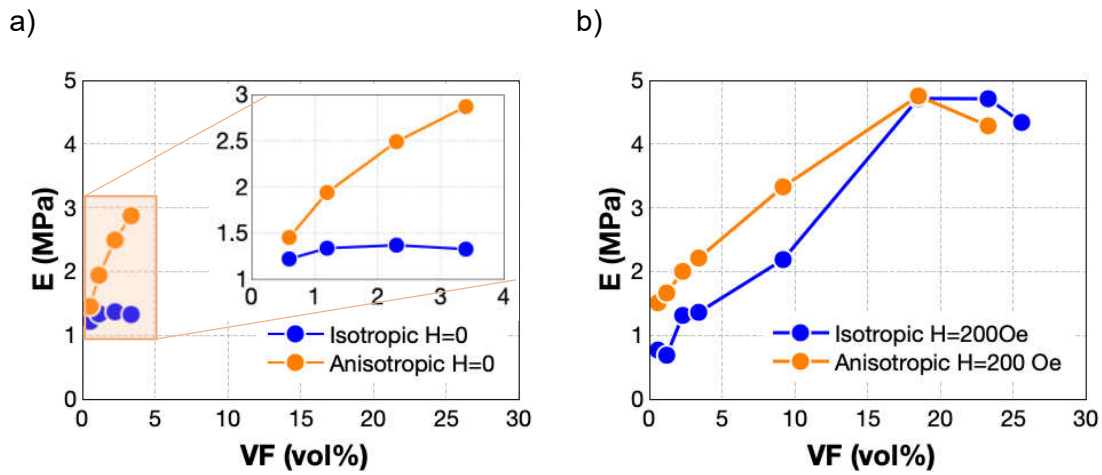
Figure 4.16 – Young's modulus of isotropic and anisotropic samples, measured at H=0 (a) and at H = 200 Oe (b).

a)   b)
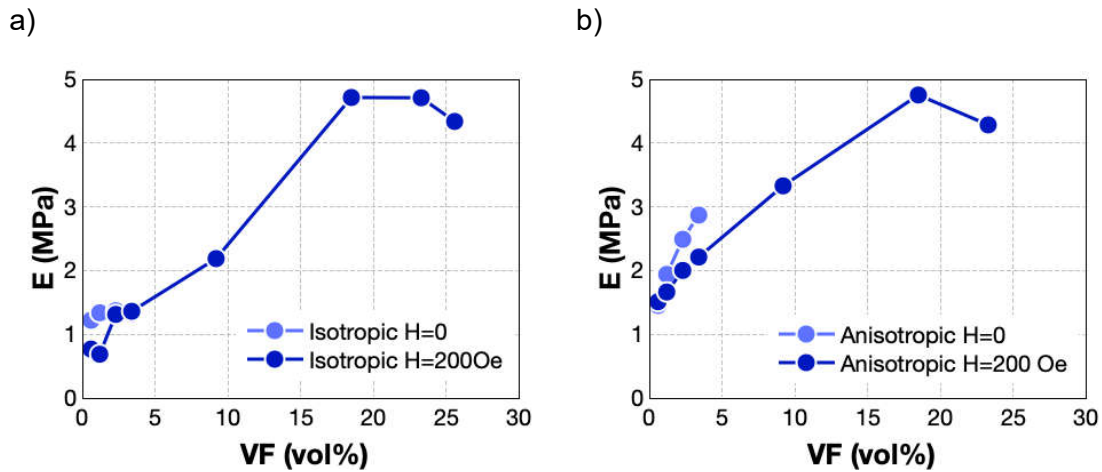
Figure 4.17 – Young's modulus measured in different magnetic field conditions, a) isotropic and b) anisotropic samples.

i)   Range 0 – 3.4 vol%

The graph in Figure 4.18 shows the volume fraction-dependent Young's modulus values of the isotropic and anisotropic MAEs. When analyzing the isotropic samples at H=0, it appears that E is unchanged regardless of the composition of the MAE or the external

magnetic field. Invariability with VF can be attributed to the fact that the concentration is sufficiently low to prevent elasticity changes at low strains with an isotropic distribution. In addition, at H=200Oe, the field intensity is insufficient to magnetically change the elastic modulus of the isotropic material, which we propose to be related to the low $(dM/dH)_{H=0}$.

In the case of anisotropic MAEs, a linear increase in the Young's modulus E with VF is observed. Additionally, E is lower under a magnetic field of H=200Oe, than at equivalent VFs when H=0. An increase in the elastic modulus with VF was expected as the particles have significantly larger E than the matrix. The drop in the E as the magnetic field is increased suggests that the particles interact with each other and with the magnetic field to spread along the magnetic field lines. Such effect could lead to an apparent drop in the elastic modulus.
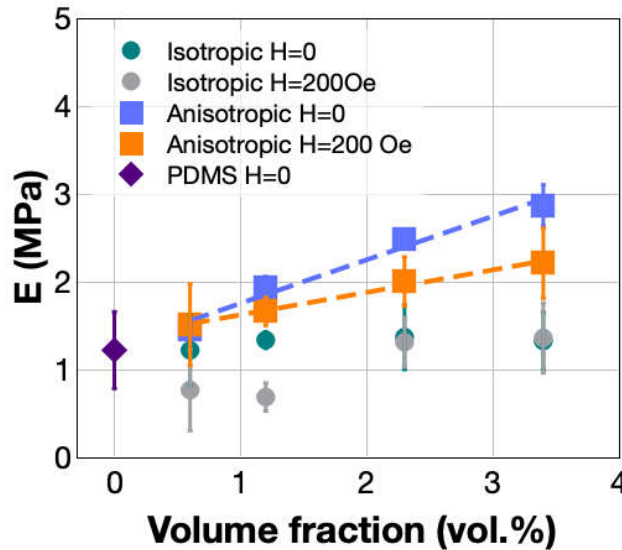
Figure 4.18 – Young's modulus E as a function of VF.

ii)   Range 9.2 – 25.6 vol%

At these high concentrations, there are two notorious behaviors. The first is characterized by the rise in elastic modulus and occurs for increasing VF up to 18.5vol%. For higher concentrations, the trend changes and E stabilizes and drops.

It is intuitive to understand the rise in elastic modulus with increasing VF. The addition of particles that have a much superior stiffness than that of the polymer matrix would naturally contribute to the rise of the stiffness of the composite and consequently the growth of the Young's modulus. At concentrations higher than 18.5vol%, however, we see a stabilization in E. This can be understood by analyzing the microstructure of the

MAE. The geometry of the helicoidal particles is complex. They occupy a large volume due to their shape, but a significant portion of it is empty space. In high concentration MAEs, the available volume of PDMS may not be enough to fill the volume generated by the particles. When that happens, voids are established in the MAE, and it can no longer be perceived as a simple composite. The presence of voids largely compromises the integrity of the MAE and can even lead to a decline in its mechanical properties. In fact, this decline is observed in samples with concentrations >18.5vol%, where the drop in E can be interpreted as a decrease in the resistance to a deformation induced by a tensile force. This occurs because a fraction of the material is air, which has virtually no stiffness.

The strength and the ductility of the MAEs were also determined from the stress-strain curves and are summarized in Figure 4.19 a) and b), respectively. Both exhibit a negative trend with increasing VF. Even though the particles individually have more strength than the polymer matrix, its addition leads to the reduction in the overall strength of the composite, suggesting that the particles do not play a relevant role in the improvement of the mechanical properties of the MAE. Regarding the drop in ductility, it suggests that the inclusions establish fragility points, leading to fracture at smaller deformations. Both of these behaviors can be coupled to the fact that the particles do not form a strong connection to the PDMS.

a)

b)
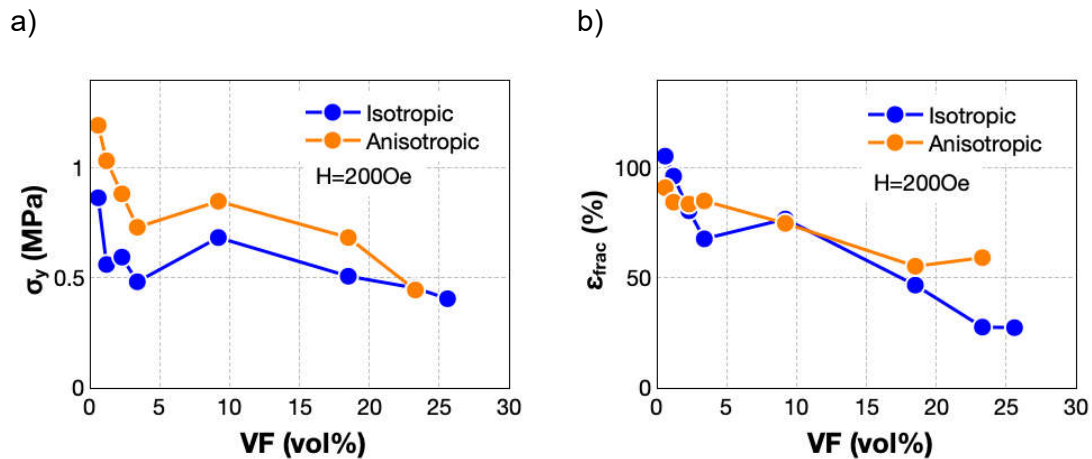
Figure 4.19 – a) Yield stress and b) ductility of isotropic and anisotropic MAEs with helicoidal at H=200Oe.

4.2.2.4 Magnetostriction

The measurement of λ as a function of the magnetic field is plotted in Figure 4.20, in a) of isotropic MAEs and b) of anisotropic MAEs. The presented values are in the range of thousands of ppm, which is considered giant magnetostriction. The graphs show that

both isotropic and anisotropic MAEs suffer magneto-deformation in the form of elongation and show that the strain follows a positive trend with the magnetic field. Within the magnetic field range of 0 to 6500Oe, the magnetostrictive behavior fits a linear curve in each MAE of different VF and does not reach saturation. Generally, the isotropic samples exhibit larger magnetostriction than the anisotropic samples of the same concentration.

Figure 4.21 a) depicts λ in isotropic samples as a function of VF for a magnetic field of 3600Oe. The magneto-induced strain exhibits a sharp rise until VF=3.4vol%, after which it stabilizes and drops slightly. The ratio between λ of isotropic and anisotropic MAEs, plotted in Figure 4.21 b), exhibits a behavior that also highlights the two different ranges of VF. Up until VF=3.4vol%, we see a sudden drop in the ratio, indication that the particle distribution is more influential in low concentration MAEs. For higher concentration samples, the ratio $\lambda_{iso}/\lambda_{ani}$ is generally unchanged.

For this reason, the analysis of the magnetostriction is sectioned into two parts. One corresponding to the low concentration MAEs, and another to the higher concentration MAEs.

a)   b)
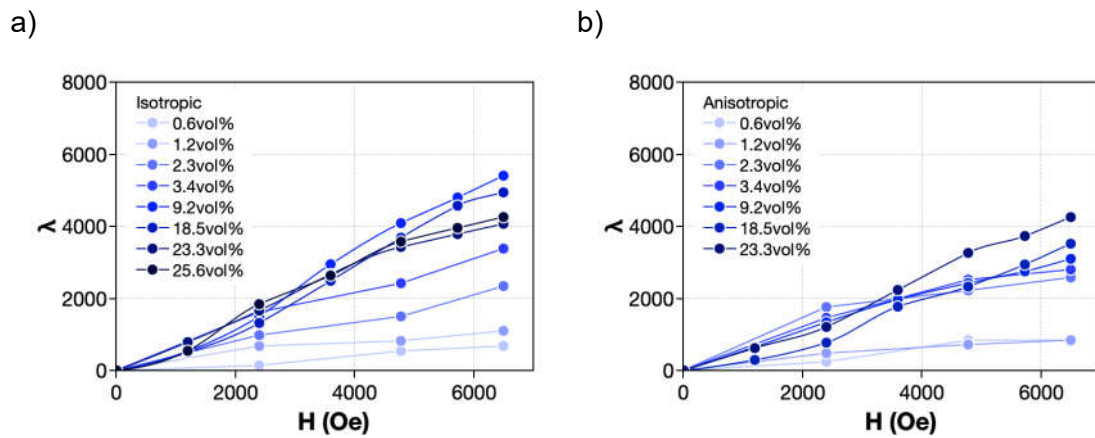
Figure 4.20 – λ as a function of the magnetic field of (a) isotropic and (b) anisotropic samples with VF ranging from 0.6vol% to 25.6vol%, at RT.

a)

b)
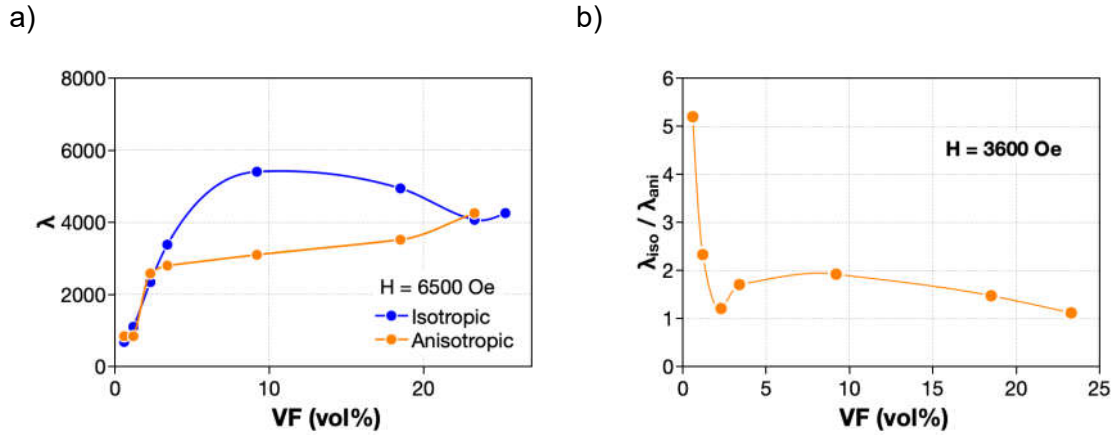
Figure 4.21 – a) λ as a function of the volume fraction of composite samples of PDMS and Hiperco 50 helicoidal particles, with isotropic and anisotropic particle distributions, at H = 6500Oe; b) Ratio of λ of isotropic and anisotropic samples at H = 3600Oe.

i) Range 0 – 3.4 vol%

In this range, λ exhibits a linear trend with increasing concentration of particles, both in isotropic and anisotropic MAEs. Notably, the isotropic samples have larger magnetostriction values compared to the anisotropic || counterparts. λ increases proportionally with volume fraction in isotropic MAEs by a factor of 9.59×10^{-4} vol%$^{-1}$, and in anisotropic MAEs by a factor of 6.95×10^{-4} vol%$^{-1}$.

ii) Range 9.2 – 25.6 vol%

The magnetostriction in this range does not follow the same linear trend as in lower VF. In fact, λ of the isotropic MAEs plateaus at VF=9.2vol% and sees a decrease for higher concentrations. This drop is continuous for increasing VF. As for the anisotropic samples, λ follows a small positive trend as the VF increases.

4.2.3 Discussion

In both MAEs with spherical and helicoidal particles, the isotropic samples exhibit greater magneto-induced strain than their anisotropic || counterpart. This result suggests that the amplitude of λ is notably related to the particle distribution. This result has also been experimentally demonstrated by Guan *et al.* [165] and Bodelot *et al.* [84]. According to the latter study, the increased stiffness of the anisotropic MAEs inhibits elongation. Because the anisotropic MAEs exhibit more stiffness that the isotropic ones, they will naturally deform less when exposed to an external magnetic field. Furthermore, Romeis and co-authors [178] have expressed that the rearrangement of magnetic particles can occur independently of magnetostriction due to the action of the magnetic field. For soft

elastomer matrix materials, such as PDMS, this effect can enhance λ, explaining the large magnetostriction effect observed in our low concentration MAE samples.

4.2.3.1   Magnetostriction in 9.2vol% MAEs

Figure 4.22 a) depicts the λ-H curves of the isotropic MAEs of VF=9.2vol% with spherical and helicoidal particles. It shows that the MAE with helicoidal particles has a linear correlation with H within the range 0 to 6500Oe, whilst the MAE with spherical particles does not follow a linear trend, but rather an S-shaped curve, typical of magnetostrictive materials reaching saturation. Below H=4780Oe, λ of the MAEs with spherical particles was too small to be accurately measured by the used set-up. The curve that follows the experimental points depicts a trend that is qualitatively representative of the dependence with H.

Figure 4.22 b) shows that λ takes similar values in spherical and helicoidal particle-MAEs at H=6500Oe. The increase in magnetostriction in a first instance is expected since the magnetic properties improve as the particle concentration rises, which occurs until VF=9.2vol%. Nonetheless, the magnetostriction is an interplay between the magnetic and mechanical properties, resulting that as the VF increases, the stiffness rise leads to a decline in the λ_s.

a)   b)
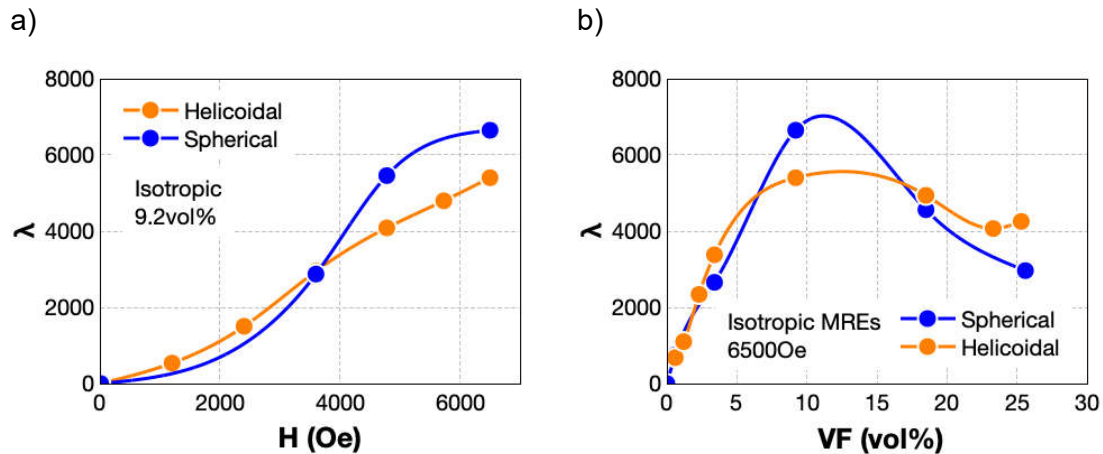
Figure 4.22 – λ of isotropic MAEs with spherical and helicoidal particles: a) VF=9.2vol% as a function of H and b) at H=6500Oe as a function of VF.

The conclusion that for low magnetic field (H<3500Oe) the magnetostriction of the MAE with spherical particles is smaller than the one with helicoidal particles is also related to the magnetic and mechanical properties. $(dM/dH)_{H=0}$ is 3 times lower in the sample with spherical particles than in helicoidal one (Figure 4.23 a), indicating that the state of

magnetization at a given H below 3500Oe is lower (Figure 4.24 a), and this is directly related to the degree of deformation. Moreover, at H=200Oe, the spherical particle-MAE has an elastic modulus that is 50% larger than that of the helicoidal counterpart (Figure 4.23 b and Figure 4.24 b), suggesting that the material requires more energy to be deformed comparatively. These properties explain why the helicoidal particle-MAE shows larger λ than the spherical one bellow H=3500Oe.

a)

b)
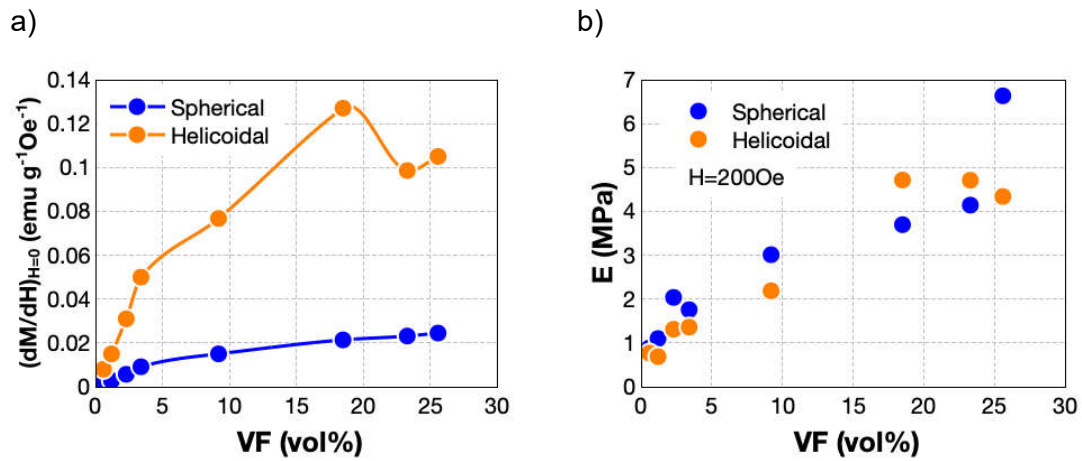
Figure 4.23 – Comparison of magnetic and mechanical properties of isotropic MAEs as a function of VF: a) $(dM/dH)_{H=0}$ and b) elastic modulus at H=200Oe.

a)

b)
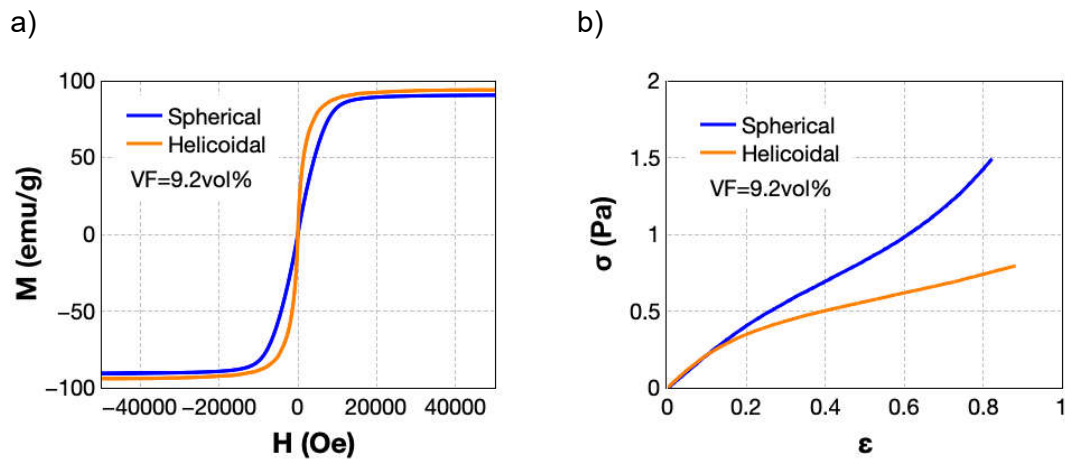
Figure 4.24 – a) M-H curves and b) stress-strain curves of isotropic MAEs of VF=9.2vol% with spherical and helicoidal particles.

The λ of the 9.2vol% helicoidal particle-MAE exhibits a linear trend within the magnetic field range that was investigated, while the MAE with spherical particles has the characteristic S-shaped curve of magnetostriction. This suggests that the helicoidal particle-MAE has not reached saturation at H=6500Oe. Even though its magnetization

is saturated faster than that of the spherical particle-MAE, the λ-H profile is also governed by the mechanical properties of the composite. Particularly with VF=9.2vol%, the helicoidal particles form an intertwined network which leads to increased stiffness as strain is also increased. Essentially the particles get entangled in with themselves much like fillings that result from the milling of a bulk piece of metal or alloy. This stiffness is detrimental to the magnetostriction because it requires that more energy is applied for the same degree of deformation.

4.2.3.2   Mechanical properties in MAEs with spherical or helicoidal particles

The helicoidal particle-MAEs require less energy to deform compared to the spherical particle-MAEs because of the state of magnetization of the samples. The greater the magnetization, the less mechanical energy is required to strain the sample, as concluded previously. As the helicoidal particles provide larger $(dM/dH)_{H=0}$ in small magnetic fields, it results in a drop in the elastic modulus comparing to the MAEs with spherical particles.

Despite the similar composition between the MAEs with spherical and helicoidal particles, we have seen that the magnetic properties and the magnetostriction can be affected by the shape and size of the particles. Here we discuss how the mechanical strength is also influenced by the filler of the material. Figure 4.25 shows the dependence of the yield stress and ductility on the VF. Typically, these properties have an inverse correlation, such that if one increases, the other tends to decrease. As seen from a), the σ_y in samples with VF>3.4vol% is nearly constant, showing a small negative slope. The change in the strength occurs at low concentrations, between 0.6 and 3.4vol%. In spherical particle-MAEs, the contribution of the VF is particularly notable, exhibiting a sharp increase in the yield stress by 100%. This behavior does not occur in the MAEs with helicoidal particles, where σ_y follows a small negative linear trend throughout the range of investigated concentrations. This occurs due to the difference in geometry of the samples. The sharp edges of the helicoidal particles lead to a stress concentration in these extremities and result in precocious permanent deformation. The spherical particles, on the other hand, have a smooth surface that is less damaging to the anticipation of the failure of the elastomer.

Notably, as the strength decreases with VF, so does the ductility. This is inherently related to the fact that inclusions create points of increased fragility in the MAEs, that cannot withstand such loads without fracturing. The fragility is a consequence of the lack of adhesion between the PDMS and the FeCo-2V particles.

a)

b)
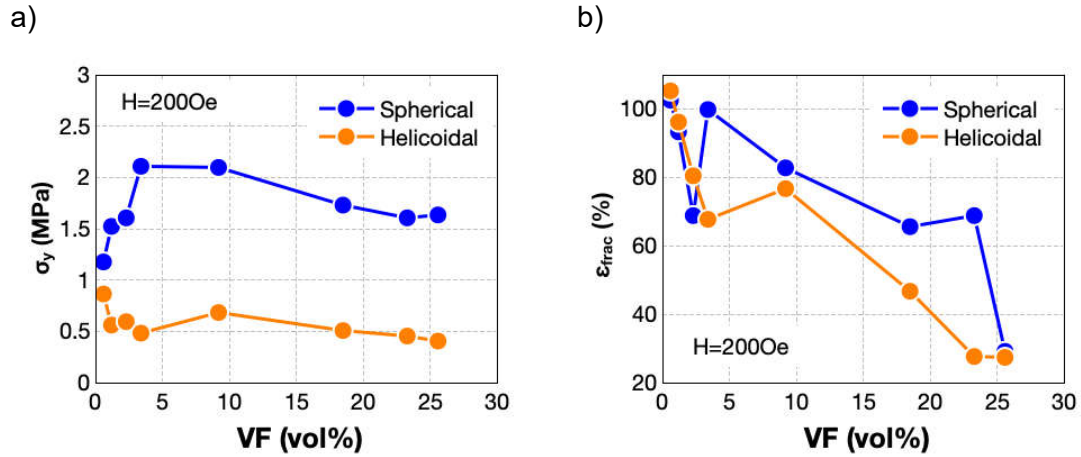
Figure 4.25 – Mechanical properties of MAEs as a function of VF: a) yield stress and b) ductility.

The λ and $(dM/dH)_{H=0}$ measurements can also provide an understanding of the determined elastic modulus of the samples. Anisotropic || MAEs have larger $(dM/dH)_{H=0}$, meaning higher sensitivity to low magnetic fields. As the deformation is dependent on the state of magnetization of the MAE then, the larger $(dM/dH)_{H=0}$, the larger the deformation for low fields. At H=200Oe and at near-zero stress, both the strain induced by the mechanical stress, and the strain caused by the magnetic field are responsible for the magneto deformation. λ takes values on the order of the mechanical strain when mechanical stress is low. This explains the drop in *E* that occurs in the anisotropic MAEs when the field is changed from H=0 to H=200Oe.

4.2.3.3 Particle shape anisotropy

Particularly in the MAEs with helicoidal particles, the difference in λ between isotropic and anisotropic MAEs is strongly coupled to the shape anisotropy of the embedded particles. Two main mechanisms at the microscale can be attributed to the magneto deformation of the present MAEs.

1. As a result of the singular shape of the particles within the polymer, a sufficiently strong magnetic field may cause them to elongate in the direction of the field (Figure 4.26). Considering that the particles have a helicoidal shape, the elongation is accompanied by a reduction in the inner radius. In a similar manner, a spring under uniaxial tensile stress exhibits the same effect.

2. As the angle between the particle's length direction and the field direction increases, the particle's shape anisotropy becomes increasingly relevant. As a result of its shape anisotropy and its demagnetizing field, the particle rotates

toward the direction of the field [157]. Although the matrix resists stress, its softness allows a certain amount of rotation, resulting in an elongation of the MAE along the field direction. In Figure 4.26 this effect has been exaggerated for the purpose of ease of understanding.
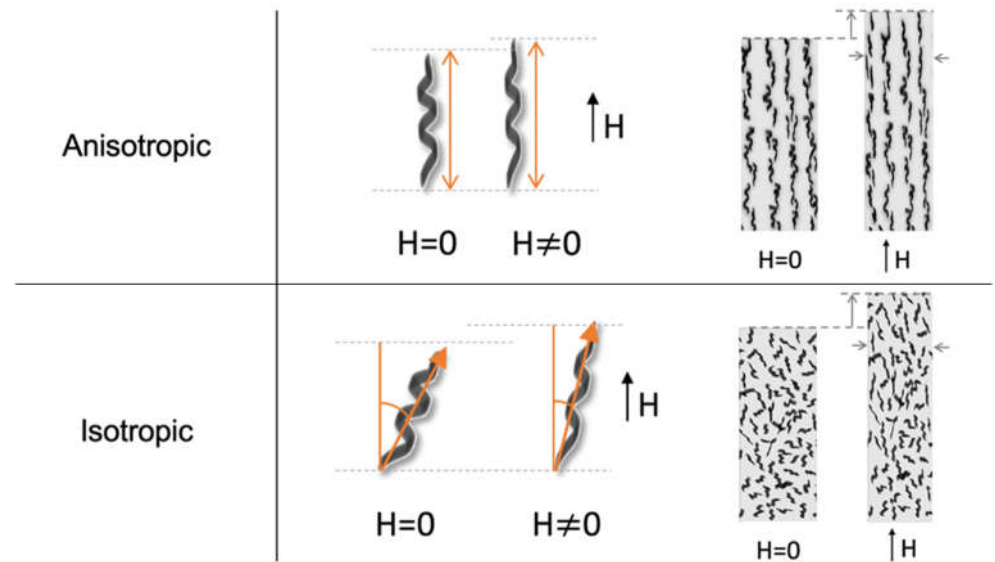
Figure 4.26 – Illustration of the magneto-induced deformation in helicoidal particle-MAEs.

In the case of the anisotropic MAEs, due to the alignment of the particles, the rotational contribution to magnetostriction decreases significantly. As a result, λ values of the anisotropic and isotropic samples differ. Also, the increased stiffness of anisotropic MAEs, as illustrated in Figure 4.18 a), could reduce specimen elongation.

The significant change in the magnetostrictive behavior in the VF range could be related to intrinsic changes in the properties of the MAEs. As seen previously, both the mechanical elasticity and magnetic properties diverged from the trend that is observed at VF≤3.4 vol%. This divergence further confirms that the anisotropy caused by the particle shape is only beneficial up to a certain concentration (between 9.2vol% and 18.5vol%), after which the particles get entangled in a intricate network, leading to increased stiffness and to reduced magnetostriction.

4.2.3.4   Low concentration MAEs vs the state-of-the-art

The λ values plotted in Figure 4.27 are a small representation of the state of the art of the magnetostriction of MAEs. It is plotted as function of the volume fractions regardless of the materials of the composite, particle size, shape and distribution, shape of macroscopic sample and measuring magnetic field. It serves the purpose of illustrating

the range of investigated concentrations and the respective measured λ. Although a direct comparison between different results in the literature is inaccurate, a superficial analysis of the order of magnitude of the λ_s reported in the literature reveals interesting conclusions. In the present work, we were able to obtain λ values up to 6649ppm, as highlighted. The use of low concentration MAEs highly stands out from previous literature results. This suggests that the range of concentrations that is mostly investigated has been missing out on some key concentrations, namely below 18.5vol%. The present work has revealed that giant magnetostriction is achievable by establishing a compromise between the magnetic and mechanical properties. In the two composition that were used, the largest λ was achieved at the same VF of 9.2vol%.
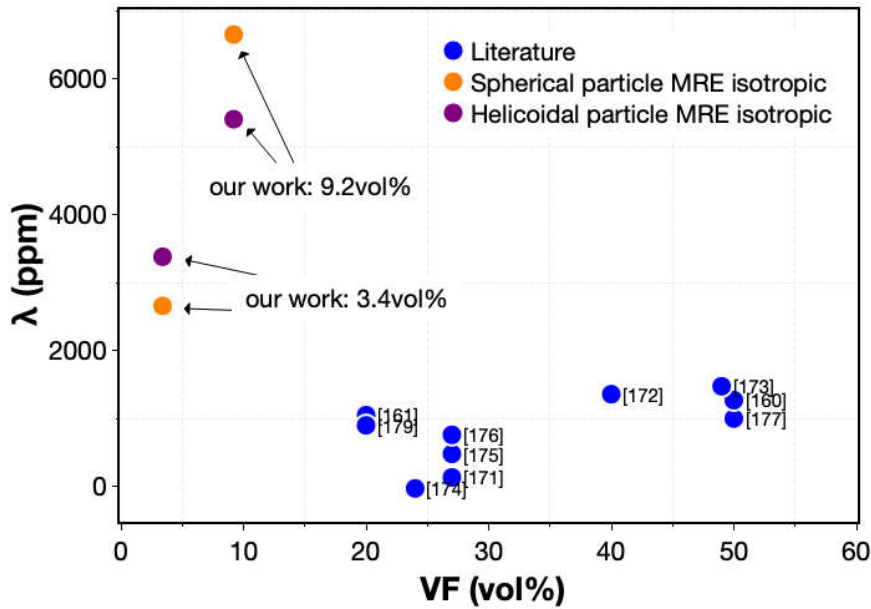
Figure 4.27 – Largest λ values obtained in this work compared to the literature examples.

4.2.4   Conclusions

The state-of-the-art review indicates that the study of magnetic field-induced deformation in MAE samples tends to focus on VF$\geq$30%. The investigation carried out in this work has focused on the preparation and characterization of MAEs with lower concentrations, from VF=0.6vol% to VF=25.6vol%.

Two types of fillers were used, the first consisted of commercial FeCo-2V spherical particles, with an average diameter of 22$\pm$9μm. The second consisted of FeCo-2V particles with a helicoidal geometry and length in the order of hundreds of micrometers. The samples were varied in composition, but also in particle distribution. For each

composition, isotropic and anisotropic samples were prepared. The MAEs were thoroughly characterized on the magnetic and mechanical properties.

We observed that the elasticity and the state of magnetization of the MAEs are connected. This was evidenced by the change in elasticity, strength, and ductility of the MAEs when an external magnetic field was applied. The change became particularly clear in anisotropic samples due to the combination of small applied magnetic field (H=200Oe) and larger permeability when the particle alignment is in the field direction.

Regarding the difference between the spherical and helicoidal particles, the MAEs with the later have shown less strength and ductility, corresponding to an overall increase in fragility. We proposed that this occurs due to the geometry of the helicoidal particles, which is composed of sharp edges that promote the concentration of stress when tensile loads are applied, leading to permanent damage and failure at lower yields.

As for the magnetostriction, all the samples exhibited magneto-induced deformation, even the ones with VF=0.6vol%. Helicoidal particle-MAEs exhibited a linear behavior within the investigated magnetic field range, suggesting that at H=6500Oe they are still far from saturation.

In isotropic MAEs, the helicoidal particles perform better than the spherical particles at H<3500Oe. This is reversed at H>3500Oe, where the λ of spherical particle-MAEs becomes dominant. We attributed this to the increasing stiffness induced by the intertwining helicoidal particles, which is detrimental to the deformation, and particularly to λ.

In this chapter we have reported on the giant magnetostriction in MAEs with VF≤30vol%. We also showed that the λ peaks at VF=9.2vol% in MAEs with both particles and reaches its maximum value at λ=6649ppm when H=6500Oe in spherical particle-MAE with isotropic distribution. This work has revealed that low concentration MAEs are, not only potentially superior in magneto-induced deformation, but also that a non-linear dependence with VF occurs in this range of concentrations.

Chapter 5　Innovative magnetostrictive devices using thin films for ultrasonic testing

The work detailed in this chapter concerns the fabrication of an all-in-one device based on a magnetostrictive film for ultrasonic testing. This approach was carried out in collaboration with the Instituto de Nanociencia y Materiales de Aragón (INMA), which belongs to the University of Zaragoza, in Spain.

We will present the characterization of FeCo films prepared by magnetron sputtering, using different substrates. Because the amplitude of perturbation is proportional to the thickness of the transducer, thick films will be required, in which case magnetron sputtering is beneficial since it can offer relatively high deposition rates. The films were characterized to understand the effect of increased thickness on the crystal structure, and its impact on the physical properties. An ultrasonic sensing device was made from Kapton. The implementation of the films on the device will be detailed.

5.1   State of the Art

FeCo thin films have been extensively investigated to apply in the field of recording [179]. Large magnetic saturation, low coercivity and high permeability are required for such applications [180]. The magnetic saturation of the Fe_xCo_{1-x} is the highest among commercial magnetic materials, peaking at M_s=1950emu/cm^3 within the range $0.5 \leq x \leq 0.7$ [107], [181]. The magnetocrystalline anisotropy (the source of the large magnetostriction) in Fe-Co alloys is detrimental to its soft ferromagnetic properties. Specifically, large anisotropy has been linked to increased coercivity and magnetic loss, and efforts are currently being made to reduce it. Many studies on Fe-Co alloy films were driven by the goal of reducing λ, strain or any kind of anisotropy, some of which are mentioned bellow.

Several studies investigated the addition of a third element to the Fe-Co alloy in an effort to reduce the coercivity [182]–[184]. However, this method has shown to result in a reduction of the magnetic saturation. Alternatively, Li *et al.* [181] have used different underlayers in an effort to control the texture of a film of $Fe_{65}Co_{35}$ and improve the coercivity. They report that the soft ferromagnetic properties of the alloy are improved when the texture is changed from (110) to (200) and link it to the increased anisotropy in (110)-textured films. In a similar way, Fu an co-authors [185] used an underlayer of Fe_xCo_{1-x} ($0 \leq x \leq 11$) to stimulate texture changes in the $Fe_{65}Co_{35}$ thin films. They were able to improve the soft ferromagnetic properties by growing the films with less strain due to the (200) texture. Vas'ko and co-authors [186] investigated the use of different substrates on the stress, transport and magnetic properties of $Fe_{50}Co_{50}$ films. Wolloch *et al.* [187] compared the dependence of the magnetocrystalline anisotropy energy on the strain of the materials, in an effort to minimize the λ. They have shown, via numerical simulations, that the magnetostriction in FeCo thin films can be tuned by a combination of film orientation, thickness, and strain. Yang and co-authors [179] experimentally demonstrated that the soft ferromagnetic properties of FeCo could be controlled with the film thickness and the deposition temperature, thus avoiding the addition of underlayers or third elements that can lead to a drop in M_s. They concluded that by increasing the thickness of the film, the stress was reduced, and led to the growth of the film in the (110) direction. As the stress reduces with the rising thickness, the anisotropy also reduces, resulting in a drop in H_c, however, M_s also drops. Deposition temperatures as high as 550°C showed to result in improved M_s and lower H_c. Another work [185], however, reports a decrease in H_c with increasing deposition temperature in $Fe_{65}Co_{35}$ films, but

there seem to be conflicting justifications for why that happens, namely the effect of the grain size on the coercivity.

Notably, Hunter *et al.* [113] reported that the magnetostriction of the Fe-Co binary alloy depends on its composition. They identified two compositional peaks of λ in thin films, the first one is around the $Fe_{30}Co_{70}$ composition (90 ppm), and the second one is around $Fe_{60}Co_{40}$ (70 ppm). Figure 5.1 shows the λ values obtained by Hunter and co-authors, for different compositions of Fe-Co alloys and different preparations. According to the phase diagram of the Fe-Co alloy, a phase transition exists around 75at% of Co content between the bcc Fe region and the bcc Fe + fcc Co region. The authors propose that this phase boundary may be the reason behind the magnetostriction enhancement. The authors have also reported the effect of temperature treatments on the improvement of magnetostriction, in particular by quenching the films from a high temperature.
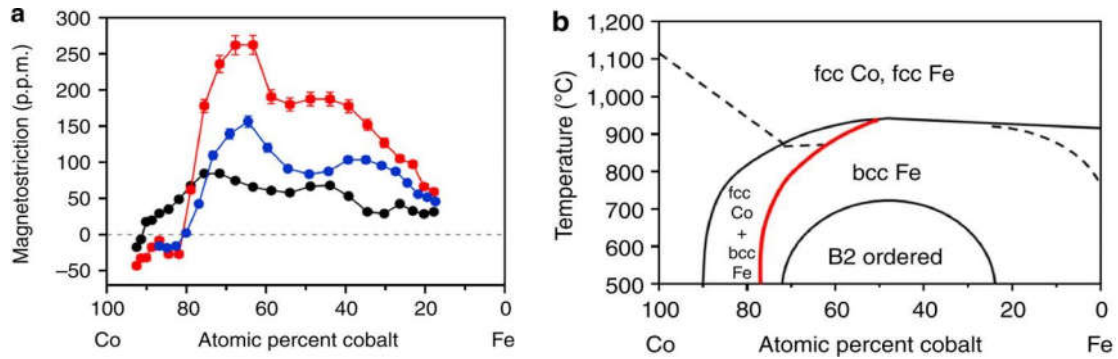
Figure 5.1 – (a) Magnetostriction of Fe-Co alloys versus the composition. The black dots are as-deposited films, the blue dots are slow-cooled heat-treated films, and the red dots are the quenched heat-treated films. (b) Phase diagram of Fe-Co, where the red line indicates the approximate phase boundary between the bcc region and the bcc + fcc region (obtained from [113]).

Cooke and co-authors [188] conducted a compositional study on Fe_xCo_{1-x} alloys ($45 \leq x \leq 53$), their texture and the effect of a post-deposition thermal treatment. They determined that the equiatomic Fe-Co alloy shows the largest λ across the investigated composition range. In the same work, they further report on the effects of the thermal treatments on the reduction of anisotropy and stress and on the formation of grains. In the work by Nakajima and co-authors, they reveal an increase in λ with the rise of the annealing temperature in $Fe_{32}Co_{88}$ sputtered thin films [109]. They propose that the large magnetostriction after the annealing is a result of the (fcc+bcc)/bcc phase boundaries that are formed in the film. They reached a similar conclusion to that obtained by Hunter, that the reorientation of the face centered tetragonal (fct) precipitates by effect of the magnetic field results in the enhancement of the λ. The magnetic domain rotation model

as the mechanism of the enhanced magnetostriction has also been attributed to the giant magnetostriction observed in Fe-Ga alloys within the 15-20at.% Ga range [189].

5.2   Experimental Results

5.2.1   Thin films Preparation

The group of magnetism at INMA has extensive knowledge on the deposition of thin films by magnetron sputtering. Concerning the Fe-Co alloy, optimization of the sputtering power and work pressure had already been undertaken, which greatly sped up the film fabrication process.

An equiatomic FeCo target as described in 2.1.1.1 was used to prepare the films. The effect of the substrate (Si/Si$_3$N$_4$ and Kapton flexible substrate) on the physical properties of the films was investigated. As previously mentioned, the samples were produced using p_w=0.4Pa, with sputtering power P_{sp}=125W. The conditions yielded a deposition rate of 6.25nm/min. The obtained films have thickness varying from 50nm to 850nm.

5.2.1.1   Morphological analysis

SEM analysis allows to take a look on the morphology of the surface of these films. Figure 5.2 depicts the surface of the films with different thickness deposited on Si/Si$_3$N$_4$, and on Kapton in Figure 5.3. Images were obtained using SE electrons. In the first case, the images reveal a continuous surface. Some defects can also be seen, such as dust particles and/or other contaminants on the surface. The Kapton-based samples, on the other hand, exhibit a cracked surface, except for the 50nm film. We justify the discontinuous surface with the difference in thermal expansion coefficients between the substrates and the film. The FeCo alloy has a thermal expansion coefficient of ~9.33ppmK^{-1} [190], which compares with the coefficient of Si$_3$N$_4$ (1.2–3.3ppmK^{-1}) [191] and Kapton (30-60ppmK^{-1}) [192]. Naturally, for each degree of temperature that is increased during deposition, the thermal expansion mismatch between the film and the substrate is larger in the films deposited on Kapton. This means that after deposition, when the temperature is dropped, the severe contraction of the substrate compared to that of the film, results in a large concentration of compressive stress on the film which leads to the formation of cracks on its surface, as seen in Figure 5.3. The thinnest sample on Kapton reveals a continuous surface, topped with a considerable density of particles.

It was not detected a different elemental composition in these structures with EDS, suggesting that the material aggregated to form these clusters is the same as the one from the film. Alternatively, the points could correspond to oxidation since oxygen was also extensively detected in the sample but is attributed to the polymer substrate. Samples with t=850nm exhibit a different morphology, in the sense that the cracks are not all connected in a network, unlike what happens in thinner films. Moreover, some of the cracks seem to be covered and not exposed. We suggest that both these features result from the deposition by steps. After each deposition step and consequent temperature drop, a new set of fractures is formed. When the deposition resumes these cracks are covered by the new layer of FeCo. As the new deposition step ends and the temperature drops once again, the contraction results in fractures along the previous fissures or in other higher-stress areas resulting in new cracks.
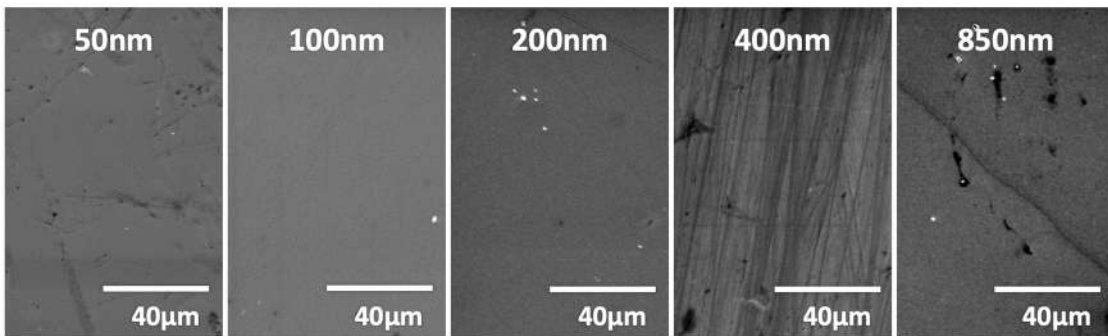
Figure 5.2 – SEM images obtained of the surface of films deposited on Si/Si_3N_4, with different thickness.
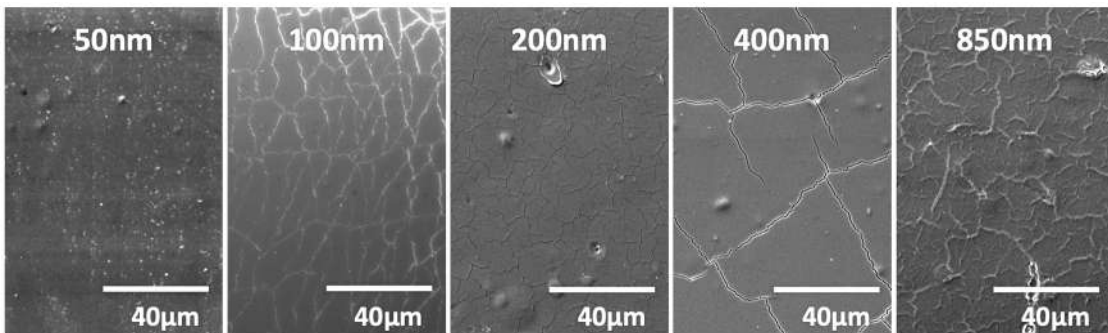
Figure 5.3 – SEM images obtained of the surface of films deposited on Kapton, with different thickness.

An EDS analysis to the surface of the film reveals the presence of Fe and Co, but also of the elements composing the substrates. Figure 5.4 depicts the graphs of the determined stoichiometries of the films, where they were normalized to the atomic concentration of Fe and Co. Since the thickness range that is covered by the detector is

of several micrometers, the quantifying error of the thinnest films is quite large, and the results should be considered conservatively.

a)

b)
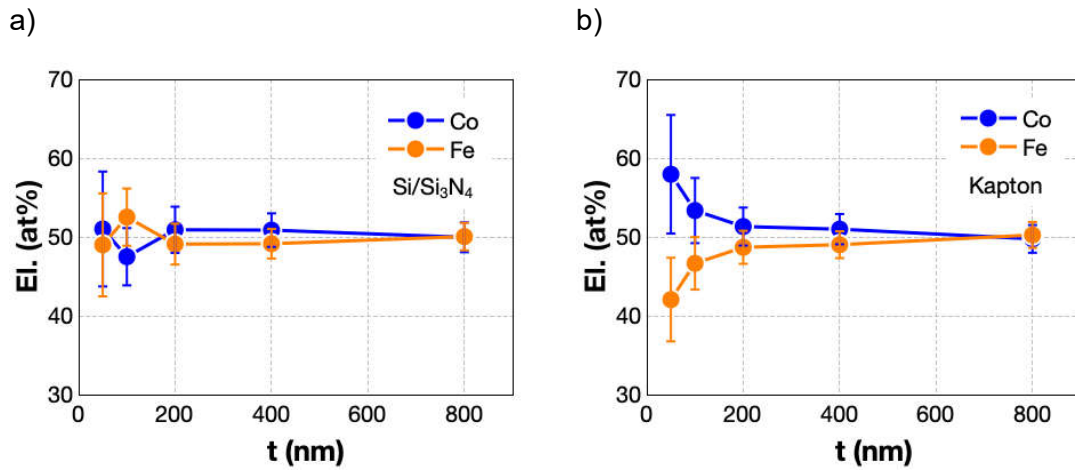
Figure 5.4 – EDS analysis results reveal the stoichiometry of the films deposited on a) Si/Si$_3$N$_4$ and b) Kapton.

5.2.1.2 Crystallographic properties

The spectra obtained of the films deposited on Si/Si$_3$N$_4$ and Kapton are plotted in Figure 5.5 a) and b), respectively. All the films exhibit the peaks corresponding to the reflection of the crystal planes of FeCo near 2θ=45º, 65º and 82º. These reflection peaks are characteristic of a bcc crystal structure, like FeCo. Additionally, the reflections corresponding to Si and Si$_3$N$_4$ are also visible in a).

Notably, in the reflections corresponding to FeCo, a transition to larger 2θ is visible and it is shown in detail in Figure 5.6. The two sets of peaks correspond to two distinct bcc phases of FeCo, with the first phase having larger lattice parameter and being predominant in samples with thickness t<400nm. We will address the two phases as α_a and α_b. As the thickness increases, the second phase α_b becomes more relevant, with larger 2θ and smaller lattice parameter. The transition occurs in the peaks corresponding to the reflections (110) and (200), but it is more evident in the first reflection (Figure 5.6). This suggests that the second phase forms with an off-plane (110) preferential crystal orientation.

a)

b)
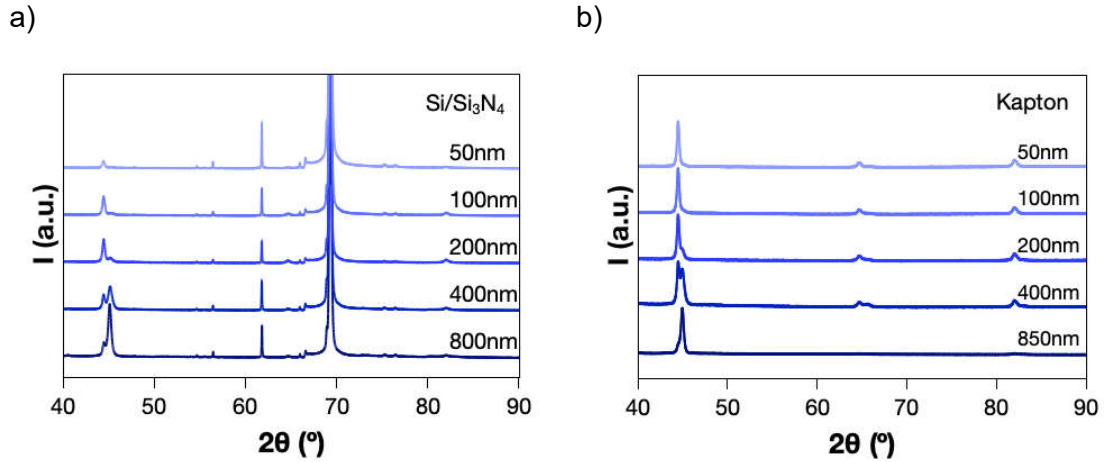
Figure 5.5 – XRD spectra of the thin films deposited on a) Si/Si$_3$N$_4$ and b) Kapton.

a)

b)
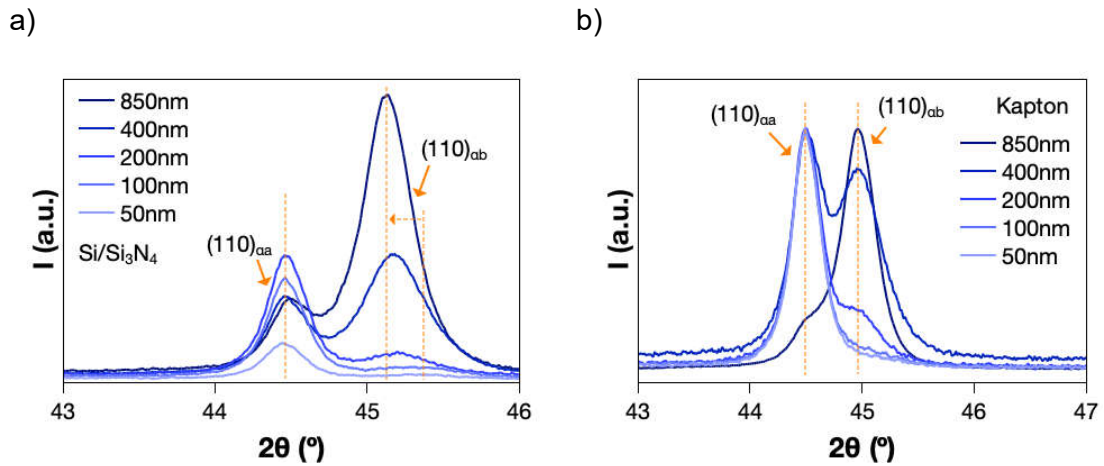
Figure 5.6 – Detail of the (110) reflection peaks of the two bcc phases in the films deposited on a) Si/Si$_3$N$_4$ and b) Kapton.

The analysis of the spectra indicated that the crystallography is marginally influenced by the substrate. In both cases, the film grows in a bcc structure with a lattice parameter of approximately 2.877Å. This phase is almost exclusive when $t \leq 100$nm. In samples with larger thickness, the second phase forms more extensively and becomes increasingly more relevant. The ratio of the (110) peaks of the two phases is plotted in Figure 5.7 a) and b) of the films deposited on Si/Si$_3$N$_4$ and Kapton, respectively, where this increase in the second phase is evident. The increase in the α_b phase is clear in the films with $t=400$nm, as it becomes predominant (the ratio is >1). Notably, the ratio is largest in the thickest samples, with the use of Kapton as a substrate resulting in the samples with most predominance of the second phase.

a)
b)
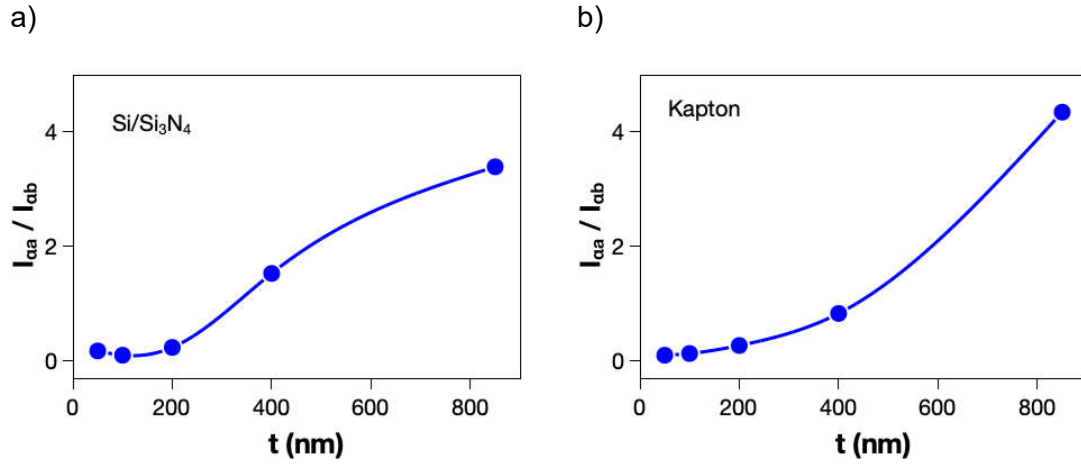
Figure 5.7 – Ratio between (110) reflection peaks of the two phases of FeCo in the films deposited on a) Si/Si$_3$N$_4$ and b) Kapton.

The determined lattice parameters of the two phases were plotted in Figure 5.8 of the films deposited on Si/Si$_3$N$_4$ (a) and Kapton (b). Notably, the first phase α_a shows approximately the same lattice parameter in both substrates (~2.880Å), while the α_b phase has a larger lattice parameter when deposited on Kapton, such that the difference between the lattice parameters of α_a and α_b (Δa) is largest in the films deposited on Si/Si$_3$N$_4$ than on Kapton. Moreover, in both substrates, phase Δa exhibits a negative trend with increasing thickness, by reducing by 0.01Å between 50nm and 850nm. This is caused by the positive trend of the lattice parameter of the α_b phase with t. In films on Kapton, a varies from 2.839Å to 2.849Å between 50nm and 850nm. In films on Si/Si$_3$N$_4$, a goes from 2.831Å to 2.839Å.

a)
b)
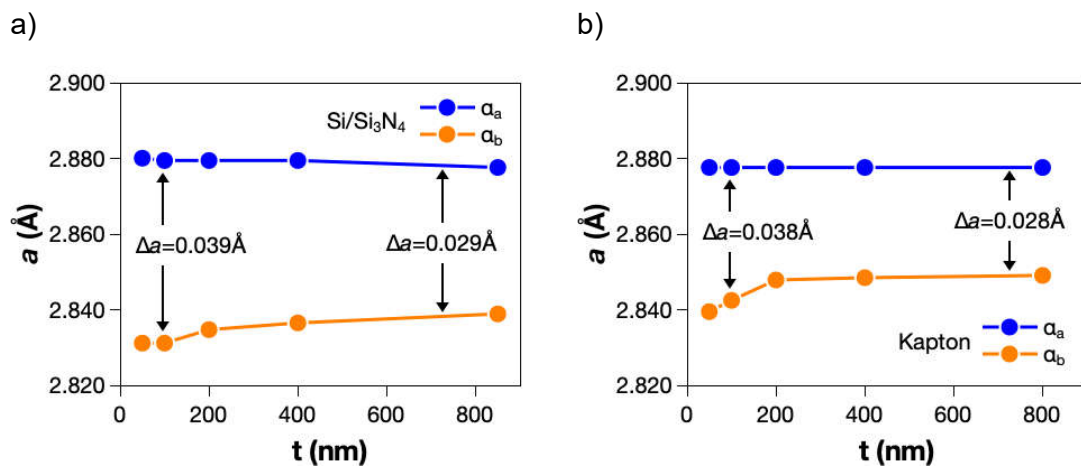
Figure 5.8 – Lattice parameter of the two phases of FeCo in the films deposited on a) Si/Si$_3$N$_4$ and b) Kapton.

5.2.1.3   Magnetic properties

The magnetic properties of the films were determined from the isothermal in-plane M-H curves. Figure 5.9 depicts the hysteretic cycles measured along two perpendicular in-plane directions, which exhibit similar curves, with a sharp magnetic orientation transition at H_c. The M-H curves of the samples deposited on Kapton exhibit a similar soft ferromagnetic behavior to those deposited on Si/Si_3N_4, but with smoother magnetization process and smaller remanence.

a)   b)
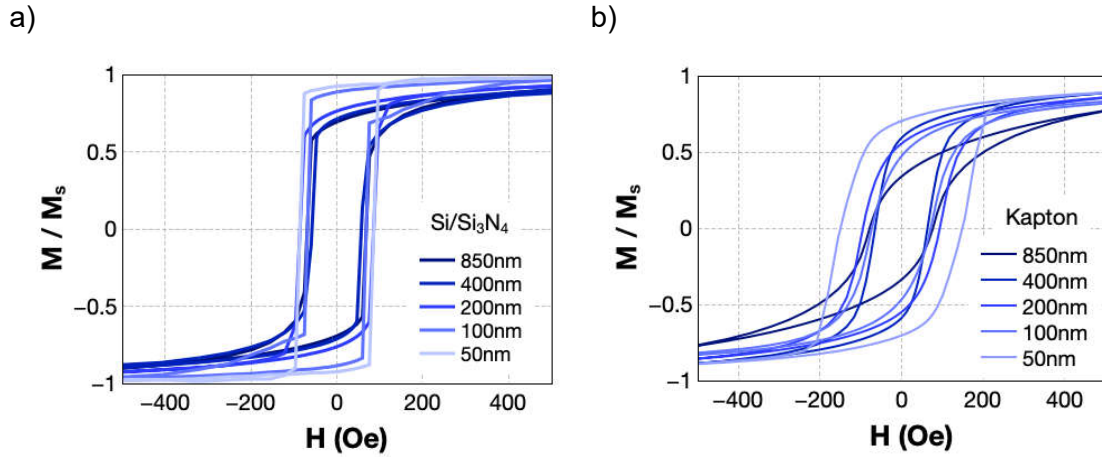
Figure 5.9 - Isothermal magnetization curves as a function of magnetic field for sputtered films of FeCo with various thickness values deposited on a) Si/Si_3N_4 and b) Kapton.

The magnetic saturation of the samples as a function of the thickness is depicted in Figure 5.10. Both substrates yield films with similar magnetization, indicating that they have little influence on their magnetic properties. The films with t=50nm deposited on Si/Si_3N_4 (a) and Kapton (b) exhibit the lowest M_s. This is attributed to the interfaces (substrate/film and film/surface), at the expense of which the magnetic contribution is reduced due to spin canting and uncompensated surface spins [193]. When the thickness is increased to 100nm, M_s reaches its maximum within the investigated range. Not only that, but the 100nm-thick films have a saturation magnetization that surpasses that of the bulk M_s for stoichiometric FeCo (~1990emu/g) at RT [107]. Notice that in the samples with t=200nm, a second phase is formed, as evidenced by the XRD spectra. This is accompanied by a drop in M_s compared to the sample with t=100nm, possibly related to the formation of an interface between the two phases, which reduces the magnetic contribution of the film due to spin canting. At t=400nm, the magnetization is once again increased since the adverse interface contribution is diluted through the thickness of the material. Finally, the thickest film exhibits a drop in M_s, probably a consequence of the step deposition. The interfaces are detrimental to the magnetization process and explain the drop in M_s in these samples.

a)

b)
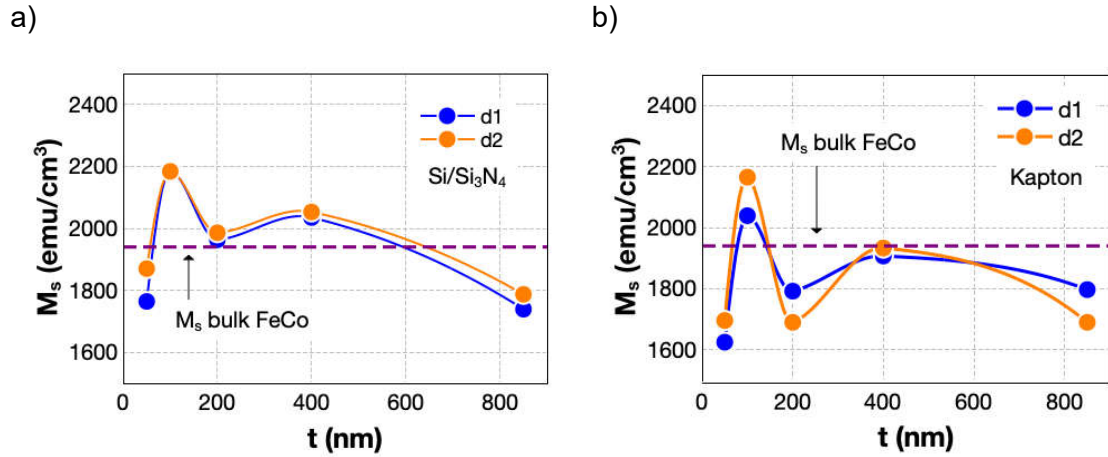
Figure 5.10 – Magnetic saturation of the FeCo films deposited on a) Si/Si$_3$N$_4$ and b) Kapton.

The remanence M_r follows a similar behavior with t to that of M_s, as can be seen in Figure 5.11. An initial increase of M_r from 50nm to 100nm is seen, followed by a drop at 200nm. It then stabilizes between 200nm and 400nm and drops when t=850nm. Like in the previous case of M_s, the decrease in M_r is related to the formation of interfaces that occur in the films, between the substrate, the two phases of FeCo and the different deposition layers (in the sample with t=850nm). In both substrates, the films yielding the largest remanence are the ones with 100nm. In the case of Si/Si$_3$N$_4$, M_r reached 1886emu/cm^3, corresponding to 86% of the M_s at the same thickness, in both directions of measurement. The M_r of the film deposited on Kapton yielded 72% of M_s, 1459emu/cm^3, in the d1 direction and 47% (1024emu/cm^3) in the d2 direction. The peak in M_r at t=100nm Is related to the formation of a higher magnetization phase, which is dominant at this thickness. At t=200nm, the formation of a second phase with smaller magnetization results in the subsequent drop of M_r in thicker films. The deposition of four layers in the sample with t=850nm is detrimental to the remanence and leads to the minimum value obtained within the studied thickness range, 1195emu/cm^3 (d1) and 1074emu/cm^3 (d2) in Si/Si$_3$N$_4$ and 573emu/cm^3 in Kapton (d1 and d2).

a)

b)
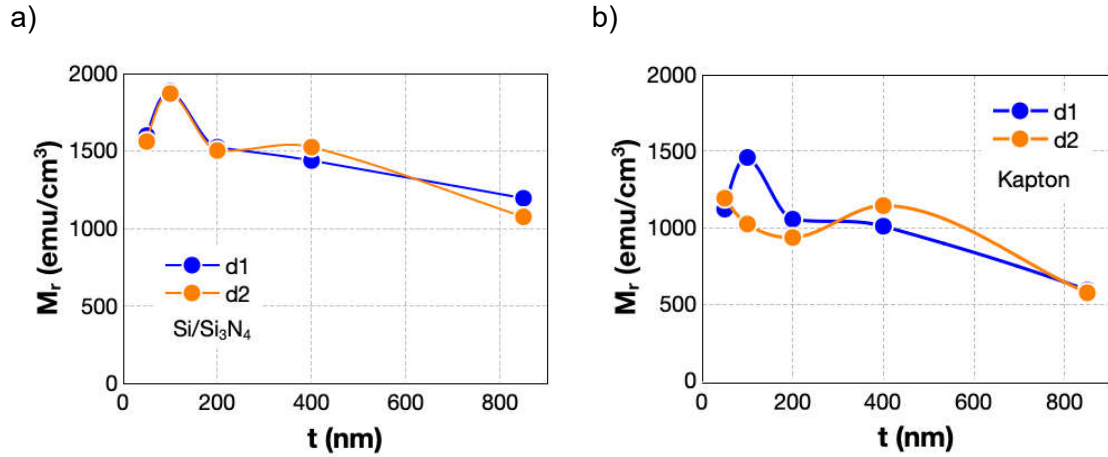
Figure 5.11 – Remanent magnetization of the FeCo films deposited on a) Si/Si$_3$N$_4$ and b) Kapton.

The coercivity H$_c$ is plotted in Figure 5.12. The largest H$_c$ is obtained in samples with t=50nm, particularly the ones deposited on Kapton, where H$_c$=150Oe. The minimum coercivity is achieved in samples with t=200nm, taking values between 55Oe and 70Oe, both in Si/Si$_3$N$_4$ and Kapton and in the two directions of measurement. The coercivity takes similar values in both substrates, despite one being polycrystalline (Si/Si$_3$N$_4$) and the other amorphous (Kapton), suggesting that the substrates have a similar effect on the formation of magnetic domains in the film. Moreover, H$_c$ is not severely affected by the direction of measurement, especially in the films deposited on Kapton, which take the same values independently of the direction. In the case of films on Si/Si$_3$N$_4$, there is a small difference in coercivity between d1 and d2 of no more than 20%. This difference decreases with increasing thickness and is nulled in the film with t=850nm.

a)

b)
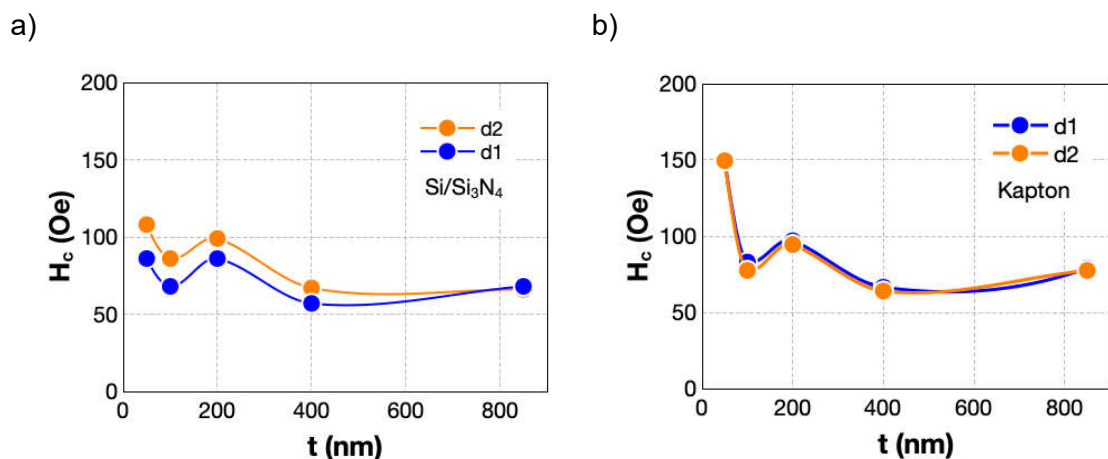
Figure 5.12 – Coercivity of the FeCo films deposited on a) Si/Si$_3$N$_4$ and b) Kapton.

5.2.1.4   Electric transport properties

The resistivity ρ of the films was determined by measuring the resistance using a 4-point probe method (Figure 5.13) on films deposited on Si/Si_3N_4, Kapton and SiO_2 substrates. The determined values are compared to the resistivity of the target, indicated by a purple dashed line. In the films deposited on SiO_2, the determined resistivity of the films is relatively constant in the range $t \leq 400nm$, and it is very close to that of the target. The resistivity of the film with $t=850nm$ of thickness is 3 times larger than that of the bulk material. We attribute this increase to the preparation of the sample, which is composed of 4 layers, with 3 interfaces between them. The deposition breaks can lead to lattice mismatches caused by temperature differences between the end of the previous deposition and the beginning of the next one, which contributes negatively to the electrical conductivity. Moreover, impurities present in the chamber can deposit of the surface of the film during the deposition breaks and also contribute to increasing the electrical resistivity.

Due to the small surface area of the samples deposited on Si/Si_3N_4, it was only possible to measure the resistivity of the films with $t=50nm$ and $t=400nm$. The obtained values are close to those obtained with the films deposited on SiO_2, which suggests that the resistivity of the remaining samples on Si/Si_3N_4 follows a similar trend.

The films deposited on Kapton exhibit larger values of resistivity compared to the ones of the samples on SiO_2. Notably, ρ increases with rising thickness, possibly due to the decreased flexibility of the film and consequently the formation of a larger density of film cracks.
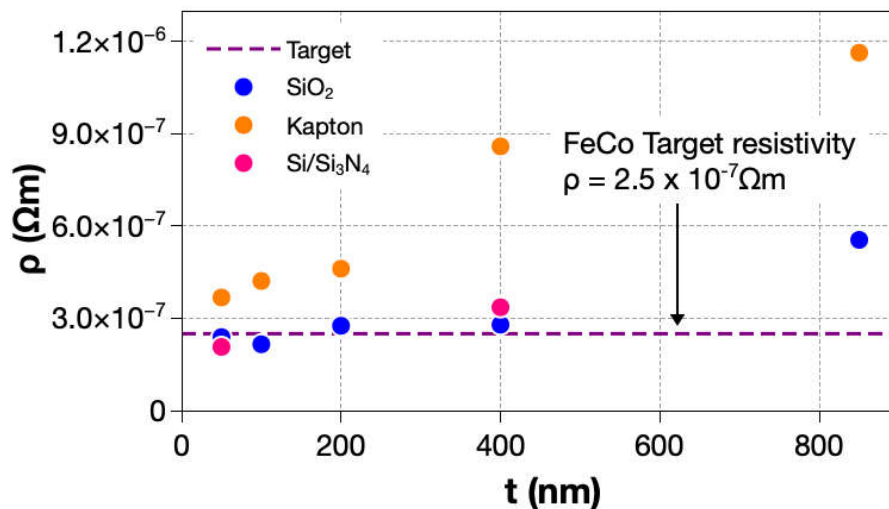
Figure 5.13 – Resistivity of deposited films of FeCo as a function of their thickness.

Increased resistivity is good in UT because it reduces the energy that is wasted in Eddy currents and decreases the noise of the signal. Moreover, in the present case, the perturbation is intended in the off-plane direction, such that the cracked surface is not significantly detrimental to the purpose of the application.

5.3   Integration of the transducer on the UT device

After the characterization of the thin films of different thickness, their integration in the device was carried out. Because the films are so thin, the coupling between the film and the magnetic field elements must be excellent. The device was fabricated and coated with a Kapton layer. This coating was used as a substrate for the film deposition, such that the device becomes all-in-one. An illustration of this structure can be seen in Figure 5.14 a). The system consists of two induction coils, separated by a Kapton layer, and coated by more Kapton. The film is deposited on the top facing side, with thickness t=400nm and t=850m. The permanent magnet is placed on the other side and is used to press the device against the surface of the pipe. Figure 5.14 b) shows the deposition of a FeCo films on the device and Figure 5.15 depicts the device ready to be used.

a)

b)
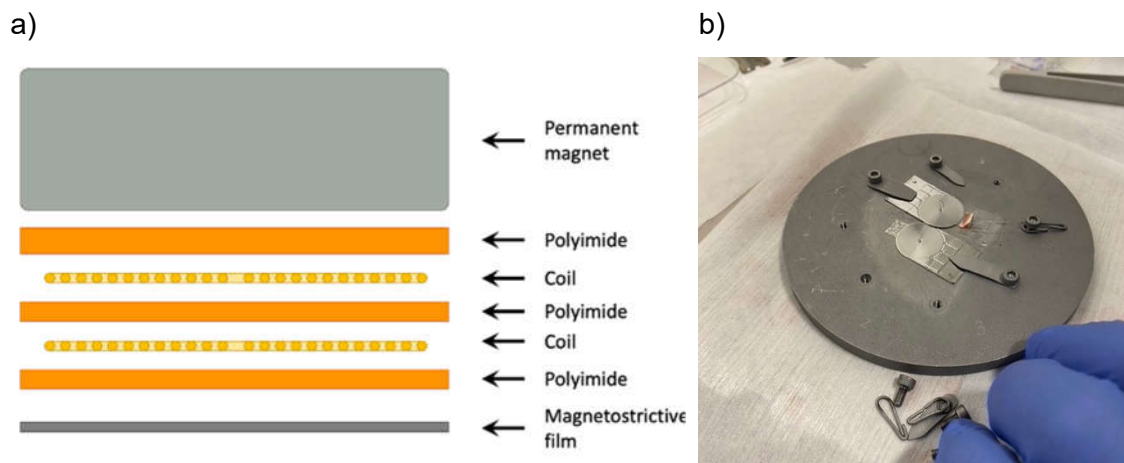
Figure 5.14 – a) Illustration of the structure of the BW UT device, b) deposition on the device.

The attached electrical contacts will be used to connect the sensor the CPU of the BW UT set-up. The results on the BW tests will be presented and discussed in 6.2.

a)   b)
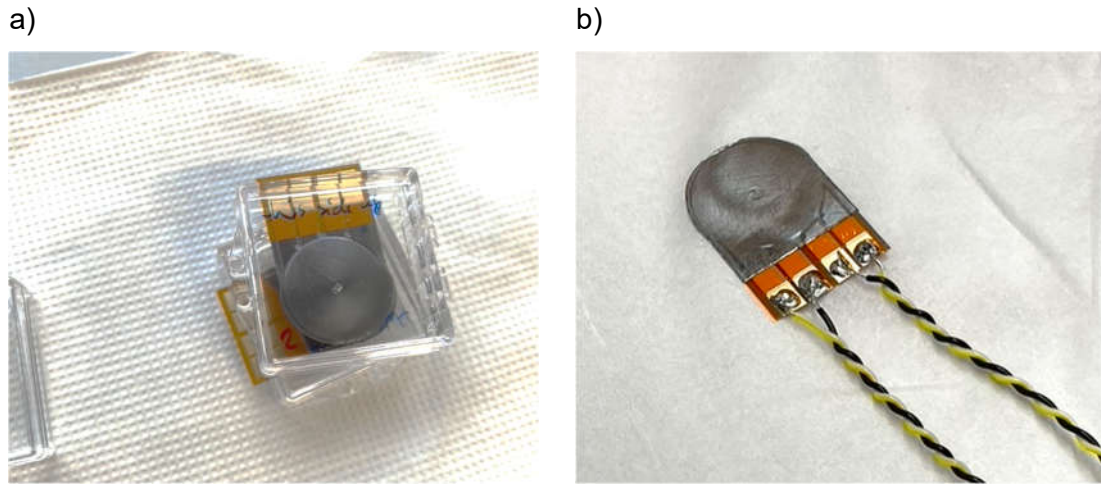
Figure 5.15 – a) Devices before and b) after application of the electrical contacts.

5.4   Conclusion

FeCo films were prepared by magnetron sputtering and deposited on Si/Si_3N_4 and Kapton substrates. The thickness of the films was varied between 50nm and 850nm. Regarding the crystallography of the films, they have all exhibited a bcc crystal structure. As the thickness increases, we see the formation of a second bcc phase with smaller lattice parameter, and with a strong (110) off-plane preferential direction.

We were able to correlate the existence of the two distinct bcc phases and respective interfaces with the evolution of the magnetic properties. The first phase shows both larger M_s and M_r than the second phase. Moreover, the interfaces between the substrate and the film and even between different layers of the film are detrimental to the magnetization process, resulting in the reduction of M_s and M_r and on the increase of H_c.

We have shown that the substrate can influence the integrity of the film. The use of a soft polymer with relatively larger thermal expansion coefficient such as Kapton leads to severe compressive stress that results in fractures along the surface of the films. The cracked films exhibit a significant increase in the electrical resistivity.

Generally, the changes in the physical properties that the substrate causes are not critical for the preparation of the all-in-one device since it is intended for off-plane perturbation. The devices were prepared, and the results of the tests are presented in Chapter 6.

Chapter 6   Ultrasonic Tests & Technology Transfer

This chapter is focused on testing the samples that were described and characterized in the previous chapters. The transduction capability of the samples is tested by using two configurations of the MsS: guided wave UT and bulk wave UT. A new set of samples was developed during these tests and the test results will also be presented.

Firstly, the magnetostrictive strips and the giant magnetostrictive MAEs will be applied in the guided wave set-up, and the results will be demonstrated. Then, the innovative UT device using thin films will be tested as a BW ultrasonic transducer. And finally, an alternative set of materials will be described using the conclusions that are possible to draw from the previous tests and will be applied as transducers.

An overview of the results and a discussion on the technology transfer will be presented, highlighting the novelty and the potential of the magnetostrictive materials of different size scales, 3D, 2D and composites, in the fabrication of transducers for magnetostrictive ultrasonic sensors.

6.1   Ultrasonic guided wave testing

The used method for GW UT has been described in 2.2.11. As previously mentioned, this technique requires that the transducer is of the same length as the diameter of the pipe under test so the samples must be prepared accordingly. After being appropriately sized, the samples are dry coupled to the pipe using duck-tape and magnetized with a permanent magnet, which is then removed. The flexible coil that generates the AC field is placed around the pipe around the sample, and the measurement is conducted using the automated software.

The GW tested samples include those described and characterized in Chapter 3 and the isotropic MAEs described in Chapter 4.

6.1.1   Hiperco annealed strips

The samples produced in 2.1.4 were tested as transducers, using the guided waves set-up. The set-up operates in a pulse-echo configuration, such that the samples are

responsible for both the emission and detection of the acoustic waves. Each sample is wrapped around the pipe with the necessary equipment at approximately 0.8m from one of the edges. The detected signals by the quenched and slow cooled samples are plotted in Figure 6.1 a) and b), respectively. The visible peaks correspond to both ends of the pipe, which is 3.5m-long. Given that the waves travel at the same speed to each side of the strip, the reflection coming from the farthest end is detected later than the closest end.

Figure 6.1 plots the signals at three different frequencies: 32kHz, 64kHz and 128kHz. It is evident from the graphs that the tests conducted at 32kHz exhibit a clearer signal. Using higher frequencies, such as 64kHz and 128kHz, results in the generation of additional modes of propagation, which brings added complexity to the interpretation of the signals. For the sake of clarity, the performance of the samples will be determined from measurements at f=32kHz.

a)   b)
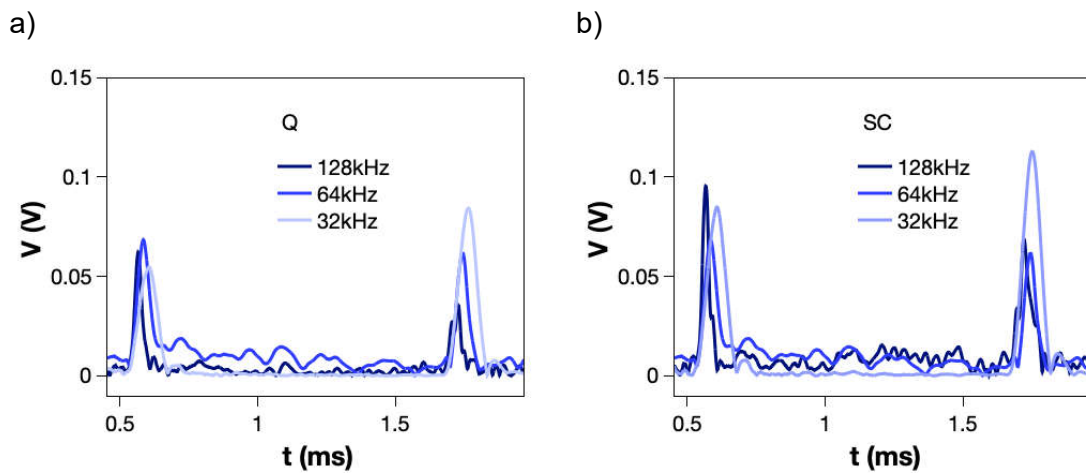
Figure 6.1 – Guided wave signal of 650°C annealed samples, measured using different frequencies.

Figure 6.2 depicts the detected signals of the Q and SC samples. Two peaks are visible, which correspond to the reflections from each edge of the pipe. Both in Q and SC samples, the samples that exhibit the largest amplitudes are the ones annealed between 450ºC and 650ºC. Annealing at $T_a \geq 750$ºC results in a significant drop in the signal mode generation and detection. The difference in intensities between each peak relates to placement mismatches between the strip and the coil, which results in different signal amplitudes to each side of the strip.

a)

b)
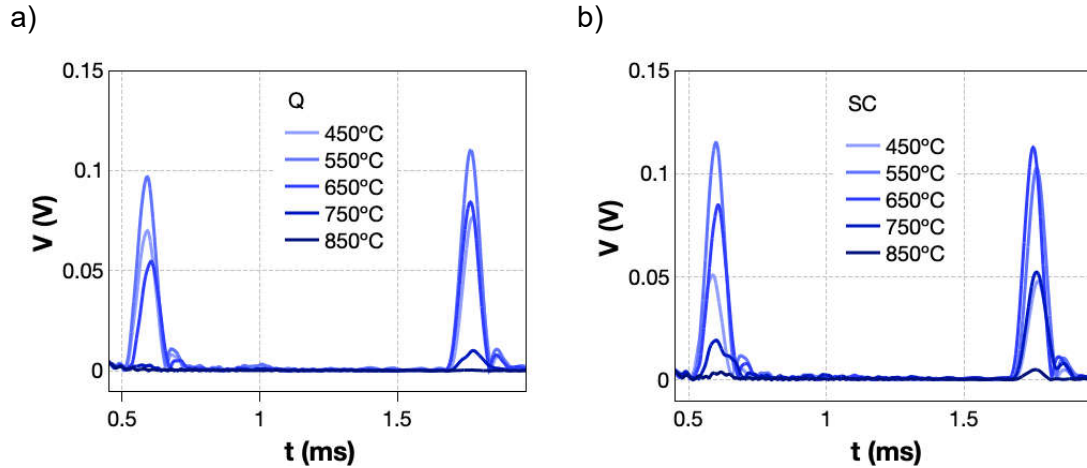
Figure 6.2 – Ultrasonic guided wave testing of a) Q and b) SC samples, annealed at different temperatures, obtained at f=32kHz.

The maximum amplitudes of the reflected signals were determined from Figure 6.2 and are plotted in Figure 6.3. For reference, the maximum amplitude of the original Hiperco 50 sample and of the SwRI are plotted. Both were tested under the same conditions. The samples annealed at T_a<750°C were greatly improved from the original performance, surpassing that of the best performing Fe-Co alloy (SwRI). Samples that are annealed at 850°C exhibit V_{pk}=0.00375V, similar to the Hiperco 50 sample, which yields 0.00035V. The largest values are obtained for annealing temperatures between 550°C and 650°C. Additional samples were prepared to investigate the 550°C<T_a<650°C range. The best performing strip is obtained after annealing at 640°C and slow cooling, resulting in V_{pk}=0.125V, which is 357x larger than the signal obtained from the original sample.
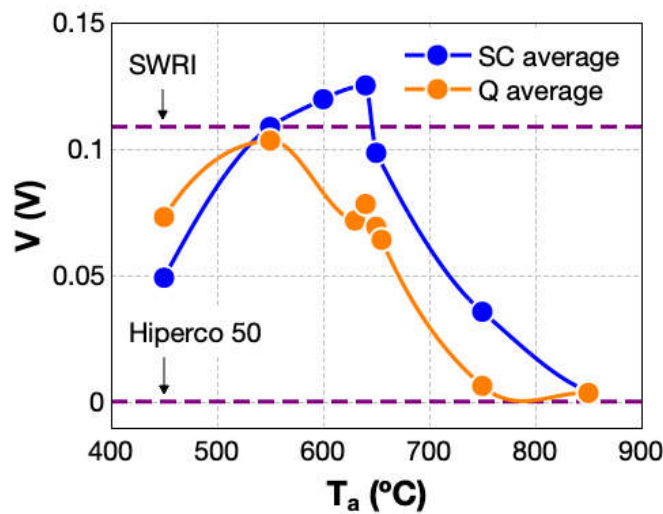
Figure 6.3 – Peak voltage of the reflected signals in ultrasonic guided wave testing.

The samples annealed at $T_a \geq 750ºC$ exhibit the worst performance as magnetostrictive transducers, even though λ was improved compared to the samples annealed at $T_a=650ºC$.

The fact that this set-up utilizes the remanence as permanent field, entirely influences the performance of the strips. The remanence provides the necessary permanent magnetic field to the generation of torsional wave mode in the pipe. As M_r decreases substantially with increasing annealing temperature, it explains the drop in signal amplitude observed when $T_a>650°C$ (Figure 3.33 a). Moreover, small coercivity is also required for optimum wave generation, which explains the smaller amplitude obtained after annealing at 450°C compared to 650ºC.

These successful results have led to the adoption of this solution in the industrial context by EQS.

6.1.2   On the Giant Magnetostrictive MAEs

6.1.2.1   MAEs with spherical particles

The prepared isotropic MAE samples were tested with the guided wave UT set-up. The tests were carried out using a pulse-echo configuration and the detected signals of the higher concentration MAEs are plotted in Figure 6.4 (VF=9.2vol% to 23.3vol%). No distinguishable reflection peaks related to the bulk mode propagation were observed with any of the MAEs. The samples are sensitive to the external magnetic field, since the signal exhibits the generation of many propagation modes. However, the reading is compromised by the hindering of the bulk wave propagation mode, and proper interpretation of the signal is not possible. This could be a direct consequence of the low remanence and susceptibility, since the amplitude of the signal is directly related to the amplitude of deformation caused by the remanence and the oscillating magnetic field. Additionally, the attenuating properties of the elastomer also play a detrimental role in the transmission of the acoustic waves. The use of different frequencies and amplitudes did not alter the results, so they are not presented.
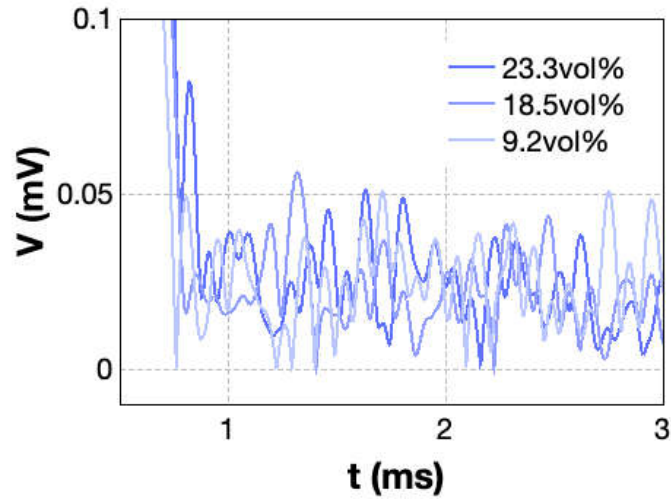
Figure 6.4 – Ultrasonic guided wave testing of the MAEs with spherical particles at f=32kHz.

6.1.2.2   MAEs with helicoidal particles

The isotropic MAEs prepared with helicoidal particles were tested using the UT guided wave set-up. MAEs with VF<9.2vol% did not result in coherent signals with clear reflection peaks, so their signals were omitted. Like in the previous case with spherical particles, the low magnetic remanence and the large attenuating power of the matrix are linked to the ineffective mode transmission and detection. The particle concentrations that yielded a discernible bulk mode signal were VF=9.2vol% and VF=18.5vol% and their signals are plotted in Figure 6.5.
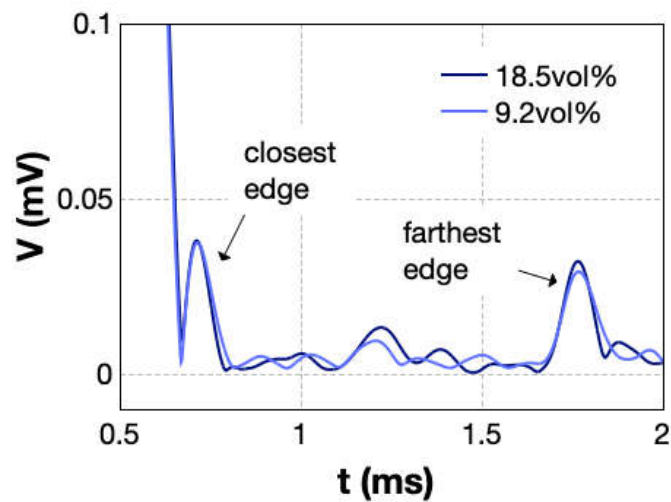
Figure 6.5 – Ultrasonic guided wave testing of the MAEs with helicoidal particles of VF=9.2vol% and 18.5vol% at f=32kHz.

The graph exhibits a reflection related to each edge of the pipe, as indicated. The samples, despite the different concentrations, exhibit a similar signal. The peak voltage related to the reflection on the closest edge is 0.038mV (both VF MAEs), and of the farthest edge is 0.029mV (VF=9.2vol%) and 0.032mV (VF=18.5vol%). Despite the very small amplitude, the signal is relatively clear from contaminating modes. We suggest that the improvement of the magnetostriction by using MAEs with helicoidal particles instead of spherical particles has to do with the larger $(dM/dH)_{H=0}$ that these MAEs exhibit, approximately 2 times larger than the ones with spherical particles. Moreover, the elastic modulus of the MAEs with spherical particles is smaller than that obtained with helicoidal particles, which indicates that less energy is required to deform them.

The peak voltage is, however, small compared to that obtained with the FeCo-2V strip, which we attribute to the complex mechanical properties of the PDMS under dynamical loads [194], [195]. Even so, PDMS is a viscoelastic material, meaning that it exhibits a phase lag in the strain as a response to a stress. This property is generally described by the storage and loss modulus and justifies the vibration attenuation that PDMS causes as well as potential generation of different modes.

In order to decrease this attenuation, and since increasing the concentration of helicoidal particles is to be avoided due to the loss of elasticity, an alternative solution was explored, consisting of the addition on carbon nanotubes.

6.1.2.3   Helicoidal particles w/ Carbon nanotubes

The use of carbon nanotubes (CNTs) has been shown to increase the hardness of materials [150]. In this approach, CNTs were added during the formulation of the MAE with FM particle VF=9.2vol%. In one case, they were mixed together with the helicoidal particles. The other case consisted of coating the top part of the MAE (after de-airing) with a layer of CNTs using a sieve to homogenize their distribution and reduce the presence of CNT clusters. The integration of CNTs did not compromise the conformability of the MAE.

These alternative samples were tested using the same set-up. In the case of the mixed CNTs (mCNT), the two surface sides are similar so only one was tested. As for the sample topped with CNTs, it was tested both with the CNTs facing the pipe (tCNT in) and opposite to the surface of the pipe (tCNT out). The detected signals of each sample are plotted in Figure 6.6, along with the signal of the 9.2vol% sample without CNTs for reference.
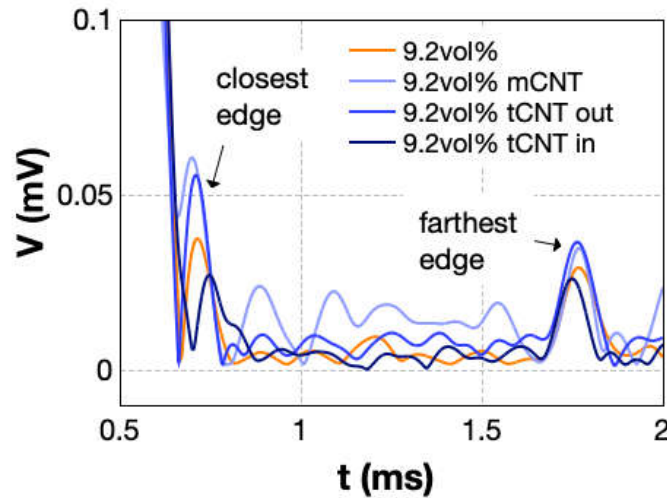
Figure 6.6 – Ultrasonic guided wave testing of the MAEs with helicoidal particles and CNTs at f=32kHz.

The signal in orange is related to the sample without CNTs and represents the baseline to understand the influence of the addition of the carbon-based particles. All the samples yielded the reflections corresponding to the edges of the pipe. The sample with mixed CNTs excited further modes hence why the time range between the peaks is filled with larger oscillations compared to the other samples.

Of the three samples with CNTs, the "tCNT in" sample yields the lowest signal, achieving 70.7% and 88.7% of the voltage peak corresponding to the closest and farthest edge, respectively, compared to the original sample without CNTs. Both the "mCNT" and "tCNT out" samples exhibit an improvement compared to the sample without CNTs, respectively of 19% and 25%.

λ was measured as a function of the H for each sample, and the results are plotted in Figure 6.7. Contrary to the UT test, the sample with the largest deformation is the one without CNTs. This difference suggests that the change in performance in UT is a consequence of improved dynamic response in signal transmissibility.
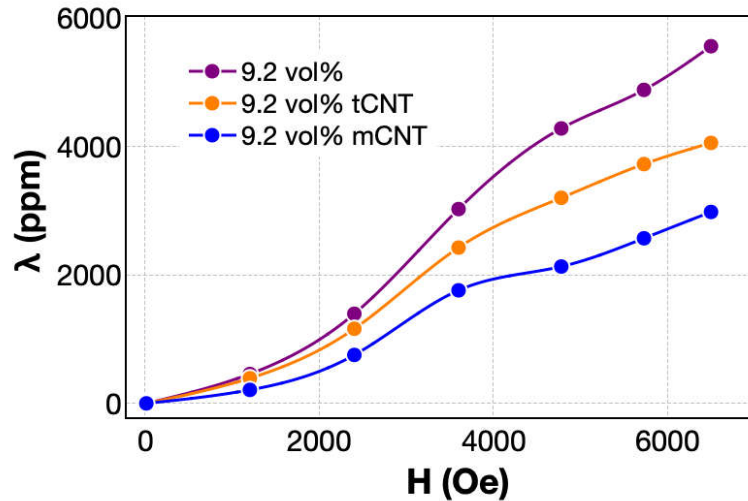
Figure 6.7 – λ as a function of the H of isotropic MAEs with VF=9.2vol% with and without CNTs.

We suggest that the reason for the different behaviors between mixed and topped CNTs is that the presence of CNTs in the MAE generate new interface points, which influence the dynamic mechanical response of the MAE as a whole. When the CNTs are blended in the elastomer, the random distribution of the particles leads to the generation of new modes as a response to the dynamic magnetic field, hence the increased amplitude of the signal between the edge reflection peaks in the mCNT sample. On the other hand, by forming a homogeneous top layer of CNTs, the response is amplified because there is one single interface, composed of a material with less amplitude attenuating properties.

Even though some signal improvement was possible by using helicoidal particles and by adding CNTs, the results are still far from those obtained by annealing the FeCo-2V strip, which can be up to one order of magnitude larger.

6.2 Ultrasonic bulk wave testing

Bulk wave UT is a measuring method that requires smaller transducers, compared to the GW set-up. The samples need to be approximately 2cm in diameter, which is ideal for small samples prepared by magnetron sputtering.

The samples that were tested in this configuration include the thin films of different thickness. These were deposited as described in 2.1.1.1, in order to obtain an all-in-one transducer. The results of the fabricated are presented in this section.
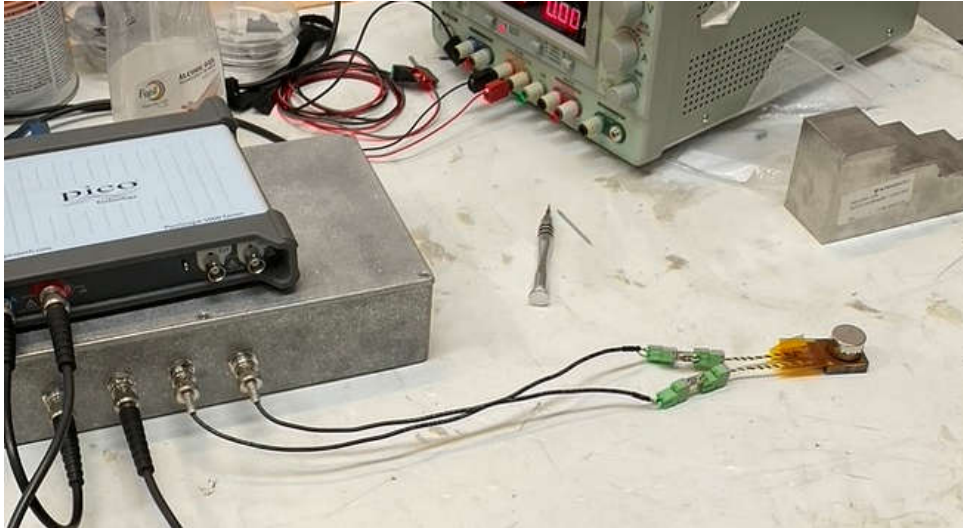
Figure 6.8 – Picture of the set-up configuration and of the magnetostrictive transducer.

Given the shortcomings of this solution, which will be described in the following sections, an alternative material was devised, using the knowledge gathered from this study. Its preparation is detailed, along with the unveiling of a very promising magnetostrictive performance.

6.2.1 Thin films

The thin films produced at INMA by magnetron sputtering were tested using the ultrasonic bulk wave testing set-up. The test was carried out in a pitch-catch configuration, such that the detection coil is placed on top of the emission coil, which is closer to the transducer (as illustrated in Figure 5.14). The test was performed at a range of frequencies between 3MHz and 5MHz. Figure 6.9 exhibits the measurement of the calibration blocks using no transducer. The test performed without the transducer operates like an EMAT (1.3.2), such that the acoustic waves are generated directly on the calibration block. This happens because steel is a ferromagnet, and it also exhibits magnetostriction. The difference in the signals at each frequency is thought to be related to internal electronic resonance in the CPU of the set-up. The voltage peaks become increasingly smaller for incremental reflections due to the loss of energy in each reflection and due to the natural attenuation of the material. The use of other frequencies in the range 3-5MHz yielded smaller amplitudes, so they are not presented and will not be discussed further.
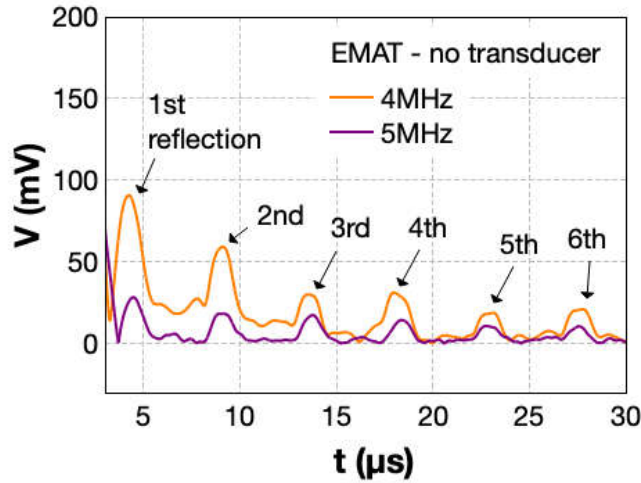
Figure 6.9 – Detected signal after processing of the calibration block, without using a transducer and using signal frequencies 4MHz and 5MHz.

Figure 6.10 exhibits the detected signal after processing at f=5MHz (a) and f=4MHz (b) of the devices with transducer thickness of 400nm and 850nm, as well as the calibration block without a transducer.

a)

b)
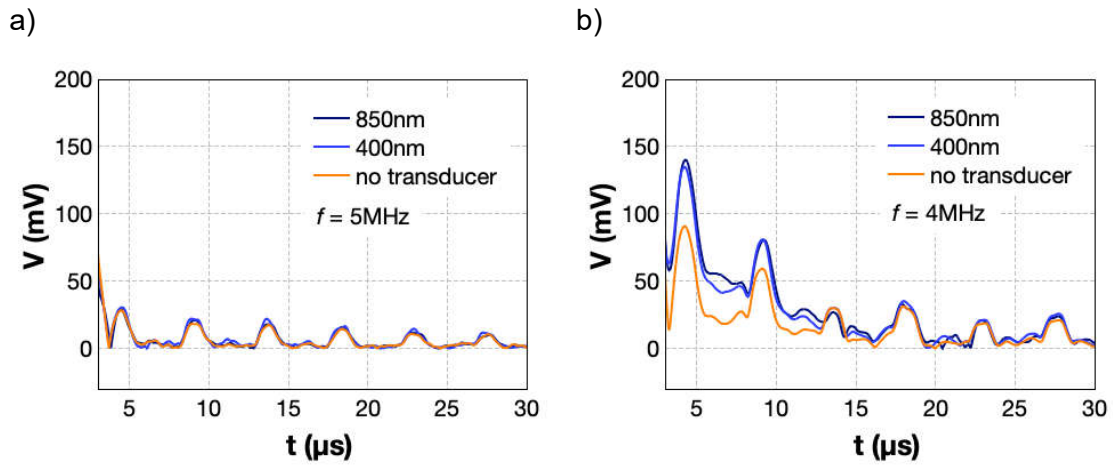
Figure 6.10 – Detected signal after processing of the calibration block, without using a transducer and using signal frequencies 4MHz and 5MHz.

Using a frequency of 5MHz yields no significant difference in the signals. The 1st reflection, at t≈4.45μs, peaks at ~30mV, either using a transducer or not. On the other hand, using f=4MHz, a difference is noticeable between the EMAT (no transducer) and the use of a transducer. When using EMAT, the 1st reflection peaks at 91mV. In the case of using a transducer, the signal is improved by more that 50%, with a thickness of either 400nm or 850nm. In the case of the thickest transducer, the 1st reflection yields V_{pk}=140mV, and the transducer with 400nm yields V_{pk}=135mV. The small difference in

the signals of the two transducers suggests one of two options. One is that the thickness variation is insufficient to generate more deformation amplitude. And the second is that the increase in thickness increases the amplitude but the layered structure of the 850nm-thick film causes an attenuation of the magnetostriction.

The use of films with thickness ≥400nm was successful in improving the sensitivity of the set-up, however the increase was not so significant that would justify the industrial investment of preparing transducers by sputter deposition.

6.2.2   Industrial alternative: High-concentration PVA coating

Within the conventional UT using bulk waves thin film were tested. The results were analyzed and described in the previous section. Despite the promising features of the thin film transducer, its application in the ultrasonic frequency did not bring an outstanding performance and does not represent a beneficial industrial investment. Nevertheless, the conclusions from the study provided relevant information that can be used in the design of alternative transducers. Some of the required properties include:

- Transducers with thickness in the range of 1 to 10 μm,
- Low attenuation materials,
- High concentration in the case of a composite.

Using this set of conditions, an exploratory approach was undertaken based on the composite knowledge obtained from the MAEs. A solution-based polymer was considered, PVA instead of PDMS, with smaller attenuating power. The preparation of the solution consisted of the dissolution of PVA pellets in water as described in 2.1.3.2, enabling its use as a liquid, which allows for the fabrication of higher concentration composites. This is true because the available liquid allows for the dispersion and homogenization of the composite, but it is then removed in the curing step. PDMS, on the other hand, consists of a hardening of the liquid parts, such that the concentration of the powder is limited by the dispersion in the liquid elastomer.

PVA offers several advantages such as being water-based, having a temperature of degradation of approximately 300°C, and having a lower attenuation power compared to PDMS [196]. Additionally, the formulation of the PVA based composites is simple, as well as the application and the curing process, which can be carried out at room temperature.

Firstly, the concentration and PVA solution were considered as calibration parameters and three samples were prepared as described in Table 6.1. The calibration samples consisted of two different concentrations, and the use of PVA solutions with and without acid. Figure 6.11 exhibits the steel substrates where the films were applied on (a), the formulation of the PVA powder paste (b) and the cured calibration samples (c).

Table 6.1 – Concentrations of the composite samples prepared with PVA

Sample	PVA aqueous solution	Annealed spherical particles (VF)
n1	PVA w/ acid	93.6vol%
n2	PVA w/ acid	88.0vol%
n3	PVA w/o acid	93.6vol%
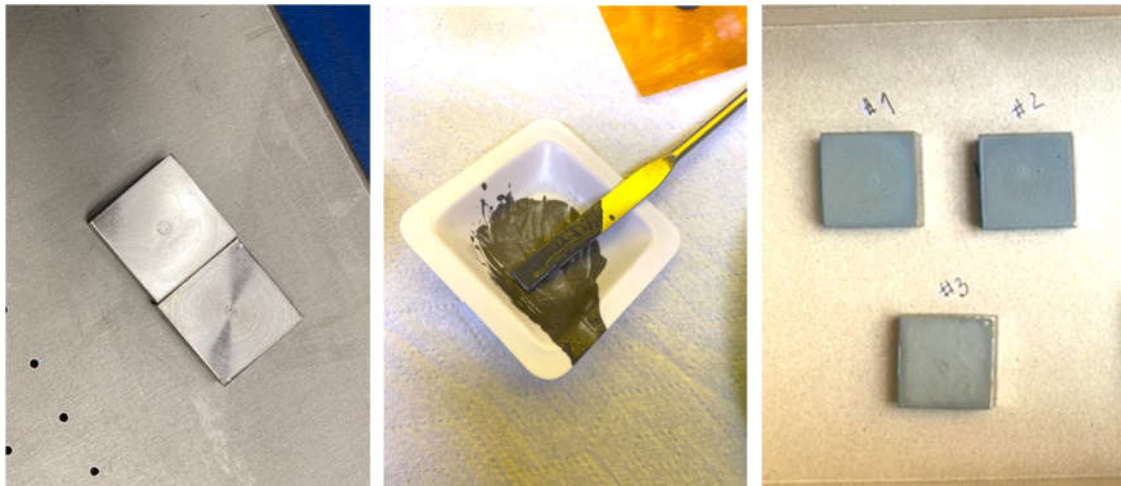
Figure 6.11 – Preparation of the high-concentration magnetostrictive coating: a) the calibration blocks on top of which the coating is applied, b) the paste that is a mixture of the PVA solution and of the ferromagnetic powder and c) the coatings cured at room temperature.

The prepared samples were then tested in the context of UT using bulk waves with a frequency of 5MHz. The measured signals of each sample are plotted in Figure 6.12. The signals consist of two peaks in the range up to t=11μs, which correspond to the first and second reflections of the acoustic wave on the bottom surface of the calibration block. The amplitude reduction between the 1st and the 2nd is explained by energy loss of the wave due to transmission and attenuation by the medium.
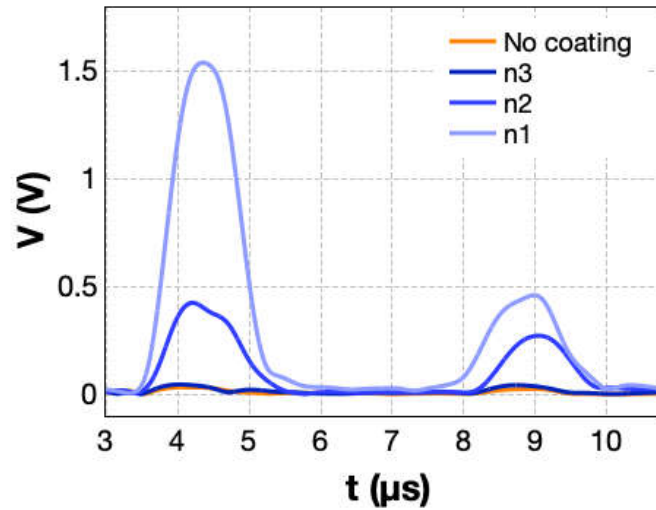
Figure 6.12 – Detected signal of the calibration coatings at f=32kHz.

The analysis of this test with different calibration parameters is described in the following sections.

6.2.2.1 Particle concentration

Regarding the particle concentration, using a VF=93.6vol% yielded the best results. Using VF=88.0vol%, the peak voltage was 0.42V, but it can be as high as 1.54V with VF=93.6vol%. This result is 45 times larger than the signal without the magnetostrictive coating. Even with a lower concentration of polymer, the magnetostrictive coating maintains its adhesion to the substrate and cohesiveness. The samples can withstand a UT test, which is mechanically demanding on the surface of the test block, without disintegrating. A few scratch marks are visible after each test, but the coating showed reproducibility in the results even after several cycles.
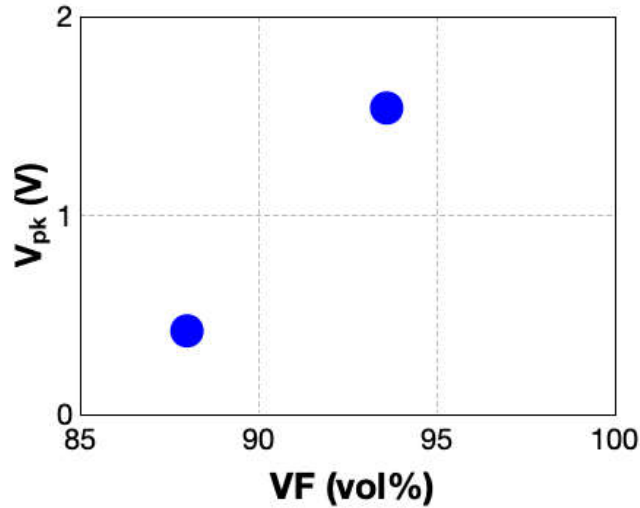
Figure 6.13 – Peak voltage of the first reflection of the high-concentration PVA coating of different concentrations.

6.2.2.2   PVA preparation

The use of phosphoric acid in the formulation of PVA increases the polymer's elasticity and flexibility. However, the acid reacts with the particles upon contact. This reaction is visible due to the formation of bubbles in the paste. The influence of the acid was investigated by preparing samples with distinct PVA solutions: one with acid, and the other without. Figure 6.14 depicts the obtained results.
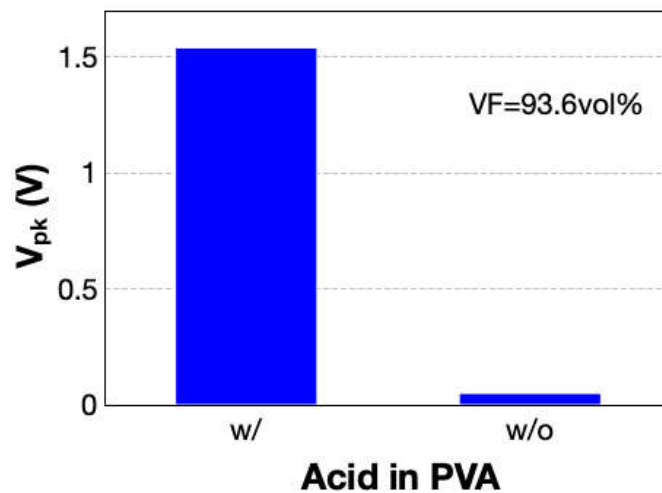
Figure 6.14 – Peak voltage of the first reflection of the high-concentration PVA coating with different PVA formulations.

The use of acid in the formulation of the PVA solution increases the peak voltage from 0.05V to 1.54V, which is 30 times larger than without acid! This can be a consequence

of the improvement in the elasticity and conformability of the PVA. Besides enabling oscillations with more, the elasticity of the PVA also ensures that those vibrations are reversible and that they do not cause permanent deformations of the matrix.

6.2.2.3 Application method

Finally, different methods of preparation of the magnetostrictive coating were investigated. The options included spatula coating, spin coating, and application with a brush. The methods were applied independently or in pairs. The samples produced with different processes are depicted in Figure 6.15. All the samples used a concentration of 93.6vol% and using PVA with acid. The first two samples are only composed of one layer of composite, while the others are composed of two.
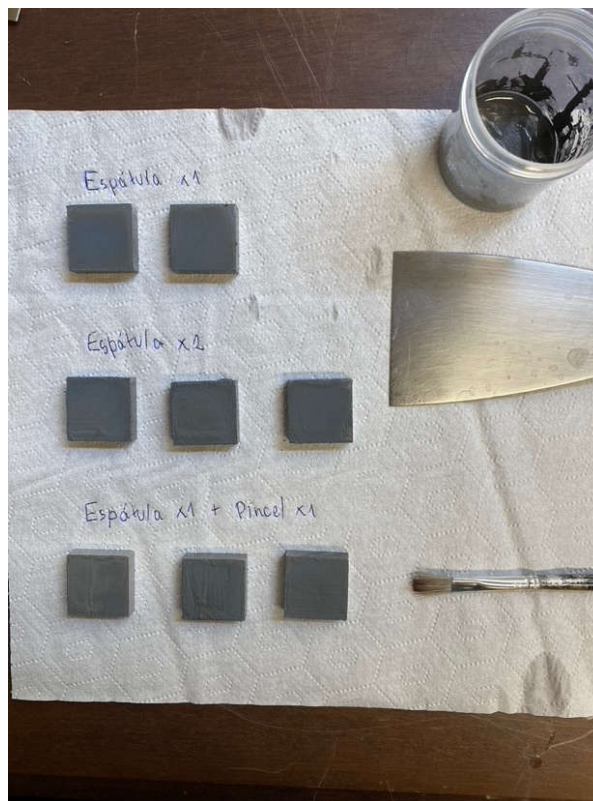
Figure 6.15 – Picture of samples produced with different methods.

The results from the tests are plotted in Figure 6.16, showing the detected signal with each sample in a) and the peak voltage of the 1st reflection in b). The worst performing sample was the one produced with one coating applied with a spatula and the second coating with a brush, taking a peak voltage of 0.03V. The best performance was by the sample prepared with spin and spatula coating, peaking at 2.6V.

a)

b)
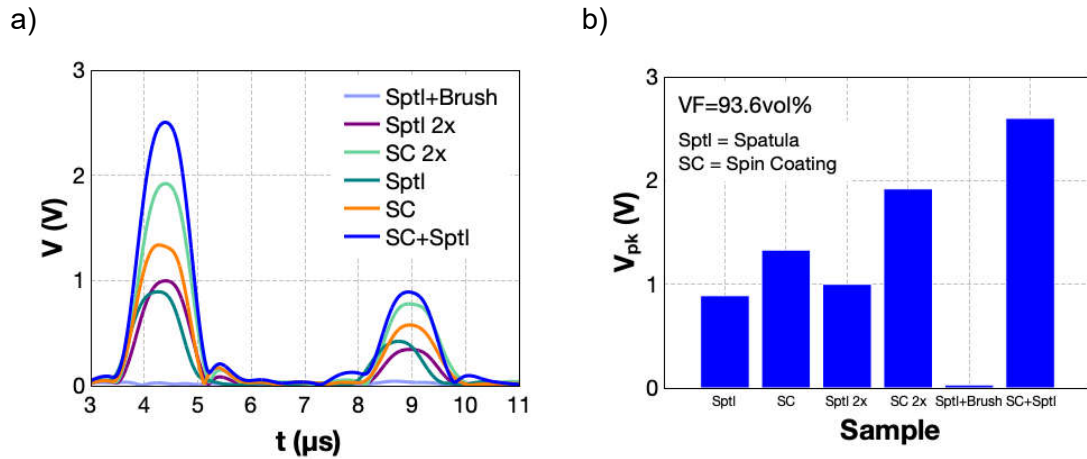
Figure 6.16 – a) Detected signal of the samples produced with different methods, b) summary of the peak voltages of the first reflection of each sample.

From this data, we can conclude that the wave transmission and detection is dependent on the application method of the transducer. The reason for that in that the application methods influence the thickness and the roughness (using a brush yields the largest roughness) of the coating. It was clear that increased roughness was not beneficial for the enhancement of the signal, given that the performance was hindered by the generation of other modes, and the amplitude was not significant.

6.3   Conclusions

In this chapter we have shown that it was possible to successfully apply magnetostrictive materials to UT applications.

Regarding the guided wave configuration, the best performance was achieved at intermediate annealing temperatures. In particular, the best sample was the one annealed at 640°C and slow cooled. We have proposed that the good performance at this temperature is linked with a balance between the remanence and the drop in the coercivity. We were able to achieve a peak voltage of 0.125V, which is 357x larger than that of the original strip, and it represents and improvement of 15% over the only competitor in the market.

Still regarding the GW UT, the MAEs prepared with spherical particles had disappointing results, despite exhibiting giant magnetostriction. Since these composites generated many propagation modes, coupled with the signal attenuation by the matrix, proper interpretation of the results was not feasible. The helicoidal particle-MAEs had similar results, with the exception of VF=9.2vol% and 18.5vol%, which provided a significantly

clearer signal. Still the obtained peak voltage is very small (0.038mV for VF=18.5vol%), because of the low M_r and of the large attenuating power of the matrix. The use of CNTs in the 9.2vol% MAE was explored in an effort to reduce the attenuation, and it was shown that the signal was improved by 25% when the CNTs were applied as a coating at the surface facing the pipe.

Regarding the BW configuration, the use of thin films as transducers was able to improve the signal by 50%. The difference in performance between 400nm and 850nm was not significant, which can be a consequence of the layered structure of the thickest films. But could also be related with the fact that the thickness difference is not enough to cause significant deformation amplification.

An alternative approach to BW transducers was investigated. A high-concentration PVA coating, which consisted of spherical FeCo-2V particles embedded in a PVA matrix with VF>80%. The composition of the coating was tested for two different concentrations and two different PVA formulations (with and without phosphoric acid). The highest concentration has been shown to yield the largest signal, rising from V_{pk}=0.42V (88.0%) to V_{pk}=1.54V (93.6vol%). As for the PVA formulation, the best performance is obtained using the acid in the formulation, because it leads to the improvement of the elasticity of the matrix. Moreover, different application methods were also investigated, as they result in different thickness and roughness. The method that yielded the best result was spin coating followed by spatula coating, achieving a peak voltage of 2.3V, which is 65x greater than that of the EMAT configuration.

The presented solutions yielded very satisfactory results. Currently, EQS Global is applying the annealed strip as a transducer in GW UT devices internationally. Regarding the BW UT, the latest development involving the high concentration magnetostrictive coating has also gained their interest, which resulted in the preparation of a patent, which will be filed in 2023.

Conclusions and Future Perspectives

In this chapter, the main highlights and conclusions from this thesis will be addressed. In the first section, we will focus on the results and achievements regarding the Fe-Co-based magnetostrictive transducers. In the second section, a reflection on the possible next steps regarding the addressed topics will be presented. Finally, we will provide an outlook on the future role of magnetostrictive sensors and ultrasound testing in the world.

6.4 Main conclusions

The three approaches proposed in the beginning of this document have been extensively reported and have resulted in the implementation of the developed materials as transducers in GW and BW UT applications. The understanding of the materials' properties has been critical to the interpretation of their performance and improvement as magnetostrictive transducers.

Starting with the 3D approach, we have seen the improvement of the magnetostriction in the alloy by eliminating the hysteresis in the longitudinal direction. This was done by subjecting the FeCo-2V strip to thermal treatments. Moreover, we were able to correlate λ with other physical properties of the material which depend on the annealing temperature T_a, namely:

- At $T_a < 650°C$: the internal stress of the alloy leads to enhanced magnetostriction via the magnetoelastic coupling.
- At $T_a > 650°C$: the formation of fcc precipitates results in increased magnetostriction due to their coupling to the bcc lattice as fcc tetragonal nanoinclusions.

The highest λ_s was obtained with the sample annealed at 450°C and quenched, yielding $\lambda_s = 75$ppm. Generally, Q samples exhibited larger λ than the SC ones, which was related to the presence of a higher density of precipitates, caused by a longer exposure to a high temperature.

When tested as transducers in the GW UT set-up, the annealed strips of FeCo-2V were able to improve the signal with respect to the original FeCo-2V strip. The best performance was obtained with samples annealed between 550ºC and 650ºC. These results differ from the λ measurements, which revealed that T_a=550ºC and 650ºC yielded the lowest magneto-deformation. This difference is justified by the different magnetic properties that the alloy develops at each annealing temperature. The remanence and coercivity values obtained between 550ºC and 650ºC are optimal for the generation of guided waves using the current configuration of the set-up. The best performing transducer was able to increase the peak voltage by 357x with respect to the original strip with no treatment. This was obtained with the sample prepared at 640ºC and slow cooled, which yielded V_{pk}=0.125V. Additionally, this result overcame the performance of the current competitor's strip.

Regarding the MAEs, every composition exhibited giant magnetostriction. This was true for MAEs with spherical and helicoidal particles. The largest λ_s was obtained with the isotropic 9.2vol% spherical particle MAE, which showed a magneto-induced strain of 6649ppm when H=6500Oe. We reported on the influence of the particle size and shape on the λ-H profile and showed that the use of helicoidal particles results in a linear relationship with H and that the use of spherical particles yields a characteristic non-linear behavior. We also observed that further increasing the concentration of particles results in the stabilization and drop of λ, which occurs because the deformation of the material becomes energetically more demanding. Regarding magnetostriction, the MAEs largely surpassed the magnetic field-induced deformation of the FeCo-2V strips, in some cases by 2 orders of magnitude.

However, the magnetostriction performance was reversed when these materials were tested in the GW UT set-ups. The MAEs rendered disappointing results, indicating a poor performance under dynamic magnetic fields. We have attributed this to the low remanence and susceptibility of the MAEs, as well as to the damping power of the matrix. The only MAEs yielding discernible signal were the ones produced with helicoidal particles in the concentrations 9.2vol% (V_{pk}=0.029V) and 18.5vol% (V_{pk}=0.032V). But these results were still unsatisfactory when compared with the annealed strip.

Regarding the BW UT set-up measurements, we have shown that the use of a device with magnetostrictive thin films with thickness 400nm and 850nm can improve the signal by 50%, yielding V_{pk}=0.14V. One possible way to further improve the performance with the use of thin films would be to increase their thickness. To do so, different deposition methods would have to be used. Alternatively, the use of a high-concentration

magnetostrictive coating as a transducer in the BW UT set-up results in a signal increase of 65-fold over the EMAT alternative, i.e. V_{pk}=2.30V. The improvement is enabled by using a thicker magnetostrictive layer composed of FM particles which are attached to the surface of the test subject with an elastic PVA matrix.

The implementation of the transducers in the UT set-ups was successful and has led to the following achievements:

- The integration of the annealed FeCo-2V strip in the streamline of EQS Global. This means that the 640SC strip is already being used as a transducer in a real environment.

- The preparation of a patent application, which will cover the sensor configuration and the high concentration magnetostrictive coating.

- Development of a magnetostriction measurement setup system to be used at ambient conditions, complemented by a LabVIEW program.

- The publication as first author of one article regarding the giant magnetostriction in low concentration MAEs, in the high impact factor journal Composites Part B: Engineering, with the title "Giant magnetostriction in low concentration magnetorheological elastomers".

- The preparation of 3 scientific papers for publication in international scientific journals involving the study of
    - the property evolution and correlation to λ in annealed FeCo-2V strips,
    - the properties of thin films of varying thickness and substrate and their use as magnetostrictive transducers and
    - the comparison between spherical and helicoidal particles in the magneto-induced deformation of an MRE.

- Numerous communications in national and international conferences and 2 awards for best communication.

6.5   Future perspectives

Despite the successful outputs of this thesis, additional data could provide more fruitful conclusions and lead to improved results. In this section, suggestions on the possible future work are provided.

6.5.1   FeCo-2V strips (Hiperco 50)

- Tailor the nanoinclusion precipitation dynamics and optimize for improved λ.

- Determination of the internal stress of the strip after annealing: this could provide greater insight on the influence of the stress on the magnetoelastic properties.

- Composition of the strip along its thickness: this information can be obtained by performing XPS and could be relevant in understanding the segregation of Fe to the surface and how the alloy forms new stoichiometric phases.

- Measurement of magnetic hyperfine splitting using Mossbauer spectroscopy: to understand the distribution of the Fe atoms in the lattice and their contribution to the magnetic process.

- Synchrotron X-ray diffraction or Electron backscattered diffraction or other texture determination technique, to understand the evolution of the recrystallization with the annealing temperature.

6.5.2   Magnetoactive elastomers

- Compressive mechanical tests: to determine the storage and loss moduli, which are key parameters to understanding the attenuation power of the material.

- Dynamic mechanical tests: both tensile and compressive, to investigate the mechanical behavior of the MAEs under dynamic loads, which closely simulated the effect under an oscillating magnetic field.

- Further studies using CNTs or other carbon-based materials such as graphene: the preliminary tests that were carried out using CNTs were promising. A more comprehensive study could yield improved results.

- Embed hard ferromagnets in the matrix: this approach could result in increased remanence and improve the performance of MAEs in the present GW set-up.

6.5.3   Thin films

- Use alternative deposition methods: faster deposition methods should be explored like electrodeposition, which would enable the preparation of thicker films in one single layer.

- Magnetic anisotropy measurements: measure magnetization as a function of magnetic field for different in-plane angles, which could provide more information on the magnetocrystalline anisotropy of the films.

- Measure the effective paramagnetic moment above T_c, to determine the overall magnetic moment of the samples, and understand the underlying effect that occurs in films with different thickness.
- Neutron diffraction, to determine the magnetic profile of the samples along the thickness of the film.
- λ measurements in thin films: although it was not a focus point on this work due to the complexity of the sample preparation and set-up implementation, we reckon that it could provide relevant information of the films.
- Explore different compositions: the binary Fe_xCo_{1-x} system has been shown to have improved λ at x=0.56 and x=0.27 [113].
- Use of other magnetostrictive materials such Terfenol-D or Galfenol since flexibility can be slightly overlooked in the BW UT configuration.

6.5.4 High-concentration PVA coating

- Standardize the application process, since it is currently unreliable in the sense that the output is slightly different every time the same procedure is used.
- Increase the abrasion resistance of the coating: as it is, the coating is very sensitive to mechanical stress and to water, which makes it very fragile and unsuitable for applications in heavy duty and humid environments.

6.5.5 MsS and UT

The field of NDT is becoming more relevant, especially as concerns for health and safety are becoming more mainstream. This calls for more efficient monitoring tools, not only in the oil and gas industry but for infrastructures in general.

MsS can be an alternative to current piezoelectric and EMAT solutions, which cannot have widespread application due to their inherent limitations. Efforts are in place to develop efficient MsS, and this thesis was a step forward in that direction. It is our understanding that MsS are not a question of *If?*, but *When?*.

And in fact, the time is now.

The FeCo-2V annealed strips have been successfully implemented in the streamline of EQS Global and are currently in use over hundreds of meters of pipes across Portugal and abroad. Moreover, EQS Global is dedicated to integrating the innovative BW UT as

a commercial product and a patent is currently being filed to protect the intellectual property generated through the collaboration between IFIMUP, EQS and CMEMS.

Moreover, with this thesis, IFIMUP is now equipped with knowledge on how to prepare high output magnetostrictive FeCo-based alloys and composites. Detailed set-ups were devised for the measurement of magnetostriction (for deformations in the nano and microscale), which are now available to any future work regarding magneto-induced deformation. Additionally, relationships with other research groups and companies were established or revived, which paves the way for new collaborations.

References

[1]   Concawe, "Performance of European cross-country oil pipelines. Statistical summary of reported spillages in 2019 and since 1971."

[2]   European Gas Pipeline Incident Data Group (EGIG), "11th Report of the European Gas Pipeline Incident Data Group (period 1970 – 2019)," European Gas Pipeline Incident Data Group (EGIG), 2020.

[3]   PHMSA, "10 Year Incident Summary Reports," PHMSA.

[4]   PHMSA, "Yearly Incident Summary Reports," PHMSA.

[5]   "Global Energy Monitor," *Global Energy Monitor*, 25-Nov-2020. [Online]. Available: https://globalenergymonitor.org/. [Accessed: 04-Dec-2022].

[6]   J. G. Ramírez-Camacho, F. Carbone, E. Pastor, R. Bubbico, and J. Casal, "Assessing the consequences of pipeline accidents to support land-use planning," *Saf. Sci.*, vol. 97, pp. 34–42, Aug. 2017.

[7]   Y. Guo, X. Meng, T. Meng, D. Wang, and S. Liu, "A novel method of risk assessment based on cloud inference for natural gas pipelines," *Journal of Natural Gas Science and Engineering*, vol. 30, pp. 421–429, Mar. 2016.

[8]   J. Kim, D. Ryu, and B. K. Sovacool, "Critically assessing and projecting the frequency, severity, and cost of major energy accidents," *The Extractive Industries and Society*, vol. 8, no. 2, p. 100885, Jun. 2021.

[9]   "Annual Report Mileage for Hazardous Liquid or Carbon Dioxide Systems." [Online]. Available: https://www.phmsa.dot.gov/data-and-statistics/pipeline/annual-report-mileage-hazardous-liquid-or-carbon-dioxide-systems. [Accessed: 05-Dec-2022].

[10]   "PCI transparency platform," 09-Apr-2013. [Online]. Available: https://ec.europa.eu/energy/infrastructure/transparency_platform/map-viewer/main.html. [Accessed: 02-Jan-2023].

[11]   C. I. Ossai, B. Boswell, and I. J. Davies, "Pipeline failures in corrosive environments – A conceptual analysis of trends and effects," *Eng. Fail. Anal.*, vol. 53, pp. 36–58, Jul. 2015.

[12]   US Department of Transportation, "The State of the National Pipeline Infrastructure." [Online]. Available: https://www.hsdl.org/?view&did=804318. [Accessed: 20-Apr-2022].

[13]   C. Belvederesi and M. R. Dann, "Statistical analysis of failure consequences for oil and gas pipelines," *Int. j. saf. secur. eng.*, vol. 7, no. 2, pp. 103–112, Jun. 2017.

[14]   M. Gupta, M. A. Khan, R. Butola, and R. M. Singari, "Advances in applications of Non-Destructive Testing (NDT): A review," *Adv. Technol. Mater. Mater. Process. J.* , pp. 1–22, Apr. 2021.

[15]   A. S. H. Makhlouf and M. Aliofkhazraei, Eds., *Handbook of materials failure analysis with case studies from the oil and gas industry*. Oxford, England: Butterworth-Heinemann, 2015.

[16]   R. Bickerstaff, M. Vaughn, G. Stoker, M. Hassard, and M. Garrett, "Review of Sensor Technologies for In-line Inspection of Natural Gas Pipelines," Jan. 2002.

[17]   A. A. Carvalho, J. M. A. Rebello, M. P. V. Souza, L. V. S. Sagrilo, and S. D. Soares, "Reliability of non-destructive test techniques in the inspection of pipelines used in the oil industry," *Int. J. Pressure Vessels Piping*, vol. 85, no. 11, pp. 745–751, Nov. 2008.

[18]   M. Saade and S. Mustapha, "Assessment of the structural conditions in steel pipeline under various operational conditions – A machine learning approach," *Measurement*, vol. 166, no. 108262, p. 108262, Dec. 2020.

[19]   J. Blitz and G. Simpson, *Ultrasonic Methods of Non-destructive Testing*. Springer Science & Business Media, 1995.

[20]   F. A. Firestone, "Flaw detecting device and measuring instrument," 2280226, 21-Apr-1942.

[21]   Z. Yang, S. Zhou, J. Zu, and D. Inman, "High-Performance Piezoelectric Energy Harvesters and Their Applications," *Joule*, vol. 2, no. 4, pp. 642–697, Apr. 2018.

[22]   B. Yoo, S.-M. Na, A. B. Flatau, and D. J. Pines, "Directional magnetostrictive patch transducer based on Galfenol's anisotropic magnetostriction feature," *Smart Mater. Struct.*, vol. 23, no. 9, p. 095035, Aug. 2014.

[23]   "EMAT Technology." [Online]. Available: https://www.innerspec.com/emat-technology. [Accessed: 22-Dec-2022].

[24]   Y. Y. Kim and Y. E. Kwon, "Review of magnetostrictive patch transducers and applications in ultrasonic nondestructive testing of waveguides," *Ultrasonics*, vol. 62, pp. 3–19, Sep. 2015.

[25]   J. Fuchs, "Ultrasonics – Transducers – Magnetostrictive Hardware," *Cleaning Technologies Group.* [Online]. Available: https://techblog.ctgclean.com/2012/01/ultrasonics-transducers-magnetostrictive-hardware/. [Accessed: 22-Dec-2022].

[26]   R. Chaunsali, F. Li, and J. Yang, "Stress Wave Isolation by Purely Mechanical Topological Phononic Crystals," *Sci. Rep.*, vol. 6, p. 30662, Aug. 2016.

[27]   J. P. Joule, "XVII. On the effects of magnetism upon the dimensions of iron and steel bars," *The London, Edinburgh, and Dublin Philosophical Magazine and Journal of Science*, vol. 30, no. 199, pp. 76–87, Feb. 1847.

[28]   S. Blundell, "Magnetism in Condensed Matter," *Am. J. Phys.*, vol. 71, no. 1, pp. 94–95, Jan. 2003.

[29]   A. B. Flatau, M. J. Dapino, and F. T. Calkins, "High Bandwidth Tunability in a Smart Vibration Absorber," *J. Intell. Mater. Syst. Struct.*, vol. 11, no. 12, pp. 923–929, Dec. 2000.

[30]   C. Kittel, "Physical Theory of Ferromagnetic Domains," *Rev. Mod. Phys.*, vol. 21, no. 4, pp. 541–583, Oct. 1949.

[31]   M. J. Dapino, "On Magnetostrictive Materials and Their Use in Smart Material Transducer," *Structural Engineering and Mechanics Journal*, vol. 17, no. 3, pp. 1–28, 2002.

[32]   E. W. Lee, "Magnetostriction and Magnetomechanical Effects," *Rep. Prog. Phys.*, vol. 18, no. 1, p. 184, 1955.

[33]   R. Becker and W. Döring, *Ferromagnetismus*. Springer Berlin Heidelberg, 1939.

[34]   G. Balaji, R. A. Narayanan, A. Weber, F. Mohammad, and C. S. S. R. Kumar, "Giant magnetostriction in magnetite nanoparticles," *Mater. Sci. Eng. B*, vol. 177, no. 1, pp. 14–18, Jan. 2012.

[35]   F. Narita and M. Fox, "A review on piezoelectric, magnetostrictive, and magnetoelectric materials and device technologies for energy harvesting applications," *Adv. Eng. Mater.*, vol. 20, no. 5, p. 1700743, May 2018.

[36]   G. Engdahl, *Handbook of giant magnetostrictive materials*. San Diego, CA: Academic Press, 1999.

[37]   A. E. Clark, B. F. DeSavage, and R. Bozorth, "Anomalous Thermal Expansion and Magnetostriction of Single-Crystal Dysprosium," *Phys. Rev.*, vol. 138, no. 1A, pp. A216–A224, Apr. 1965.

[38]   R. Abbundi and A. Clark, "Anomalous thermal expansion and magnetostriction of single crystal Tb0.27Dy73Fe2," *IEEE Trans. Magn.*, vol. 13, no. 5, pp. 1519–1520, Sep. 1977.

[39]   C. Gao, Z. Zeng, S. Peng, and C. Shuai, "Magnetostrictive alloys: Promising materials for biomedical applications," *Bioact Mater*, vol. 8, pp. 177–195, Feb. 2022.

[40]   J. G. Wan, J.-M. Liu, H. L. W. Chand, C. L. Choy, G. H. Wang, and C. W. Nan, "Giant magnetoelectric effect of a hybrid of magnetostrictive and piezoelectric composites," *J. Appl. Phys.*, vol. 93, no. 12, pp. 9916–9919, Jun. 2003.

[41]   H. Fujimori, H. Yoshimoto, T. Masumoto, and T. Mitera, "Anomalous eddy current loss and amorphous magnetic materials with low core loss (invited)," *J. Appl. Phys.*, vol. 52, no. 3, pp. 1893–1898, Mar. 1981.

[42]   J. Atulasimha and A. B. Flatau, "A review of magnetostrictive iron–gallium alloys," *Smart Mater. Struct.*, vol. 20, no. 4, p. 043001, Mar. 2011.

[43]   R. A. Kellogg, "Development and modeling of iron-gallium alloys."

[44]   T. V. Jayaraman, N. Srisukhumbowornchai, S. Guruswamy, and M. L. Free, "Corrosion studies of single crystals of iron–gallium alloys in aqueous environments," *Corros. Sci.*, vol. 49, no. 10, pp. 4015–4027, Oct. 2007.

[45]   S. Datta, J. Atulasimha, and A. B. Flatau, "Figures of merit of magnetostrictive single crystal iron–gallium alloys for actuator and sensor applications," *J. Magn. Magn. Mater.*, vol. 321, no. 24, pp. 4017–4031, Dec. 2009.

[46]   J. C. Slater, "The Ferromagnetism of Nickel. II. Temperature Effects," 1936.

[47]   L. Pauling, "The Nature of the Interatomic Forces in Metals," *Phys. Rev.*, vol. 54, no. 11, pp. 899–904, Dec. 1938.

[48]   C.-W. Chen, *Magnetism and Metallurgy of Soft Magnetic Materials*, vol. 15. Elsevier North-Holland, 1977.

[49]   G. W. Elmen, "Magnetic material and appliance," 1739752, 17-Dec-1929.

[50]   "mp-2090: FeCo (Cubic, Pm-3m, 221)," *Materials Project*. [Online]. Available: https://materialsproject.org/materials/mp-2090/. [Accessed: 22-Dec-2022].

[51]   R. S. Sundar and S. C. Deevi, "Soft magnetic FeCo alloys: alloy development, processing, and properties," *Int. Mater. Rev.*, vol. 50, no. 3, pp. 157–192, Jun. 2005.

[52]   R. S. Sundar and S. C. Deevi, "Effect of heat-treatment on the room temperature ductility of an ordered intermetallic Fe–Co–V alloy," *Materials Science and Engineering: A*, vol. 369, no. 1, pp. 164–169, Mar. 2004.

[53]   H. Kwun, S.-Y. Kim, J. Crane, and M.-S. Choi, "Method and apparatus generating and detecting torsional wave inspection of pipes or tubes," 20040095137:A1, 20-May-2004.

[54]   H. Kwun and K. A. Bartels, "Magnetostrictive sensor technology and its applications," *Ultrasonics*, vol. 36, no. 1, pp. 171–178, Feb. 1998.

[55]   G. Sha and C. J. Lissenden, "Modeling Magnetostrictive Transducers for Structural Health Monitoring: Ultrasonic Guided Wave Generation and Reception," *Sensors* , vol. 21, no. 23, Nov. 2021.

[56]   F. Bertoncini, G. Giunta, M. Raugi, and F. Turcu, "Overview and Experimental Evaluation of Magnetostrictive Transducers for Guided Wave Inspection," *NDT E J*, vol. 17, p. 13162, 2012.

[57]   T. Heo and S. H. Cho, "Thin-Plate-Type Embedded Ultrasonic Transducer Based on Magnetostriction for the Thickness Monitoring of the Secondary Piping System of a Nuclear Power Plant," *Nuclear Engineering and Technology*, vol. 48, no. 6, pp. 1404–1411, Dec. 2016.

[58]   P. Tse, Z. Fang, and K. Ng, "Novel design of a smart and harmonized flexible printed coil sensor to enhance the ability to detect defects in pipes," *NDT E Int.*, vol. 103, pp. 48–61, Apr. 2019.

[59]   H. Kwun and A. E. Holt, "Feasibility of under-lagging corrosion detection in steel pipe using the magnetostrictive sensor technique," *NDT E Int.*, vol. 28, no. 4, pp. 211–214, Aug. 1995.

[60]   M. J. S. Lowe and P. Cawley, "Long Range Guided Wave Inspection Usage – Current Commercial Capabilities and Research Directions," Imperial College London, Mar. 2006.

[61]   P. J. Kelly and R. D. Arnell, "Magnetron sputtering: a review of recent developments and applications," *Vacuum*, vol. 56, no. 3, pp. 159–172, Mar. 2000.

[62]   J. Horwath, Z. Turgut, and R. Fingers, "High temperature properties and aging-stress related changes of FeCo materials," Air Force Research Laboratory, Jul. 2006.

[63]   Carpenter, "Hiperco 50 Datasheet."

[64]   I. M. Watt, *The Principles and Practice of Electron Microscopy*. Cambridge University Press, 1997.

[65]   "Principles of SEM," in *Principles and Practice of Variable Pressure/Environmental Scanning Electron Microscopy (VP-ESEM)*, Chichester, UK: John Wiley & Sons, Ltd, 2008, pp. 17–62.

[66]   "Scanning electron microscope," *Wikiwand*. [Online]. Available: https://www.wikiwand.com/en/Scanning_electron_microscope. [Accessed: 22-Dec-2022].

[67]   "SEM vs TEM," *Analysis & Separations from Technology Networks*, 25-Feb-2020. [Online]. Available: https://www.technologynetworks.com/analysis/articles/sem-vs-tem-331262. [Accessed: 16-Dec-2022].

[68]   Y. Waseda, E. Matsubara, and K. Shinoda, *X-Ray Diffraction Crystallography*. Springer Berlin Heidelberg.

[69]   S. Foner, "Versatile and sensitive vibrating-sample magnetometer," *Rev. Sci. Instrum.*, vol. 30, no. 7, pp. 548–557, Jul. 1959.

[70]   D. Jiles, *Introduction to Magnetism and Magnetic Materials*. CRC Press, 2015.

[71]   D. K. Schroder, *Semiconductor Material and Device Characterization*. John Wiley & Sons, 2006.

[72]   H. Topsoe, *Geometric Factors in 4 Probe Resistivity measurement*. Bridge Technologies, 1966.

[73]   N. Saba, M. Jawaid, and M. T. H. Sultan, "1 - An overview of mechanical and physical testing of composite materials," in *Mechanical and Physical Testing of Biocomposites, Fibre-Reinforced Composites and Hybrid Composites*, M. Jawaid, M. Thariq, and N. Saba, Eds. Woodhead Publishing, 2019, pp. 1–12.

[74]   W. F. Hosford, "Tensile Testing," in *Mechanical Behavior of Materials*, Cambridge University Press, 2005, pp. 39–52.

[75]   M. Sasso, G. Palmieri, G. Chiappini, and D. Amodio, "Characterization of hyperelastic rubber-like materials by biaxial and uniaxial stretching tests based on optical methods," *Polym. Test.*, vol. 27, no. 8, pp. 995–1004, Dec. 2008.

[76]   H. Lim and S. W. Hoag, "Plasticizer effects on physical-mechanical properties of solvent cast Soluplus® films," *AAPS PharmSciTech*, vol. 14, no. 3, pp. 903–910, Sep. 2013.

[77]   N. B. Ekreem, A. G. Olabi, T. Prescott, A. Rafferty, and M. S. J. Hashmi, "An overview of magnetostriction, its use and methods to measure these properties," *J. Mater. Process. Technol.*, vol. 191, no. 1, pp. 96–101, Aug. 2007.

[78]   K. Hoffmann, *An Introduction to Measurement Using Strain Gages*. Hottinger Baldwin, 1989.

[79]   T. R. Kuphaldt, "Strain Gauges," 12-Feb-2015. [Online]. Available: https://www.allaboutcircuits.com/textbook/direct-current/chpt-9/strain-gauges/. [Accessed: 01-Mar-2023].

[80]   W. S. Rasband, "ImageJ," *U. S. National Institutes of Health, Bethesda, Maryland, USA*, 1997-2018.

[81]   M.-A. Keip and M. Rambausek, "Computational and analytical investigations of shape effects in the experimental characterization of magnetorheological elastomers," *Int. J. Solids Struct.*, vol. 121, pp. 1–20, Aug. 2017.

[82]   G. Diguet, E. Beaugnon, and J. Y. Cavaillé, "Shape effect in the magnetostriction of ferromagnetic composite," *J. Magn. Magn. Mater.*, vol. 322, no. 21, pp. 3337–3341, Nov. 2010.

[83]   V. Lefèvre, K. Danas, and O. Lopez-Pamies, "A general result for the magnetoelastic response of isotropic suspensions of iron and ferrofluid particles in rubber, with applications to spherical and cylindrical specimens," *J. Mech. Phys. Solids*, vol. 107, pp. 343–364, Oct. 2017.

[84]   L. Bodelot, J.-P. Voropaieff, and T. Pössinger, "Experimental investigation of the coupled magneto-mechanical response in magnetorheological elastomers," *Exp. Mech.*, vol. 58, no. 2, pp. 207–221, Feb. 2018.

[85]   E. Salas and R. Bustamante, "Numerical solution of some boundary value problems in nonlinear magneto-elasticity," *J. Intell. Mater. Syst. Struct.*, vol. 26, no. 2, pp. 156–171, Jan. 2015.

[86]   T. Sourmail, "Near equiatomic FeCo alloys: Constitution, mechanical and magnetic properties," *Prog. Mater Sci.*, vol. 50, no. 7, pp. 816–880, Sep. 2005.

[87]   I. Ohnuma *et al.*, "Phase equilibria in the Fe–Co binary system," *Acta Mater.*, vol. 50, no. 2, pp. 379–393, Jan. 2002.

[88]   C. W. Chen, "Metallurgy and Magnetic Properties of an Fe-Co-V Alloy," *J. Appl. Phys.*, vol. 32, no. 3, pp. S348–S355, Mar. 1961.

[89]   R. S. Sundar, S. C. Deevi, and B. V. Reddy, "High Strength FeCo–V Intermetallic Alloy: Electrical and Magnetic Properties," *J. Mater. Res.*, vol. 20, no. 6, pp. 1515–1522, Jun. 2005.

[90]   A. I. C. Persiano and R. D. Rawlings, "A Mössbauer Investigation of Equiatomic FeCo with Vanadium and Niobium Additions," *Physica Status Solidi A Appl. Res.*, vol. 103, no. 2, pp. 547–556, Oct. 1987.

[91]   A. Williams, G. H. Kwei, A. T. Ortiz, M. Karnowski, and W. K. Warburton, "Combined neutron and x-ray powder diffraction study of Fe0.50Co0.48V0.02," *J. Mater. Res.*, vol. 5, no. 6, pp. 1197–1200, Jun. 1990.

[92]   Z. Pei, M. Eisenbach, S. Mu, and G. M. Stocks, "Error controlling of the combined Cluster-Expansion and Wang–Landau Monte-Carlo method and its application to FeCo," *Comput. Phys. Commun.*, vol. 235, pp. 95–101, Feb. 2019.

[93]   J. Deng *et al.*, "Texture Evolution in Heavily Cold-Rolled FeCo-2V Alloy during Annealing," *J. Mater. Sci. Technol.*, vol. 25, 2009.

[94]   K. Kawahara, "Structures and mechanical properties of an FeCo-2V alloy," *J. Mater. Sci.*, vol. 18, no. 11, pp. 3427–3436, Nov. 1983.

[95]   M. R. Pinnel, S. Mahajan, and J. E. Bennet, "Influence of thermal treatments on the mechanical properties of an Fe-Co-V alloy (Remendur)," *Acta Metallurgica*, vol. 24, no. 12, pp. 1095–1106, 1976.

[96]   N. S. Stoloff and R. G. Davies, "The plastic deformation of ordered FeCo and Fe3Al alloys," *Acta Metallurgica*, vol. 12, no. 5, pp. 473–485, 1964.

[97]   H. Sussman and S. L. Ehrlich, "Evaluation of the magnetostrictive properties of hiperco," *J. Acoust. Soc. Am.*, vol. 22, no. 4, pp. 499–506, Jul. 1950.

[98]   B. T. Hailer, "Effect of heat treatment on magnetic and mechanical properties of an iron-cobalt-vanadium-niobium alloy," Virginia Tech, 2001.

[99]   A. Díaz-Ortiz, R. Drautz, M. Fähnle, H. Dosch, and J. M. Sanchez, "Structure and magnetism in bcc-based iron-cobalt alloys," *Phys. Rev. B Condens. Matter*, vol. 73, no. 22, p. 224208, Jun. 2006.

[100]   E. Hug, O. Hubert, and I. Guillot, "Effect of strengthening on the magnetic behaviour of ordered intermetallic 2% V–CoFe alloys," *J. Magn. Magn. Mater.*, vol. 215–216, pp. 197–200, Jun. 2000.

[101]   B. Lorenz and C. Graham, "Magnetostriction Versus Magnetization of Hiperco 50 From 20ºC to 700ºC," *IEEE Trans. Magn.*, vol. 42, no. 12, pp. 3886–3888, Dec. 2006.

[102]   B. E. Lorenz and C. D. Graham, "High-temperature magnetostriction in polycrystalline Fe–co alloys," *IEEE Trans. Magn.*, vol. 40, no. 4, pp. 2751–2753, Jul. 2004.

[103]   D. Titus, E. James Jebaseelan Samuel, and S. M. Roopan, "Chapter 12 - Nanoparticle characterization techniques," in *Green Synthesis, Characterization and Applications of Nanoparticles*, A. K. Shukla and S. Iravani, Eds. Elsevier, 2019, pp. 303–319.

[104]   M. Matsumoto *et al.*, "Magnetic Properties of Rapidly Solidified Ribbon of Fe49Co49V2 and Spark-Plasma-Sintered Pellet of Its Powder," *Mater. Trans.*, vol. 51, no. 10, pp. 1883–1886, 2010.

[105]   D. M. Clifford, C. E. Castano, M. H. M. Tsui, J. V. Rojas, and E. E. Carpenter, "Tailoring the magnetic properties of FexCo(1-x) nanopowders prepared by a polyol process," *Dalton Trans.*, vol. 46, no. 31, pp. 10364–10373, Aug. 2017.

[106]   F. Sánchez-De Jesús, A. M. Bolarín-Miró, C. A. Cortés Escobedo, G. Torres-Villaseñor, and P. Vera-Serna, "Structural Analysis and Magnetic Properties of FeCo Alloys Obtained by Mechanical Alloying," *NML Tech. J.*, vol. 2016, Jul. 2016.

[107]   R. Bozorth, *Ferromagnetism*. Wiley-IEEE Press, 1978.

[108]   H. C. Fiedler and A. M. Davis, "The formation of gamma phase in Vanadium Permendur," *Metallurgical Transactions*, vol. 1, no. 4, pp. 1036–1037, Apr. 1970.

[109]   T. Nakajima *et al.*, "Effect of Annealing on Magnetostrictive Properties of Fe–Co Alloy Thin Films," *Mater. Trans.*, vol. 55, no. 3, pp. 556–560, 2014.

[110]   J. A. Ashby, H. M. Flower, and R. D. Rawlings, "Gamma phase in an Fe-Co-2%V alloy," *Met. Sci. Heat Treat.*, vol. 11, no. 3, pp. 91–96, 1977.

[111] T. Hasegawa, T. Niibori, Y. Takemasa, and M. Oikawa, "Stabilisation of tetragonal FeCo structure with high magnetic anisotropy by the addition of V and N elements," *Sci. Rep.*, vol. 9, no. 1, p. 5248, Mar. 2019.

[112] Y. Han, H. Wang, T. Zhang, Y. He, J. Coey, and C. Jiang, "Tailoring the heterogeneous magnetostriction in Fe-Co alloys," *J. Alloys Compd.*, vol. 699, pp. 200–209, Mar. 2017.

[113] D. Hunter *et al.*, "Giant magnetostriction in annealed Co(1-x)Fe(x) thin-films," *Nat. Commun.*, vol. 2, p. 518, Nov. 2011.

[114] R. G. Davies and N. S. Stoloff, "A study of grain growth in FeCo-V," *Trans Met Soc AIME*, vol. 236, pp. 1605–8, 1966.

[115] D. R. Thornburg, "High-strength high-ductility cobalt-iron alloys," *J. Appl. Phys.*, vol. 40, no. 3, pp. 1579–1580, Mar. 1969.

[116] N. S. Stoloff, "Ordered alloys — physical metallurgy and structural applications," *International Metals Reviews*, vol. 29, no. 1, pp. 123–135, Jan. 1984.

[117] C.-H. Shang, R. C. Cammarata, T. P. Weihs, and C. L. Chien, "Microstructure and Hall–Petch behavior of Fe–Co-based Hiperco© alloys," *J. Mater. Res.*, vol. 15, no. 4, pp. 835–837, Apr. 2000.

[118] J. A. Silva, C. Gouveia, G. Dinis, A. M. Pinto, and A. M. Pereira, "Giant magnetostriction in low-concentration magnetorheological elastomers," *Composites Part B*, vol. 243, p. 110125, Aug. 2022.

[119] A. K. Bastola, M. Paudel, L. Li, and W. Li, "Recent progress of magnetorheological elastomers: a review," *Smart Mater. Struct.*, vol. 29, no. 12, p. 123002, Nov. 2020.

[120] X. Gong, G. Liao, and S. Xuan, "Full-field deformation of magnetorheological elastomer under uniform magnetic field," *Appl. Phys. Lett.*, vol. 100, no. 21, p. 211909, May 2012.

[121] L. Ding, S. Xuan, J. Feng, and X. Gong, "Magnetic/conductive composite fibre: A multifunctional strain sensor with magnetically driven property," *Compos. Part A Appl. Sci. Manuf.*, vol. 100, pp. 97–105, Sep. 2017.

[122] A. K. Bastola and M. Hossain, "The shape – morphing performance of magnetoactive soft materials," *Mater. Des.*, vol. 211, p. 110172, Dec. 2021.

[123] H.-X. Deng and X.-L. Gong, "Application of magnetorheological elastomer to vibration absorber," *Commun. Nonlinear Sci. Numer. Simul.*, vol. 13, no. 9, pp. 1938–1947, Nov. 2008.

[124] H. Böse, T. Gerlach, and J. Ehrlich, "Magnetorheological elastomers — An underestimated class of soft actuator materials," *J. Intell. Mater. Syst. Struct.*, vol. 32, no. 14, pp. 1550–1564, Aug. 2021.

[125] X. Wang, F. Gordaninejad, M. Calgar, Y. Liu, J. Sutrisno, and A. Fuchs, "Sensing Behavior of Magnetorheological Elastomers," *J. Mech. Des.*, vol. 131, no. 9, Sep. 2009.

[126] G. Yun *et al.*, "Liquid metal-filled magnetorheological elastomer with positive piezoconductivity," *Nat. Commun.*, vol. 10, no. 1, p. 1300, Mar. 2019.

[127] L. Ding *et al.*, "Magnetism-Responsive Anisotropic Film with Self-Sensing and Multifunctional Shape Manipulation," *ACS Appl. Mater. Interfaces*, vol. 13, no. 11, pp. 13724–13734, Mar. 2021.

[128] A. Alkhalaf, A. Hooshiar, and J. Dargahi, "Composite magnetorheological elastomers for tactile displays: Enhanced MR-effect through bi-layer composition," *Composites Part B*, vol. 190, p. 107888, Jun. 2020.

[129] S. Qi, J. Fu, Y. Xie, Y. Li, R. Gan, and M. Yu, "Versatile magnetorheological plastomer with 3D printability, switchable mechanics, shape memory, and self-healing capacity," *Compos. Sci. Technol.*, vol. 183, p. 107817, Oct. 2019.

[130] Y. Li, J. Li, W. Li, and H. Du, "A state-of-the-art review on magnetorheological elastomer devices," *Smart Mater. Struct.*, vol. 23, no. 12, p. 123001, Nov. 2014.

[131] R. Ahamed, S.-B. Choi, and M. M. Ferdaus, "A state of art on magneto-rheological materials and their potential applications," *J. Intell. Mater. Syst. Struct.*, vol. 29, no. 10, pp. 2051–2095, Jun. 2018.

[132] R. Elhajjar, C.-T. Law, and A. Pegoretti, "Magnetostrictive polymer composites: Recent advances in materials, structures and properties," *Prog. Mater Sci.*, vol. 97, pp. 204–229, Aug. 2018.

[133] T. Liu and Y. Xu, "Magnetorheological elastomers: materials and applications," *Smart and Functional Soft Materials*, 2019.

[134] J. Winger, M. Schümann, A. Kupka, and S. Odenbach, "Influence of the particle size on the magnetorheological effect of magnetorheological elastomers," *J. Magn. Magn. Mater.*, vol. 481, pp. 176–182, Jul. 2019.

[135]   D. Garcia-Gonzalez, M. A. Moreno, L. Valencia, A. Arias, and D. Velasco, "Influence of elastomeric matrix and particle volume fraction on the mechanical response of magneto-active polymers," *Composites Part B*, vol. 215, p. 108796, Jun. 2021.

[136]   Y. Qiao, J. Zhang, M. Zhang, L. Liu, and P. Zhai, "A magnetic field- and frequency-dependent dynamic shear modulus model for isotropic silicone rubber-based magnetorheological elastomers," *Compos. Sci. Technol.*, vol. 204, p. 108637, Mar. 2021.

[137]   A. A. Zainudin *et al.*, "Rheological and Resistance Properties of Magnetorheological Elastomer with Cobalt for Sensor Application," *NATO Adv. Sci. Inst. Ser. E Appl. Sci.*, vol. 10, no. 5, p. 1638, Mar. 2020.

[138]   P. Soledad Antonel, G. Jorge, O. E. Perez, A. Butera, A. Gabriela Leyva, and R. Martín Negri, "Magnetic and elastic properties of CoFe2O4- polydimethylsiloxane magnetically oriented elastomer nanocomposites," *J. Appl. Phys.*, vol. 110, no. 4, p. 043920, Aug. 2011.

[139]   E. Yu Kramarenko *et al.*, "Magnetic and viscoelastic response of elastomers with hard magnetic filler," *Smart Mater. Struct.*, vol. 24, no. 3, p. 035002, Feb. 2015.

[140]   A. K. Bastola and M. Hossain, "A review on magneto-mechanical characterizations of magnetorheological elastomers," *Composites Part B*, vol. 200, p. 108348, Nov. 2020.

[141]   L. Chen, X.-L. Gong, W.-Q. Jiang, J.-J. Yao, H.-X. Deng, and W.-H. Li, "Investigation on magnetorheological elastomers based on natural rubber," *J. Mater. Sci.*, vol. 42, no. 14, pp. 5483–5489, Jul. 2007.

[142]   M. Lokander and B. Stenberg, "Performance of isotropic magnetorheological rubber materials," *Polym. Test.*, vol. 22, no. 3, pp. 245–251, May 2003.

[143]   M. Cvek, M. Kracalik, M. Sedlacik, M. Mrlik, and V. Sedlarik, "Reprocessing of injection-molded magnetorheological elastomers based on TPE matrix," *Composites Part B*, vol. 172, pp. 253–261, Sep. 2019.

[144]   C. Rodríguez *et al.*, "New elastomer–Terfenol-D magnetostrictive composites," *Sens. Actuators A Phys.*, vol. 149, no. 2, pp. 251–254, Feb. 2009.

[145]   Y. Kimura, S. Kanauchi, M. Kawai, T. Mitsumata, S. Tamesue, and T. Yamauchi, "Effect of Plasticizer on the Magnetoelastic Behavior for Magnetic Polyurethane Elastomers," *Chem. Lett.*, vol. 44, no. 2, pp. 177–178, Feb. 2015.

[146]   X. L. Gong, X. Z. Zhang, and P. Q. Zhang, "Fabrication and characterization of isotropic magnetorheological elastomers," *Polym. Test.*, vol. 24, no. 5, pp. 669–676, Aug. 2005.

[147]   L. Ge, X. Gong, Y. Fan, and S. Xuan, "Preparation and mechanical properties of the magnetorheological elastomer based on natural rubber/rosin glycerin hybrid matrix," *Smart Mater. Struct.*, vol. 22, no. 11, p. 115029, Oct. 2013.

[148]   L. Chen, X. L. Gong, and W. H. Li, "Effect of carbon black on the mechanical performances of magnetorheological elastomers," *Polym. Test.*, vol. 27, no. 3, pp. 340–345, May 2008.

[149]   R. Li and L. Z. Sun, "Dynamic mechanical behavior of magnetorheological nanocomposites filled with carbon nanotubes," *Appl. Phys. Lett.*, vol. 99, no. 13, p. 131912, Sep. 2011.

[150]   M. H. Ahmad Khairi *et al.*, "Role of additives in enhancing the rheological properties of magnetorheological solids: A review," *Adv. Eng. Mater.*, vol. 21, no. 3, p. 1800696, Mar. 2019.

[151]   S. H. Kwon, J. H. Lee, and H. J. Choi, "Magnetic Particle Filled Elastomeric Hybrid Composites and Their Magnetorheological Response," *Materials* , vol. 11, no. 6, Jun. 2018.

[152]   V. Kumar and D.-J. Lee, "Iron particle and anisotropic effects on mechanical properties of magneto-sensitive elastomers," *J. Magn. Magn. Mater.*, vol. 441, pp. 105–112, Nov. 2017.

[153]   S. R. Khimi and K. L. Pickering, "Comparison of dynamic properties of magnetorheological elastomers with existing antivibration rubbers," *Composites Part B*, vol. 83, pp. 175–183, Dec. 2015.

[154]   C. Y. Lo, S. W. Or, and H. L. W. Chan, "Large Magnetostriction in Epoxy-Bonded Terfenol-D Continuous-Fiber Composite With [112] Crystallographic Orientation," *IEEE Trans. Magn.*, vol. 42, no. 10, pp. 3111–3113, Oct. 2006.

[155]   T. Du, T. Zhang, H. Meng, X. Zhou, and C. Jiang, "A study on laminated structures in Terfenol-D/Epoxy particulate composite with enhanced magnetostriction," *J. Appl. Phys.*, vol. 115, no. 24, p. 243909, Jun. 2014.

[156]   M. Shamonin and E. Y. Kramarenko, "Highly Responsive Magnetoactive Elastomers," in *Novel Magnetic Nanostructures*, Elsevier, 2018, pp. 221–245.

[157]   A. Dobroserdova, M. Schümann, D. Borin, E. Novak, S. Odenbach, and S. Kantorovich, "Magneto-elastic coupling as a key to microstructural response of magnetic elastomers with flake-like particles," *Soft Matter*, vol. 18, no. 3, pp. 496–506, Jan. 2022.

[158]   E. Galipeau and P. Ponte Castañeda, "Giant field-induced strains in magnetoactive elastomer composites," *Proceedings of the Royal Society A: Mathematical, Physical and Engineering Sciences*, vol. 469, no. 2158, p. 20130385, Oct. 2013.

[159]   E. Galipeau and P. Ponte Castañeda, "The effect of particle shape and distribution on the macroscopic behavior of magnetoelastic composites," *Int. J. Solids Struct.*, vol. 49, no. 1, pp. 1–17, Jan. 2012.

[160]   S. M. Na, S. J. Suh, K. H. Shin, and S. H. Lim, "Effects of particle shape on magnetostrictive properties of polymer-bonded Fe–Co based alloy composites," *J. Magn. Magn. Mater.*, vol. 272–276, pp. 2076–2078, May 2004.

[161]   Q. Jin, Y. G. Xu, Y. Di, and H. Fan, "Influence of the particle size on the rheology of magnetorheological elastomer," in *Materials Science Forum*, 2015, vol. 809, pp. 757–763.

[162]   H. Vatandoost, S. Rakheja, and R. Sedaghati, "Effects of iron particles' volume fraction on compression mode properties of magnetorheological elastomers," *J. Magn. Magn. Mater.*, vol. 522, p. 167552, Mar. 2021.

[163]   C. Rodríguez *et al.*, "High magnetostriction polymer-bonded Terfenol-D composites," *Sens. Actuators A Phys.*, vol. 142, no. 2, pp. 538–541, Apr. 2008.

[164]   S. H. Lim, S. R. Kim, S. Y. Kang, J. K. Park, J. T. Nam, and D. Son, "Magnetostrictive properties of polymer-bonded Terfenol-D composites," *J. Magn. Magn. Mater.*, vol. 191, no. 1, pp. 113–121, Jan. 1999.

[165]   X. Guan, X. Dong, and J. Ou, "Magnetostrictive effect of magnetorheological elastomer," *J. Magn. Magn. Mater.*, vol. 320, no. 3, pp. 158–163, Feb. 2008.

[166]   H. Meng, T. Zhang, C. Jiang, and H. Xu, "Grain-⟨111⟩-oriented anisotropy in the bonded giant magnetostrictive material," *Appl. Phys. Lett.*, vol. 96, no. 10, p. 102501, Mar. 2010.

[167]   G. P. McKnight and G. P. Carman, "[112] Oriented Terfenol-D Composites," *Mater. Trans.*, vol. 43, no. 5, pp. 1008–1014, 2002.

[168]   N. Nersessian, S.-W. Or, and G. P. Carman, "Magneto-thermo-mechanical characterization of 1–3 type polymer-bonded Terfenol-D composites," *J. Magn. Magn. Mater.*, vol. 263, no. 1, pp. 101–112, Jul. 2003.

[169]   J. J. Liu, Z. B. Pan, X. H. Song, Z. R. Zhang, and W. J. Ren, "Enhanced magnetostrictive effect in epoxy-bonded TbxDy0.9−xNd0.1(Fe0.8Co0.2)1.93 pseudo 1–3 particulate composites," *J. Appl. Phys.*, vol. 117, no. 17, p. 17A914, May 2015.

[170]   J. J. Liu, Z. B. Pan, P. Z. Si, and J. Du, "Giant low-field magnetostriction of epoxy/TbxDy1−x(Fe0.8Co0.2)2 composites (0.20 ≤ x ≤ 0.40)," *Appl. Phys. Lett.*, vol. 103, no. 4, p. 042406, Jul. 2013.

[171]   X. Dong, M. Qi, X. Guan, J. Li, and J. Ou, "Magnetostrictive properties of titanate coupling agent treated Terfenol-D composites," *J. Magn. Magn. Mater.*, vol. 324, no. 6, pp. 1205–1208, Mar. 2012.

[172]   H. Y. Yin *et al.*, "Magnetostriction of TbxDy0.9−xNd0.1(Fe0.8Co0.2)1.93 compounds and their composites (0.20⩽x⩽0.60)," *J. Alloys Compd.*, vol. 582, pp. 583–587, Jan. 2014.

[173]   T. A. Duenas and G. P. Carman, "Large magnetostrictive response of Terfenol-D resin composites (invited)," *44th Annual Conference on Magnetism and Magnetic Materials*, vol. 87, no. 9 II, pp. 4696–4701, 2000.

[174]   R. Raveendran and M. A. G. Namboothiry, "Surface-Treated Poly(dimethylsiloxane) as a Gate Dielectric in Solution-Processed Organic Field-Effect Transistors," *ACS Omega*, vol. 3, no. 9, pp. 11278–11285, Sep. 2018.

[175]   P. Ferreira, Á. Carvalho, T. R. Correia, B. P. Antunes, I. J. Correia, and P. Alves, "Functionalization of polydimethylsiloxane membranes to be used in the production of voice prostheses," *Sci. Technol. Adv. Mater.*, vol. 14, no. 5, p. 055006, Oct. 2013.

[176]   K. Persson, "Materials Data on FeCo (SG:221) by Materials Project." Nov-2014.

[177]   A. Bellelli and A. Spaggiari, "Magneto-mechanical characterization of magnetorheological elastomers," *J. Intell. Mater. Syst. Struct.*, vol. 30, no. 17, pp. 2534–2543, Oct. 2019.

[178]   D. Romeis, V. Toshchevikov, and M. Saphiannikova, "Effects of local rearrangement of magnetic particles on deformation in magneto-sensitive elastomers," *Soft Matter*, vol. 15, no. 17, pp. 3552–3564, Apr. 2019.

[179]   F. Yang *et al.*, "The influence of film composition and annealing temperature on the microstructure and magnetic properties of FeCo thin films," *J. Mater. Sci.: Mater. Electron.*, vol. 28, no. 16, pp. 11733–11737, Aug. 2017.

[180]   V. A. Vas'ko *et al.*, "High saturation magnetization films of FeCoCr," *J. Appl. Phys.*, vol. 91, no. 10, pp. 6818–6820, May 2002.

[181]   Y. Li *et al.*, "Investigation of microstructure and soft magnetic properties of Fe65Co35 thin films deposited on different underlayers," *J. Appl. Phys.*, vol. 107, no. 9, p. 09A325, May 2010.

[182]   X.-L. Liu, L.-S. Wang, Q. Luo, L. Xu, B.-B. Yuan, and D.-L. Peng, "Preparation and high-frequency soft magnetic property of FeCo-based thin films," *Rare Met.*, vol. 35, no. 10, pp. 742–746, Oct. 2016.

[183]   F. Xu, Z. Xu, and Y. Yin, "Tuning of the Microwave Magnetization Dynamics in Dy-Doped Fe65Co35-Based Thin Films," *IEEE Trans. Magn.*, vol. 51, no. 11, pp. 1–4, Nov. 2015.

[184]   M. Liu, L. Hu, Y. Ma, M. Feng, S. Xu, and H. Li, "Effect of Pt doping on the preferred orientation enhancement in FeCo/SiO2 nanocomposite films," *Sci. Rep.*, vol. 9, no. 1, p. 10670, Jul. 2019.

[185]   Y. Fu, X. Cheng, and Z. Yang, "Magnetically soft and high-saturation-magnetization FeCo films fabricated by co-sputtering," *Phys. Status Solidi* , vol. 202, no. 6, pp. 1150–1154, May 2005.

[186]   V. A. Vas'ko, J. O. Rantschler, and M. T. Kief, "Structure, stress, and magnetic properties of high saturation magnetization films of FeCo," *IEEE Trans. Magn.*, vol. 40, no. 4, pp. 2335–2337, Jul. 2004.

[187]   M. Wolloch and D. Suess, "Strain-induced control of magnetocrystalline anisotropy energy in FeCo thin films," *J. Magn. Magn. Mater.*, vol. 522, p. 167542, Mar. 2021.

[188]   Cooke, M. R. J. Gibbs, and R. F. Pettifer, "Sputter deposition of compositional gradient magnetostrictive FeCo based thin films," *J. Magn. Magn. Mater.*, vol. 237, no. 2, pp. 175–180, Dec. 2001.

[189]   J. Boisse, H. Zapolsky, and A. G. Khachaturyan, "Atomic-scale modeling of nanostructure formation in Fe–Ga alloys with giant magnetostriction: Cascade ordering and decomposition," *Acta Mater.*, vol. 59, no. 7, pp. 2656–2668, Apr. 2011.

[190] H. Masumoto, "On the Thermal Expansion of Alloys of Cobalt, Iron and Chromium, and a New Alloy 'Stainless-Invar,'" *J. Jpn. Inst. Met.*, vol. 2, no. 4, pp. 141–146, 1938.

[191] C. M. Fang, G. A. de Wijs, H. T. Hintzen, and G. de With, "Phonon spectrum and thermal properties of cubic Si3N4 from first-principles calculations," *J. Appl. Phys.*, vol. 93, no. 9, pp. 5175–5180, May 2003.

[192] P. Plastics, "Thermal Properties of Plastic Materials." [Online]. Available: https://www.professionalplastics.com/professionalplastics/ThermalPropertiesofPlasticM aterials.pdf. [Accessed: 20-Feb-2023].

[193] M. Abdellahi, M. Tajally, and O. Mirzaee, "The effect of the particle size on the heating and drug release potential of the magnetic nanoparticles in a novel point of view," *J. Magn. Magn. Mater.*, vol. 530, p. 167938, Jul. 2021.

[194] W. S. Lee, K. S. Yeo, A. Andriyana, Y. G. Shee, and F. R. Mahamd Adikan, "Effect of cyclic compression and curing agent concentration on the stabilization of mechanical properties of PDMS elastomer," *Mater. Des.*, vol. 96, pp. 470–475, Apr. 2016.

[195] F. C. P. Sales, R. M. Ariati, V. T. Noronha, and J. E. Ribeiro, "Mechanical Characterization of PDMS with Different Mixing Ratios," *Procedia Structural Integrity*, vol. 37, pp. 383–388, Jan. 2022.

[196] G. Filipcsei, I. Csetneki, A. Szilágyi, and M. Zrínyi, "Magnetic Field-Responsive Smart Polymer Composites," in *Oligomers - Polymer Composites - Molecular Imprinting*, B. Gong, A. R. Sanford, and J. S. Ferguson, Eds. Berlin, Heidelberg: Springer Berlin Heidelberg, 2007, pp. 137–189.